

Copyright
by
Amy Dove Forestell
2009

The Dissertation Committee for Amy Dove Forestell
certifies that this is the approved version of the following dissertation:

**Exploring the Dynamics and Dark Halos of Elliptical
Galaxies at Large Radii**

Committee:

Karl Gebhardt, Supervisor

Thomas G. Barnes III

John Kormendy

Pawan Kumar

Christopher Sneden

P. Tim de Zeeuw

**Exploring the Dynamics and Dark Halos of Elliptical
Galaxies at Large Radii**

by

Amy Dove Forestell, B.A.; M.A.

DISSERTATION

Presented to the Faculty of the Graduate School of
The University of Texas at Austin
in Partial Fulfillment
of the Requirements
for the Degree of

DOCTOR OF PHILOSOPHY

THE UNIVERSITY OF TEXAS AT AUSTIN

August 2009

Dedicated to my family.
You are crazy and I love it.

Acknowledgments

I have very much enjoyed my time here at UT, and there have been many people along the way who deserve an acknowledgement. First I would like to thank my advisor Karl Gebhardt for his guidance and his understanding of the importance of my non-research activities. Many thanks to my committee: John Kormendy, Pawan Kumar, Chris Sneden, Tim de Zeeuw, and particularly Tom Barnes for being an excellent advisor during my early years here. Thanks to all the faculty and staff of the Astronomy Department for genuinely caring about the students and helping us succeed. I have also been fortunate to work with some of the great administrators here at UT; thanks to you all for striving to make this university the best that it can be. Thanks to the Graduate Student Assembly for giving me the sense of university community that graduate students often miss. Thanks to all of the other student leaders for all that you do and for welcoming me into the fraternity, particularly the Inner Circle. Thanks to the Friar Society for its membership, which is amazing, inspiring, and humbling. Thanks to all the graduate students, past and present, in the Astronomy Department for knowing how to have fun and making tons of wonderful memories. Thanks for the Tomaritas. And lastly, as the dedication indicates, thank you to my family for always supporting me.

Exploring the Dynamics and Dark Halos of Elliptical Galaxies at Large Radii

Publication No. _____

Amy Dove Forestell, Ph.D.

The University of Texas at Austin, 2009

Supervisor: Karl Gebhardt

Dark matter is now accepted as an integral part of our universe, and galaxy dynamics have long provided the most convincing observational evidence for dark matter. Spiral galaxies have traditionally been used for these studies because of their more simple kinematics, however elliptical galaxies need to be understood as well. In this dissertation I present deep long-slit spectroscopy from the University of Texas' Hobby-Eberly Telescope for a sample of elliptical galaxies. For a subsample of galaxies I fit axisymmetric orbit-superposition models with a range of dark halo density profiles. I find that all three galaxies modeled require a significant dark halo to explain their motions. However, the shape of the dark halo is not the expected NFW profile, but rather a profile with a flat central slope. I also discuss the galaxy masses, anisotropies, and stellar mass-to-light ratios.

Table of Contents

Acknowledgments	v
Abstract	vi
List of Tables	x
List of Figures	xi
Chapter 1. Introduction	1
1.1 Historical Background	1
1.2 Dark Matter in Elliptical Galaxies	3
1.2.1 Dynamical Models	4
1.2.2 Recent Results	7
1.3 This Study	7
Chapter 2. The Dark Halo of NGC 821	9
2.1 Introduction	9
2.2 Observations and Data Reduction	12
2.3 Kinematics	16
2.4 Dynamical Models	25
2.4.1 NFW Halo	28
2.4.2 Power-Law Halo	30
2.5 Results	30
2.5.1 NFW Halo	35
2.5.2 Power-Law Halo	47
2.5.3 Model Tests	47
2.5.4 Comparisons to Other Studies	51
2.5.5 Smoothing	56
2.5.6 Planetary Nebula Data	59
2.6 Conclusions	59

Chapter 3. The Dark Halo of NGC 6702	63
3.1 Introduction	63
3.2 Observations and Data Reduction	64
3.3 Kinematics	67
3.4 Dynamical Models	71
3.4.1 Dark Matter Halo Profiles	71
3.5 Results	77
3.5.1 NFW Halo	77
3.5.2 Logarithmic Potential Halo	83
3.5.3 Mass Measurement	90
3.6 Conclusions	93
Chapter 4. The Dark Halo of NGC 4697	98
4.1 Introduction	98
4.2 Data	101
4.2.1 Stellar Kinematics	101
4.2.2 Planetary Nebulae Kinematics	101
4.2.3 Light Profile	104
4.3 Dynamical Models	104
4.4 Results	107
4.4.1 Stellar data with no dark halo	109
4.4.2 All data with no dark halo	109
4.4.3 All data with logarithmic potential dark halo	109
4.4.4 NFW Halo	116
4.4.5 Mass-to-light ratio	116
4.4.6 Mass results	120
4.5 Conclusions	123
Chapter 5. Galaxy Kinematic Data	130
5.1 Observations	130
5.2 Data Reductions	144
5.3 Kinematic Measurements	149
5.4 Results	167

Chapter 6. Summary and Conclusions	183
Bibliography	187
Vita	200

List of Tables

2.1	NGC 821 Major Axis Kinematics	23
2.2	NGC 821 Minor Axis Kinematics	24
2.3	NGC 821 Best-Fitted Halo Model Results	39
2.4	NGC 821 Smoothing Model Results	58
3.1	NGC 6702 Major Axis Kinematics	73
3.2	NGC 6702 Minor Axis Kinematics	74
3.3	NGC 6702 Best-Fitted Halo Model Results	79
3.4	NGC 6702 Best-Fitted Halo Model Mass Results at $1R_e$ ($29''$)	90
3.5	NGC 6702 Best-Fitted Halo Model Mass Results Within Our Data	90
4.1	NGC 4697 Best-Fitted Parameters	124
4.2	NGC 4697 Best-Fitted Halo Model Mass Results at $1R_e$	125
4.3	NGC 4697 Best-Fitted Halo Model Mass Results Within The Kinematic Data	129
5.1	Grisms	131
5.2	Galaxy Observations	132
5.3	Galaxy Properties	133
5.4	g2 Template Stars	155
5.5	g3 Template Stars	156
5.6	NGC 2832 Major Axis Kinematics	176
5.7	NGC 2832 Minor Axis Kinematics	177
5.8	NGC 3379 Major Axis Kinematics	178
5.9	NGC 3842 Major Axis Kinematics	179
5.10	NGC 4889 Major Axis Kinematics	180
5.11	NGC 4889 Minor Axis Kinematics	181
5.12	NGC 661 Major Axis Kinematics	182

List of Figures

1.1 Rubin’s M31 rotation curve	3
1.2 Dark halo density profiles	6
2.1 NGC 821 major axis preparatory image	14
2.2 NGC 821 minor axis preparatory image	15
2.3 Example spectrum fit	18
2.4 Example line-of-sight velocity distributions	20
2.5 Gauss-Hermite moments of the LOSVDs	22
2.6 Major axis rms line-of-sight velocity as a function of radius . .	26
2.7 Surface brightness profile	29
2.8 Match of model and data LOSVDs	32
2.9 χ^2 as a function of mass-to-light ratio for all NFW halos . . .	33
2.10 χ^2 as a function of mass-to-light ratio for all logarithmic poten- tial halos	34
2.11 Scale radius and scale density χ^2 grid for NFW halos	36
2.12 χ^2 as a function of scale radius and scale density for NFW halos	37
2.13 Density and circular velocity for the best-fitted dark halo profiles	40
2.14 Enclosed mass within our kinematic data as a function of χ^2 .	41
2.15 Dark matter mass fraction	42
2.16 Internal moments for the model with no dark halo	44
2.17 Internal moments for the best-fitted NFW halo	45
2.18 Model and data Gauss-Hermite moments	46
2.19 Slope and density χ^2 grid for power-law halos	48
2.20 χ^2 as a function of power-law index and scale density for power- law halos	49
2.21 Internal moments for the best-fitted power-law halo.	50
2.22 Difference in χ^2 between the no dark halo and the best-fitted power law halo in each spatial bin	52

2.23	Difference in χ^2 between the no dark halo and the best-fitted NFW halo in each spatial bin	53
2.24	Ratio of radial to tangential dispersion with planetary nebula data	60
3.1	NGC 6702 major axis preparatory image	65
3.2	NGC 6702 minor axis preparatory image	66
3.3	Surface brightness profile	68
3.4	Example spectrum fit	70
3.5	Example line-of-sight velocity distributions	72
3.6	Gauss-Hermite moments of the LOSVDs	75
3.7	Match of model and data LOSVDs	78
3.8	χ^2 grids for the NFW halos	80
3.9	χ^2 as a function of scale radius, scale density, concentration, and M/L_V for the NFW halo models	81
3.10	Density and circular velocity for the best-fitted dark halo profiles	82
3.11	Internal moments for the model with no dark halo	84
3.12	Internal moments for the best-fitted NFW halo	85
3.13	Model and data Gauss-Hermite moments	86
3.14	χ^2 grids for the logarithmic potential halos	87
3.15	χ^2 as a function of M/L_V , radius, and circular velocity for the logarithmic potential halos	88
3.16	Internal moments for the best-fitted logarithmic potential halo	89
3.17	Mass within our kinematic data range for the NFW halos . . .	91
3.18	Mass within our kinematic data range for the logarithmic potential halos	92
3.19	Mass profiles for the NFW halos	94
3.20	Mass profiles for the logarithmic potential halos	95
3.21	Mass profiles for the best-fitted halos	96
4.1	NGC 4697 composite image from 2MASS	100
4.2	Location of planetary nebulae on the sky	102
4.3	Example line-of-sight velocity distribution	103
4.4	Gauss-Hermite moments of the LOSVDs	105

4.5	Surface brightness profile	106
4.6	Match of model and data LOSVDs	108
4.7	χ^2 grid for the models with no dark halo and stellar data only	110
4.8	χ^2 grid for the models with no dark halo	111
4.9	χ^2 grid for the logarithmic potential halos	113
4.10	Density and circular velocity for the best-fitted dark halo profile	114
4.11	Difference in χ^2 between the no dark halo and the best-fitted logarithmic potential halo in each spatial bin	115
4.12	Internal moments for the model with no dark halo	117
4.13	Internal moments for the best-fitted NFW halo	118
4.14	χ^2 grids in M/L_V , black hole mass, concentration, and core radius for the NFW halos	119
4.15	$B-R$ color and derived V band mass-to-light ratio as a function of radius	121
4.16	Density and circular velocity using the mass-to-light ratio derived from data	122
4.17	Mass within $1R_e$	124
4.18	Mass within our kinematic data range	125
4.19	Mass profiles for the best-fitted halos	126
5.1	NGC 2832 major axis preparatory image	134
5.2	NGC 2832 minor axis preparatory image	135
5.3	NGC 3379 major axis preparatory image	136
5.4	NGC 3842 major axis preparatory image	137
5.5	NGC 3842 minor axis preparatory image	138
5.6	NGC 4889 major axis preparatory image	139
5.7	NGC 4889 minor axis preparatory image	140
5.8	NGC 6086 major axis preparatory image	141
5.9	NGC 6086 minor axis preparatory image	142
5.10	NGC 661 major axis preparatory image	143
5.11	NGC 821 major axis data before reductions	145
5.12	NGC 821 major axis reduced data	146
5.13	NGC 2832 major axis data before reductions	147
5.14	NGC 2832 major axis reduced data	148

5.15	NGC 2832 major axis example continuum fit	150
5.16	NGC 2832 major axis example continuum fit	151
5.17	Example spectrum fit for g2	153
5.18	Example spectrum fit for g3	154
5.19	NGC 2832 major axis example spectrum fit	157
5.20	NGC 4889 major axis example spectrum fit	158
5.21	NGC 4889 minor axis example spectrum fit	159
5.22	NGC 661 major axis example spectrum fit	160
5.23	NGC 2832 minor axis example spectrum fit	161
5.24	NGC 3379 major axis example spectrum fit	162
5.25	NGC 3842 major axis example spectrum fit	163
5.26	NGC 3842 minor axis example spectrum fit	164
5.27	NGC 6086 major axis example spectrum fit	165
5.28	NGC 6086 minor axis example spectrum fit	166
5.29	Example line-of-sight velocity distributions	168
5.30	Gauss-Hermite moments of the LOSVDs for NGC 2832 major axis	169
5.31	Gauss-Hermite moments of the LOSVDs for NGC 2832 minor axis	170
5.32	Gauss-Hermite moments of the LOSVDs for NGC 3379 major axis	171
5.33	Gauss-Hermite moments of the LOSVDs for NGC 3842 major axis	172
5.34	Gauss-Hermite moments of the LOSVDs for NGC 4889 major axis	173
5.35	Gauss-Hermite moments of the LOSVDs for NGC 4889 minor axis	174
5.36	Gauss-Hermite moments of the LOSVDs for NGC 661 major axis	175

Chapter 1

Introduction

1.1 Historical Background

Studies of galaxies have long provided the most convincing observational evidence for dark matter. Useful reviews of early dark matter studies are provided by Faber & Gallagher (1979) and Trimble (1987). Fritz Zwicky showed perhaps the first dark matter evidence in 1933, though the result was not widely accepted by the astronomical community. He measured the velocity dispersions of clusters of galaxies and found that they required 10 to 100 times more mass than accounted for by luminous matter to keep them bound. There followed a considerable time period without much study in this area (Kahn & Woltjer, 1959; Neyman et al., 1961) until the subject resurfaced in the late 1960s.

Vera Rubin is credited with pioneering the modern field of studying dark matter via galaxy rotation profiles. In 1970 she and Kent Ford published a rotation curve of our nearby neighbor Andromeda (M31) based on HII regions extending well beyond the main stellar bulk of the galaxy. Figure 1.1 shows this original result (Rubin & Ford, 1970) overlaid on a visible image of M31 for comparison. Although basic Newtonian gravitational theory says that an

object farther from a central mass will orbit more slowly, M31 clearly shows objects far away from the center traveling as fast as those close to the center. There must be mass at large radii other than what we can see.

Other groups, such as Ostriker et al. (1974) and Einasto et al. (1974) also showed similar results, and the following Annual Review of galaxy masses (Faber & Gallagher, 1979) concluded that, “After reviewing all the evidence, it is our opinion that the case for invisible mass in the Universe is very strong and getting stronger.” Rubin then revisited the subject and published velocity curves of 21 spiral (Sc) galaxies (Rubin et al., 1980). All of them showed increasing or constant velocities at large radii. The authors conclude that, “This form for the rotation curves implies that the mass is not centrally condensed, but that significant mass is located at large R. . . . The mass is not converging to a limiting mass at the edge of the optical image. The conclusion is inescapable that non-luminous matter exists beyond the optical galaxy.” They further propose that all Sc galaxies sit in potential wells, that we would now call dark halos, and that the optical galaxies define only that region in which matter happens to be luminous. Rubin herself wrote that, “This paper was enormously influential in convincing astronomers that most of the matter in the universe is dark, and much of it is clumped about galaxies.” (CWP, 2001)

Meanwhile, evidence for dark matter had started to come from other places as well, such as stability arguments (Ostriker & Peebles, 1973) and x-ray observations (Fabricant & Gorenstein, 1983). Since that time innumerable studies of galaxies, dwarf galaxies, and galaxy clusters have strengthened the

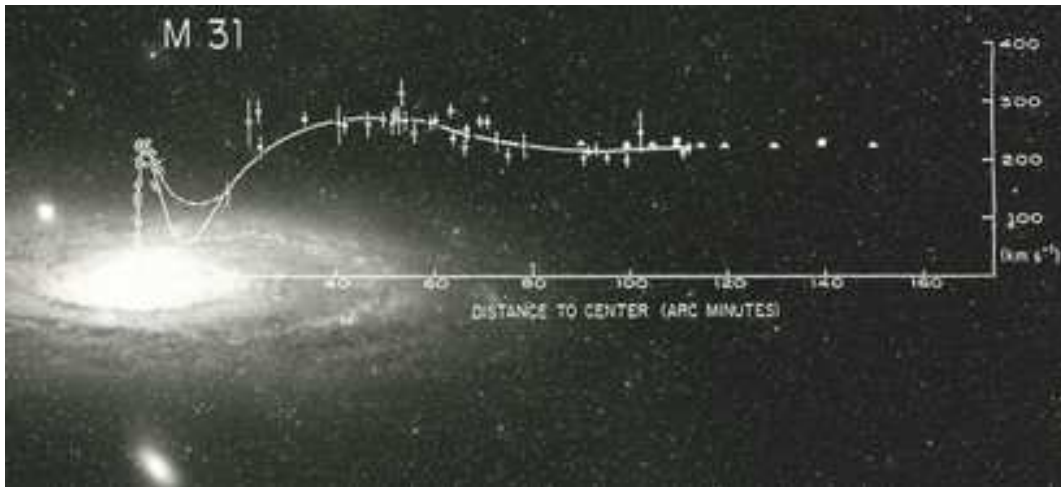


Figure 1.1: Rotation curve of M31 from Rubin & Ford (1970) overlaid on an optical image. Photo credit Vera Rubin and Janice Dunlap, <http://www.dtm.ciw.edu/component/content/122?task=view>

evidence for this missing dark matter to the point that it is now standardly accepted as an integral component of galaxies, influencing nearly all aspects of a galaxy’s formation and structure.

These early results seemed to show that dark matter made up as much as 90% of the universe. Our current picture shows that they were on the right track, as we now think that only 4.4% of the universe is composed of normal luminous matter, 21.4% is dark matter, and 74.2% is dark energy (Hinshaw et al., 2009).

1.2 Dark Matter in Elliptical Galaxies

Most of the early dynamical studies of the mass in individual galaxies focused on spiral galaxies because of their relatively simple disk structure and

the ability to use gas to measure kinematics well beyond the visible stellar light. Elliptical galaxies are more difficult to study, but it is also important to understand their dark halo structure because of their different formation and evolutionary history. When it is possible, elliptical galaxy potentials are often probed using test particles (e.g. globular clusters and planetary nebulae), x-ray gas, or gravitational lensing. Elliptical galaxies are not flattened by rotation, but by the anisotropy of their velocity dispersion tensor (Binney, 1978; Davies et al., 1983). Thus one must assume something about isotropy, or lack thereof, and the level of rotational support in order to derive a mass measurement.

1.2.1 Dynamical Models

Previous studies of elliptical galaxies have depended on many assumptions in order to model the kinematics. Often the spherical Jeans equation was used, either assuming isotropy or introducing anisotropy through an assumed analytic distribution function (DF, the number of stars per unit volume in the phase space of positions and velocities). Saglia et al. (1992) studied the velocity dispersion profiles of 10 elliptical galaxies using anisotropic two-component models and found that the amount of dark matter at the half-light radius is of the order of the luminous mass. van der Marel (1991) modeled 37 ellipticals with axisymmetric two-integral models and interpreted his results as evidence for radial anisotropy. Kronawitter et al. (2000) and Gerhard et al. (2001) modeled a sample of 21 elliptical galaxies using spherical models and analytic functions of the DF. They found that most galaxies show radial anisotropy

and that dark matter constitutes about 10%-40% of the mass at one effective radius, predicting equal luminous and dark matter at 2-4 effective radii.

More recently, orbit-based models based on the technique of Schwarzschild (1979) have been developed by a few groups. Beginning with spherical models (Richstone & Tremaine, 1984; Rix et al., 1997) and then axisymmetric models (Cretton et al., 1999; Gebhardt et al., 2000), this orbit-based technique is routinely used to measure central black holes (van der Marel et al., 1998; Gebhardt et al., 2000; Cappellari et al., 2002; Verolme et al., 2002; Gebhardt et al., 2003), and have been expanded to model dark halos as well (Rix et al., 1997; Thomas et al., 2005; Gebhardt & Thomas, 2009). Now these three-dimensional, non-parametric, axisymmetric, orbit-based models utilizing the full velocity distribution are considered the gold standard for dynamical modeling of galaxies.

One characteristic, and perhaps weakness, of these models is that a dark matter density profile must be assumed. The Navarro, Frenk, and White (Navarro et al., 1996b, NFW) profile has become the standard of cosmological studies, but other profiles such as isothermal and logarithmic potential are also frequently used for these models. Several well-known dark matter halo density profiles are shown in Figure 1.2.

Aside from the details of the models, another weakness of these previous studies is the radial extent of the data. It is difficult to obtain stellar kinematics to even one effective radius, where the dark mass is only beginning to have a measurable effect on motions. Additionally, most models used

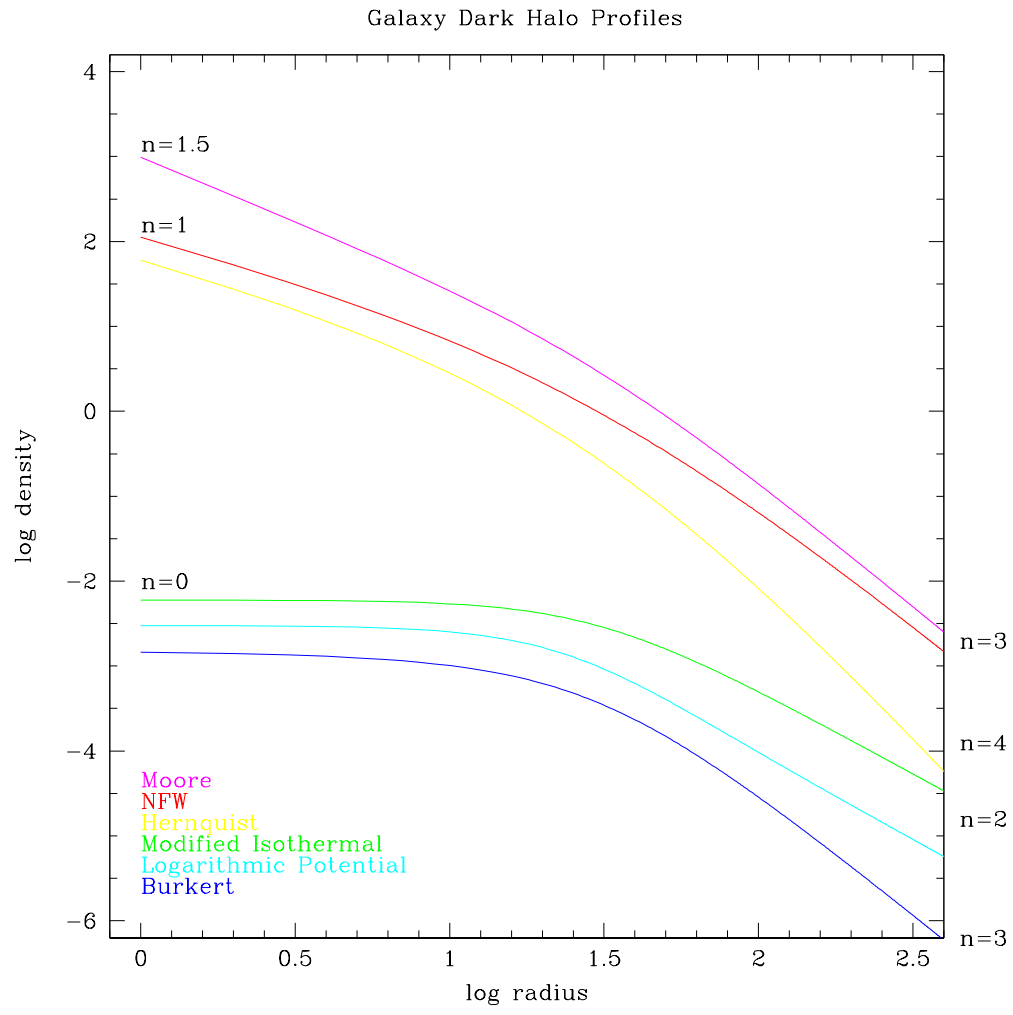


Figure 1.2: Several well-known dark matter halo density profiles.

only velocity and velocity dispersion information, rather than utilizing the full velocity distribution or its higher order moments.

1.2.2 Recent Results

The so-called standard picture of dark matter in elliptical galaxies has not been without its challenges. In the past there have been several elliptical galaxies that have been well-fit without any dark mass (Katz & Richstone, 1985; Bertin et al., 1994), and more recently this possibility has been brought to the forefront. Romanowsky et al. (2003) studied three elliptical galaxies using planetary nebulae as tracers and found small line-of-sight velocity dispersions. They applied spherical Jeans models and concluded that these galaxies are consistent with having little or no dark halo. Dekel et al. (2005) used disk galaxy merger simulations to show that large anisotropies can be created in the resulting elliptical galaxies, and that this anisotropy in combination with the different density profile of a young population could explain how the low dispersions from planetary nebulae measurements are also consistent with typical dark matter halos. The planetary nebulae group then revisited one of their galaxies in detail and defended their conclusion, saying that they had accounted for reasonable anisotropy in their models (Douglas et al., 2007).

1.3 This Study

In this dissertation I analyze the dynamics and dark halos of a sample of elliptical galaxies. My kinematic data come from the 9.2-meter Hobby-Eberly

Telescope (HET), which is ideally suited for deep spectral observations. I use fully general orbit-superposition models as described above to resolve the degeneracy between mass and anisotropy. In Chapter 2 I model HET data of NGC 821, one of the galaxies in the Romanowsky et al. (2003) study described above. In Chapter 3 I similarly model another elliptical galaxy, NGC 6702. Chapter 4 gives models of planetary nebula kinematics of NGC 4697. Chapter 5 shows the kinematic results of my remaining HET galaxy sample. And finally, Chapter 6 gives a summary and conclusions.

Chapter 2

The Dark Halo of NGC 821

2.1 Introduction

Cold dark matter is now accepted as an integral part of our universe, and recent observations have continued to provide support for its existence (Komatsu et al., 2008). Part of the picture of the universe is that galaxies are surrounded by massive dark matter halos in which they formed (White & Rees, 1978; Blumenthal et al., 1984). Recently cosmological simulations have become detailed enough to reach the level of individual galaxy formation (Naab et al., 2007; Governato et al., 2007), and comparisons with data can help further constrain cosmological theory (Ostriker & Steinhardt, 2003). Indeed, spiral galaxy rotation curves are one of the strongest pieces of observational evidence for the existence of dark matter (van Albada et al., 1985; Persic et al., 1996; Sofue & Rubin, 2001). It is also important to study the dark halo structure of elliptical galaxies because of their different formation and evolution. However it is more difficult to measure dark matter in elliptical galaxies because of a lack of tracers at large radii where dark matter is thought to dominate. The best way to measure the underlying gravitational potential is to use kinematics from the stellar population, but this has been limited due to the faintness of stellar light in the outer regions of galaxies (Gerhard

et al., 2001). Dark matter in elliptical galaxies has therefore been studied in other ways, such as via X-ray emission (Loewenstein & White, 1999; Mathews & Brighenti, 2003), gravitational lensing (Keeton, 2001; Mandelbaum et al., 2008), and using individual velocities as in nearby dwarf ellipticals (Mateo, 1998; Kleya et al., 2002). In order to study a more representative sample of galaxies, tracers such as globular clusters (Zepf et al., 2000; Pierce et al., 2006) and planetary nebulae (Méndez et al., 2001; Romanowsky et al., 2003; Coccato et al., 2009) have been used to probe the outer parts of elliptical galaxies, though it is difficult to get a significant sample size. Additional issues arise with these tracers, as discussed below, such as understanding their radial profile. With larger telescopes we are now able to measure stellar kinematics from integrated light to larger radii, thus closing the gap between stars and the large-radii tracers.

Meanwhile dynamical models of galaxies have also improved. Rather than previous spherical models that use analytic distribution functions (DFs; Gerhard et al., 2001), orbit-based axisymmetric models are now available. These fully general models, based on the technique of Schwarzschild (1979), provide detailed information on the orbital structure of the galaxy, including the DF and its projections, such as velocity anisotropy. Orbit-based models are now frequently applied to galaxies for studies of both dark halos and central black holes (Rix et al., 1997; van der Marel et al., 1998; Cretton et al., 1999; Gebhardt et al., 2000; Cappellari et al., 2002; Verolme et al., 2002; Gebhardt et al., 2003; Thomas et al., 2005).

The elliptical galaxy NGC 821 is an example in which the use of large-radii tracers has provided an intriguing result. Romanowsky et al. (2003) study the dark halo of NGC 821 using approximately 100 planetary nebula velocities and found small line-of-sight velocity dispersions that are consistent with little or no dark halo. Dekel et al. (2005) use disk galaxy merger simulations to show that large anisotropies can be created in the resulting elliptical galaxies, and that this anisotropy in combination with the different density profile of a young population could explain how the low dispersions from planetary nebulae measurements are also consistent with typical dark matter halos. Our study uses deep long-slit spectroscopy of NGC 821 from the 9.2-meter Hobby-Eberly Telescope to obtain stellar kinematics to greater than 2 effective radii in hopes of further constraining the dark halo of this interesting galaxy.

Weijmans et al. (2009) model NGC 821 using data from SAURON, both at small radii (which we include in our analysis) and newer data at large radii. We find similar results both for the kinematics and for the dark halo properties. Comparison between the two studies is presented in their paper and within this paper.

NGC 821 is classified as an E6? (de Vaucouleurs et al., 1991). It has disk-like isophotes (Lauer, 1985; Bender et al., 1988) and a power-law surface brightness profile (Ravindranath et al., 2001). The blue absolute magnitude is -20.27 (Trager et al., 2000). We use a distance of 23.44 Mpc taken from Cappellari et al. (2006), which adjusts the Tonry et al. (2001) values for the new Cepheids zero-point of Freedman et al. (2001). NGC 821 is not detected

in $H\alpha$ (Macchetto et al., 1996) or OIII (Sarzi et al., 2006). Point source and diffuse X-ray emission has been detected but there is no evidence for hot gas (Pellegrini et al., 2007a,b). NGC 821 is considered a fast rotator (Cappellari et al., 2007; Emsellem et al., 2007). Proctor et al. (2005) find that NGC 821 has very strong age and metallicity gradients, from ~ 4 Gyr and 3 times solar in the center to ~ 12 Gyr and less than $\frac{1}{3}$ solar at $1R_e$. It has an α -element enhancement of +0.3 dex. They conclude that NGC 821 has experienced a recent (~ 1 -4 Gyr ago) burst of star formation, most likely from in-situ gas and perhaps triggered by the accretion of a small satellite galaxy. This may be an indication that there are young planetary nebulae in this galaxy.

§2.2 describes the observations and data reduction; in §2.3 we describe the kinematic extraction; the dynamical models are described in §2.4; we present our results in §2.5 and give conclusions in §2.6.

2.2 Observations and Data Reduction

Long-slit spectra were taken with the Low-Resolution Spectrograph (Hill et al., 1998) on the Hobby-Eberly Telescope. We used the g2 grism and $1''$ by $4'$ slit over the wavelength range 4300 - 7300\AA . This setup gives a resolving power of 1300 or a full-width half-maximum (FWHM) resolution of about 230 km s^{-1} . Measurements of night sky line widths show that we can measure dispersions to about 110 km s^{-1} . The CCD frame (binned 2×2) has a plate scale of $0.47''/\text{pix}$ spatially and $2\text{\AA}/\text{pix}$ spectrally. The gain is $1.832 e^- \text{ ADU}^{-1}$ and readout noise is $5.10 e^-$. We used the Schott Glass blocking filter GG385,

which has a half-power point of the transmission around 385 nm. Preparatory images showing the sky before the slit has been inserted are shown in Figures 2.1 and 2.2. The slit runs from the top center to the bottom center.

NGC 821 was observed over eight nights in November 2003 for a total exposure time of approximately 5.5 and 2.3 hours on the major and minor axes respectively. Cadmium and Neon calibration lamp exposures and white light illumination flat fields were taken each night.

The data reduction was performed using standard techniques with fortran code developed from FITSIO programs. First we overscan correct and trim the images. Then we apply a flat correction using a normalized flat frame, taken from averaged instrumental flats obtained each night of observations. Next we rectify the images along the spatial axis using the calibration lamp lines as a reference.

For sky subtraction, we use the region of the slit that is furthest from the galaxy center. Since we only have a 4' slit, there will be some galaxy light in the region where we select sky. However, the surface brightness profile extends out 350" so we can accurately calculate the amount of galaxy in our background region. For our last extracted spectrum (at 90"), the amount of galaxy light that we are including as background light is 15% of the galaxy light for that last extraction. We have run simulations in order to determine whether this amount of contamination has an effect on the extracted kinematics. We take a high signal-to-noise galaxy spectrum and subtract off 15% of itself, and then extract the kinematics. Only for very high S/N does this amount have an effect

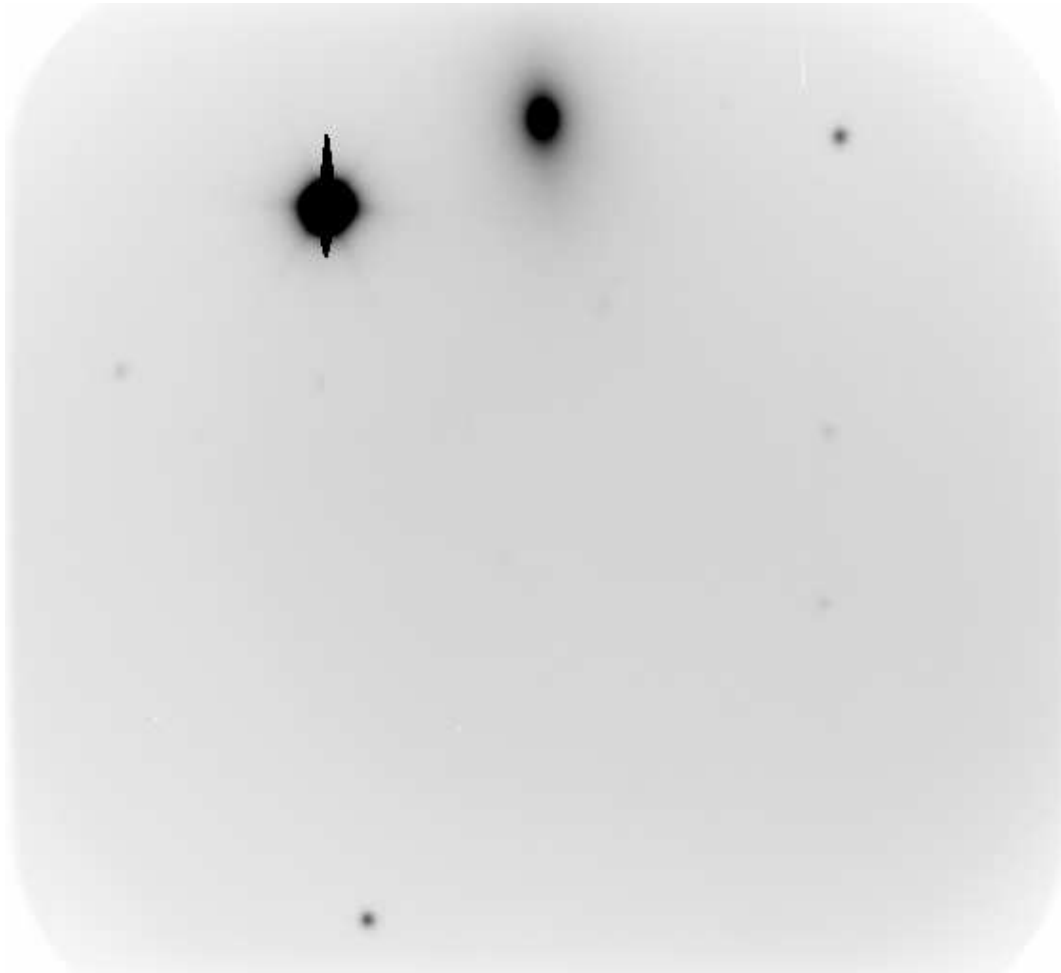


Figure 2.1: NGC 821 major axis preparatory image.

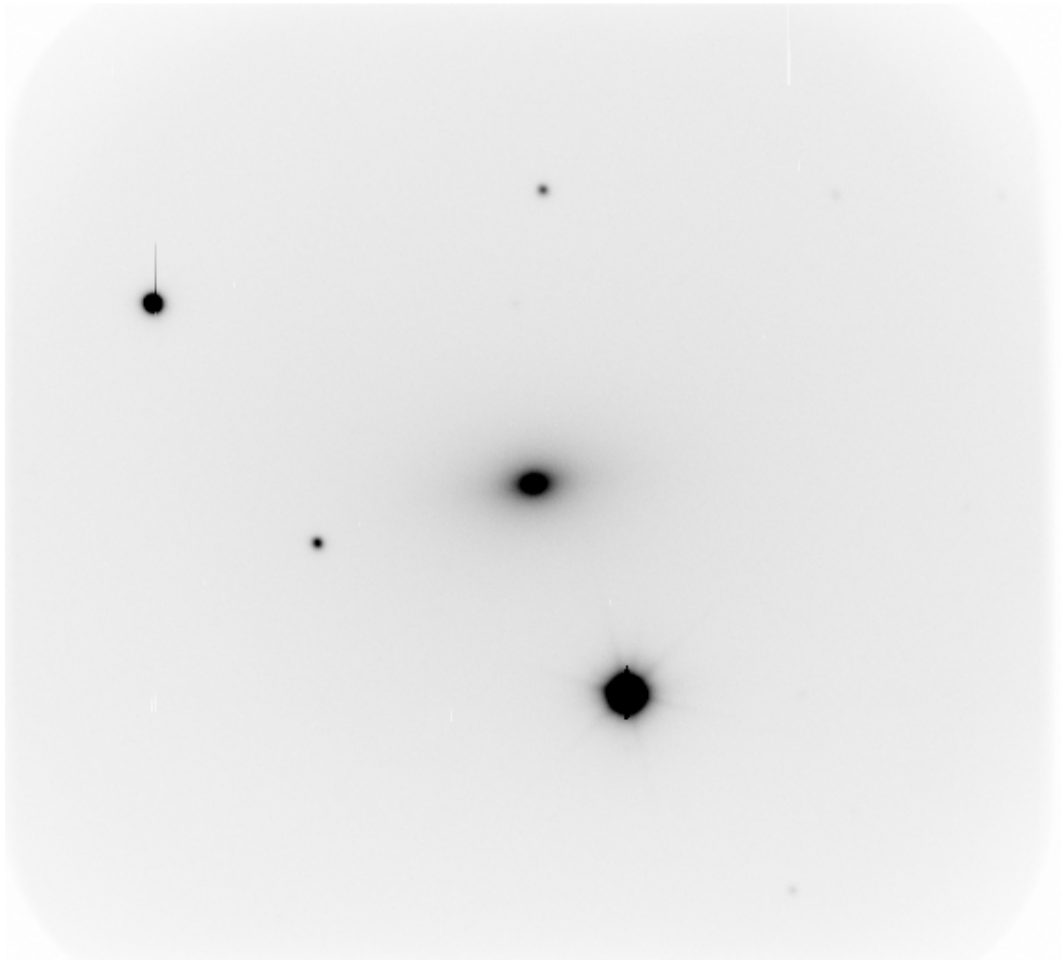


Figure 2.2: NGC 821 minor axis preparatory image.

and for the S/N for this dataset (as described below), we find no significant effect.

Finally we align and combine the images using the night sky lines and the galaxy as references.

2.3 Kinematics

We extract the spectra in radial bins along the major and minor axes. Because the seeing is approximately $2''$ we set the central bins to 5 pixels ($2.35''$). The outer bins are sized to obtain sufficient signal for kinematic analysis. Along the minor axis the spectra from either side of the galaxy were averaged at each radius. Along the major axis, the center of the galaxy was near the edge of the chip so only one side was extracted. Our farthest radial bin extends to $45''$ on the minor axis and $99''$ on the major axis, corresponding to a V-band surface brightness of 24.0 mag on the major axis. The radial extent in effective radii depends on the value of R_e used. The measured R_e of NGC 821 varies throughout the literature: $50''$ (RC3), $45''$ (Faber et al., 1989), $39''$ (Cappellari et al., 2006), $36''$ (Trager et al., 2000), and $16.7\text{--}18.3''$ (Bender et al., 1988). For the purpose of this discussion we adopt an R_e of $45''$. Thus our data extend to approximately $1R_e$ along the minor axis and $2R_e$ along the major axis.

We do not flux calibrate the spectra, and thus we remove the continuum in each spectra. We fit the local continuum by finding the biweight (Beers et al., 1990) in windows as described in Pinkney et al. (2003). The wavelength

solution was found using Cd and Ne calibration lamps.

We obtain a nonparametric line-of-sight velocity distribution (LOSVD) by deconvolving the galaxy spectrum with a set of stellar template spectra using the maximum penalized likelihood technique of Gebhardt et al. (2000). Tests of this technique are given in Pinkney et al. (2003). There are 30 evenly-spaced velocity bins of 54 km s^{-1} that represent the LOSVD. We vary the height in each bin and the weights of each template star to find the best match to the galaxy spectrum. We use nine stellar templates with types ranging from G dwarf to M giant from Leitherer et al. (1996), convolved to our spectral resolution.

For our kinematic analysis we used the spectral range $4800\text{-}5450\text{\AA}$ which matches the wavelength range of our template stars. This region includes the $H\beta$ and Mgb lines, however we exclude the Mgb region because it is enhanced (Proctor et al., 2005) and our template stars do not provide a proper fit. Barth et al. (2002) show that in pixel-space fitting routines the Mgb line is sensitive to template mismatch and the details of the fitting procedure. If the Mgb line is included in the fit, the measured dispersions are falsely high by as much as 20% to account for the abundance discrepancy. An example fit is shown in Figure 2.3.

The uncertainty of each velocity bin is obtained from Monte Carlo simulations. We convolve the best-fitted LOSVD and weighted stellar templates to obtain an initial galaxy spectrum. We then generate 100 realizations of the galaxy spectrum by adding Gaussian noise using an estimate of the initial

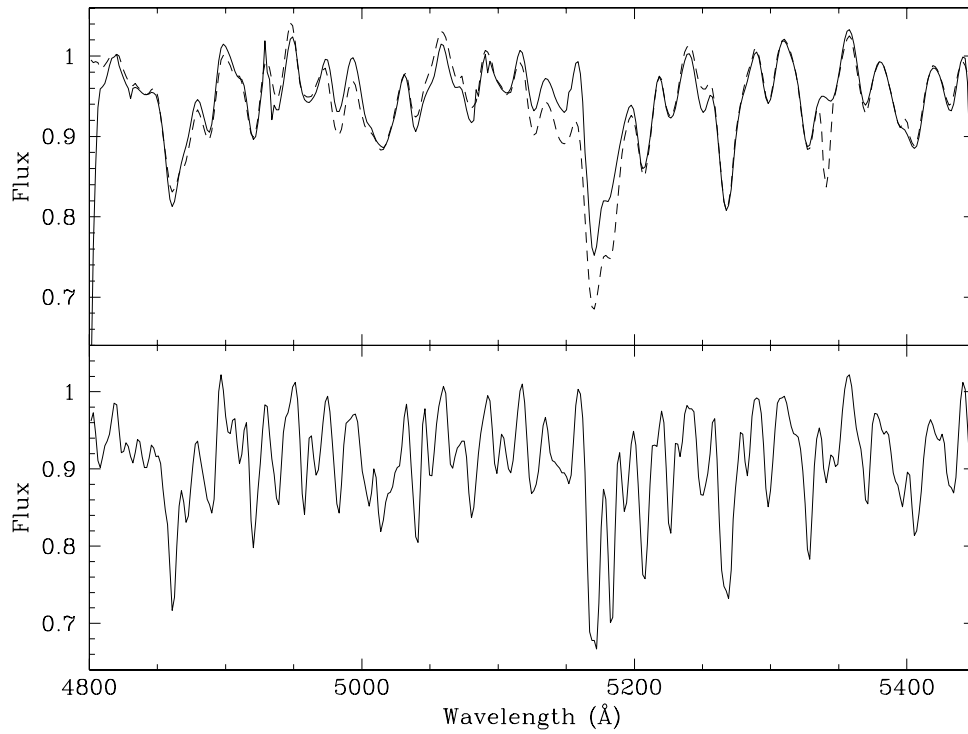


Figure 2.3: Spectrum of the combined, weighted template stars (lower panel), data from the central bin along the minor axis (dashed line, upper panel), and the template spectrum convolved with the best-fitted LOSVD (solid line, upper panel). The region from 5163 Å to 5228 Å is excluded from the fit.

rms. The LOSVD is determined for each realization as described above. The distribution of values in each velocity bin of the LOSVD provides an estimate of the 68% confidence bands. The median value of the dispersion from the 100 realizations compared to the initial dispersion reveals any possible bias in the dispersion measurement. Example LOSVDs are shown in Figure 2.4.

Although we use the full nonparametric velocity profile in the dynamic modeling, it is useful to compare moments of the distribution. In Figure 2.5 we plot, from top to bottom, the second moment as measured by $\sqrt{V^2 + \sigma^2}$, the first four Gauss-Hermite moments (mean velocity V , velocity dispersion σ , asymmetric deviations from Gaussian (skewness) h_3 , and symmetric deviations from Gaussian (kurtosis) h_4). The kinematic data are given in Table 2.1 and Table 2.2. For comparison, in Figure 2.5 are also plotted data from Pinkney et al. (2003) and Emsellem et al. (2004) extracted in a 1 arcsec slit along the major and minor axes. The second moment of the line-of-sight velocity, $(V^2 + \sigma^2)^{1/2}$ is slightly smaller than the other samples throughout the overlapping region. This may be caused by a slit misalignment (since V will be higher on the major axis) or template fitting difference. Since, however, our models are dominated by SAURON data in the center, this difference is not a major issue. We further run the dynamical models with using SAURON data alone and HET data alone, and find un-biased results from when using the combined dataset. The SAURON data are described in Emsellem et al. (2004). SAURON is a scientific project and integral-field spectrograph on the 4.2-m William Herschel Telescope on La Palma. Their kinematic data of NGC 821

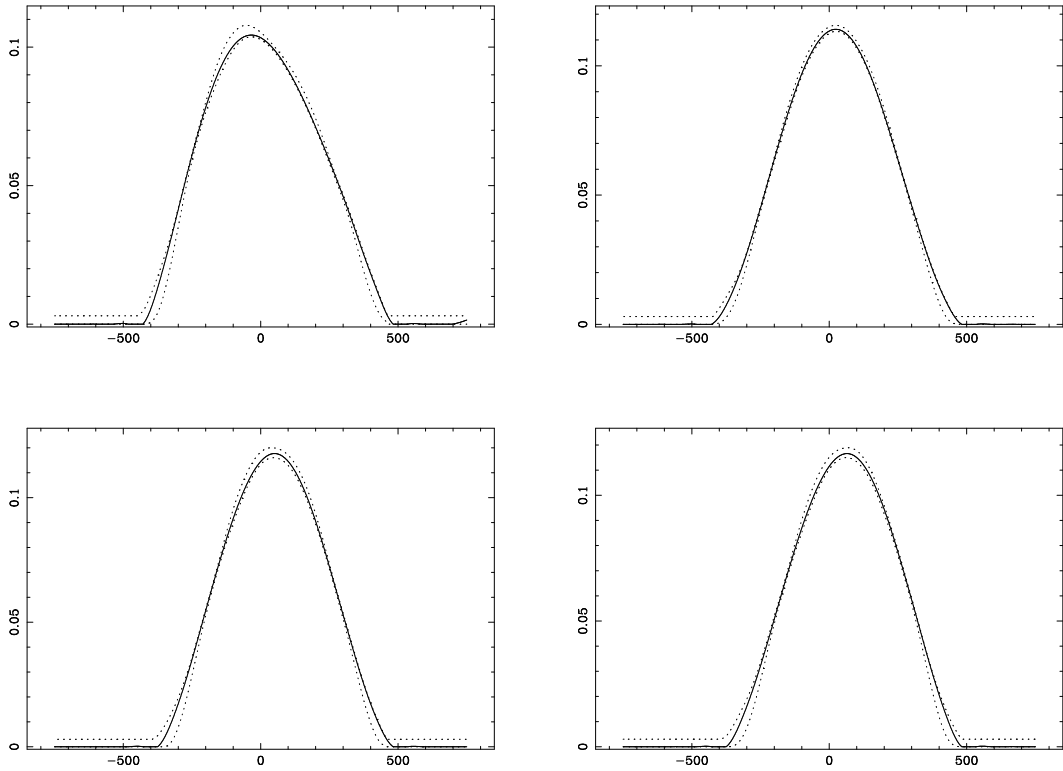


Figure 2.4: Line-of-sight velocity distributions (solid lines) with errors (dashed lines) for the first four radial bins along the major axis.

from SAURON extends to roughly $20''$.

Our h_4 values are more negative than the data from the literature. This discrepancy could be attributed to template mismatch (either in the published analysis or in ours), however we use a wide range of template stars and do not get a different result when more template stars are made available for the fit. It could also be that relying on Gauss-Hermite parameterization causes some differences since there are known correlations, especially with higher order moments (see Magorrian, 2006; Houghton et al., 2006). Since we fit the LOSVD directly in the dynamical models, a better comparison would be with those profiles, as opposed to their moments. The dark halo mass, however, is determined mainly by the radial profile of the second moment, and h_4 determines mainly the anisotropies. There is certainly some degeneracy between the two parameters, but we find no reason to believe that our h_4 values are incorrect. There are also kinematic points that have differences which are inconsistent with their reported uncertainties (for example, some of the minor axis points), and the uncertainties may be underestimated for those point. We run halo models without the most discrepant points and still find the same halo results as when they are included.

Weijmans et al. (2009) provide a new analysis of the SAURON data and also include additional data at large radii. Their furthest radial point is at $110''$ (which they refer to as $4 R_e$), whereas our last point is at $90''$ (which we refer to as $2 R_e$). The comparison between the two kinematic sets is shown in Figure 6 from Weijmans et al. (2009). There is excellent agreement between the

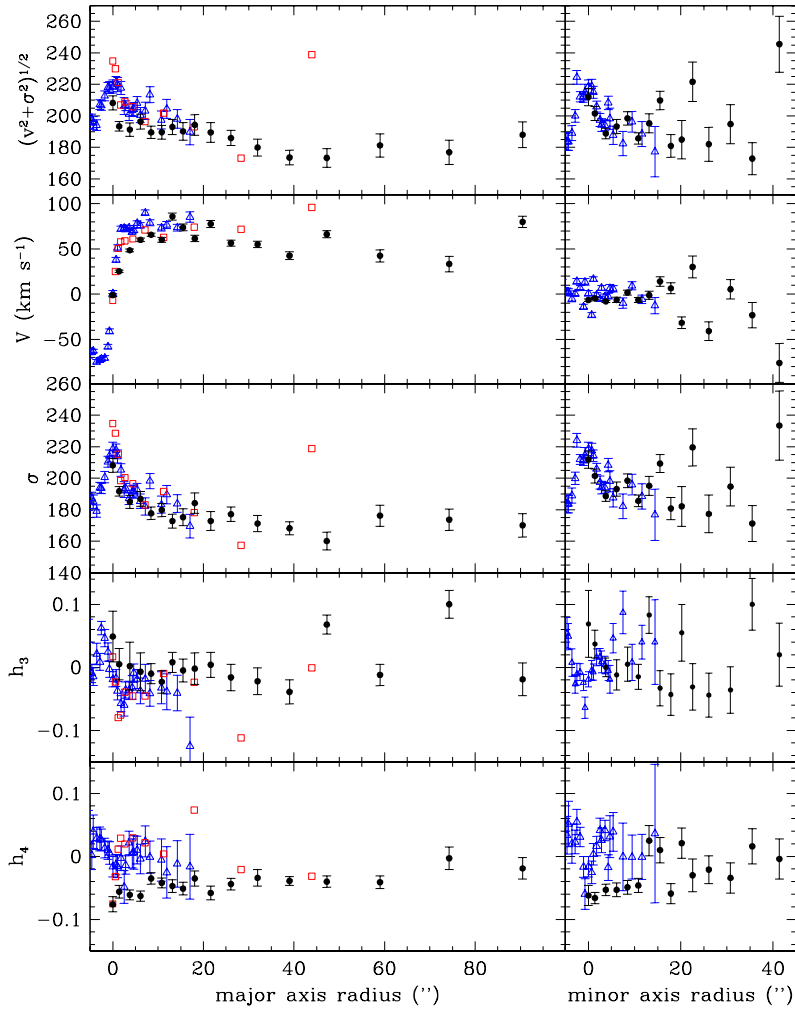


Figure 2.5: The second moment as measured by $\sqrt{V^2 + \sigma^2}$ and the Gauss-Hermite moments of the LOSVDs (mean velocity V , velocity dispersion σ , asymmetric deviations from Gaussian (skewness) h_3 , and symmetric deviations from Gaussian (kurtosis) h_4) along the major axis (left panel) and minor axis (right panel) for our data (black filled circles), SAURON (Emsellem et al., 2004) (blue open triangles), and Pinkney et al. (2003) (red open squares).

Table 2.1: NGC 821 Major Axis Kinematics

r <i>arcsec</i>	v <i>km s⁻¹</i>	ϵ_v	σ <i>km s⁻¹</i>	ϵ_σ	h_3	ϵ_{h_3}	h_4	ϵ_{h_4}
0.00	-1.052	1.652	208.238	4.428	0.049	0.040	-0.076	0.012
1.41	25.354	1.398	191.711	2.958	0.005	0.025	-0.056	0.010
3.76	48.531	1.554	185.062	4.159	0.002	0.038	-0.061	0.008
6.11	60.128	1.885	186.950	4.734	-0.007	0.030	-0.063	0.008
8.46	65.684	1.719	177.806	3.925	-0.010	0.016	-0.035	0.009
10.81	60.161	2.788	179.864	4.198	-0.023	0.018	-0.042	0.008
13.16	85.897	3.797	172.810	4.395	0.008	0.016	-0.047	0.010
15.51	73.793	3.761	175.294	5.348	-0.005	0.018	-0.051	0.010
18.09	61.667	3.374	184.249	6.398	-0.002	0.025	-0.035	0.012
21.62	77.695	3.912	172.867	5.928	0.004	0.020	-0.058	0.011
26.08	56.482	3.273	177.183	4.561	-0.016	0.021	-0.044	0.009
31.96	55.203	3.461	171.317	5.117	-0.022	0.021	-0.034	0.013
39.01	42.580	4.289	168.267	4.206	-0.039	0.019	-0.039	0.007
47.24	66.287	3.890	160.178	5.644	0.068	0.015	-0.040	0.009
58.99	42.405	6.677	176.268	6.687	-0.012	0.017	-0.041	0.010
74.26	33.396	8.498	173.736	6.793	0.100	0.022	-0.003	0.018
90.47	79.973	6.157	170.171	7.479	-0.019	0.026	-0.019	0.017

Table 2.2: NGC 821 Minor Axis Kinematics

r <i>arcsec</i>	v <i>km s⁻¹</i>	ϵ_v	σ <i>km s⁻¹</i>	ϵ_σ	h_3	ϵ_{h_3}	h_4	ϵ_{h_4}
0.00	-6.505	1.291	211.906	5.498	0.069	0.053	-0.062	0.016
1.41	-4.677	0.860	201.492	4.469	0.037	0.022	-0.066	0.009
3.76	-7.938	1.040	188.685	3.295	0.000	0.015	-0.053	0.009
6.11	-6.266	2.883	193.160	4.544	-0.012	0.024	-0.053	0.011
8.46	1.788	2.630	198.456	4.271	0.005	0.027	-0.049	0.011
10.81	-6.236	2.715	185.653	3.657	-0.015	0.020	-0.046	0.011
13.16	-1.074	4.468	195.258	6.038	0.083	0.029	0.025	0.024
15.51	14.057	5.216	209.357	5.57	-0.033	0.028	0.010	0.020
17.86	6.489	6.037	180.817	7.072	-0.043	0.033	-0.059	0.016
20.21	-31.594	6.407	182.219	12.623	0.055	0.045	0.021	0.024
22.56	30.061	12.078	219.630	11.806	-0.031	0.037	-0.030	0.026
26.08	-40.854	10.300	177.363	11.956	-0.044	0.035	-0.021	0.022
30.78	5.471	10.773	194.765	12.272	-0.036	0.037	-0.034	0.024
35.49	-23.156	14.053	171.308	11.394	0.100	0.041	0.016	0.028
41.36	-76.041	21.578	233.449	21.950	0.020	0.050	-0.004	0.032

two sets of kinematics. Furthermore, their re-analysis of the SAURON central pointing shows h_4 values now consistent with our numbers. The higher-order moments of the LOSVD are difficult to measure, and it is important to consider systematic difference in the analysis. The spectra from Weijmans et al. (2009) have lower signal-to-noise than our spectra, which could add to systematic difference. For this reason, our dynamical modeling does not include their kinematics, although we suspect there will be little difference in the overall results. Thus, we can compare the constraints on the dark matter parameters, which would include systematic differences in the kinematic samples used.

Figure 2.6 shows the rms line-of-sight velocity $(V^2 + \sigma^2)^{1/2}$ compared to the planetary nebula results of Romanowsky et al. (2003). Our largest radii data show higher rms line-of-sight velocities than the planetary nebulae, at about 3σ for their two largest radii points. Thus, there appears to be a significant difference in the kinematics between the two samples.

2.4 Dynamical Models

We use axisymmetric orbit superposition models based on the method of Schwarzschild (1979). The surface brightness profile is converted to a luminosity density profile using an assumed inclination. We assume an edge-on inclination for this analysis, which is reasonable given NGC 821's ellipticity of 0.40 (Cappellari et al., 2007). This luminosity density is converted to a mass density using a mass-to-light ratio (M/L_V) that is constant over the galaxy. A spherically symmetric dark halo density profile is added to the stellar density

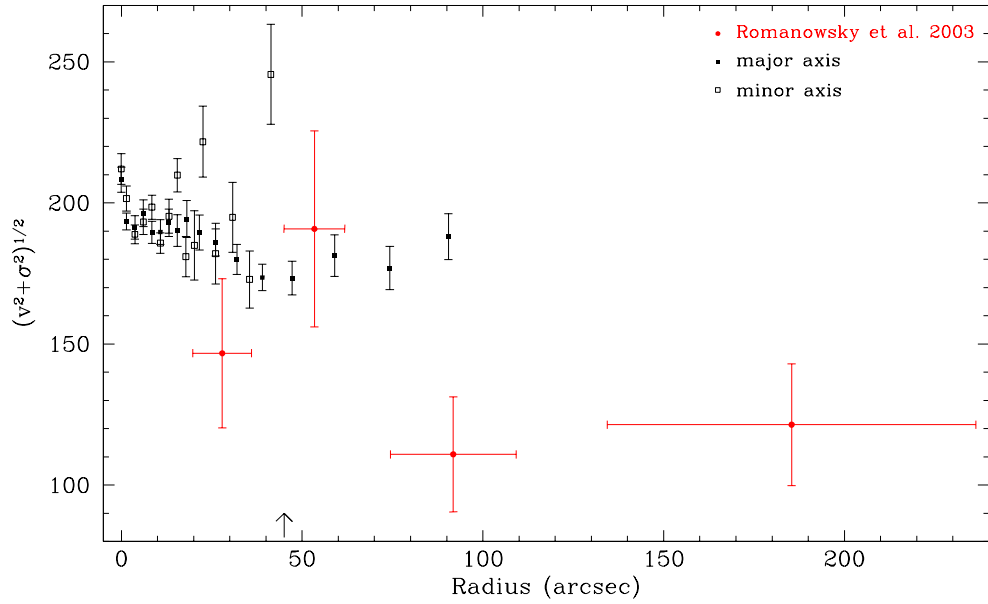


Figure 2.6: The rms line-of-sight velocity $(v^2 + \sigma^2)^{1/2}$ in km s^{-1} as a function of radius from our major axis data (filled squares) and minor axis data (open squares), compared to the data from planetary nebulae measurements (Romanowsky et al., 2003). We use v and σ as measured from a Gauss-Hermite fit; since we do not correct for the higher order moments, these values approximate the actual second moment. The arrow indicates the adopted R_e of the galaxy.

and this total mass density gives the galaxy's gravitational potential. Next individual stellar orbits are sampled in energy (E), angular momentum (L_z) and the third integral (I_3) and these orbits are integrated in the specified potentials. The galaxy is divided spatially into cells both in real space and in projection, and the amount of time that an orbit spends in a cell represents the mass contributed by that orbit. The orbits are combined with nonnegative weights to find the best-fitted superposition to match the data LOSVDs from both HET and SAURON and the light profile. This process is repeated for different dark halo density profiles and M/L_V values to find the halo potential that best fits the data, as determined by χ^2 (described in §2.5).

To reduce computational time, an orbit library is calculated for a given input dark halo plus stars with a mass-to-light ratio of one. The velocities are then scaled accordingly given the mass-to-light ratio before matching the data. The numbers reported are the actual density parameters, including this M/L factor, which gives the somewhat irregular parameter space grids (as seen in Figure 2.11).

We use the orbital weight fitting of Gebhardt et al. (2000, 2003); Siopis et al. (2009) with the orbit library sampling of Thomas et al. (2004, 2005). Our models differ from others (e.g. Cretton et al., 1999) in that we use maximum entropy (Richstone & Tremaine, 1988) and we utilize the full LOSVD, rather than its moments. Thomas et al. (2004, 2005) show the ability of our orbit libraries to recover dark halo profile from mock elliptical galaxy data. Therefore these models should accurately measure the properties of NGC 821

given the caveats that we assume an axisymmetric galaxy and spherical halo.

The orbits are computed in 4 angular bins and 15 radial bins from $0.3''$ to $300''$, which are similar in size to the HET data extraction bins. Our libraries have approximately 10000 total orbits.

To calculate our galaxy potential we use a composite surface brightness profile. Within $0.3''$ we use the profile from Lauer et al. (2005) as compiled in Pinkney et al. (2003) based on HST WFPC2 images in F555W. Outside of $0.3''$ we use a composite profile from HST PC F555W and the McDonald Observatory 0.8-m telescope in V (D. Fisher, private communication). The surface brightness deprojection is based on a nonparametric estimate of the density using smoothing splines (see Gebhardt et al., 1996). The surface brightness profile is shown in Figure 2.7.

2.4.1 NFW Halo

We use the Navarro, Frenk, and White (Navarro et al., 1996b, NFW) dark halo density profile, given as

$$\rho(r) = \frac{\rho_{crit} \delta_c}{(r/r_s)(1 + r/r_s)^2} \quad (2.1)$$

where r_s is the scale radius of the halo and $\rho_{crit} = 3H^2/8\pi G$ is the critical density. We use $H = 70 \text{ km s}^{-1} \text{ Mpc}^{-1}$. Throughout this paper we refer to $\rho_{crit}\delta_c$ as the scale density. The characteristic overdensity δ_c is approximately related to a concentration parameter c by

$$\delta_c = \frac{\Delta_{vir}}{3} \frac{c^3}{\ln(1+c) - c/(1+c)}. \quad (2.2)$$

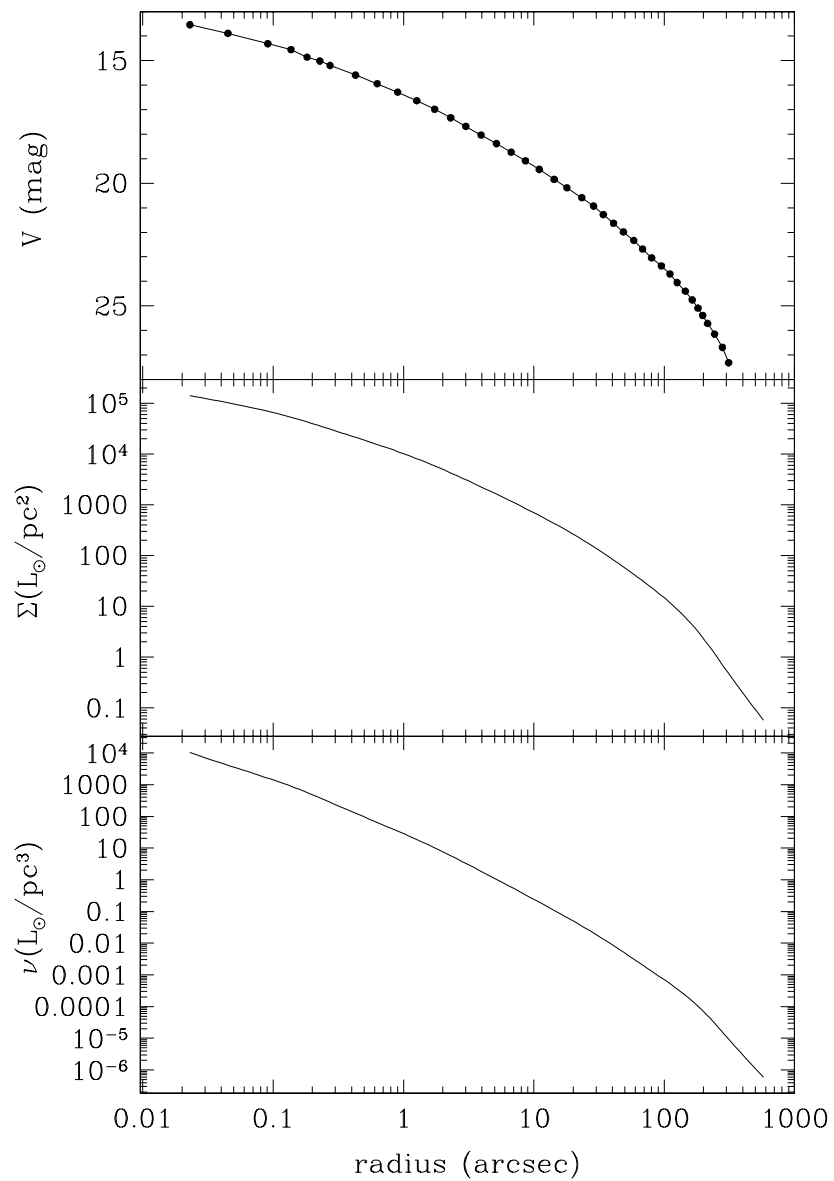


Figure 2.7: Surface brightness, luminosity density, and deprojected surface brightness profiles as a function of radius.

The virial overdensity Δ_{vir} varies with redshift and cosmological model and we use a value of $\Delta_{vir} = 101$. We vary both the concentration and scale radius, although there is a known correlation between them (Navarro et al., 1996b). This relation as given in Bullock et al. (2001) is

$$c \simeq 9 \left(\frac{M_{vir}}{1.5 \times 10^{13} h^{-1} M_{\odot}} \right)^{-0.13} \quad (2.3)$$

and can be written in the form

$$r_s^3 = \left(\frac{c}{9} \right)^{-1/0.13} \left(\Delta_{vir} \frac{4\pi}{3} \rho_{crit} c^3 \right)^{-1} (1.5 \times 10^{13} h^{-1} M_{\odot}). \quad (2.4)$$

2.4.2 Power-Law Halo

The best-fitted NFW halo profiles have a break radius beyond the extent of our modeling and therefore look like a power-law over the extent of our models (see §2.5.1 below). We therefore tried a simple power-law profile as well. We used power-law density profiles of the form

$$\rho(r) = \rho_o \left(\frac{r}{r_o} \right)^{-n} \quad (2.5)$$

where n is the power-law slope, ρ_o is the characteristic density, and r_o is the characteristic radius such that $\rho(r = r_o) = \rho_o$. We use $r_o = 0.3'' = 34 \text{ pc}$ because it is the inner-most radial point calculated in the models.

2.5 Results

The best-fitted model is determined by comparing the χ^2 between the model and data LOSVDs, with the uncertainty of the data determined from

the 68% confidence band. Example LOSVDs are shown in Figure 2.8 for several radial bins. The measure of the reduced χ^2 is not straight-forward since because determining the number of degrees of freedom is uncertain. The number of independent observables is roughly the number of radial data bins times the number of LOSVD bins at each radius ($69 \times 13 = 897$ in this case), however the LOSVD bins are correlated and thus the effective number of data points is less than this value. The best-fitted model has a χ^2 of around 2200, and with 897 data points, this provides a large reduced χ^2 . Typical values of the reduced χ^2 for the orbit-based models are around 0.5 (see Gebhardt et al. 2003), so the value reported here is not typical. The main driver for the large χ^2 is the minor axis data—removing this data gives a reduced χ^2 below one. Furthermore, the results on the parameters do not change significantly. Regardless, the change in χ^2 between different models remains a valid statistic to determine confidence levels of the fits. For example, a change in χ^2 of 2.3 corresponds to the 68.3% confidence level because we marginalize over M/L and thus have two parameters describing the halo.

Because of computational limits we first calculate models using a coarse grid of mass-to-light ratio. The χ^2 values are then fit with the IDL quadratic interpolation routine, and those models with the lowest minimum χ^2 are modeled with a finer mass-to-light ratio interval. (See Figures 2.9 and 2.10.)

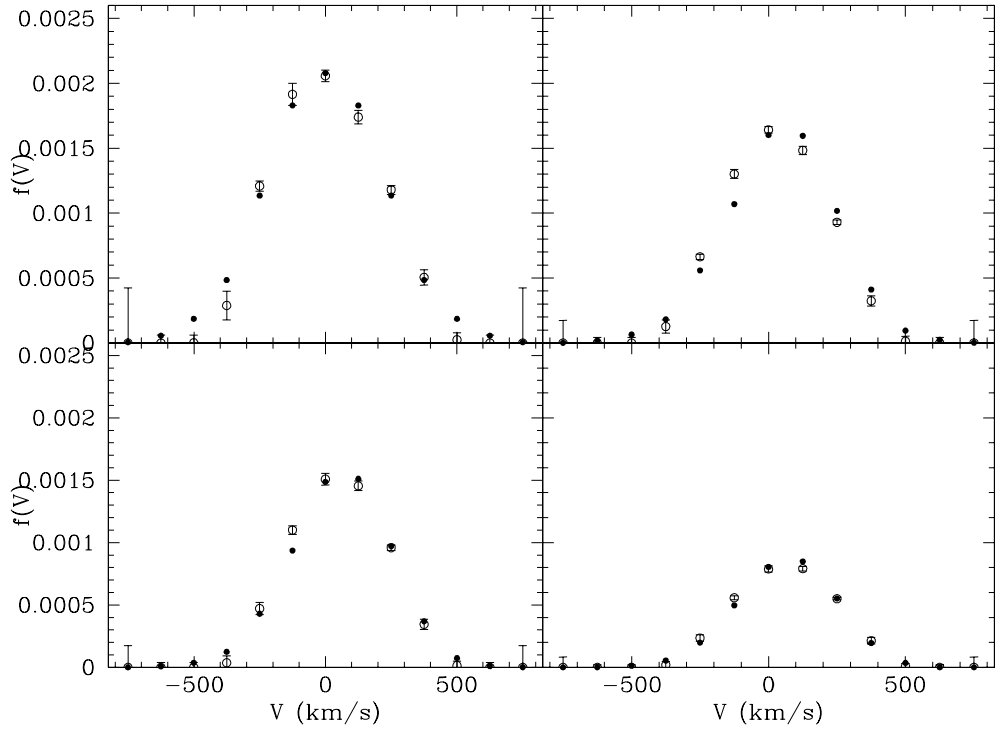


Figure 2.8: Match of data and no dark halo model LOSVDs for the central four radial bins along the major axis ($r = 0.00, 1.41, 3.76, 6.11$ arcsec). The open circles are the data values with error bars and the closed circles are the model values. The area is normalized to the total light in that bin.

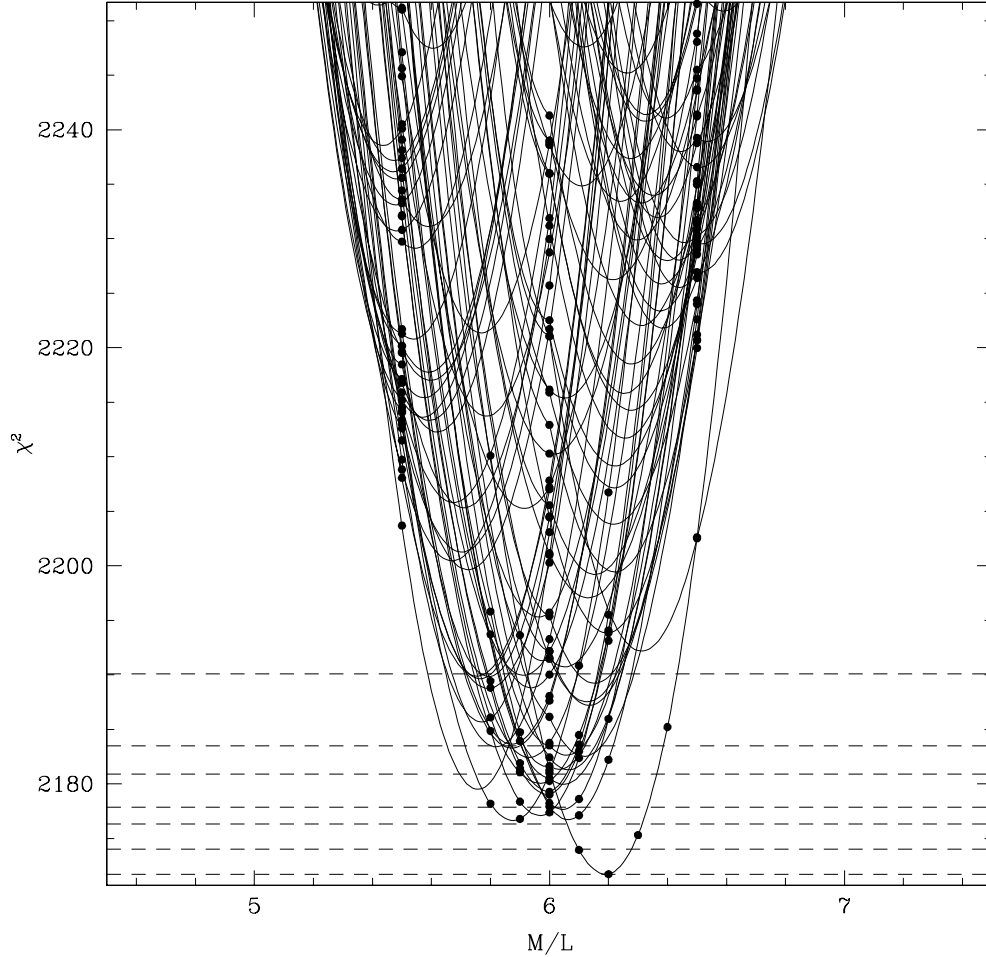


Figure 2.9: χ^2 as a function of mass-to-light ratio for all NFW halo models. The points show modeled values of M/L and the solid lines show interpolations between the points for each model, representing sequences of stellar M/L for fixed halo parameters. First a coarse interval is used, then models with small minimum χ^2 are modeled with a finer M/L interval. The dashed lines refer to $\Delta\chi^2=2.3, 4.61, 6.17, 9.21, 11.8, 18.4$, corresponding to 2 degree of freedom confidence levels of 63.8%, 90%, 95.4%, 99%, 99.73%, and 99.99%.

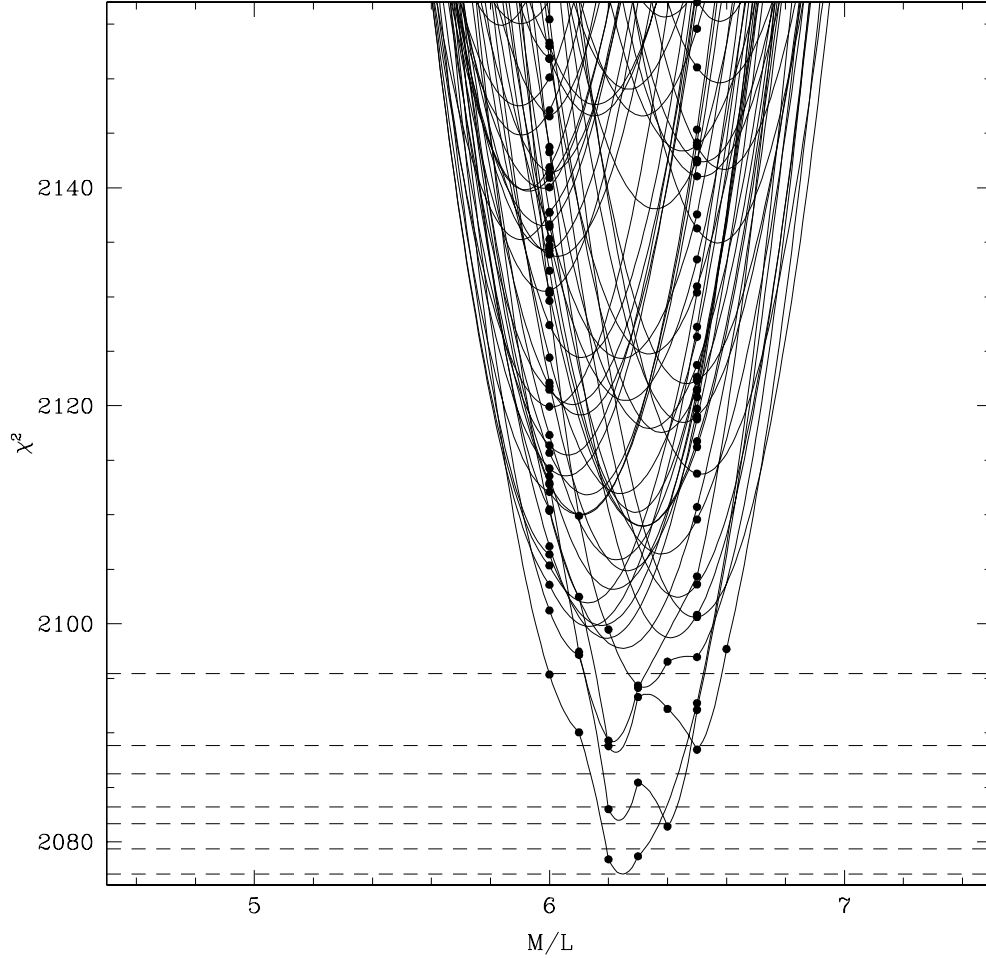


Figure 2.10: χ^2 as a function of mass-to-light ratio for all logarithmic potential halo models. The points show modeled values of M/L and the solid lines show interpolations between the points for each model, representing sequences of stellar M/L for fixed halo parameters. First a coarse interval is used, then models with small minimum χ^2 are modeled with a finer M/L interval. The dashed lines refer to $\Delta\chi^2=2.3, 4.61, 6.17, 9.21, 11.8, 18.4$, corresponding to 2 degree of freedom confidence levels of 63.8%, 90%, 95.4%, 99%, 99.73%, and 99.99%.

2.5.1 NFW Halo

We use models with scale radius from 1 to 2000 kpc and scale density from 0.05 to $3.0 \times 10^{-5} M_{\odot} pc^{-3}$, corresponding to a range in c of approximately 0.75 to 23, and M/L_V from 1.0 to 9.0. Figures 2.11 and 2.12 show the resulting χ^2 as a function of halo scale radius and scale density. The points represent actual modeled values, and the M/L_V that gives the lowest χ^2 is used at each point. The dashed line in Figure 2.11 indicates the expected correlation of concentration and scale radius as described in §2.4.1. This relation has a scatter of $\Delta \log r_s = 0.36$ (Bullock et al., 2001). Our data show a degeneracy between scale radius and scale density that is similar to, though slightly tilted from, the correlation.

χ^2 is a function of 3 variables: stellar M/L, dark halo scale radius and dark halo normalization. Due to computer resources, we do not provide a uniformly-sampled grid of the 3 variables for the χ^2 . Because of this, it is difficult to produce reliable contours for any 2 of the parameters. Figure 2.11 thus shows only the location of the points (with size related to χ^2). We do not estimate uncertainties from the contours directly, but instead rely on plotting χ^2 versus each of the parameters, including all values for the other two parameters. Figure 2.12 shows χ^2 versus scale radius and density. Uncertainties come from the envelope of these one-dimensional plots. Since we have explored neither a regular grid nor a full set of variables (e.g., black hole mass, inclination, change in the stellar M/L with radius), the uncertainties should only be used in a comparative sense with the models that we have tried. A

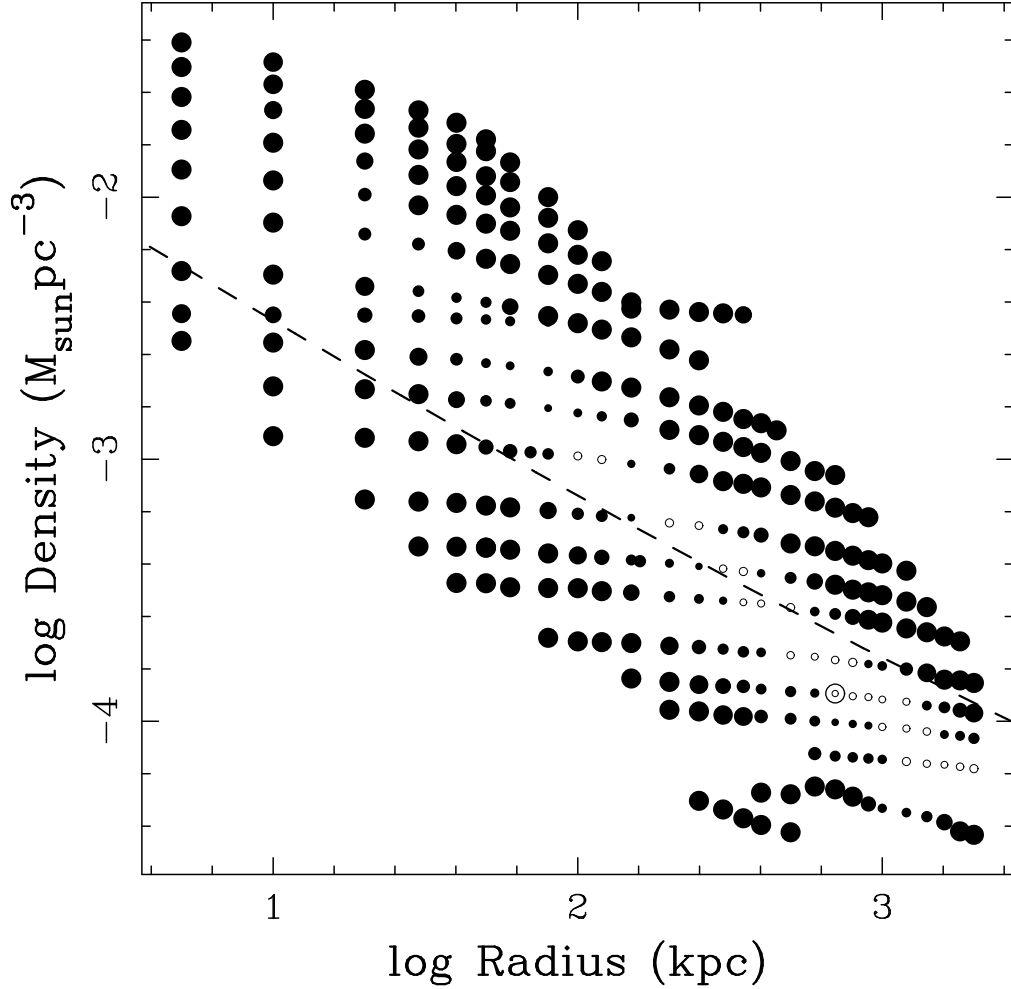


Figure 2.11: Scale radius (r_s) and scale density ($\rho_{crit}\delta_c$) χ^2 grid for NFW halo density profiles. Each point represents a model, and the size of the point reflects the value of $\Delta\chi^2$ for the best-fitted M/L_V value. Models with $\Delta\chi^2$ less than 6σ from the minimum value are plotted with open circles. The ringed point indicates the model with the lowest value of χ^2 . The dashed line shows the expected NFW parameter relation (see §2.4.1).

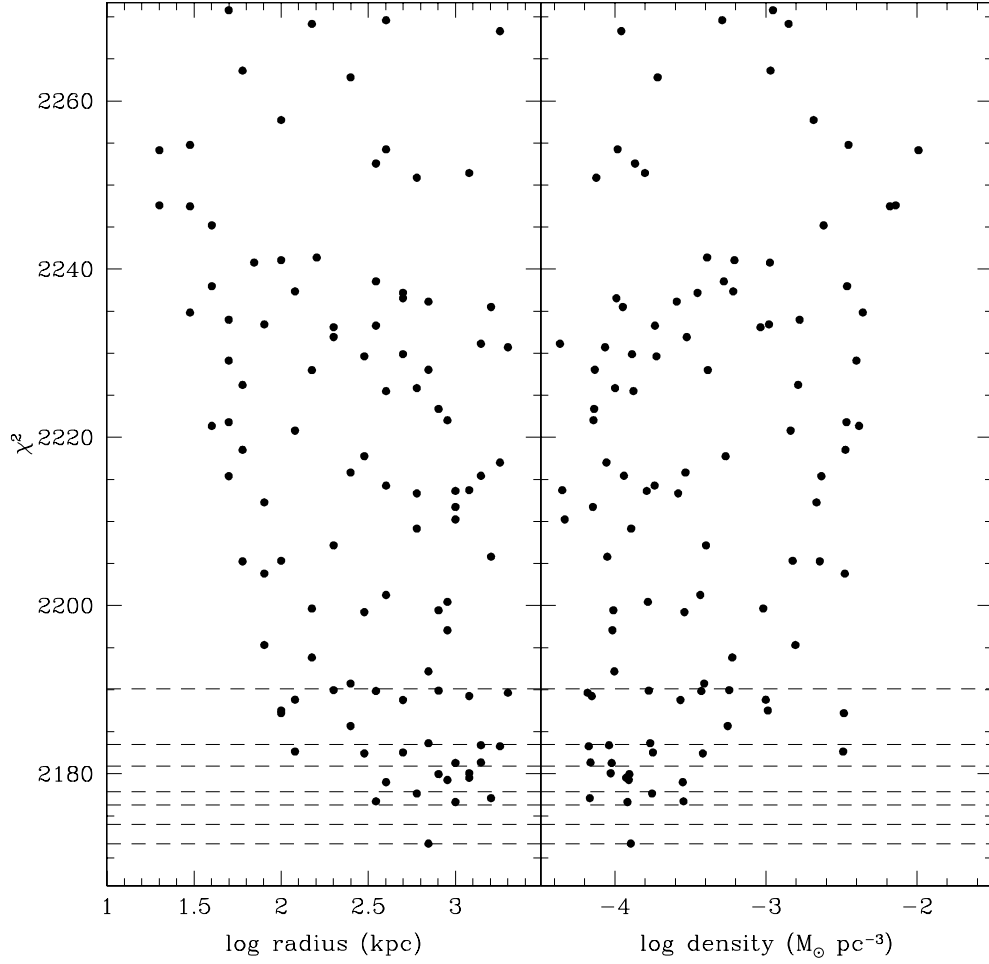


Figure 2.12: χ^2 as a function of scale radius and scale density ($\rho_{crit}\delta_c$) for NFW halo density profiles with best-fitted M/L_V . The points represent actual modeled values. The dashed lines refer to $\Delta\chi^2=2.3, 4.61, 6.17, 9.21, 11.8, 18.4$, corresponding to 2 degree of freedom confidence levels of 63.8%, 90%, 95.4%, 99%, 99.73%, and 99.99%.

full exploration of the uncertainties will come as computer resources improve.

We find that the best-fitted NFW dark halo density profile has scale radius 700_{-300}^{+500} kpc and scale density $1.28_{-0.5}^{+0.8} \times 10^{-4} M_{\odot} pc^{-3}$, corresponding to a c of 2.45. The no halo model is ruled out with a change in χ^2 of 356 (greater than 99% confidence level) from the best-fitted NFW halo. Table 2.3 shows the χ^2 values and halo parameters of the best-fitted halo model and model with no dark halo. We do not attach significance to this density, radius, and concentration. They are clearly outside the expected range for a galaxy and merely indicate that the NFW profile is not a good fit. The halo needs more mass at large radii to fit the data. The best-fitted NFW halo density profile and circular velocity profile are shown in Figure 2.13. The scale radius is well beyond the radial extent of our modeling, and is indicative of the need for a near power-law profile over the extent of our models.

Since dynamical modeling directly measures mass (as opposed to dark halo parameters), the enclosed mass provides a more robust estimate and is likely not subject to the specific parameterization of the dark halo. Figure 2.14 shows the mass enclosed within the extent of our kinematic data as a function of χ^2 . The best-fitted total enclosed mass is $1.78 \pm 0.15 \times 10^{11} M_{\odot}$, divided into $1.03 \pm 0.03 \times 10^{11} M_{\odot}$ in stars and $0.75 \pm 0.15 \times 10^{11} M_{\odot}$ in dark matter. At $1R_e$ the ratio of dark matter to total matter is 0.19. The dark matter fraction as a function of radius is shown in Figure 2.15.

Figures 2.16 and 2.17 show the internal moments σ_r , σ_{θ} , and σ_{ϕ} and

Table 2.3. NGC 821 Best-Fitted Halo Model Results

halo	χ^2	M/L_V (M/L) $_{\odot}$	r_s kpc	ρ M_{\odot}/pc^3	c	M_{vir} M_{\odot}	n	M_{tot} $10^{11}M_{\odot}$	M_{stars} $10^{11}M_{\odot}$	M_{halo} $10^{11}M_{\odot}$
(1)	(2)	(3)	(4)	(5)	(6)	(7)	(8)	(9)	(10)	(11)
none	2527.30	7.25 ± 0.05	1.20	1.20	0.00
NFW	2171.70	6.19 ± 0.09	700^{+500}_{-300}	$1.28^{+0.8}_{-0.5} \times 10^{-4}$	2.45	4.76×10^{15}	...	1.78 ± 0.15	1.03 ± 0.03	0.75 ± 0.15
power-law	2077.05	6.25 ± 0.07	...	$0.025^{+0.025}_{-0.009}$	$0.1^{+0.1}_{-0.08}$	2.01 ± 0.15	1.04 ± 0.02	0.97 ± 0.15

Note. — (1) Dark halo density profile. (2) χ^2 of best-fitted model. (3) Stellar M/L_V of best-fitted model. (4) Scale radius of best-fitted model. (5) Scale density $\rho_{crit}\delta_c$ for NFW, characteristic density ρ_o for power-law. (6) NFW concentration parameter determined from scale density. (7) Virial mass determined from NFW concentration parameter. (8) Power-law index. (9) Total mass within $100''$. (10) Mass of stars within $100''$. (11) Mass of dark halo within $100''$.

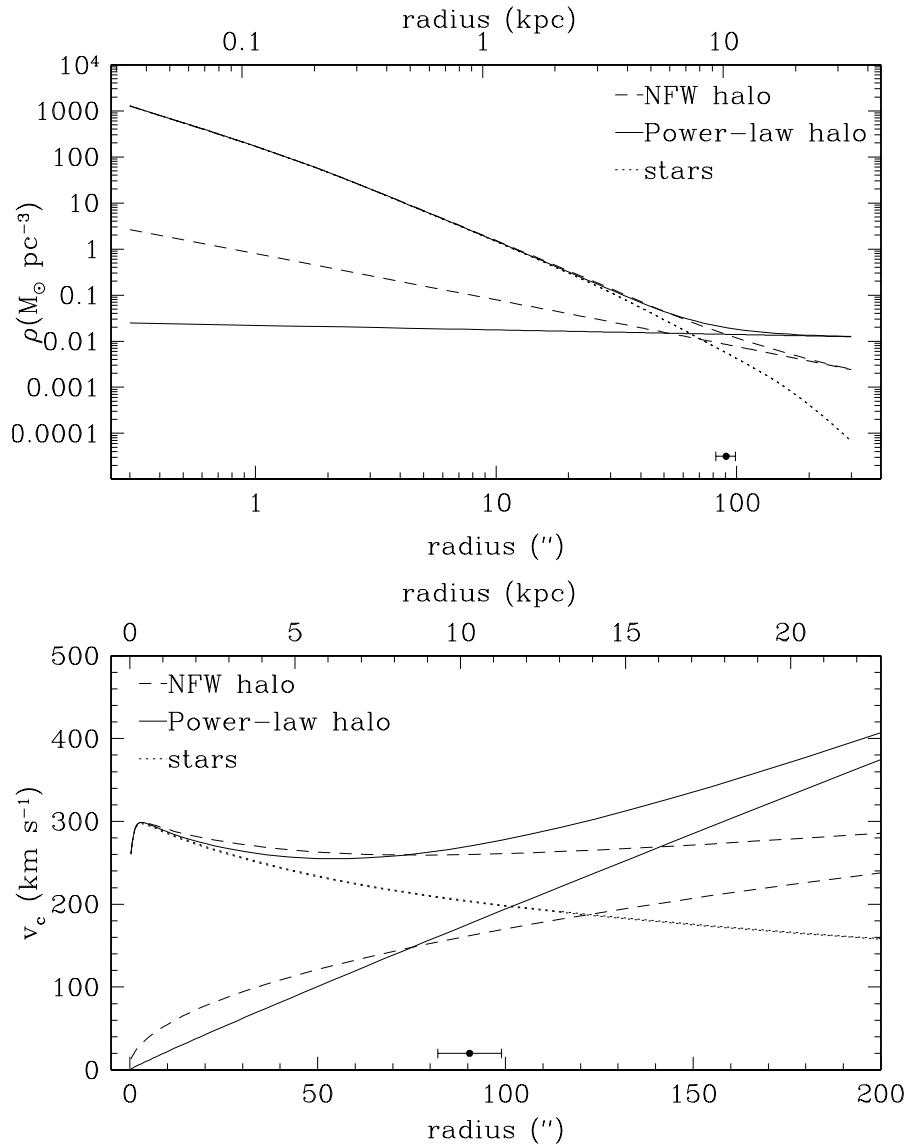


Figure 2.13: Density (top) and circular velocity (bottom) as a function of radius for the best-fitted NFW (dashed lines) and power-law (solid lines) dark halos. In each case the bottom line is the dark halo alone and the top line is the total mass (halo plus stars) The data point shows the radius of the most extended bin of our kinematic data.

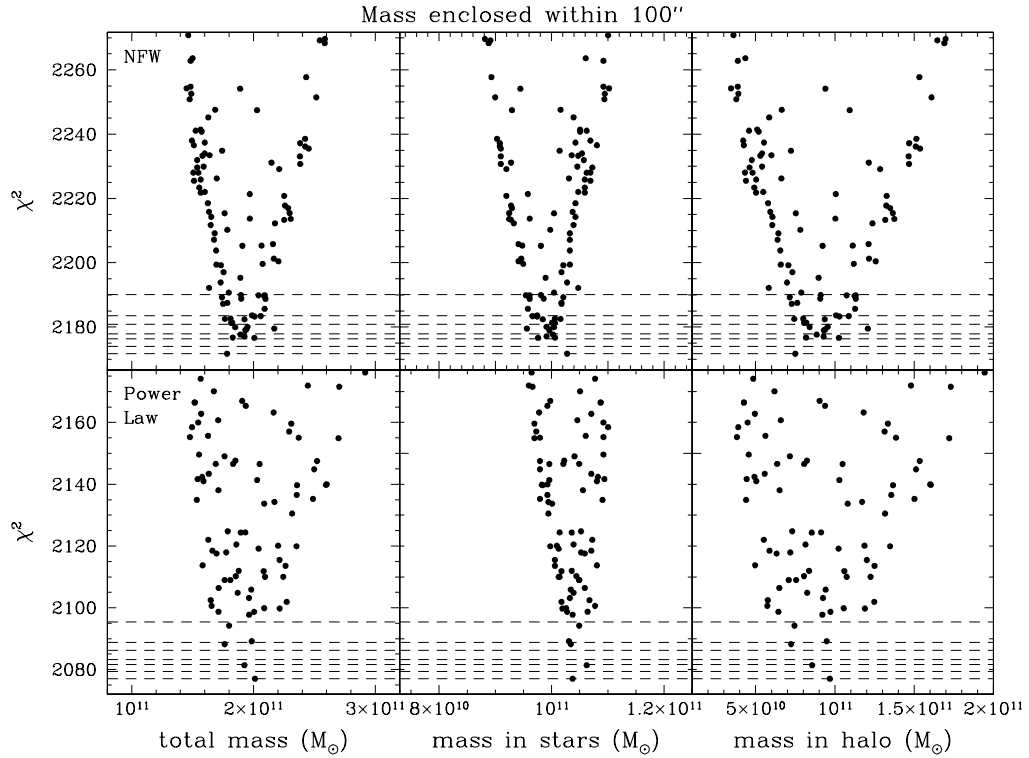


Figure 2.14: Enclosed mass within the radial extent of our kinematic data, $100''$, as a function of χ^2 for both the NFW halo density profiles (top) and power-law halo density profiles (bottom) with best-fitted M/L_V . The dotted lines refer to $\Delta\chi^2=2.3, 4.61, 6.17, 9.21, 11.8, 18.4$, corresponding to 2 degree of freedom confidence levels of 63.8%, 90%, 95.4%, 99%, 99.73%, and 99.99%.

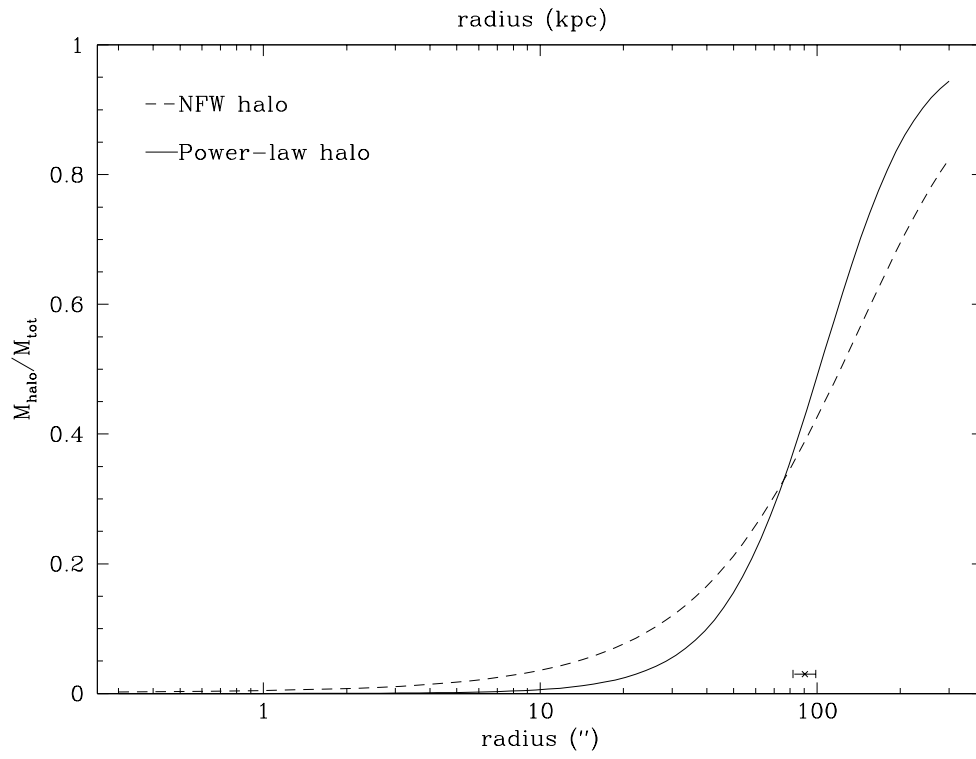


Figure 2.15: Ratio of dark matter halo mass to total mass within a given radius for the best-fitted NFW (dashed line) and power-law (solid line) dark halos. The data point shows the radius of the most extended bin of our kinematic data.

ratio of radial to tangential dispersion along the major and minor axes for the model with no dark halo and the best-fitted NFW halo model. Note that throughout the paper our major and minor axes results are for the full angular bins around the axes. The model without a dark halo shows radial anisotropy at small radii and tangential anisotropy at large radii along the major axis. Tangential anisotropy at large radii in a model with no dark halo could be an indication of the need for a dark halo because the observations largely constrain only σ_ϕ (for an edge-on configuration), so both σ_r and σ_θ may be artificially decreased to create a smaller total σ that can be fit without a dark halo. Along the minor axis, the contribution in the θ and ϕ directions are roughly equal, as is expected for an axisymmetric model. Overall the minor axis shows tangential anisotropy over the entire range of our data.

The best-fitted NFW halo model shows radial anisotropy within about $10''$ along the major axis. At larger radii the orbits are dominated by the ϕ direction and show little dispersion in the θ direction.

Although the models fit the full nonparametric velocity profile of both the HET data and SAURON data, in Figure 2.18 we plot the first four Gauss-Hermite moments for our HET data and the best-fitted halo models. The models differ most at intermediate to large radii, and do not appear to be driven by any one parameter or radius in particular.

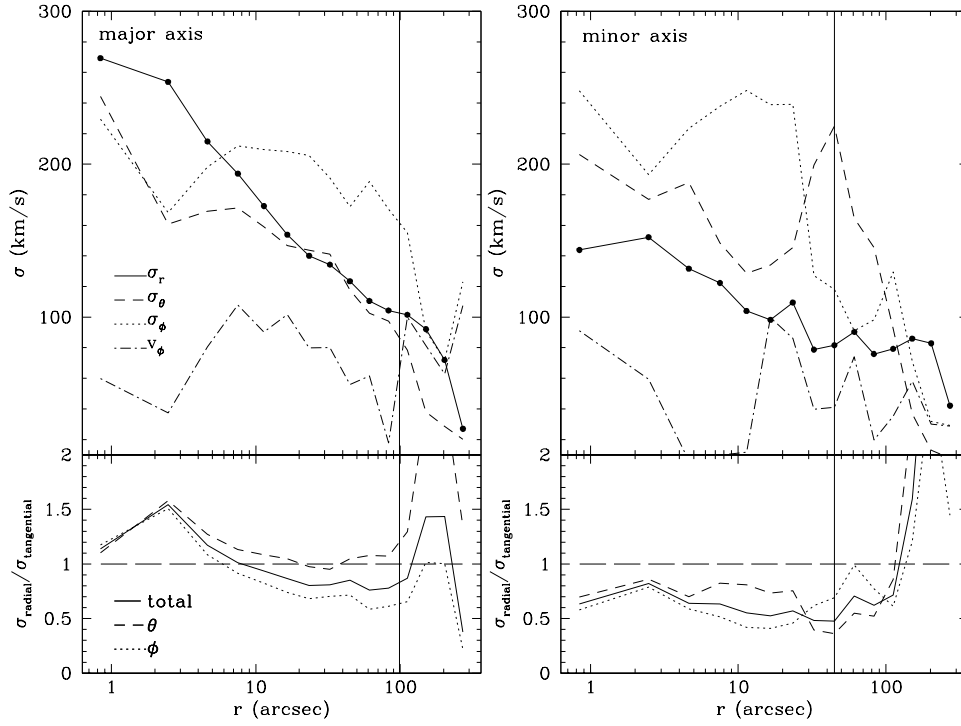


Figure 2.16: Internal moments σ_r , σ_θ , and σ_ϕ (top) and the ratio of radial to tangential dispersion (bottom) along the major axis (left) and minor axis (right) for the model with no dark halo. Note that σ_ϕ includes both random and ordered motions, which are shown (dot-dashed line) and are small. The vertical line shows the limit of our kinematic data; results beyond this radius are not reliable.

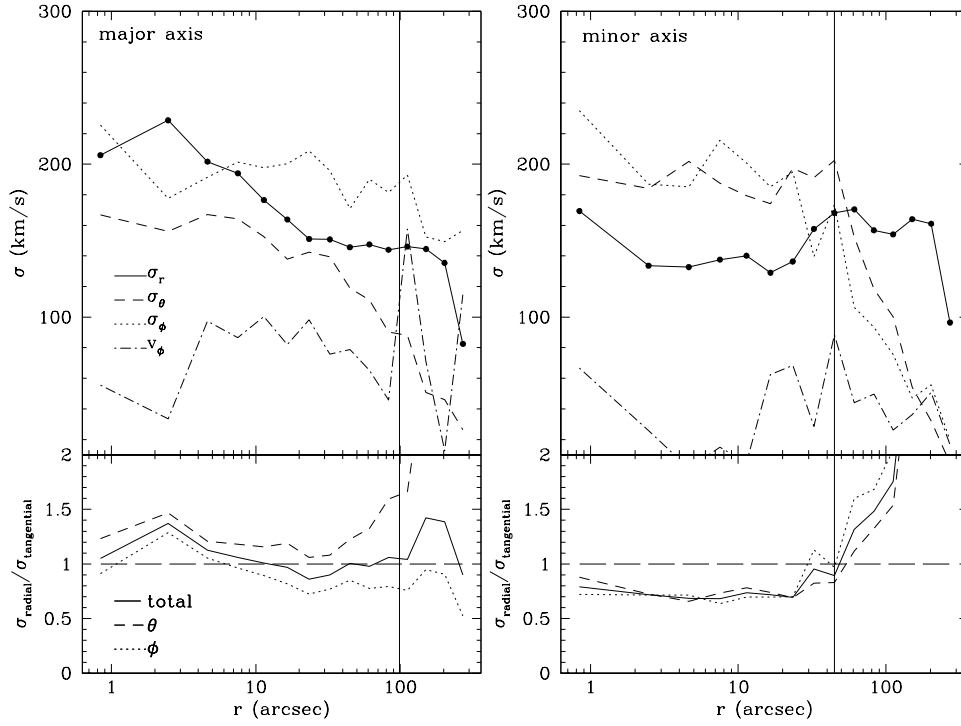


Figure 2.17: Internal moments σ_r , σ_θ , and σ_ϕ (top) and the ratio of radial to tangential dispersion (bottom) along the major axis (left) and minor axis (right) for the model with the best-fitted NFW halo. Note that σ_ϕ includes both random and ordered motions, which are shown (dot-dashed line) and are small. The vertical line shows the limit of our kinematic data; results beyond this radius are not reliable.

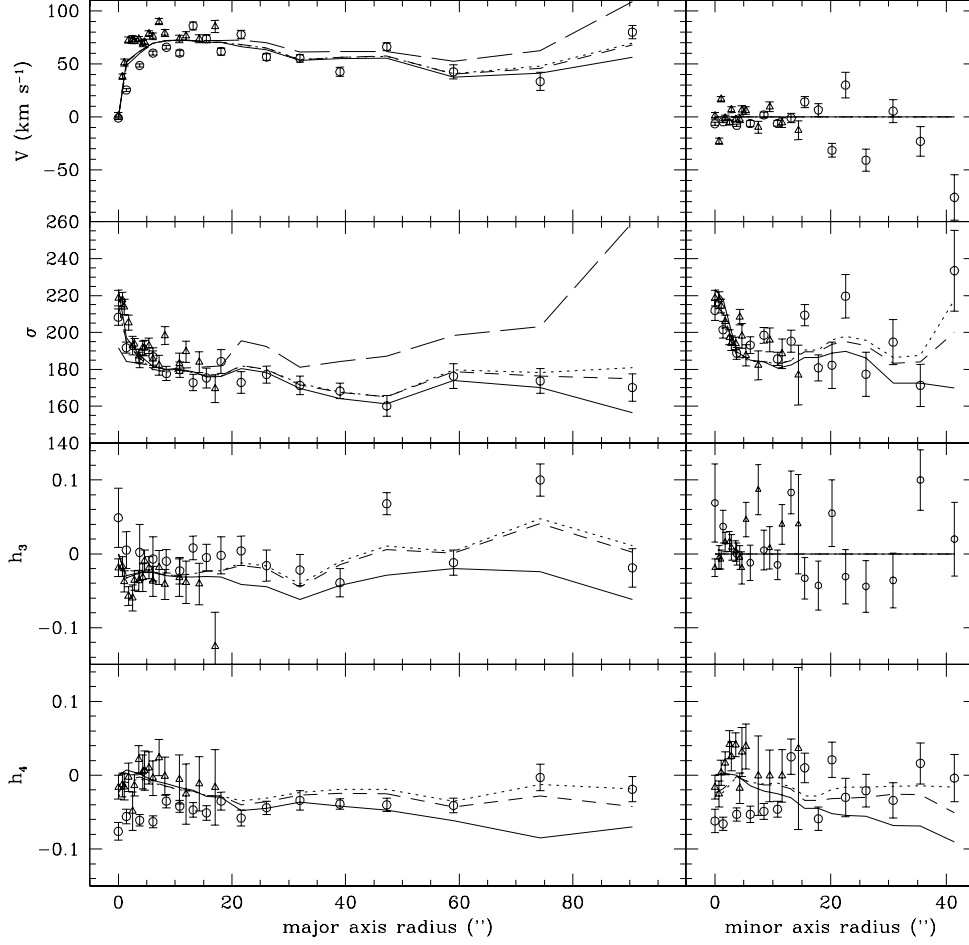


Figure 2.18: Gauss-Hermite moments (mean velocity V , velocity dispersion σ , asymmetric deviations from Gaussian (skewness) h_3 , and symmetric deviations from Gaussian (kurtosis) h_4) of the LOSVDs for our HET data and the best-fitted halo models along the major axis (left panel) and minor axis (right panel). The HET data are shown with open circles, SAURON data along the axes with open triangles, no dark halo model with solid lines, best-fitted NFW halo with dashed lines, and best-fitted power-law halo with dotted lines. The model fits the full LOSVD of the HET data and all of the SAURON data.

2.5.2 Power-Law Halo

We run models with a range of slope n from 0.0 to 1.1, density ρ_o from 0.0015 to $26 M_\odot/pc^3$, and M/L_V from 3.5 to 8.0. The resulting χ^2 grid is shown in Figure 2.19 and as a function of n and ρ_o in Figure 2.20. The best-fitted halo model has a slope $0.1_{-0.08}^{+0.1}$ and a characteristic density $\rho_o = 0.025_{-0.009}^{+0.025} M_\odot pc^{-3}$. This halo is a better fit to the data than the best NFW halo, with a $\Delta\chi^2 = 95$ (see Table 2.3). This power-law slope is significantly more shallow than the 1.0 slope of an NFW profile. A comparison of the best-fitted halo density and circular velocity profiles is shown in Figure 2.13.

The best-fitted total enclosed mass is $2.01 \pm 0.15 \times 10^{11} M_\odot$, divided into $1.04 \pm 0.02 \times 10^{11} M_\odot$ in stars and $0.97 \pm 0.15 \times 10^{11} M_\odot$ in dark matter (see Figure 2.14). At $1R_e$ the ratio of dark matter to total matter is 0.13.

The internal moments σ_r , σ_θ , and σ_ϕ and ratio of radial to tangential dispersion along the major axis are shown in Figure 2.21 and are roughly consistent with those of the best-fitted NFW halo.

Figure 2.18 shows the first four Gauss-Hermite moments for our HET data and the best-fitted halo models. Note that the models fit the full non-parametric velocity profile of both the HET data and SAURON data.

2.5.3 Model Tests

In order to learn which aspect of the data is driving the results we have performed several tests. Using an abbreviated grid of about one third

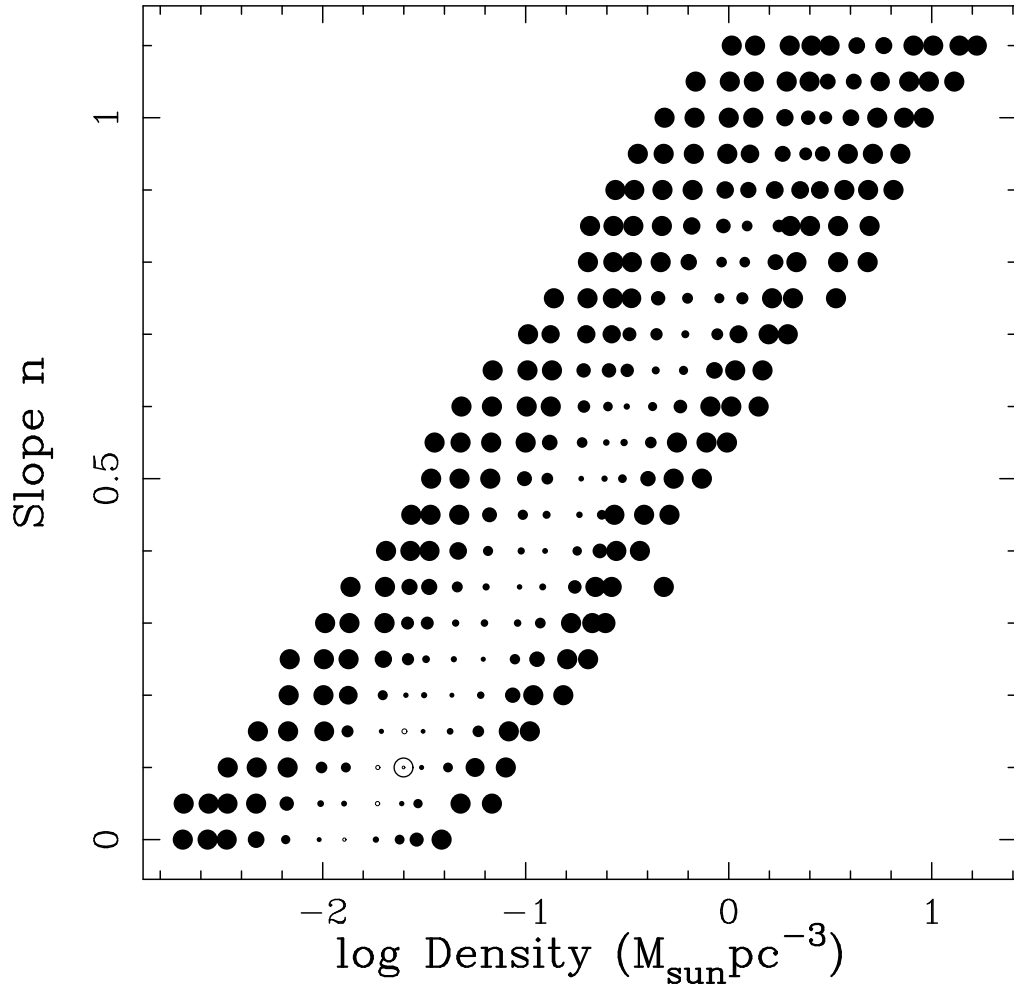


Figure 2.19: Power-law slope n and density $\rho_o \chi^2$ grid for power-law halo density profiles. Each point represents a model, and the size of the point reflects the value of $\Delta\chi^2$ for the best-fitted M/L_V value. Models with $\Delta\chi^2$ less than 6σ from the minimum value are plotted with open circles. The ringed point indicates the model with the lowest value of χ^2 .

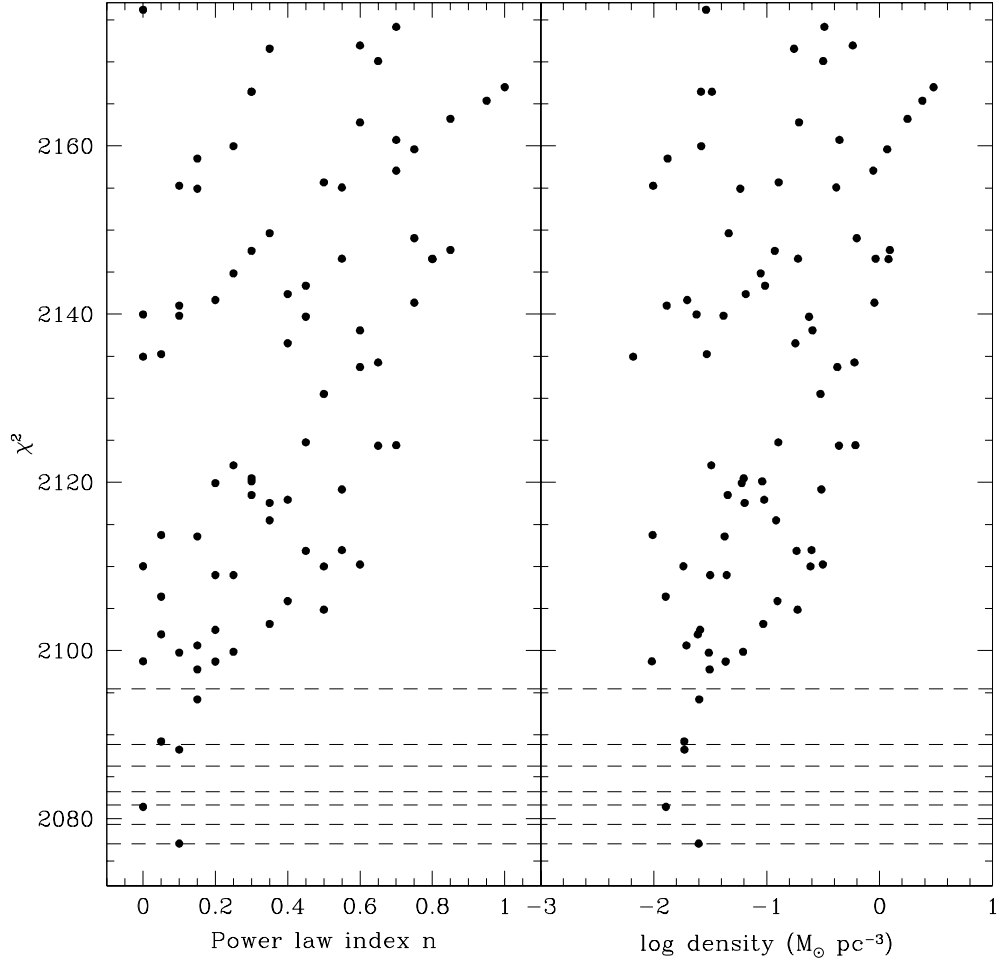


Figure 2.20: χ^2 as a function of power-law index n and scale density ρ_o for power-law halo density profiles with best-fitted M/L_V . The points represent actual modeled values. The dotted lines refer to $\Delta\chi^2=2.3, 4.61, 6.17, 9.21, 11.8, 18.4$, corresponding to 2 degree of freedom confidence levels of 63.8%, 90%, 95.4%, 99%, 99.73%, and 99.99%.

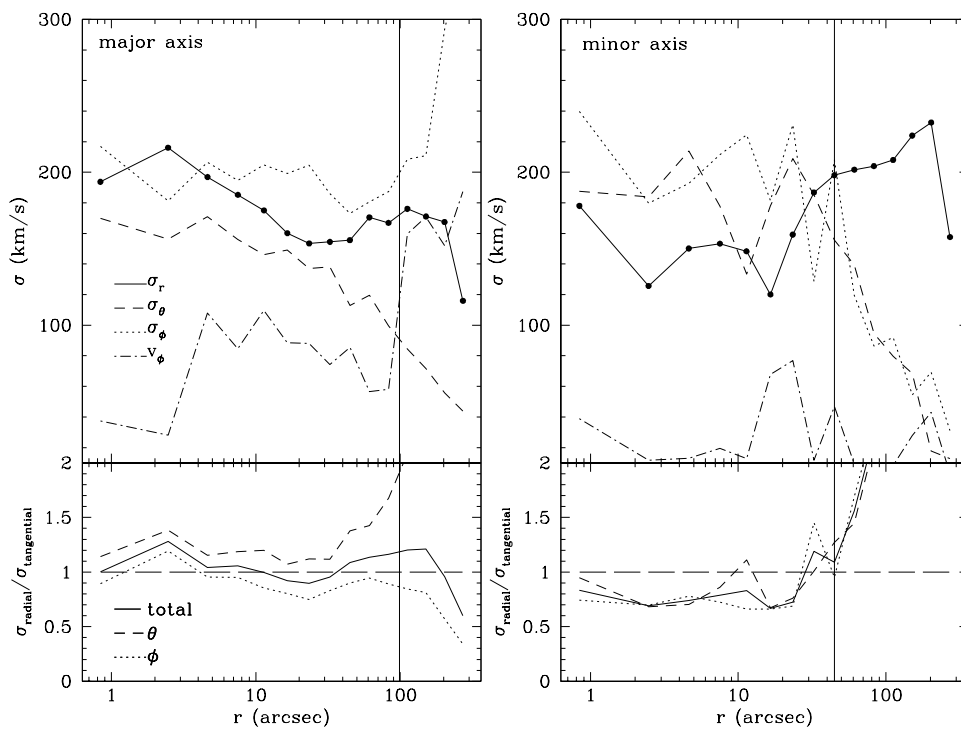


Figure 2.21: As in Figure 2.16 for the best-fitted power-law model.

of the halos in the full run and a coarse spacing in M/L_V we have re-run the models with various subsets of the data. First, to address any concerns over the scattered minor axis data we have run the test models using only the HET major axis data and SAURON data. The results are the same as the full data set; there is a clear need for a dark halo, and the best-fitted NFW halo parameters are unrealistic. Second, we removed the two points on the major axis with extreme h_3 values (at about $47''$ and $74''$) since Figure 2.18 may lead one to believe they are driving the fits. Again the results are the same as with the full data set. And third, we do a test run using only data below $0.5R_e$. In this case there is essentially no difference in χ^2 between the three best-fitted models (no dark halo, NFW halo, and power-law halo), and the best-fitted halos are quite different than those from the full data results. These tests indicate that it is the large radii data as a whole that is driving the model fits. To further demonstrate this, Figures 2.22 and 2.23 show the $\Delta\chi^2$ between the model with no halo and the best-fitted halo in each bin. The bins at large radii show the greatest change in χ^2 , again indicating that the large radii data are the major factor in the fits.

2.5.4 Comparisons to Other Studies

Gebhardt et al. (2003) model the central region of NGC 821 and find that it is radially anisotropic within a few arcseconds and isotropic to slightly tangentially anisotropic at larger radii. Given the difference in spatial resolution this roughly agrees with our result. Cappellari et al. (2007) find that

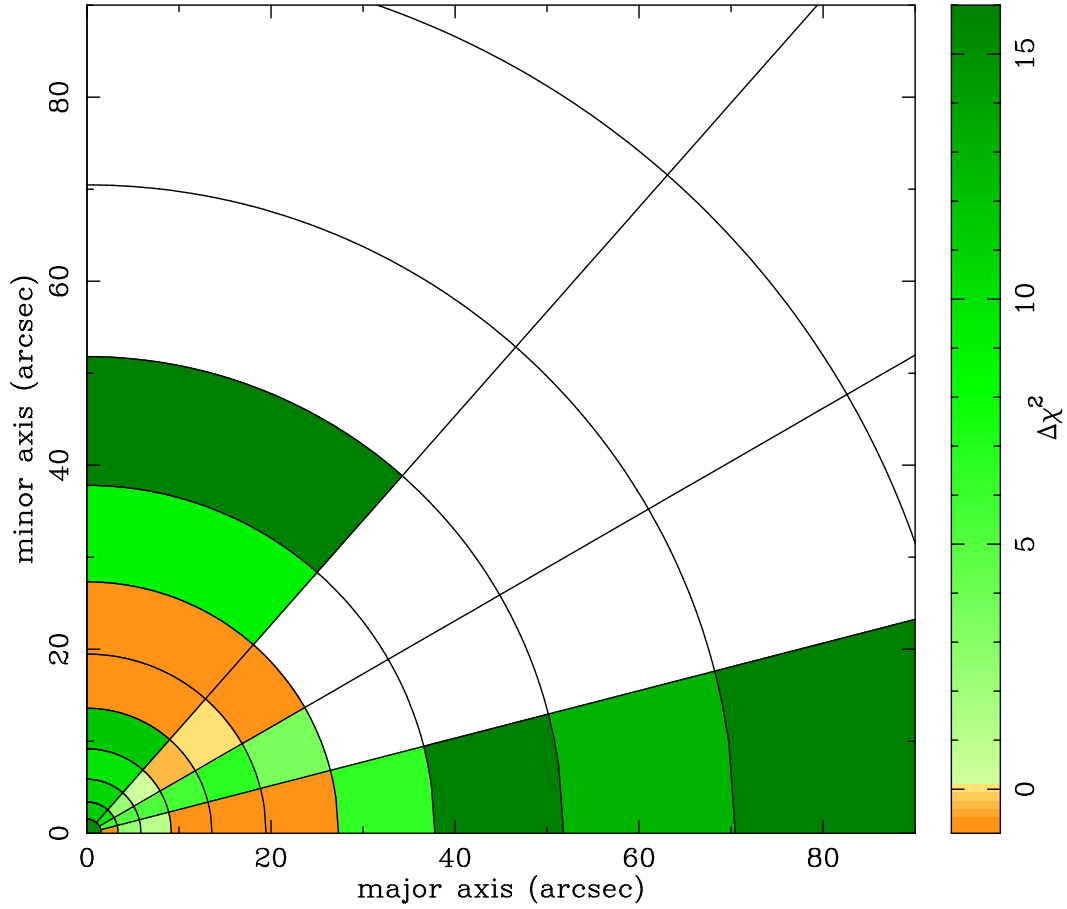


Figure 2.22: Difference in χ^2 between the LOSVDs of the model with no dark halo and the best-fitted power law halo model averaged in each spatial bin. Green indicates that the no-halo model has a larger χ^2 than the power-law model and therefore the power-law is a better fit, while orange indicates that the power-law model has a larger χ^2 than the no-halo model and therefore the no-halo model is a better fit.

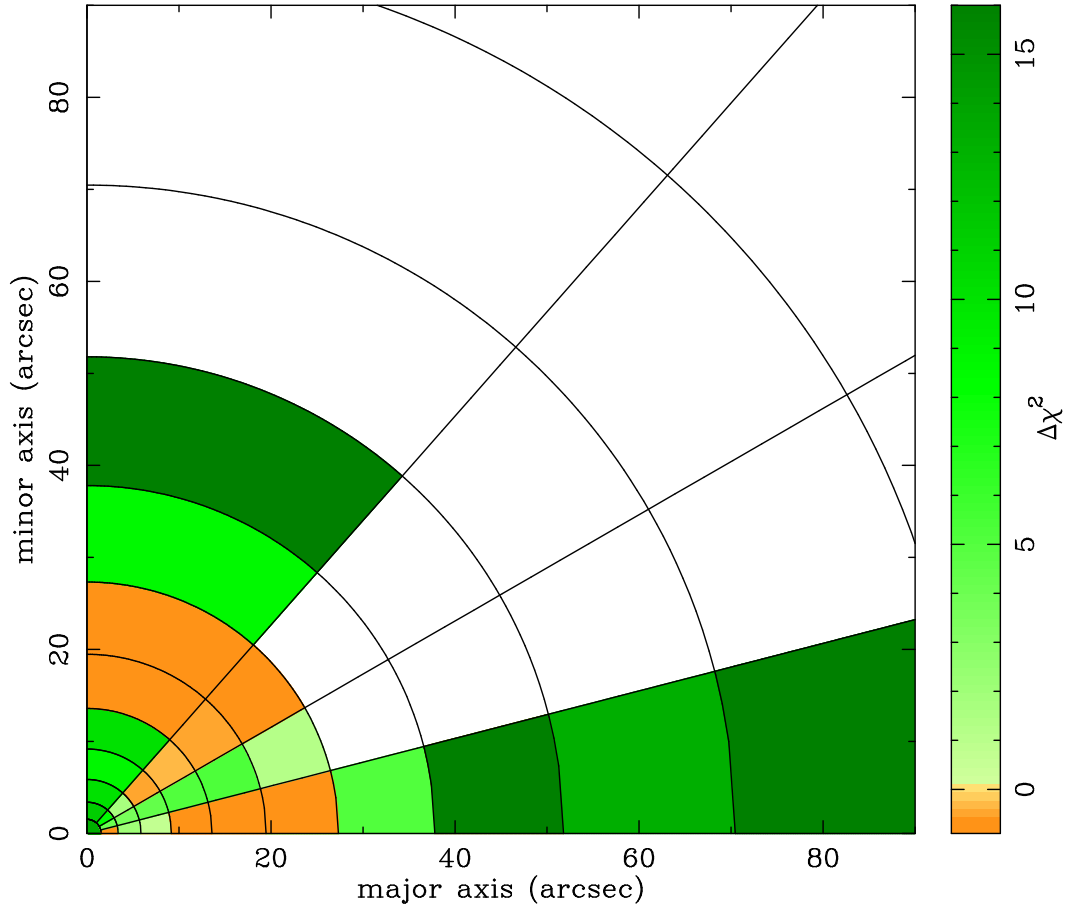


Figure 2.23: Difference in χ^2 between the LOSVDs of the model with no dark halo and the best-fitted NFW halo model averaged in each spatial bin. Green indicates that the no-halo model has a larger χ^2 than the NFW model and therefore the NFW is a better fit, while orange indicates that the NFW model has a larger χ^2 than the no-halo model and therefore the no-halo model is a better fit.

within about $20''$ N821 is radially anisotropic overall, along the major and minor axes and between. They find that the velocity ellipsoids are circular in the center and become more radial with increasing radius, in conflict with our results, but they do not include a dark halo which could change their results. Thomas et al. (2007), using similar modeling as we use, find that early-type galaxies in the Coma cluster are radial compared to the θ direction over all radii along the major axis, agreeing with our result, and vary from galaxy to galaxy in the ϕ component. The merger simulations of Dekel et al. (2005) also find a radial anisotropy. Their spherically averaged β of about 0.4 corresponds to a $\sigma_{radial}/\sigma_{tangential}$ of 1.3, which is larger than our results along the major and minor axes. However their simulations show declining projected dispersion profiles, which our data do not, that could account for the difference.

By modeling only the central part of NGC 821 Gebhardt et al. (2003) find $M/L_V = 7.6$ (without including foreground extinction), which is consistent with our no-halo value over the whole galaxy of $M/L_V = 7.25$. Correcting for NGC 821's large reddening of $A_V = 0.364$ mag (Schlegel et al., 1998, NED extragalactic database) we find our best-fitted $M/L_{V,nohalo} = 5.18$, $M/L_{V,nfw} = 4.43$, and $M/L_{V,pow} = 4.47$. Cappellari et al. (2006) find $M/L_{jeans} = 3.54$, $M/L_{schwarzschild} = 3.08$, and $M/L_{stellarpop} = 2.60$ in the I band. Using $(V - I) = 1.35$ mag (Lauer et al., 2005) and $(V - I)_{\odot} = 0.682$ mag (Ramírez & Meléndez, 2005) our V band mass-to-light ratios are converted to $M/L_{I,nohalo} = 2.80$, $M/L_{I,nfw} = 2.39$, and $M/L_{I,pow} = 2.42$. Our mass-to-light ratios are slightly lower, though roughly consistent, with their

mass-to-light ratios found using Schwarzschild modeling and stellar populations. Inclusion of a dark halo could easily explain this difference since that would lower the stellar M/L value.

We find that the enclosed mass of NGC 821 within $\sim 2R_e$ is roughly $2 \times 10^{11} M_\odot$, equally divided between stars and dark matter. At $1R_e$ the ratio of dark matter halo mass to total mass is 0.19 for the best-fitted NFW halo profile and 0.13 for the best-fitted power-law halo profile. This matches other studies that find that the dark matter is 10 – 40% of the total matter at $1R_e$ and that dark matter begins to dominate at $2 - 4R_e$ (e.g. Saglia et al., 2000; Gerhard et al., 2001; Mamon & Lokas, 2005). The simulations of Dekel et al. (2005) also show that dark matter and stellar matter are equal at $3R_e$, and at $1R_e$ have a mass fraction of 40% dark matter. Thomas et al. (2007) perform similar dynamical modeling on 17 galaxies in the Coma cluster. Using values taken by eye from their Figure 5 we find that their average dark matter fraction at $1R_e$ is 0.19, though their galaxies show a wide range of dark matter fractions, from about 0.1 to 0.5 at $1R_e$. We therefore find that the dark matter fraction at $1R_e$ is similar for N821, a field elliptical galaxy, and a selection of Coma cluster early-type galaxies, perhaps contrary to hypotheses that environment plays a role in the dark matter fraction.

Weijmans et al. (2009) provide a dynamical analysis using orbit-based models and using data that extend to similar radii. Thus, the comparison of dark halo results is informative. We find very similar numbers. Inside of $39''$ (which they call R_e), they find a dark matter fraction of 18%. Inside of

45'' (which we call R_e), we have a dark matter fraction of 13%. There are differences in the models as well. First, they use a “maximum M/L” model where they force the M/L of the stars to have a maximum value. We minimize for the M/L of the stars. Second, the modelling codes are different, with the main difference in that they use regularization (which trades the best fitted values with smoothness) and we report results for the best fit to the data. Third, they use SAURON data at large radii and we use our HET data at large radii. Their data extends to slightly larger radii (110'' compared to our limit of 90''), and our data is high signal-to-noise. Given all of these differences, it is impressive that we obtain similar results for the dark halo. This implies that systematic differences are not significant for determining the enclosed mass profile.

2.5.5 Smoothing

It is useful to constrain the orbital weighting so that the resulting DF is smooth, as a real galaxy’s DF may be presumed to be. Although we do not usually report results when smoothing our models (we argue that allowing the best fit to the data is the most robust way to provide an un-biased result), other groups suggest that it is important for their model. Rix et al. (1997) and subsequent studies minimize the variation in the DF, a process they term regularization. We employ maximum entropy to find the best combination of orbit weights to match the data, as described in Thomas et al. (2005). We define a function $f \equiv \chi^2 - \alpha S$ where χ^2 is the sum of squared residuals to the

data, S is the entropy, and α is a parameter describing the relative weights of entropy and residuals in the fit. In order to minimize f we typically start with a large value of α and make it smaller until the χ^2 no longer varies. To test the effect of smoothing we run models such that the iterations stop when $\alpha = 0.01$, a reasonable value based on Thomas et al. (2005).

Using only our HET data we ran our no-halo and NFW-halo models with and without smoothing using a coarser grid in parameter space. We find that smoothing does not alter the results. All of the models have a lower χ^2 using only the HET data than the main results of our paper which use both HET and SAURON data. The models with smoothing have a larger χ^2 than without smoothing (see Table 2.4), but the $\Delta\chi^2$ between different halo models remains the same. The best-fitted NFW dark halo parameters are consistent within the errors. The internal moments are also consistent with the unsmoothed models within the errors. Using an estimate by eye, the smoothed model's DF (plotted as I_3 versus L_z in E bins) looks similar to the unsmoothed model's DF when smoothed.

We therefore determine that adding smoothing via maximum entropy does not alter the measured halo, internal moments, or overall DF shape. We also note that these results using only our HET data are consistent with those using both HET and SAURON presented throughout this paper.

Table 2.4. NGC 821 Smoothing Model Results

halo	smoothing	χ^2	r_s <i>kpc</i>	c	ρ M_\odot/pc^3
(1)	(2)	(3)	(4)	(5)	(6)
none	no	940.857
none	yes	1033.73
NFW	no	766.47	1050	2.32	1.14×10^{-4}
NFW	yes	852.77	800	2.70	1.56×10^{-4}

Note. — (1) Dark halo density profile. (2) Smoothing or no smoothing. (3) χ^2 of best-fitted model. These χ^2 values are lower than those of Table 2.3 because the models fit fewer data points (HET data only) than the models in Table 2.3 (HET and SAURON). (4) Scale radius of best-fitted model. (5) NFW concentration parameter determined from scale density. (6) NFW Scale density $\rho_{crit}\delta_c$.

2.5.6 Planetary Nebula Data

We model the NGC 821 planetary nebula data of Romanowsky et al. (2003) with the best-fitted halos from the stellar data. We are not trying to constrain models using this data, but rather are interested in what orbital properties the planetary nebulae would require given the potential derived from the stellar data. In doing this we assume that the potential derived from stars is correct and that the planetary nebulae are distributed in the same way as the stars. This assumption may not be realistic, as Dekel et al. (2005) predicts that it is the densities, not the anisotropies, that differ. Figure 2.24 shows the ratio of radial to tangential dispersion for the models with no dark halo and best-fitted NFW and power-law halos. As expected from the results of Romanowsky et al. (2003), the model with no dark halo is roughly isotropic throughout, and tangential at large radii. The best-fitted NFW model requires radial orbits throughout and the best-fitted power-law halo requires extremely radial orbits. This again demonstrates the strong mass-anisotropy degeneracy in dynamical studies. All three models are an excellent fit to the data. There is a preference for a dark halo, but it is not statistically significant.

2.6 Conclusions

We present kinematics of NGC 821 to over 2 effective radii using long-slit spectroscopy from the Hobby-Eberly Telescope and find that our measured stellar line-of-sight velocity distributions are larger than the planetary nebulae measurements of Romanowsky et al. (2003) at large radii.

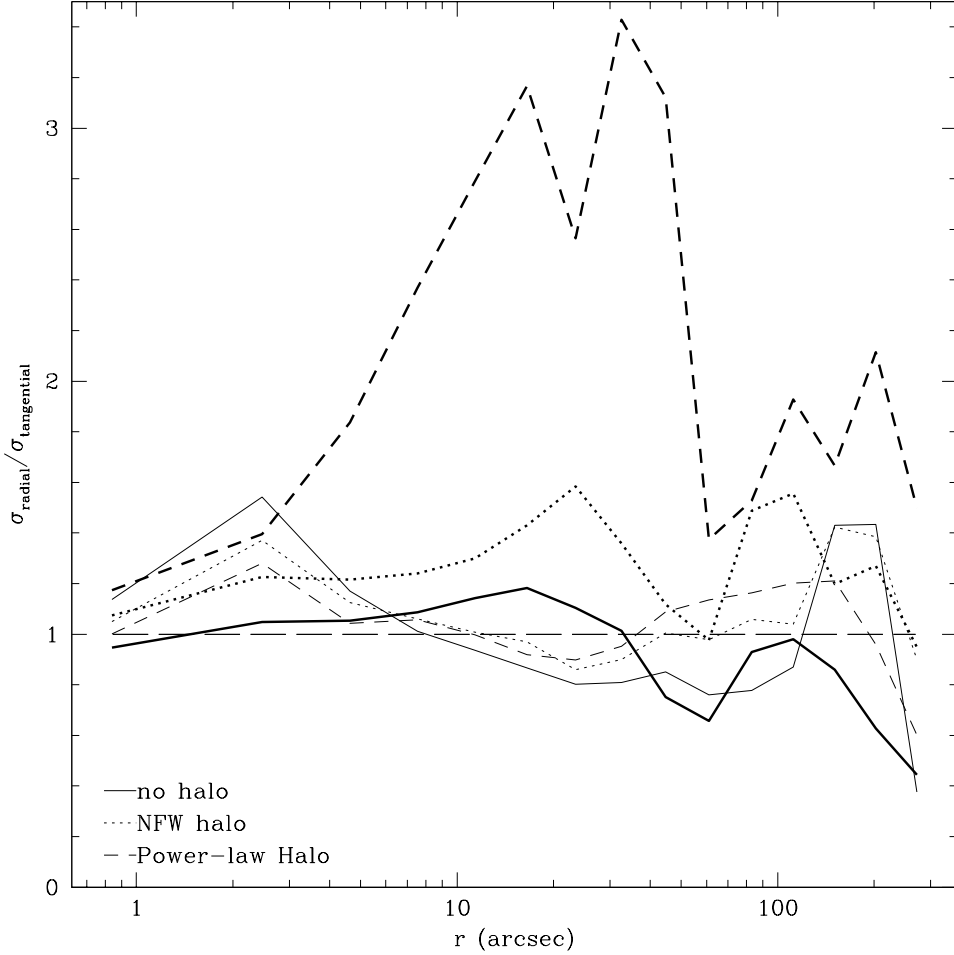


Figure 2.24: Ratio of radial to tangential dispersion (an average of σ_θ and σ_ϕ , including streaming motion) along the major axis for models with only planetary nebula data (thick lines) and the best-fitted no halo, NFW halo, and power-law halo derived from the stellar kinematics. All three models are consistent with the PN data, in terms of χ^2 , with the dark halo models providing a slightly better fit. Thin lines show results for stellar data as comparison.

Regardless of the density profile used, we are able to constrain the enclosed mass of NGC 821 within our kinematic data ($\sim 2R_e$) as roughly $2 \times 10^{11} M_\odot$, equally divided between stars and dark matter. At $1R_e$ the ratio of dark matter halo mass to total mass is 0.19 for the best-fitted NFW halo profile and 0.13 for the best-fitted power-law halo profile.

We find that the best-fitted model of the dark halo in NGC 821 has a nearly flat power-law density profile. This dark halo gives a better fit than both the NFW halo models and models without a dark halo at a greater than 99% confidence level. This slope is somewhat unexpected, and is strongly inconsistent with halo profiles with inner slopes greater than one (e.g. isothermal, Hernquist, 1990; Moore et al., 1999), and may lend support to halos with a flat inner slope (e.g. cored isothermal, logarithmic potential, and Burkert, 1995). Additionally, one would expect that adiabatic contraction would create even steeper inner halo profiles (Blumenthal et al., 1986; Gnedin et al., 2004), which is in conflict with our result. This halo result is driven by the data at large radii.

Our NFW χ^2 space shows a degeneracy in radius and density as expected. This degeneracy is slightly tilted from the expected NFW correlations. Constraining these NFW radius and density parameters using a single concentration parameter could lead to biased results.

We find a V band stellar mass-to-light ratio of 6.19 for the NFW halo and 6.25 for the best-fitted power-law halo. With no dark halo a mass-to-light ratio of 7.25 is needed. These values agree with other modeling of NGC 821

in the literature when corrected for extinction.

Including smoothing via maximum entropy to our orbital weight selection as a means of smoothing the resulting DF does not affect the halo found or internal moments within the errors.

In addition to having a significantly poorer fit, the models without a dark halo show tangential anisotropy at large radii. This may be an indication that a dark halo is necessary because the radial component of the velocity dispersion may need to be artificially decreased at large radii in order to create a smaller total velocity dispersion that can be reproduced by a haloless model. The best-fitted dark halo model shows a radial bias in the θ direction at all radii. This is in agreement with the simulation results of Dekel et al. (2005). However we do show that the velocities in the ϕ direction are greater than the radial component. If the planetary nebulae are on radial orbits, that would explain why our measured stellar velocity dispersions are larger than the reported planetary nebulae dispersions (Romanowsky et al., 2003). We show this by modeling the planetary nebula data assuming the potential of our best-fitted halo models from the stellar kinematics. We find that the planetary nebulae do require radially anisotropic orbits to match the best-fitted halo potentials.

Chapter 3

The Dark Halo of NGC 6702

3.1 Introduction

As we have previously discussed, halos of dark matter around galaxies have become an accepted part of our understanding of the universe, though there have been some questions about the dark matter content of elliptical galaxies (Romanowsky et al., 2003). In Chapter 2 we found that elliptical galaxy NGC 821 contains a significant fraction of dark matter. Here we continue by studying another elliptical, NGC 6702, to learn whether NGC 821 is unique and to grow the database of information on elliptical galaxy dark halos.

NGC 6702 is a LINER (de Vaucouleurs et al., 1991) and has been classified as E2 and E3 (Sandage & Visvanathan, 1978; de Vaucouleurs et al., 1976) with an axis ratio of 0.78 (2MASS, Skrutskie et al., 2006). It is at a distance of 62.8 Mpc (Ho et al., 1997). It does not have boxy isophotes or stellar disks, but does contain dust lanes (Lauer, 1985) and a power-law surface brightness profile (Ravindranath et al., 2001).

§3.2 describes the observations and data reduction; in §3.3 we describe the kinematic extraction; the dynamical models are described in §3.4; we

present our results in §3.5 and give conclusions in §3.6.

3.2 Observations and Data Reduction

Long-slit spectra were taken with the Low-Resolution Spectrograph (Hill et al., 1998) on the Hobby-Eberly Telescope. We used the g2 grism and 1'' by 4' slit over the wavelength range 4300-7300Å. This setup gives a resolving power of 1300 or a full-width half-maximum (FWHM) resolution of about 230 km s⁻¹. Measurements of night sky line widths show that we can measure dispersions to about 110 km s⁻¹. The CCD frame (binned 2 × 2) has a plate scale of 0.47''/pix spatially and 2Å/pix spectrally. The gain is 1.832 e⁻ ADU⁻¹ and readout noise is 5.10 e⁻. We used the Schott Glass blocking filter GG385, which has a half-power point of the transmission around 385 nm. Preparatory images showing the sky before the slit has been inserted are shown in Figures 3.1 and 3.2.

NGC 6702 was observed over fourteen nights from April to October 2002 for a total exposure time of 6.7 hours along the major axis and 4.6 hours along the minor axis. Cadmium and Neon calibration lamp exposures and white light illumination flat fields were taken each night.

The data reduction was performed using standard techniques with fortran code developed from FITSIO programs. First we overscan correct and trim the images. Then we apply a flat correction using a normalized flat frame, taken from averaged instrumental flats obtained each night of observations. Next we rectify the images along the spatial axis using the calibration

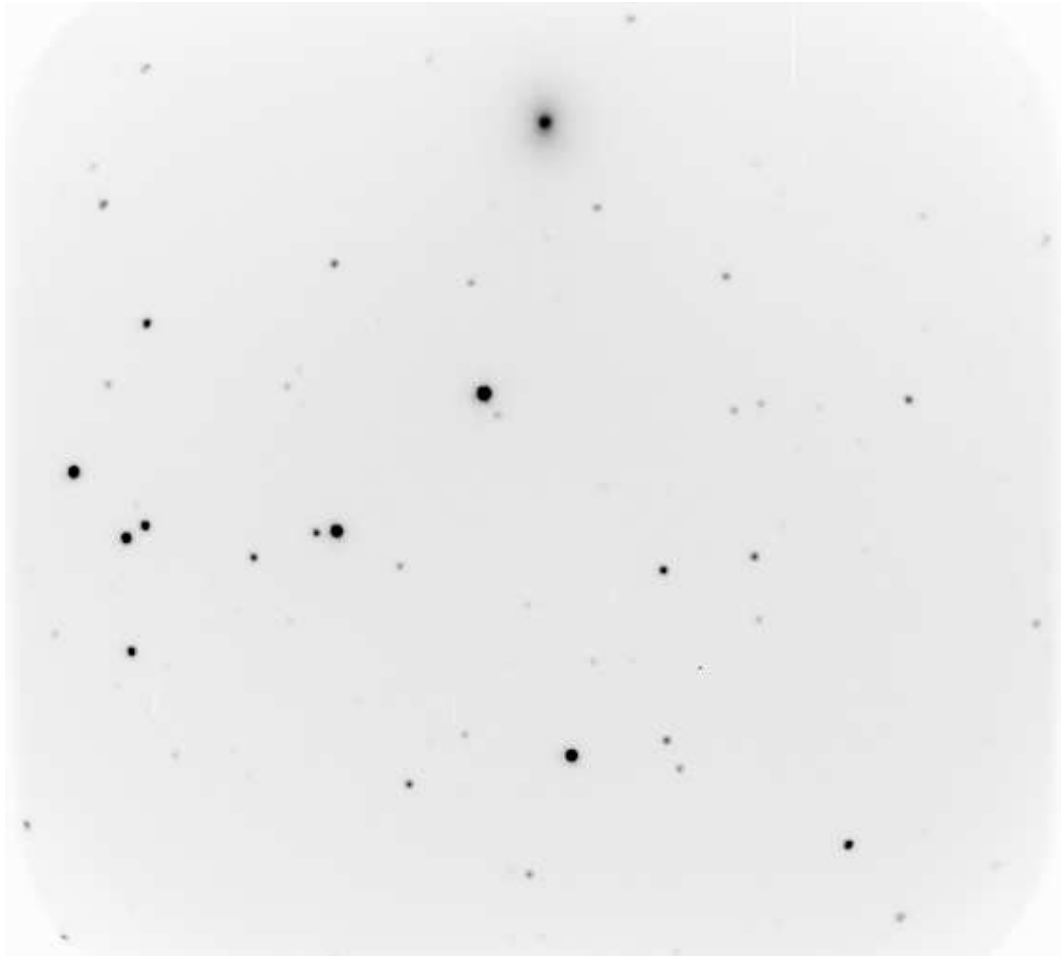


Figure 3.1: NGC 6702 major axis preparatory image.

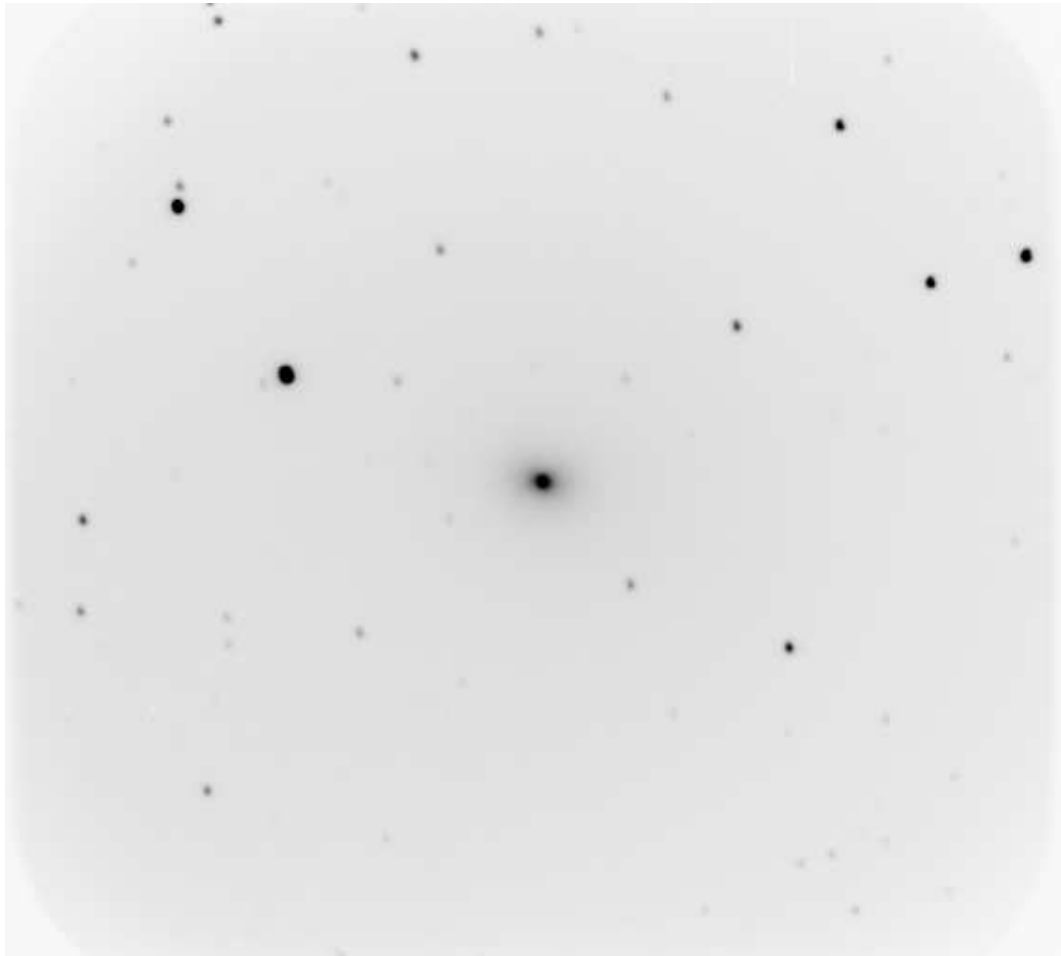


Figure 3.2: NGC 6702 minor axis preparatory image.

lamp lines as a reference. For sky subtraction, we use the region of the slit that is furthest from the galaxy center. Finally we align and combine the images using the night sky lines and the galaxy as references.

To calculate our galaxy potential we use a composite surface brightness profile. Within $3''$ we use the R-band profile from Lauer (1985). Outside of $3''$ we use a profile from the McDonald Observatory 0.8-m telescope in V normalized to the central profile. The surface brightness deprojection is based on a nonparametric estimate of the density using smoothing splines (see Gebhardt et al., 1996). The surface brightness profile is shown in Figure 3.3.

3.3 Kinematics

We extract the spectra in radial bins along the major and minor axes. Because the seeing is approximately $2''$ we set the central bins to 5 pixels ($2.35''$). The outer bins are sized to obtain sufficient signal for kinematic analysis. Along the minor axis the spectra from either side of the galaxy were averaged at each radius. Along the major axis, the center of the galaxy was near the edge of the chip so only one side was extracted. Our farthest radial bin extends to $39''$ on the minor axis and $54''$ on the major axis, corresponding to a V -band surface brightness of 24.9 on the major axis. The R_e of NGC 6702 has been measured in the literature as $24.4''$ (RC3), and $29''$ (Faber et al., 1989). For the purpose of this discussion we will adopt the Faber et al. (1989) value of $29''$. Thus our data extend to approximately $1.3R_e$ along the minor axis and $1.9R_e$ along the major axis.

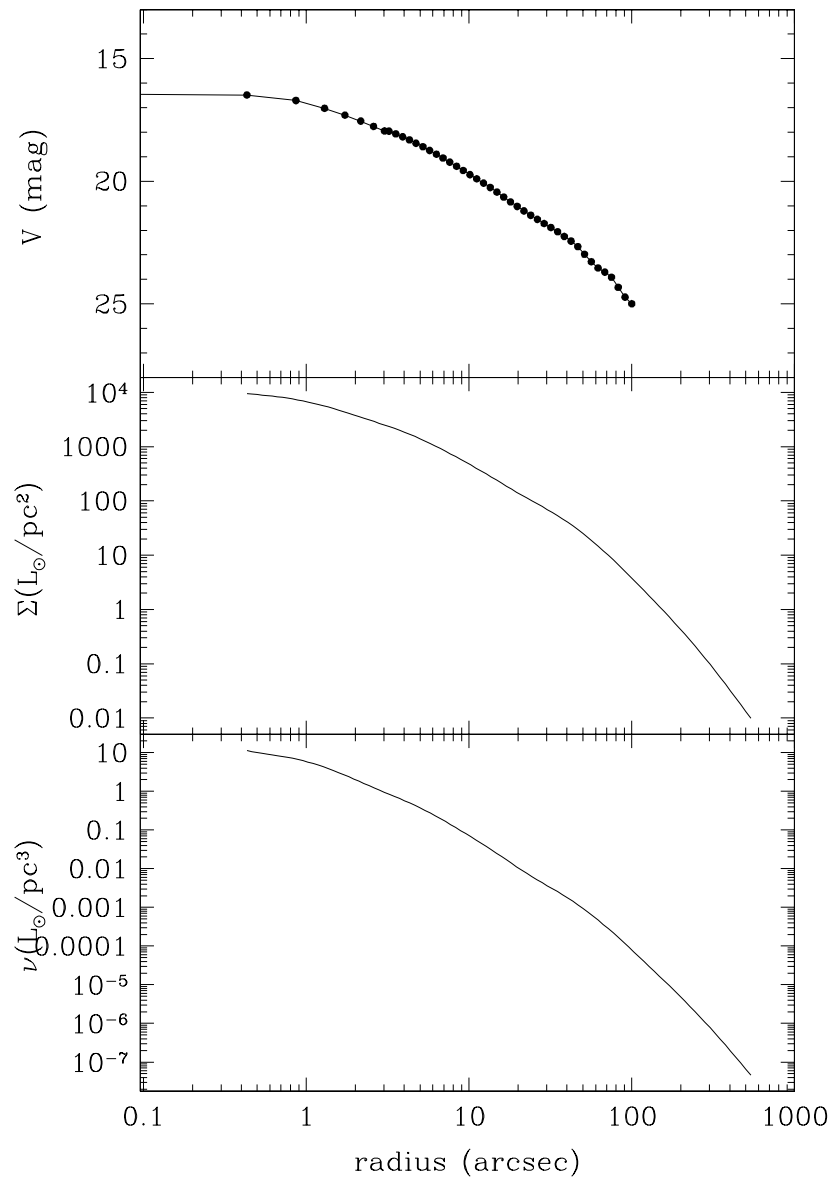


Figure 3.3: Surface brightness, luminosity density, and deprojected surface brightness profiles as a function of radius.

We fit the local continuum in the spectra by finding the biweight (Beers et al., 1990) in windows as described in Pinkney et al. (2003). The wavelength solution was found using Cd and Ne calibration lamps.

We obtain a nonparametric line-of-sight velocity distribution (LOSVD) by deconvolving the galaxy spectrum with a set of stellar template spectra using the maximum penalized likelihood technique of Gebhardt et al. (2000). Tests of this technique are given in Pinkney et al. (2003). There are 30 evenly-spaced velocity bins of 63 km s^{-1} that represent the LOSVD. We vary the height in each bin and the weights of each template star to find the best match to the galaxy spectrum. We use nine stellar templates with types ranging from G dwarf to M giant from Leitherer et al. (1996), convolved to our spectral resolution.

For our kinematic analysis we used the spectral range 4800-5450Å to match the wavelength range of our template stars. This region includes the $H\beta$ and Mgb lines, however we exclude the Mgb region because it is enhanced and our template stars therefore do not provide a proper fit. An example fit is shown in Figure 3.4.

The uncertainty of each velocity bin is obtained from Monte Carlo simulations. We convolve the best-fitted LOSVD and weighted stellar templates to obtain an initial galaxy spectrum. We then generate 100 realizations of the galaxy spectrum by adding Gaussian noise using an estimate of the initial rms. The LOSVD is determined for each realization as described above. The distribution of values in each velocity bin of the LOSVD provides an estimate

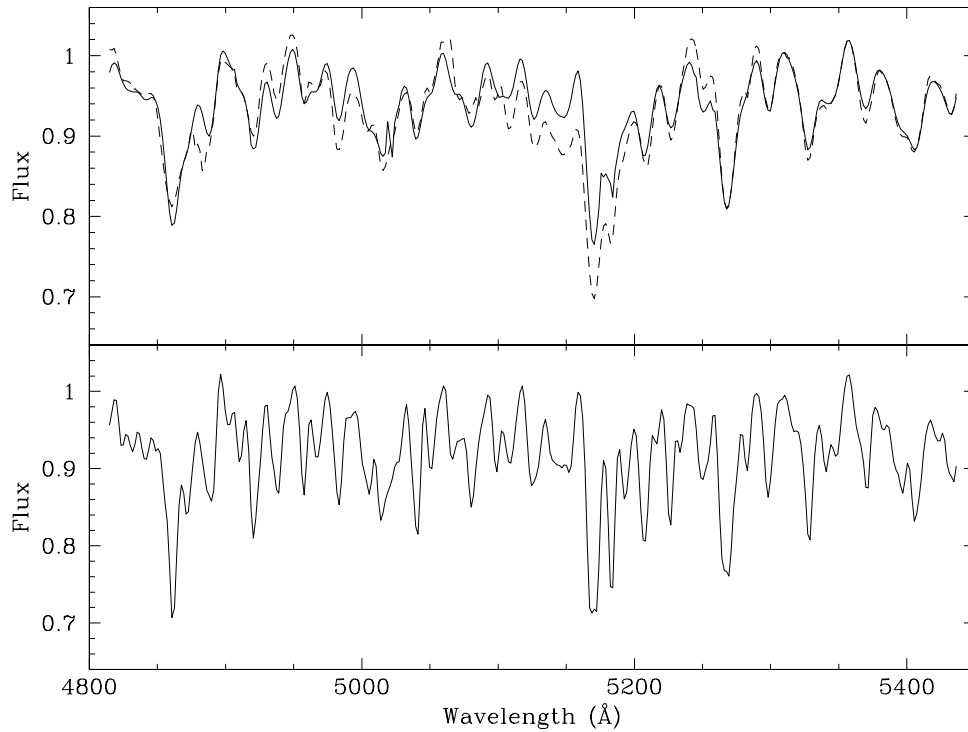


Figure 3.4: Spectrum of the combined, weighted template stars (lower panel), data from the central bin along the major axis (dashed line, upper panel), and the template spectrum convolved with the best-fitted LOSVD (solid line, upper panel). The region around Mgb from about 5125 \AA to 5200 \AA is excluded from the fit.

of the 68% confidence bands. Sample LOSVDs are shown in Figure 3.5.

Although we use the full nonparametric velocity profile in the dynamic modeling, in Figure 3.6 we plot the first four Gauss-Hermite moments (mean velocity V , velocity dispersion σ , asymmetric deviations from Gaussian (skewness) h_3 , and symmetric deviations from Gaussian (kurtosis) h_4). The kinematic data are given in Table 3.1 and Table 3.2.

3.4 Dynamical Models

We use axisymmetric orbit superposition models based on the method of Schwarzschild (1979) as described in §2.4. We again assume an edge-on inclination for this analysis, which is reasonable given NGC 6702’s axis ratio of 0.78 (2MASS, Skrutskie et al., 2006). For NGC 6702 we also include a central black hole with mass $3 \times 10^8 M_\odot$. We do not use the mass-to-light ratio scaling as described in §2.4 because of improved computational resources.

The orbital characteristics are computed in 16 angular bins and 60 radial bins from $0.2''$ to $500''$, and are compared to the data in 4 angular bins and 15 radial bins, which are similar in size to the HET data extraction bins. Our libraries have a range of approximately 12000 to 18000 total orbits.

3.4.1 Dark Matter Halo Profiles

We use both the Navarro, Frenk and White (NFW) and logarithmic potential dark halo profiles. The NFW (Navarro et al., 1996b) dark halo

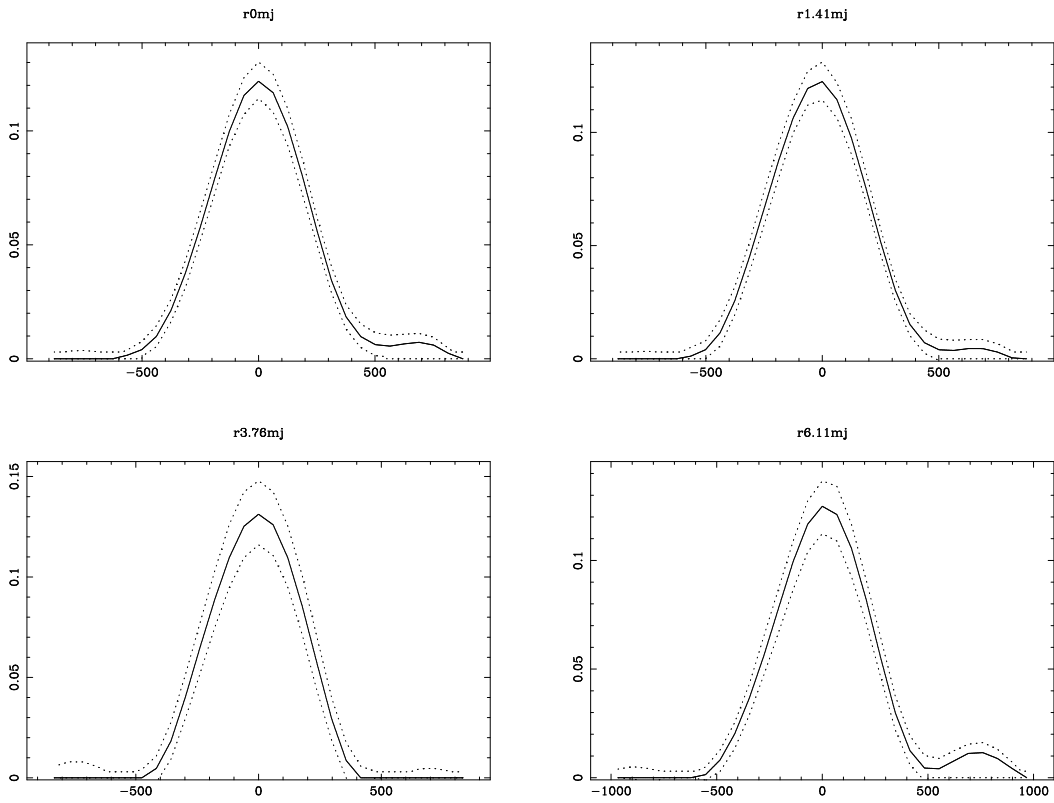


Figure 3.5: Line-of-sight velocity distributions (solid lines) with errors (dashed lines) for the first four radial bins along the major axis.

Table 3.1: NGC 6702 Major Axis Kinematics

r <i>arcsec</i>	v $km\ s^{-1}$	ϵ_v	σ $km\ s^{-1}$	ϵ_σ	h_3	ϵ_{h_3}	h_4	ϵ_{h_4}
0.00	-0.288	8.154	200.675	10.035	-0.001	0.028	0.000	0.019
1.41	-18.674	7.136	200.886	12.355	-0.002	0.029	-0.017	0.026
3.76	-7.392	8.047	179.440	11.199	-0.021	0.025	-0.055	0.019
6.11	0.777	8.690	210.964	12.571	-0.020	0.035	-0.009	0.024
8.46	-2.844	8.974	179.101	13.777	0.019	0.035	0.012	0.024
10.81	10.082	9.818	164.864	14.821	0.018	0.031	-0.031	0.022
13.16	-9.327	14.427	186.222	31.771	0.039	0.062	0.027	0.075
15.51	-11.775	17.042	187.415	23.555	0.058	0.055	0.002	0.042
17.86	3.401	18.296	173.914	25.642	-0.057	0.054	0.001	0.037
21.39	-11.180	13.395	189.440	19.272	-0.043	0.051	0.029	0.043
24.91	15.178	22.866	166.633	32.963	-0.129	0.062	0.040	0.064
35.49	0.380	25.215	129.986	49.460	0.021	0.061	-0.043	0.075
44.88	-8.592	29.393	142.033	44.079	0.145	0.121	0.022	0.128
54.28	-16.620	44.955	150.275	35.012	-0.005	0.045	-0.048	0.028

Table 3.2: NGC 6702 Minor Axis Kinematics

r <i>arcsec</i>	v $km\ s^{-1}$	ϵ_v	σ $km\ s^{-1}$	ϵ_σ	h_3	ϵ_{h_3}	h_4	ϵ_{h_4}
0.00	8.872	10.699	168.293	14.584	-0.027	0.036	-0.032	0.036
1.41	5.918	7.016	196.397	12.544	0.008	0.022	-0.039	0.016
3.76	1.700	8.748	177.389	14.339	-0.051	0.021	-0.011	0.018
6.11	17.574	8.315	176.736	15.784	0.025	0.028	0.007	0.030
8.46	5.044	9.945	164.761	16.301	-0.019	0.030	-0.027	0.024
10.81	1.467	10.381	151.915	19.279	-0.030	0.027	-0.036	0.024
13.16	2.333	15.416	185.062	24.561	-0.004	0.044	-0.040	0.038
16.68	22.194	12.643	155.309	18.871	-0.074	0.052	-0.032	0.029
21.39	1.503	19.402	188.478	28.373	-0.029	0.069	-0.038	0.061
26.08	12.356	17.650	147.983	25.784	-0.036	0.057	-0.054	0.040
31.96	51.991	34.915	203.553	41.372	0.030	0.096	0.018	0.105
39.01	-1.262	35.848	162.664	56.494	-0.036	0.154	0.134	0.211

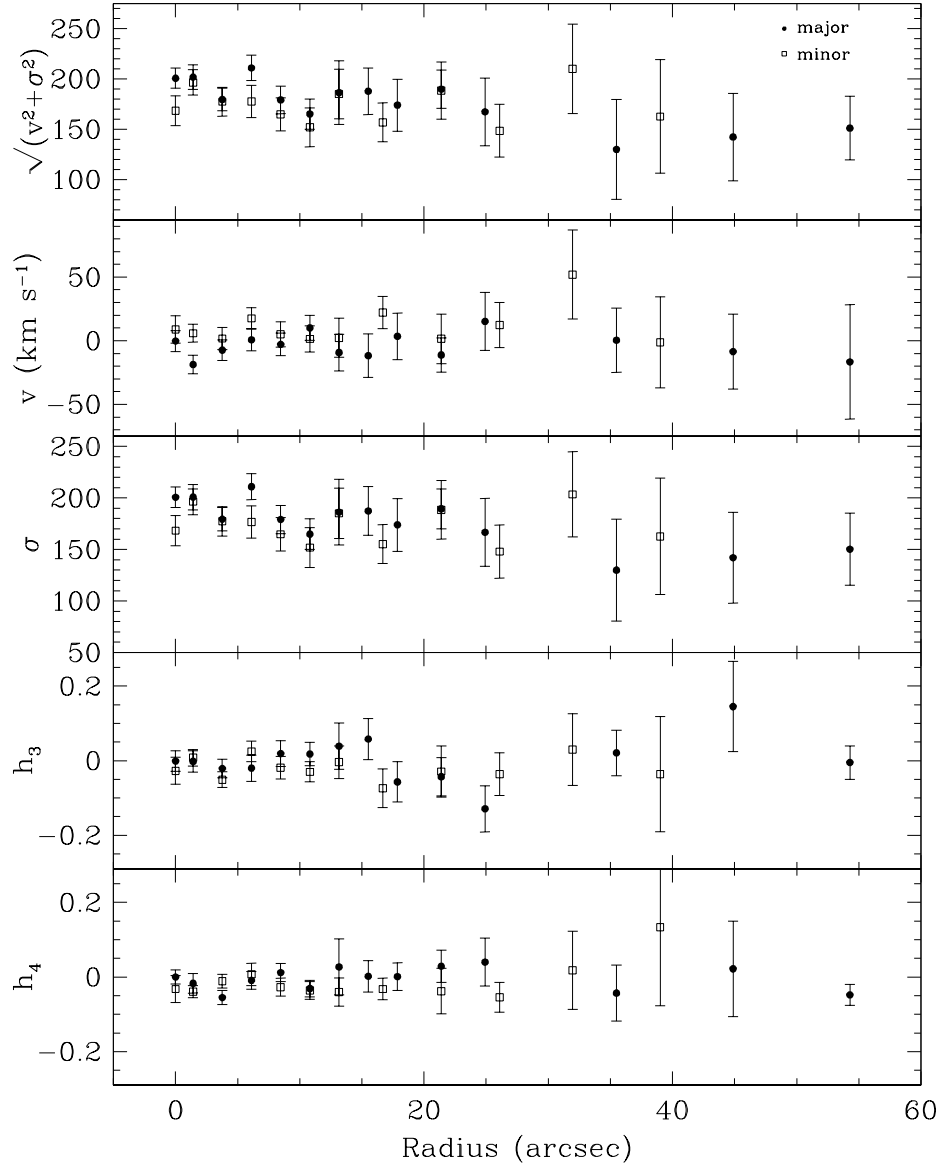


Figure 3.6: The second moment as measured by $\sqrt{V^2 + \sigma^2}$ and the Gauss-Hermite moments v , σ , h_3 and h_4 of the LOSVD along the major axis (solid circles) and minor axis (open squares).

density profile is given as

$$\rho(r) = \frac{\rho_{crit} \delta_c}{(r/r_s)(1 + r/r_s)^2} \quad (3.1)$$

where r_s is the scale radius of the halo and $\rho_{crit} = 3H^2/8\pi G$ is the critical density. We use $H = 70 \text{ km s}^{-1} \text{ Mpc}^{-1}$. Throughout this paper we refer to $\rho_{crit}\delta_c$ as the scale density. The characteristic overdensity δ_c is approximately related to a concentration parameter c by

$$\delta_c = \frac{\Delta_{vir}}{3} \frac{c^3}{\ln(1+c) - c/(1+c)}. \quad (3.2)$$

The virial overdensity Δ_{vir} varies with redshift and cosmological model and we use a value of $\Delta_{vir} = 101$. We vary both the concentration and scale radius, although there is a known correlation between them (Navarro et al., 1996b). This relation as given in Bullock et al. (2001) is

$$c \simeq 9 \left(\frac{M_{vir}}{1.5 \times 10^{13} h^{-1} M_\odot} \right)^{-0.13} \quad (3.3)$$

and can be written in the form

$$r_s^3 = \left(\frac{c}{9} \right)^{-1/0.13} \left(\Delta_{vir} \frac{4\pi}{3} \rho_{crit} c^3 \right)^{-1} (1.5 \times 10^{13} h^{-1} M_\odot). \quad (3.4)$$

The Logarithmic Potential halo is given by

$$\Phi = \frac{1}{2} v_c^2 \ln(r_c^2 + r^2) \quad (3.5)$$

which corresponds to the density distribution

$$\rho(r) = \frac{v_c^2}{4\pi G} \frac{3r_c^2 + r^2}{(r_c^2 + r^2)^2} \quad (3.6)$$

(Binney & Tremaine, 1987) where v_c is the circular velocity and r_c is the characteristic radius.

3.5 Results

The best-fitted model is determined by comparing the χ^2 between the model and data LOSVDs, with the uncertainty of the data determined from the 68% confidence band. Example LOSVDs are shown in Figure 3.7 for several radial bins. It is difficult to determine a reduced χ^2 because determining the number of degrees of freedom is problematic. The number of independent observables is roughly the number of radial data bins times the number of LOSVD bins at each radius ($26 \times 13 = 338$ in this case), however the LOSVD bins are correlated and thus the effective number of data points is less than this value. Regardless, the change in χ^2 between different models remains a valid statistic to determine confidence levels of the fits. For example, a change in χ^2 of 1 corresponds to the 68.3% confidence level.

3.5.1 NFW Halo

We ran 4900 models with scale radius from 5 to 5000 kpc, c from 0.3 to 18, corresponding to a range in scale density of 3.9×10^{-6} to $0.013 M_\odot pc^{-3}$, and M/L_V from 1.2 to 3.4. Figures 3.8 and 3.9 show the resulting χ^2 as a function of each parameter. Our results show a degeneracy between scale radius and

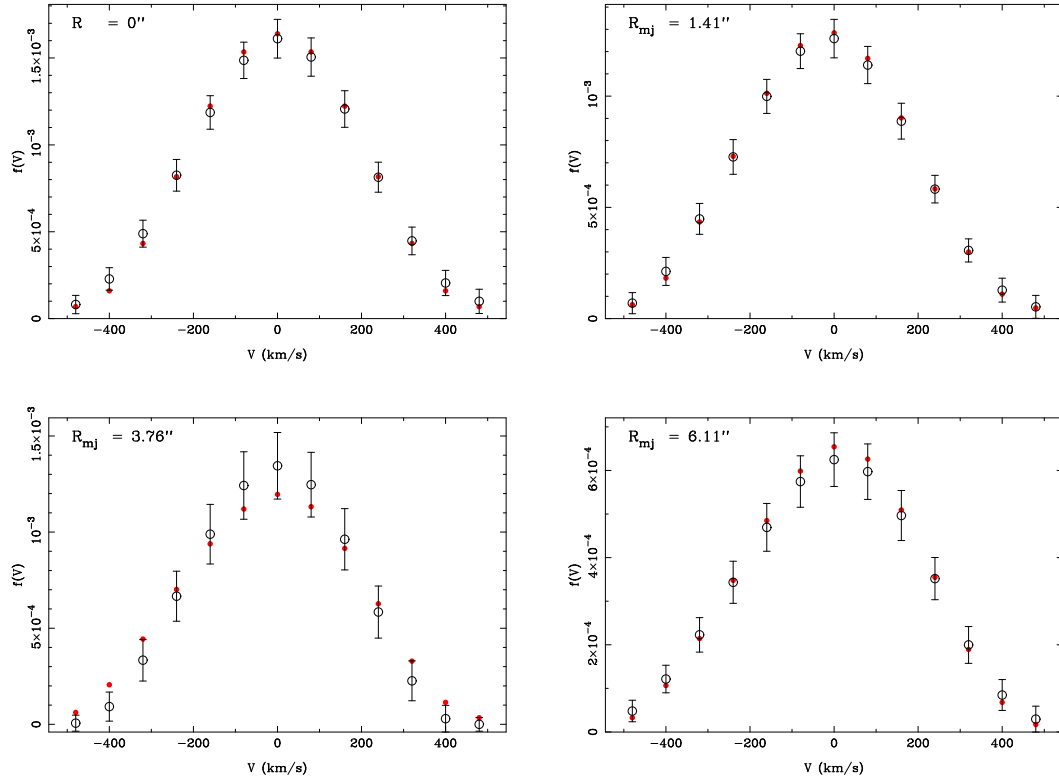


Figure 3.7: Match of data and no dark halo model LOSVDs for the central four radial bins along the major axis. The open circles are the data values with error bars and the closed red circles are the model values. The area is normalized to the total light in that bin.

Table 3.3: NGC 6702 Best-Fitted Halo Model Results

Halo	χ^2	M/L_V	Halo parameters
No halo	113.2	3.2 ± 0.2	...
Log halo	99.11	$2.4^{+0.5}_{-0.7}$	r=1800 kpc v=150 km/s
NFW halo	99.06	$2.2^{+0.4}_{-0.8}$	c=2.0 $\rho = 8.48 \times 10^{-5} M_\odot/pc^3$ r=700 kpc

scale density as expected.

We find that we are unable to constrain the shape of the dark halo in NGC 6702. Models within 1σ of the minimum span a range from 20 kpc to beyond 5000 kpc in radius and 0.5 to 16 in c (7.9×10^{-6} to $9.9 \times 10^{-3} M_\odot pc^{-3}$ in density). The mass-to-light ratio is determined to be $2.2^{+0.4}_{-0.8}$ in V . The uncertainty in M/L_V is determined from the one-dimensional envelope in χ^2 shown in Figure 3.9. The best-fitted NFW halo density profile and circular velocity curve is shown in Figure 3.10.

The no halo model is ruled out with a change in χ^2 of 14.14, corresponding to nearly 6σ (99.99% confidence level). Table 3.3 shows the χ^2 values and halo parameters of the best-fitted halo model and model with no dark halo. As discussed above, we do not attach significance to the halo parameters.

Figures 3.11 and 3.12 show the internal moments σ_r , σ_θ , and σ_ϕ and ratio of radial to tangential dispersion along the major and minor axes for the model with no dark halo and the best-fitted NFW halo model. Note that

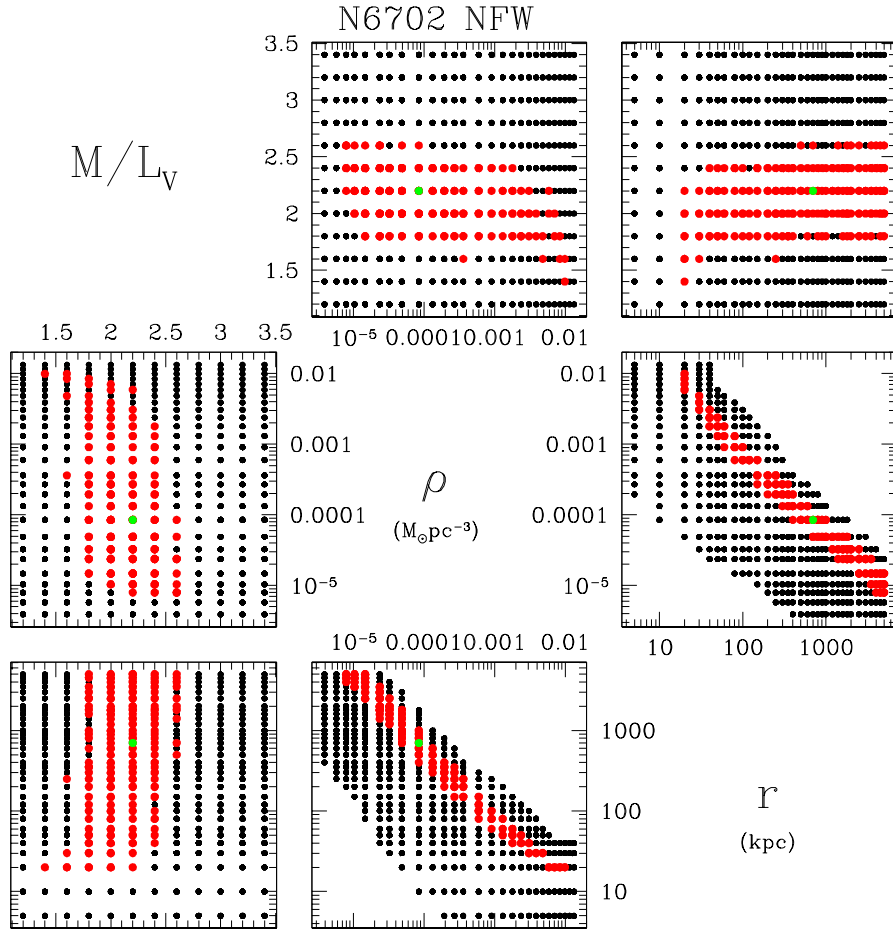


Figure 3.8: χ^2 grids in M/L_V , scale radius, and scale density for each of the NFW halo models. Black points show each halo modeled. Red points show models within $\Delta\chi^2 = 1$ of the minimum value and the green point is the model with the minimum χ^2 .

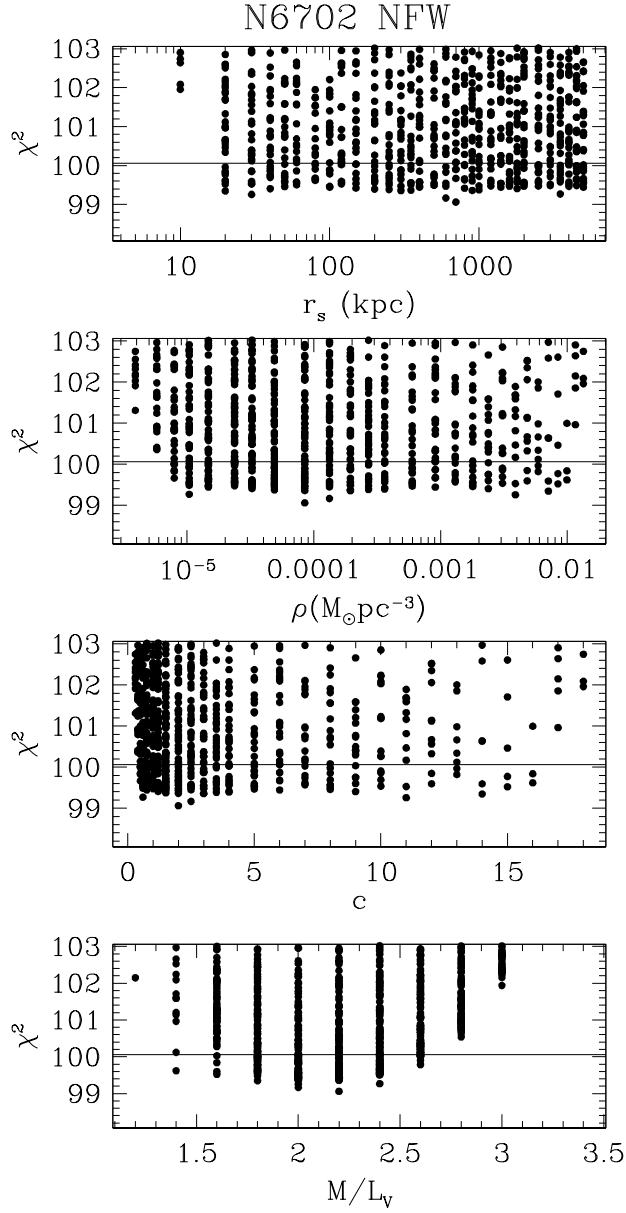


Figure 3.9: χ^2 as a function of scale radius, scale density, concentration, and M/L_V for each of the NFW halo models. The solid line shows $\Delta\chi^2 = 1$ (1σ) from the minimum value.

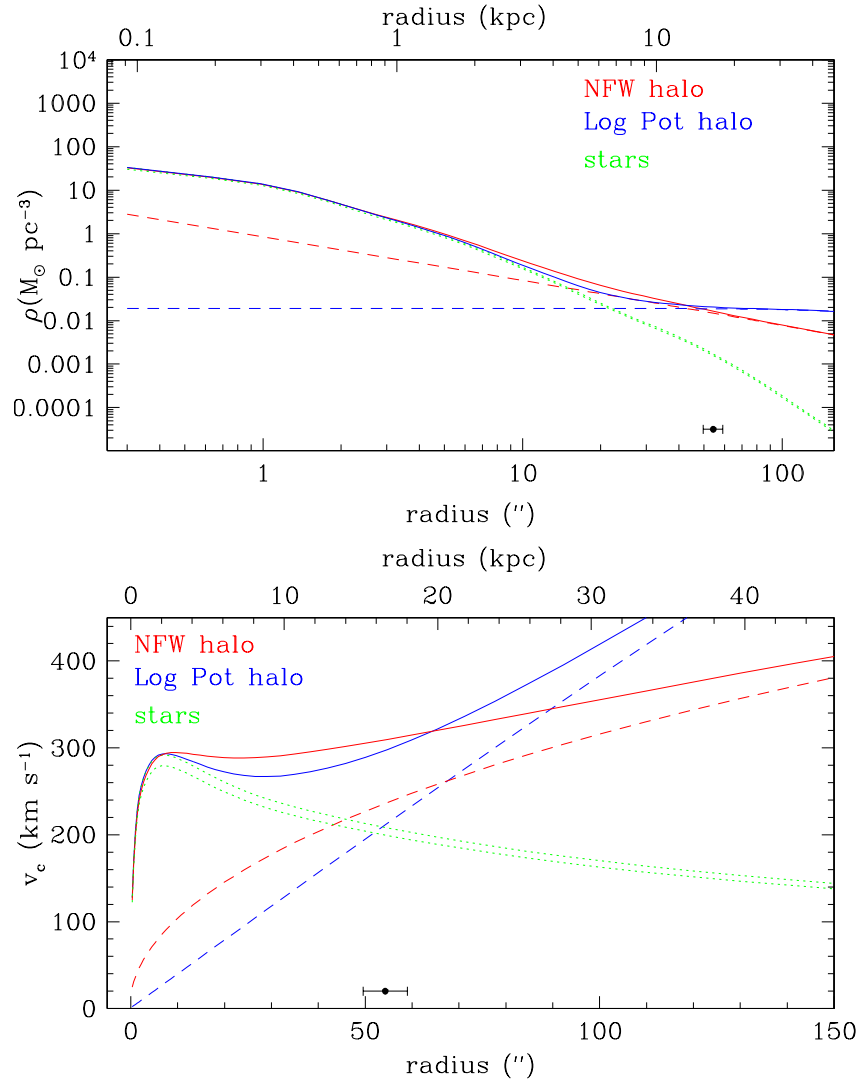


Figure 3.10: Density (top) and circular velocity (bottom) as a function of radius for the best-fitted dark halo profiles. The green dotted lines are stars only, dashed lines are halo only, and solid lines are halo plus stars for the NFW (red) and logarithmic potential (blue) halos. The data point shows the radial extent of our data.

throughout the manuscript our major and minor axes results are for the full angular bins around the axes. The model without a dark halo shows radial anisotropy at small radii and tangential anisotropy at large radii. Tangential anisotropy at large radii in a model with no dark halo could be an indication of the need for a dark halo. The observations constrain mainly σ_ϕ , so both σ_r and σ_θ may be artificially decreased to create a smaller total σ that can be fit without a dark halo. The best-fitted NFW halo model shows radial anisotropy along the major axis.

Although the models are fitted to the full nonparametric velocity profile, in Figure 3.13 we plot the first four Gauss-Hermite moments for our data and the best-fitted halo models.

3.5.2 Logarithmic Potential Halo

We ran 3700 models with a radius from from 3 to 3.2×10^4 kpc, circular velocity from 50 to 3.6×10^5 km/s, and M/L_V from 1.6 to 3.4. The χ^2 results are shown in Figures 3.14 and 3.15.

As with the NFW models we are again unable to constrain the shape of the dark halo. Models within 1 sigma of the minimum span a range from 6 to beyond 3.2×10^4 kpc in radius and from 250 to beyond 3.6×10^5 km/s in velocity. The mass-to-light ratio in V is constrained to $2.4_{-0.7}^{+0.5}$. The best-fitted halo density profile and circular velocity curve are shown in Figure 3.10.

The no halo model is again ruled out with a nearly 6σ confidence (99.99% confidence level), corresponding to a change in χ^2 of 14.09. There

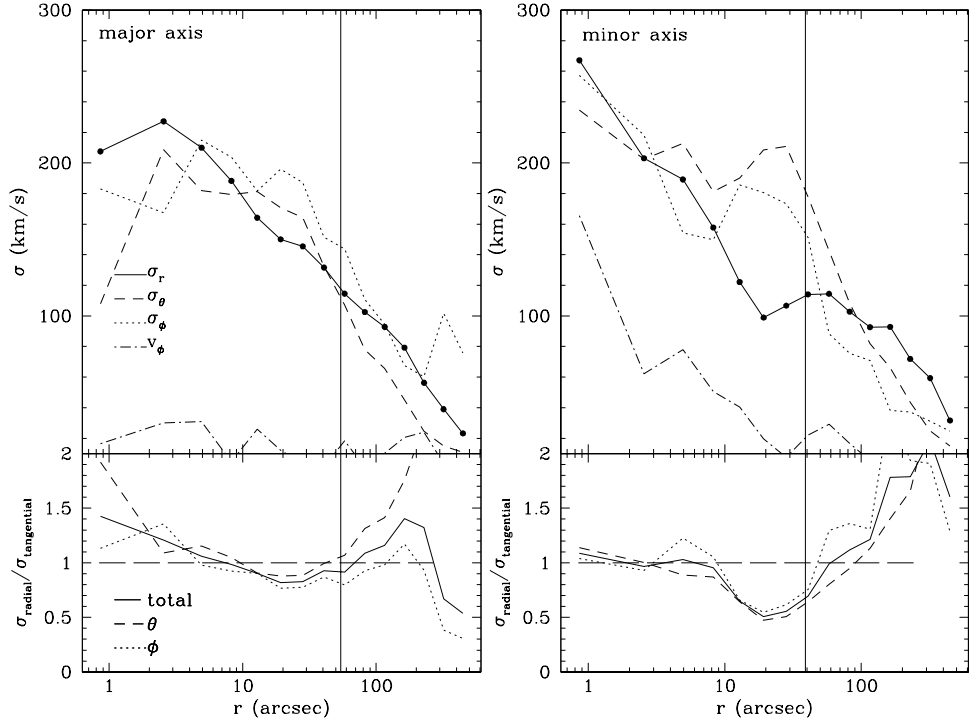


Figure 3.11: Internal moments σ_r , σ_θ , and σ_ϕ (top) and ratio of radial to tangential dispersion (bottom) for the model with no dark halo along the major axis (left) and minor axis (right). Note that σ_ϕ includes both random and ordered motions, which are shown (dot-dashed line) and are small. The solid vertical line shows the radial extent of our kinematic data; results beyond this point are not reliable.

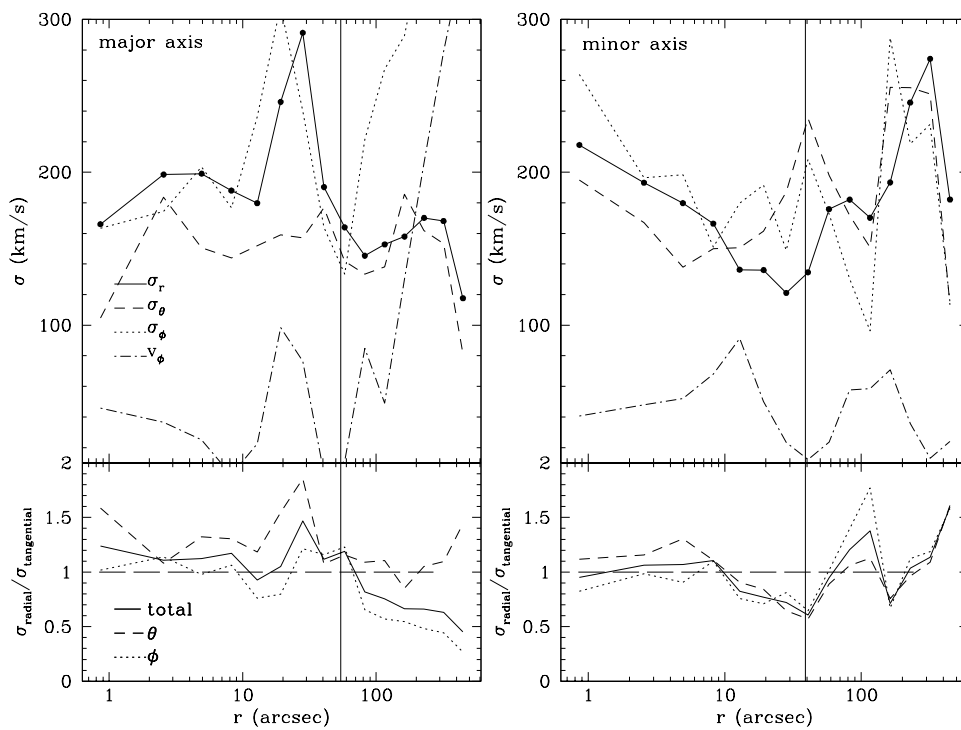


Figure 3.12: The same as 3.11 for the best-fitted NFW halo.

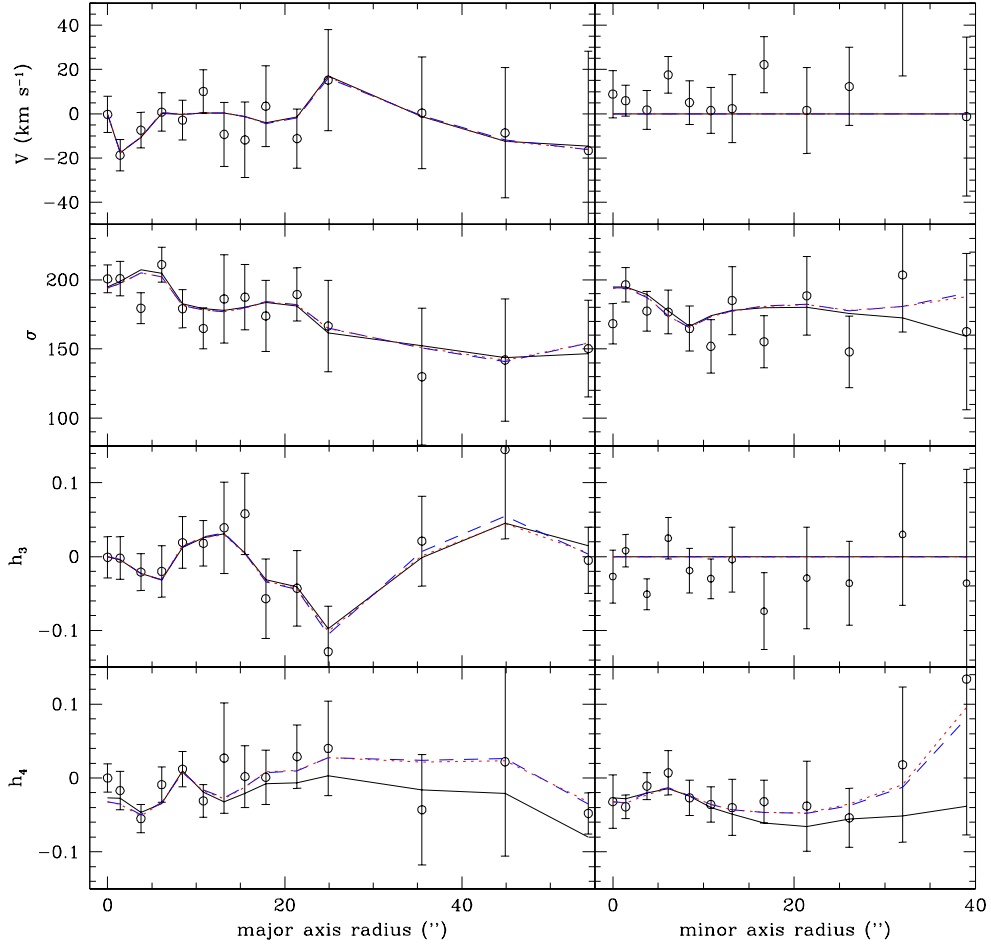


Figure 3.13: Model kinematics compared to data. Although we model the full LOSVD, we show the Gauss-Hermite parameters v , σ , h_3 and h_4 as a function of radius for our data (open circles) along the major axis (left) and minor axis (right). Lines indicate the no halo (solid black), NFW halo (blue dashed), and logarithmic potential halo (red dotted).

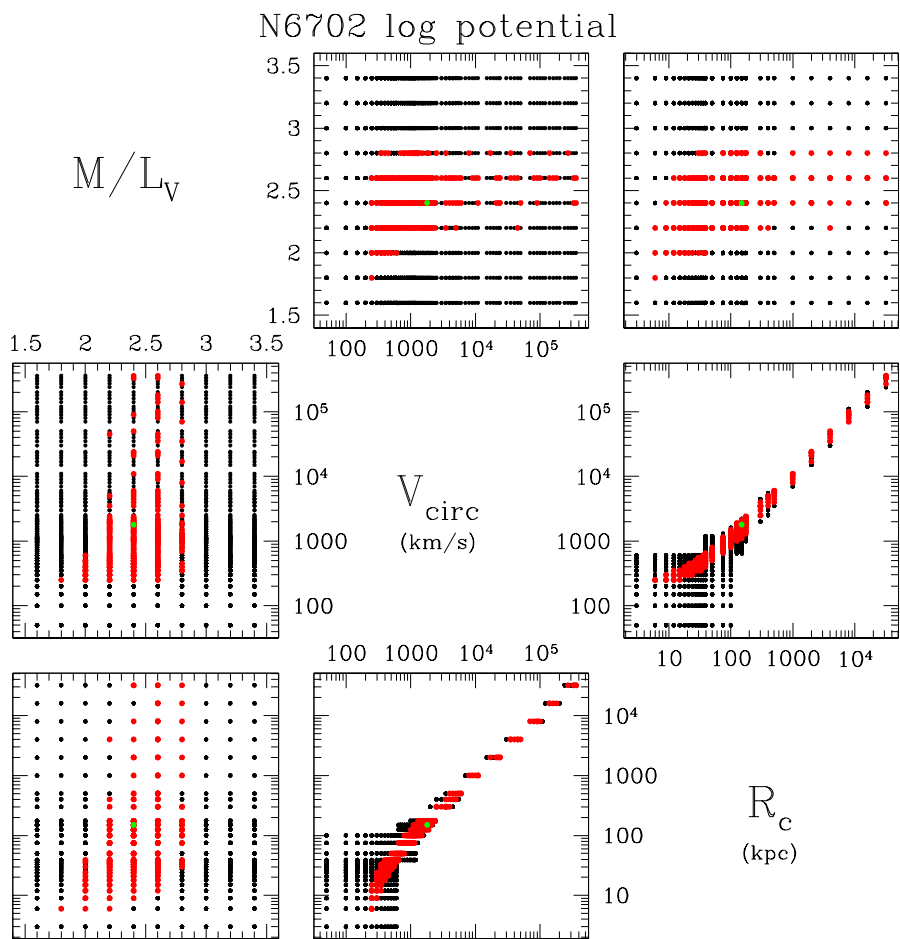


Figure 3.14: χ^2 grids in M/L_V , circular velocity, and scale radius for each of the logarithmic potential halo models. Black points show each halo modeled. Red points show models within $\Delta\chi^2 = 1$ of the minimum value and the green point is the model with the minimum χ^2 .

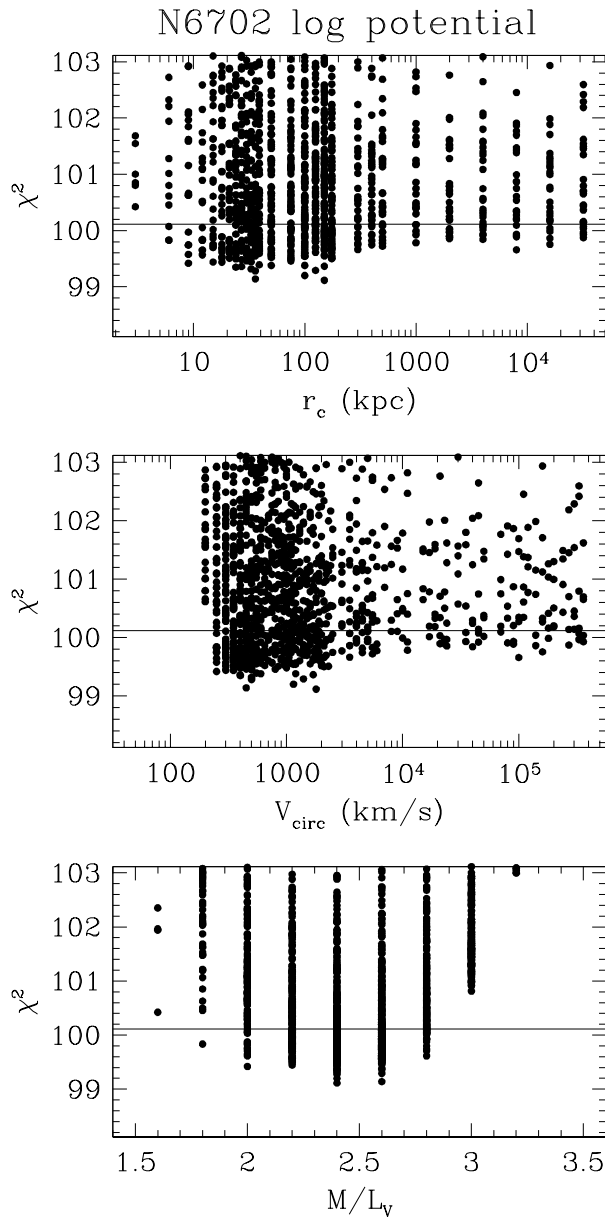


Figure 3.15: χ^2 as a function of M/L_V , radius, and circular velocity for each of the logarithmic potential halo models. The solid line shows $\Delta\chi^2 = 1$ (1σ) from the minimum value.

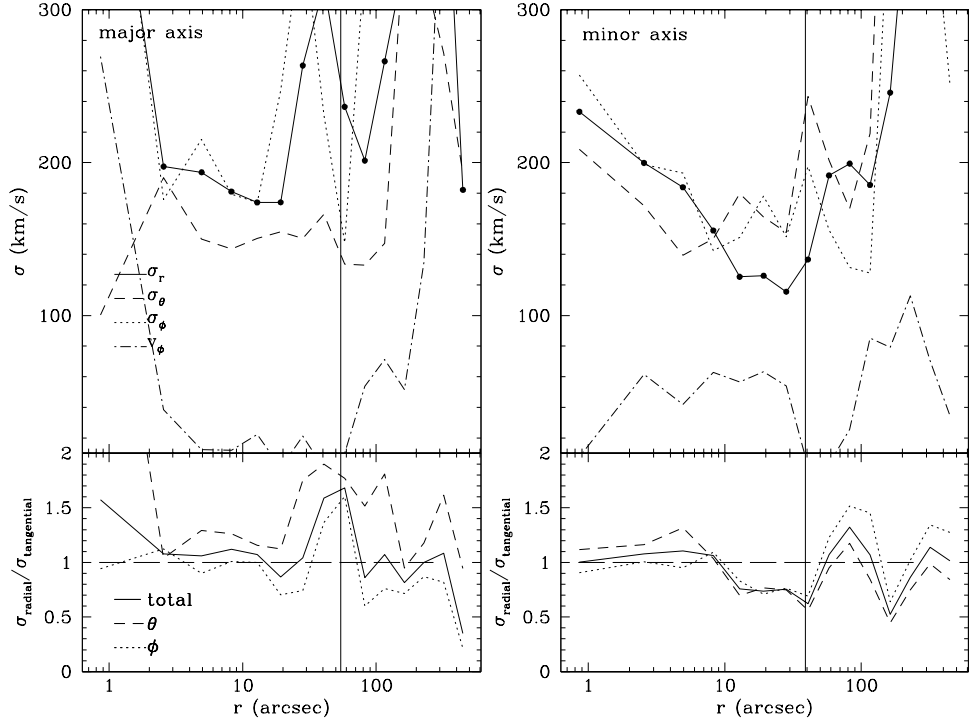


Figure 3.16: The same as 3.11 for the best-fitted logarithmic potential halo.

is no significance in the $\Delta\chi^2$ between the NFW and logarithmic potential halos (see Table 3.3).

The internal moments σ_r , σ_θ , and σ_ϕ and ratio of radial to tangential dispersion along the major axis are shown in Figure 3.16 and are roughly consistent with those of the best-fitted NFW halo.

Figure 3.13 shows the first four Gauss-Hermite moments for our HET data and the best-fitted halo models. Note that the models fit the full non-parametric velocity profile of the data.

3.5.3 Mass Measurement

Although we are unable to constrain the shape of the dark matter halo, we can constrain the amount of mass in the halo. Figures 3.17 and 3.18 show the mass enclosed within the extent of our kinematic data (about $2 R_e$) as a function of χ^2 for the NFW and logarithmic potential halos within 1σ of the best-fitted model. The mass measurements are given in Tables 3.4 and 3.5. Within the radial extent of our data the stellar mass is similar for both the NFW and logarithmic potential halos, but the NFW halo has a larger halo mass.

Table 3.4: NGC 6702 Best-Fitted Halo Model Mass Results at $1R_e$ ($29''$)

Halo	M_{tot} (low,high) $10^{11}M_{\odot}$	M_{stars} (low,high) $10^{11}M_{\odot}$	M_{halo} (low,high) $10^{11}M_{\odot}$
No halo	1.60 (1.50,1.70)	1.60 (1.50,1.70)	0.00
Log halo	1.47 (1.30,2.11)	1.20 (0.90,1.40)	0.27 (0.10,1.01)
NFW halo	1.73 (1.46,2.08)	1.10 (0.70,1.30)	0.63 (0.34,1.28)

Table 3.5: NGC 6702 Best-Fitted Halo Model Mass Results Within Our Data ($58''$, $\sim 2R_e$)

Halo	M_{tot} (low,high) $10^{11}M_{\odot}$	M_{stars} (low,high) $10^{11}M_{\odot}$	M_{halo} (low,high) $10^{11}M_{\odot}$
No halo	2.24 (2.10,2.38)	2.24 (2.10,2.38)	0.00
Log halo	3.45 (2.61,4.92)	1.68 (1.26,1.96)	1.77 (.660 3.39)
NFW halo	3.73 (2.90,4.71)	1.54 (.981,1.82)	2.19 (1.20 3.37)

N6702 NFW Halo

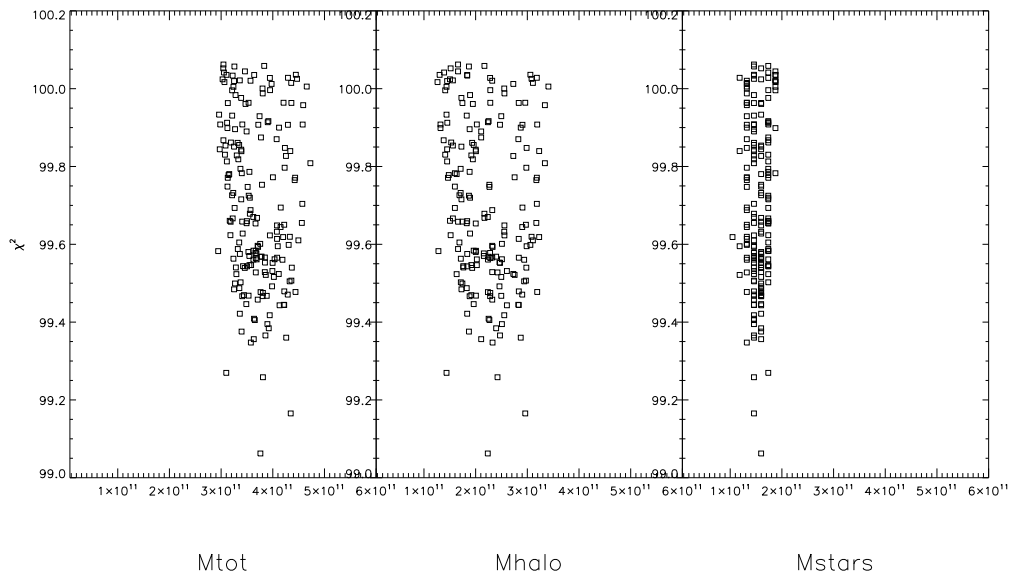


Figure 3.17: Total mass, mass in halo and mass in stars all within our kinematic data range (about $2 R_e$) for all of the models within 1σ of the minimum value for the NFW halo.

N6702 Log Pot Halo

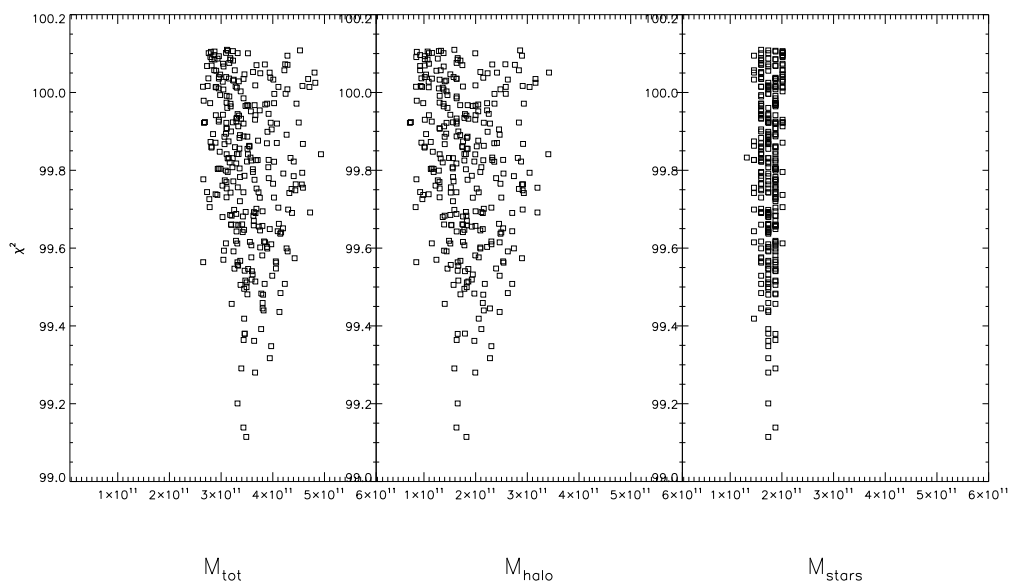


Figure 3.18: Total mass, mass in halo and mass in stars all within our kinematic data range (about $2 R_e$) for all of the models within 1σ of the minimum value for the logarithmic potential halo.

Figures 3.19 and 3.20 show the enclosed mass, total mass to light ratio, and halo mass fraction as a function of radius for all halo models within 1σ of the best-fitted model for both the NFW and logarithmic potential halos. Figure 3.21 shows these mass profiles for just the best-fitted models to compare the NFW and logarithmic potential halos.

Within the radial extent of our data, about $2R_e$, the fraction of dark matter is 0.59 for the NFW halo and 0.51 for the logarithmic potential halo. At $1R_e$ the ratio of dark matter to total matter is 0.36 for the NFW halo and 0.18 for the logarithmic potential halo. This matches other studies that find that the dark matter is 10 – 40% of the total matter at $1R_e$ and that dark matter begins to dominate at $2 - 4R_e$ (e.g. Saglia et al., 2000; Gerhard et al., 2001; Mamon & Lokas, 2005). It also agrees with our previous results for NGC 821 (see §2.5).

3.6 Conclusions

We present kinematics of NGC 6702 to approximately 2 effective radii using long-slit spectroscopy from the Hobby-Eberly Telescope. We perform axisymmetric orbit superposition models using NFW and logarithmic potential dark halos and find that dark matter is necessary (at the 5σ level) to explain the observations of NGC 6702, yet we are unable to constrain the shape of the dark matter profile for this galaxy.

We find a V band stellar mass-to-light ratio of 2.2 for the NFW halo and 2.4 for the best-fitted power-law halo. With no dark halo a mass-to-light

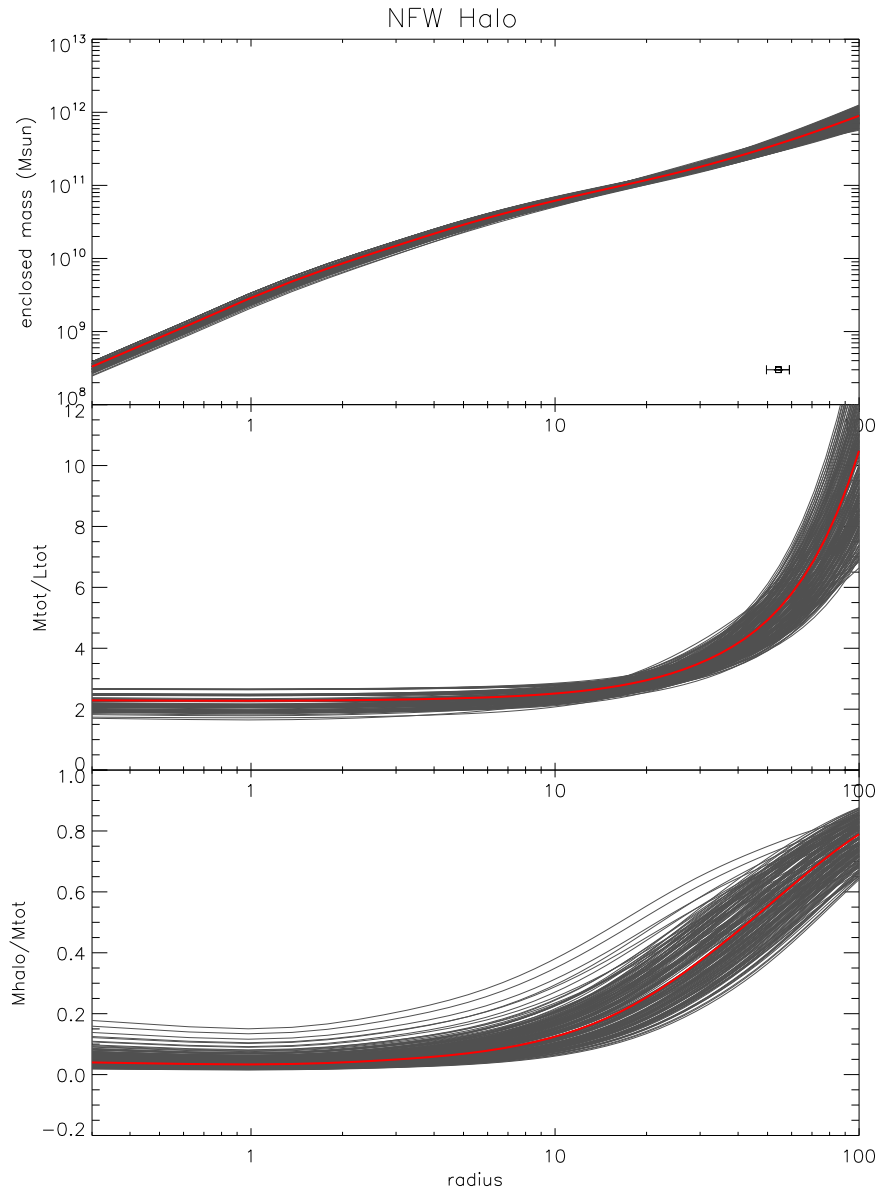


Figure 3.19: Enclosed mass, total mass to light ratio, and halo mass fraction as a function of radius for all NFW halo models within 1σ of the best-fitted NFW halo model (red line). The data point shows the radial extent of our kinematic data.

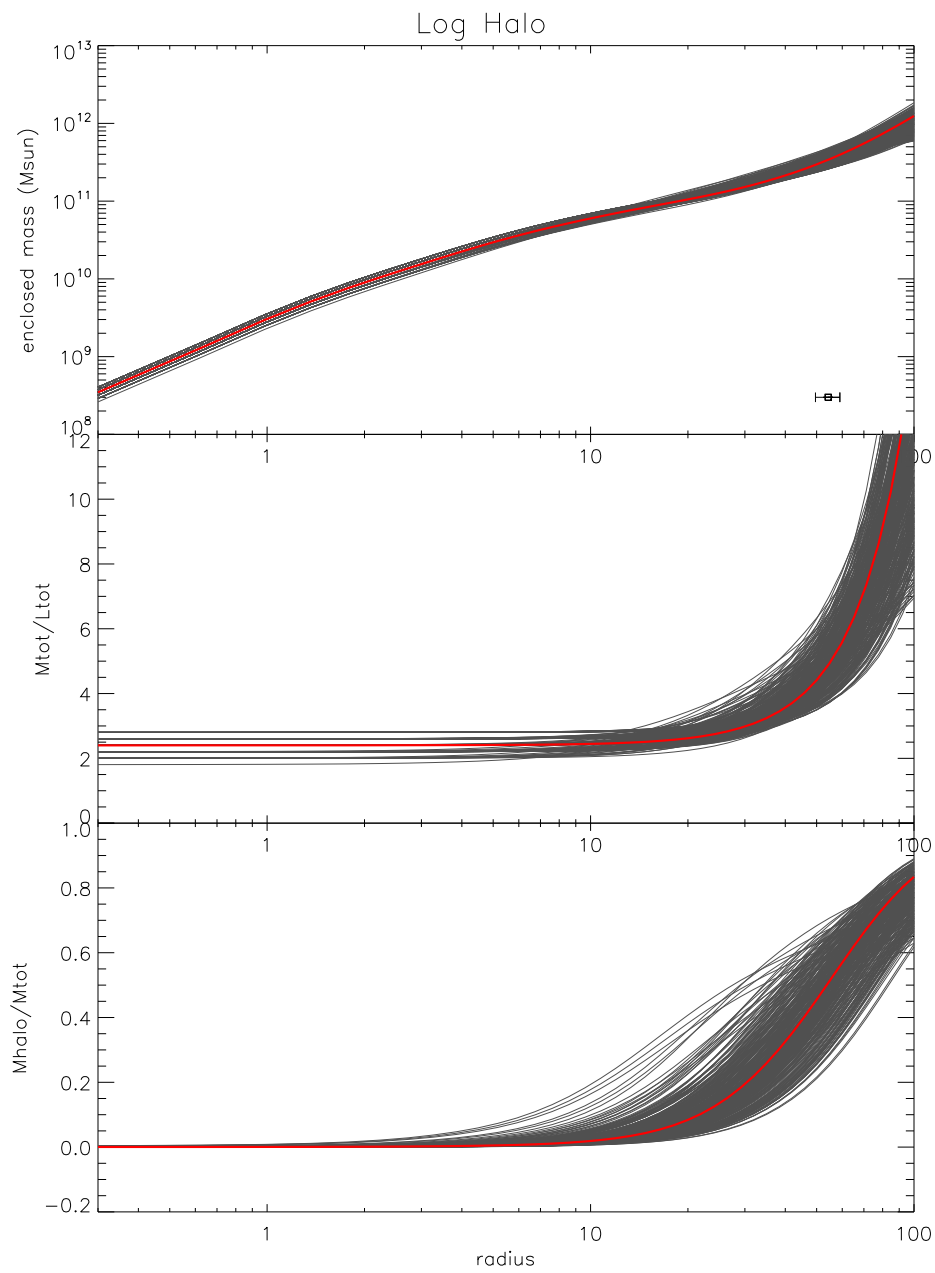


Figure 3.20: Mass profiles as in 3.19 for all logarithmic potential halo models within 1σ of the best-fitted logarithmic potential halo model (red line).

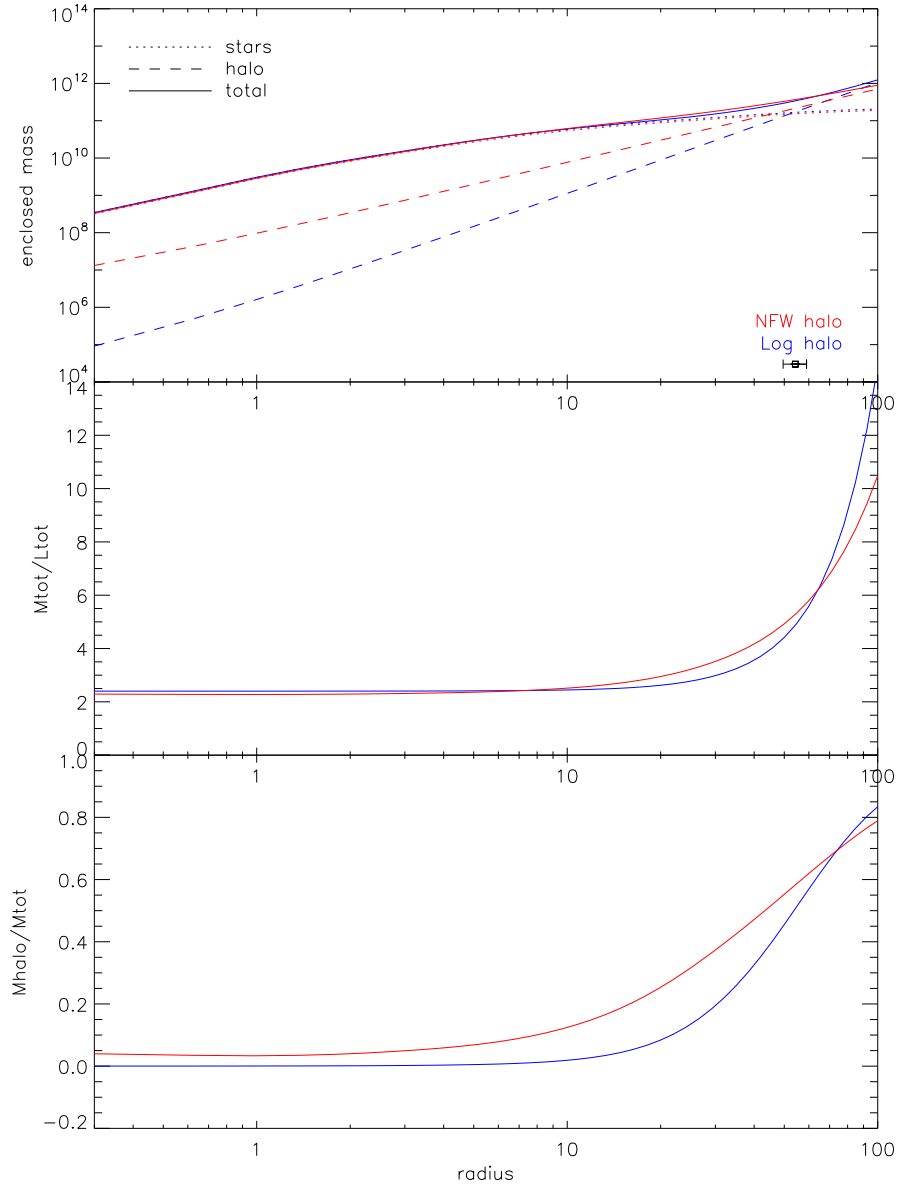


Figure 3.21: Mass profiles as in 3.19 for the best-fitted NFW (red) and logarithmic potential (blue) halo profiles. The top panel shows stars only (dotted), halo only (dashed), and total mass (solid lines).

ratio of 3.2 is needed. Correcting for galactic extinction using $A_V = 0.363\text{mag}$ (Schlegel et al., 1998, NED extragalactic database) these become M/L_V of 1.57, 1.72, and 2.29 respectively.

The models without a dark halo show tangential anisotropy at large radii. This may be an indication that a dark halo is necessary because the radial component of the velocity dispersion may be artificially decreased at large radii in order to create a smaller total velocity dispersion that can be reproduced by a haloless model. The best-fitted dark halo model shows a radial bias in the θ direction at all radii.

Even though we cannot constrain the shape of the dark matter halo, we are able to constrain the enclosed mass of NGC 6702. Within the radial extent of our kinematic data ($\sim 2R_e$) the total mass is roughly $3.6 \times 10^{11} M_\odot$, with dark matter fractions of 0.59 for the best-fitted NFW halo and 0.51 for the best-fitted logarithmic potential halo. At $1R_e$ the dark matter fraction is 0.36 for the NFW halo profile and 0.18 for the logarithmic potential halo profile. These dark matter fractions agree with previous studies of elliptical galaxies.

Chapter 4

The Dark Halo of NGC 4697

4.1 Introduction

As discussed in Chapter 2, planetary nebulae have been the subject of some controversy in previous dark matter studies. PNe may have different anisotropies than stellar light and also may be distributed differently. In this chapter we model NGC 4697 using PN kinematics only at large radii.

NGC 4697 was previously modeled by Binney et al. (1990) and Dejonghe et al. (1996) based on kinematics within $1R_e$ and was found to be consistent with having no dark matter. Méndez et al. (2001) obtained an early version of the planetary nebulae sample we use in this chapter and found that NGC 4697 is consistent with having no dark halo if the galaxy is isotropic; if anisotropic, dark matter could be present. Recently, de Lorenzi et al. (2008) used a new modeling technique, NMAGIC, to more accurately model this planetary nebula sample and found that dark matter is needed. Although they do not attempt to determine the shape of the halo, they find that a logarithmic potential halo with circular velocity greater than or equal to 250 km/s at $5R_e$ best fit the data.

NGC 4697 is also an interesting subject because of its central super-

massive black hole. Its black hole mass measurement was one of the most robust of Gebhardt et al. (2003), and through this study we can learn how adding a dark halo to the analysis changes the black hole result, if at all. Gebhardt & Thomas (2009) shows that for M87 the inclusion of the dark halo changes the black hole mass by a factor of 2. This is a result of the more accurate stellar mass-to-light ratio obtained when a dark halo is included at large radii.

NGC 4697 is classified as an E6 (de Vaucouleurs et al., 1991). It has a stellar disk along the major axis (Carter, 1987) and has significant gas and dust detections (Sofue & Wakamatsu, 1993). HST imaging reveals a central dust disk (Lauer et al., 1995). It has disk-like isophotes (Peletier et al., 1990) and a power-law profile (Faber et al., 1997). Its distance is 11.7 Mpc (Tonry et al., 2001).

The measured effective radius of NGC 4697 has a large variation. Faber et al. (1989) find an effective radius of $75''$, Binney et al. (1990) find $95''$, and (RC3) list it as $72''$. However, 2MASS finds effective radii of $42.4''$, $39.94''$, and $39.510''$ in the J, H, and K bands respectively. Our own photometry gives an effective radius of $37.24 \pm 13.12''$ including a disk or $60''$ without a disk. We adopt an R_e of $60''$.

A 2MASS image of NGC-4697 is shown in Figure 4.1.

§4.2 describes the data; the dynamical models are described in §4.3; we present our results in §4.4 and give conclusions in §4.5.

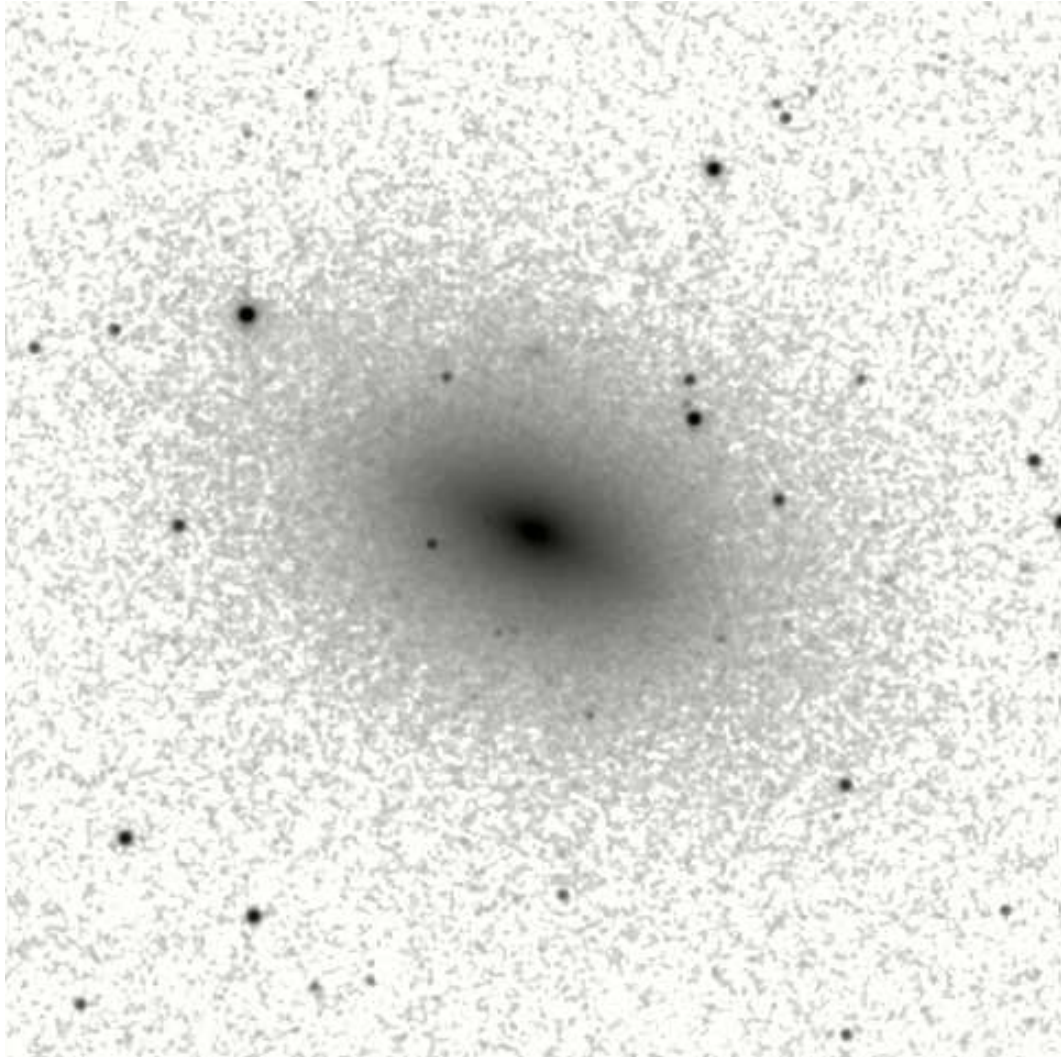


Figure 4.1: NGC 4697 JHK composite image from the 2MASS Large Galaxy Atlas (Jarrett et al., 2003).

4.2 Data

4.2.1 Stellar Kinematics

We use both stellar light and planetary nebula data from the literature to constrain our models. The stellar data come from Pinkney et al. (2003) and includes HST STIS observations in the center and ground-based data from the MDM Observatory. These data are symmetrized and binned before extracting line-of-sight velocity distributions (LOSVDs) for use in the axisymmetric models as described in Gebhardt et al. (2003).

4.2.2 Planetary Nebulae Kinematics

We use planetary nebula data from Méndez et al. (2001, 2008, 2009) who use the FORS1 Cassegrain spectrograph of the ESO Very Large Telescope and the FOCAS Cassegrain imaging spectrograph at the Subaru telescope. Their planetary nebula velocity measurements extend to over $400''$ (about 6 to $7 R_e$).

To use the planetary nebulae in our models we bin them according to the binning scheme used for the dynamical models (see §4.3 below). Because we use axisymmetric models the PNe were folded along the major axis and ipped about the minor axis so that the data are in one quadrant of the galaxy, as shown in Figure 4.2. Within each bin a line-of-sight velocity distribution was calculated using the PN velocities within that bin. Bins with less than 25 PNe were combined with the adjoining angular bin to give enough velocities to create an accurate LOSVD. An example LOSVD is shown in Figure 4.3.

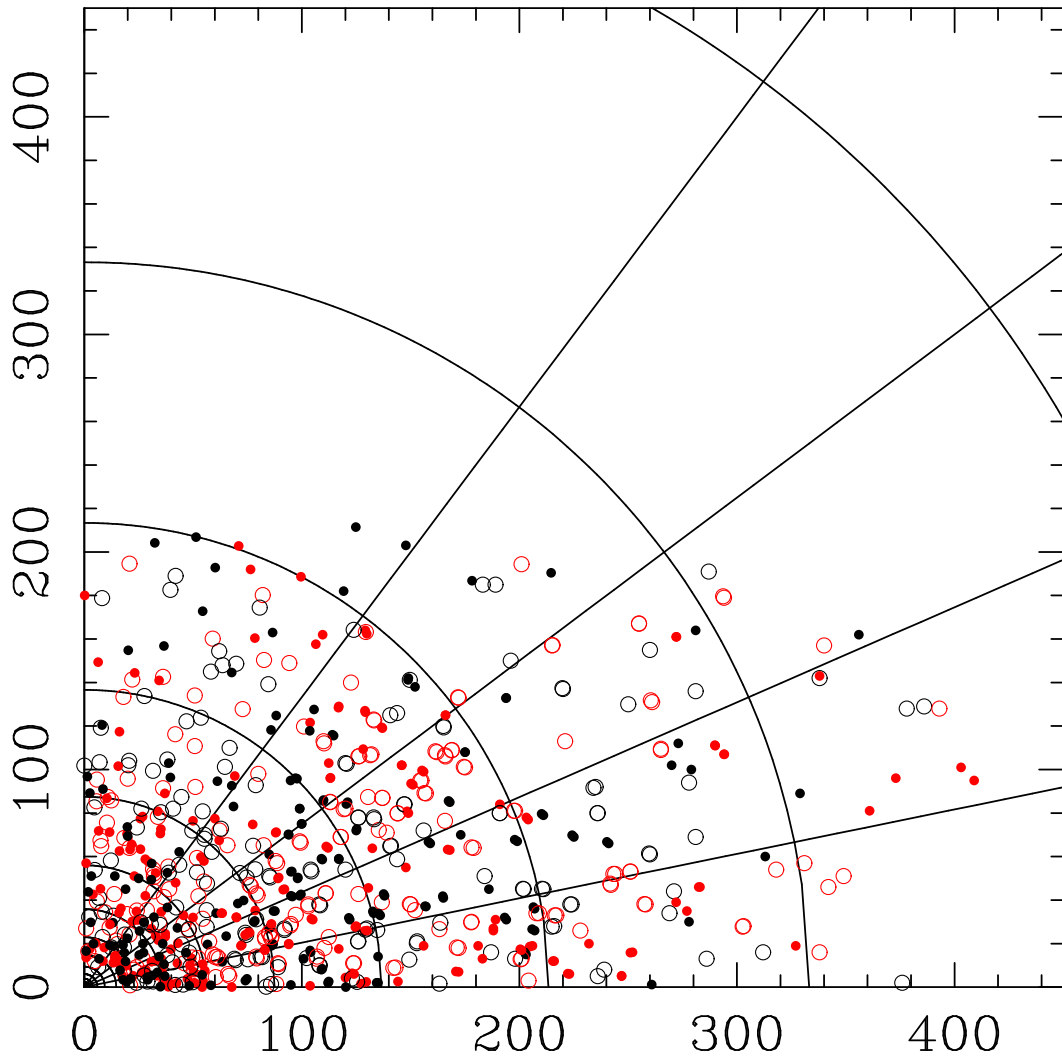


Figure 4.2: Location of planetary nebulae on the sky. Red points have been folded along the major axis and open points have been flipped along the minor axis. The x and y axes are given in arcseconds.

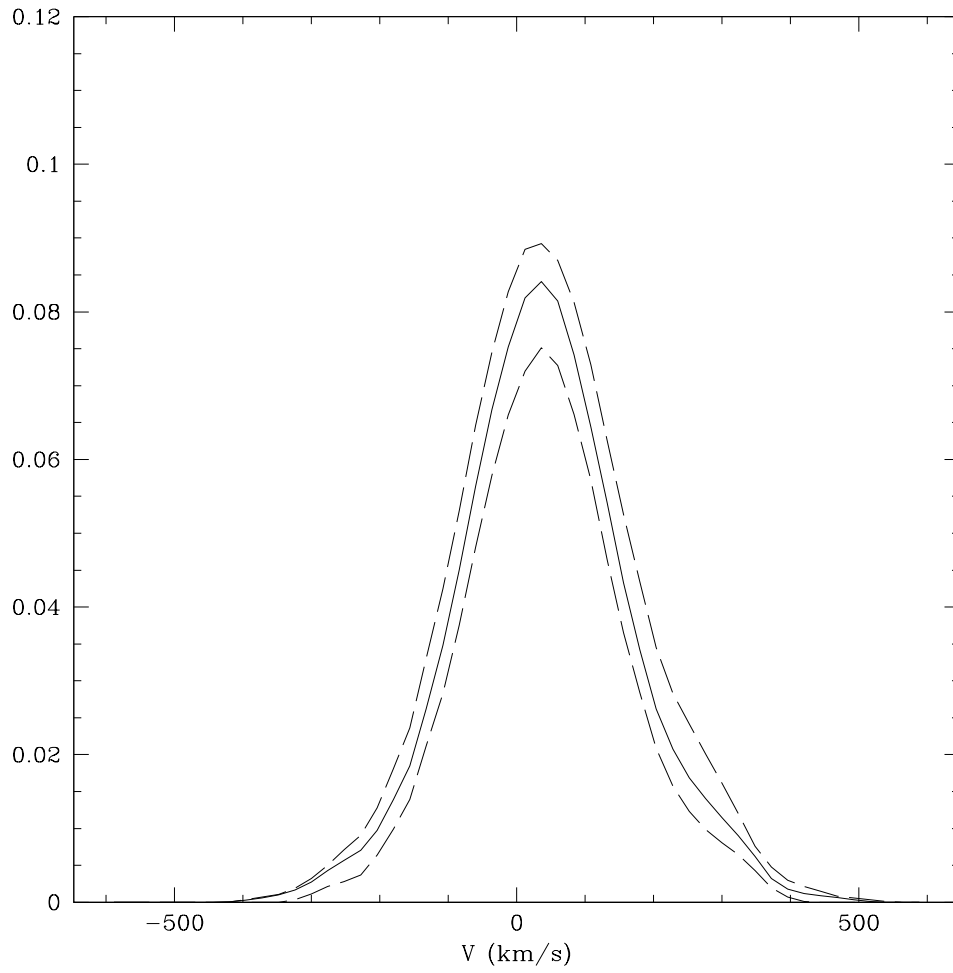


Figure 4.3: Line-of-sight velocity distribution (solid lines) with errors (dashed lines) for the twentieth bin along the major axis, from a radius of $213''$ to $333''$.

Although the full LOSVDs are used in the models, Figure 4.4 shows the Gauss-Hermite moments and the second moment as measured by $\sqrt{V^2 + \sigma^2}$ for our PN binning and the stellar data.

4.2.3 Light Profile

We use a light profile based on stellar light, though we will be modeling the kinematics of planetary nebulae. Thus we assume that the planetary nebulae are distributed in the same way as stars. In the center we use the light profile from Pinkney et al. (2003), which for NGC 4697 uses pre-COSTAR WFPC1 data in F555W (V). At larger radii we use new data from D. Fisher that is a composite profile of ACS F850LP (SDSS z band), and 2MASS J band data. The light profile is deconvolved using a non-parametric technique as described in Gebhardt et al. (1996). The light profile is shown in Figure 4.5.

4.3 Dynamical Models

We use axisymmetric orbit superposition models based on the method of Schwarzschild (1979) as described in §3.4. We again assume an edge-on inclination for this analysis, which is reasonable given NGC 4697's axis ratio of 0.63 (2MASS, Jarrett et al., 2003). We also include a central black hole which is varied in mass to best fit the data.

The orbital characteristics are computed in 20 angular bins and 92 radial bins from $0.005''$ to $1200''$, and are compared to the data in 5 angular

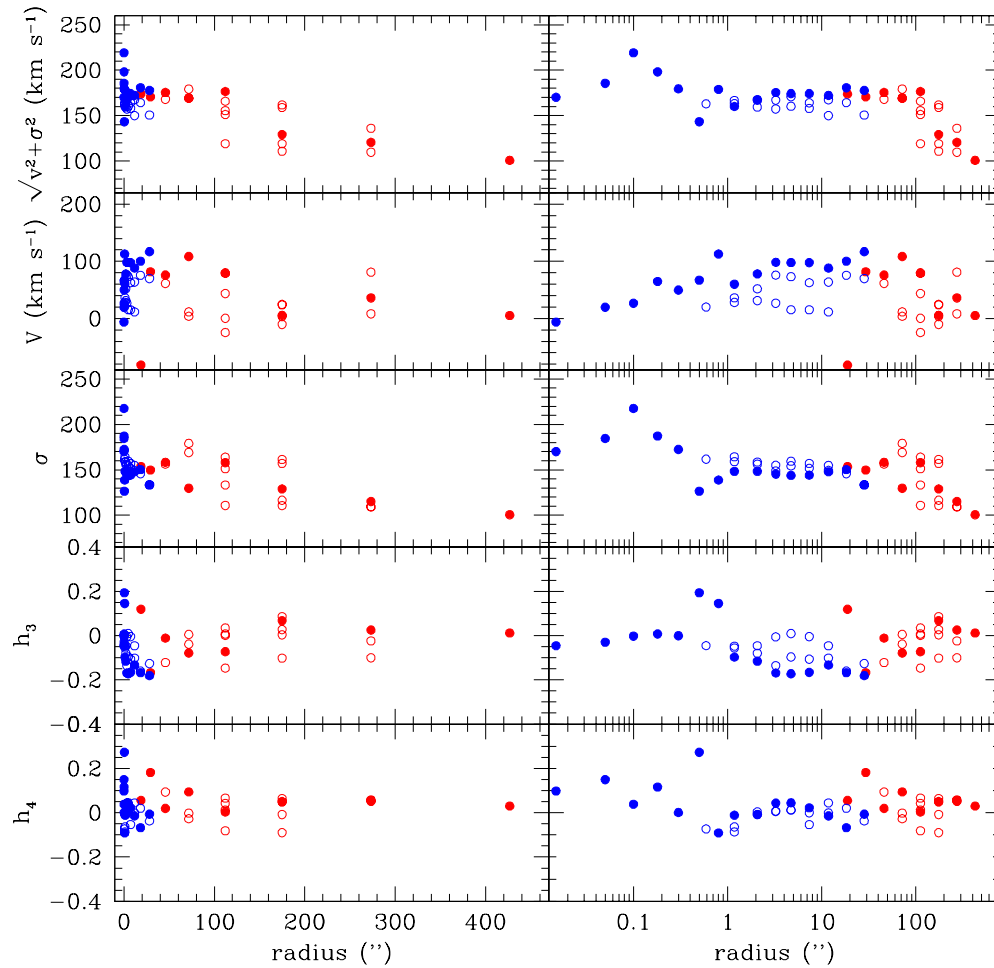


Figure 4.4: The second moment as measured by $\sqrt{V^2 + \sigma^2}$ and the Gauss-Hermite moments v , σ , h_3 and h_4 of the LOSVD as a function of distance from the center of the galaxy. The blue points show stellar data from Pinkney et al. (2003) and the red points show our planetary nebulae measurements. Solid points are along the major axis, open circles are at other angular bins. The plot is given in both linear scale (left) to show the large radii data and logarithmic scale (right) to show the central data.

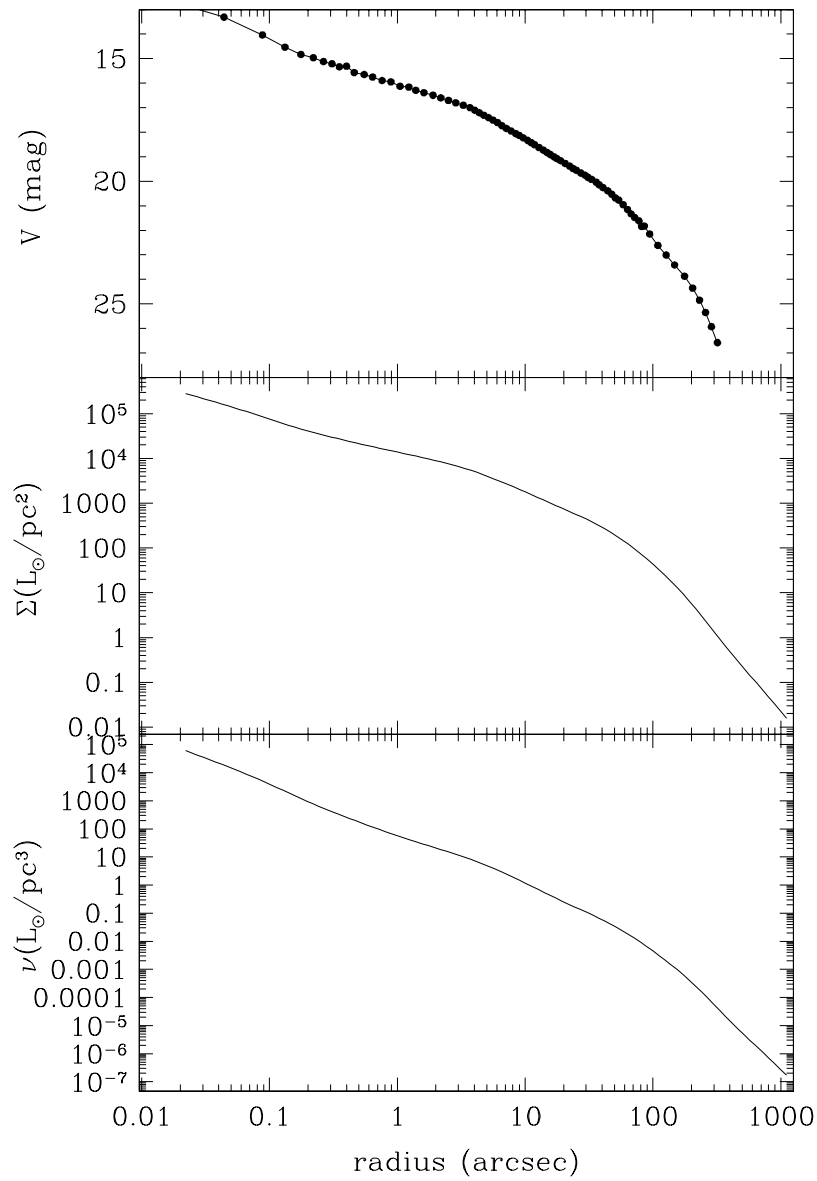


Figure 4.5: Surface brightness, luminosity density, and deprojected surface brightness profiles as a function of radius.

bins and 23 radial bins. The central bins are approximately the same as the bins used by Gebhardt et al. (2003) to model this galaxy so that the same kinematic data can be used. As described in §4.2.2 above, the bins at large radii are used to bin the planetary nebulae data for use in the models. The model and data LOSVDs are compared in 19 velocity bins. Our libraries have a range of approximately 20,000 to 30,000 total orbits.

We primarily use the Logarithmic Potential dark matter halo, given by

$$\rho(r) = \frac{v_c^2}{4\pi G} \frac{3r_c^2 + r^2}{(r_c^2 + r^2)^2} \quad (4.1)$$

where v_c is the circular velocity and r_c is the characteristic radius.

We also test the Navarro, Frenk and White (NFW) (Navarro et al., 1996b) dark halo profile, given as

$$\rho(r) = \frac{\rho_{crit} \delta_c}{(r/r_s)(1 + r/r_s)^2} \quad (4.2)$$

where r_s is the scale radius of the halo and $\rho_{crit} = 3H^2/8\pi G$ is the critical density.

4.4 Results

As described in previous chapters, the best-fitted model is determined by comparing the χ^2 between the model and data LOSVDs, such that a change in χ^2 of 1 corresponds to the 68% confidence band. Example LOSVD fits are shown in Figure 4.6.

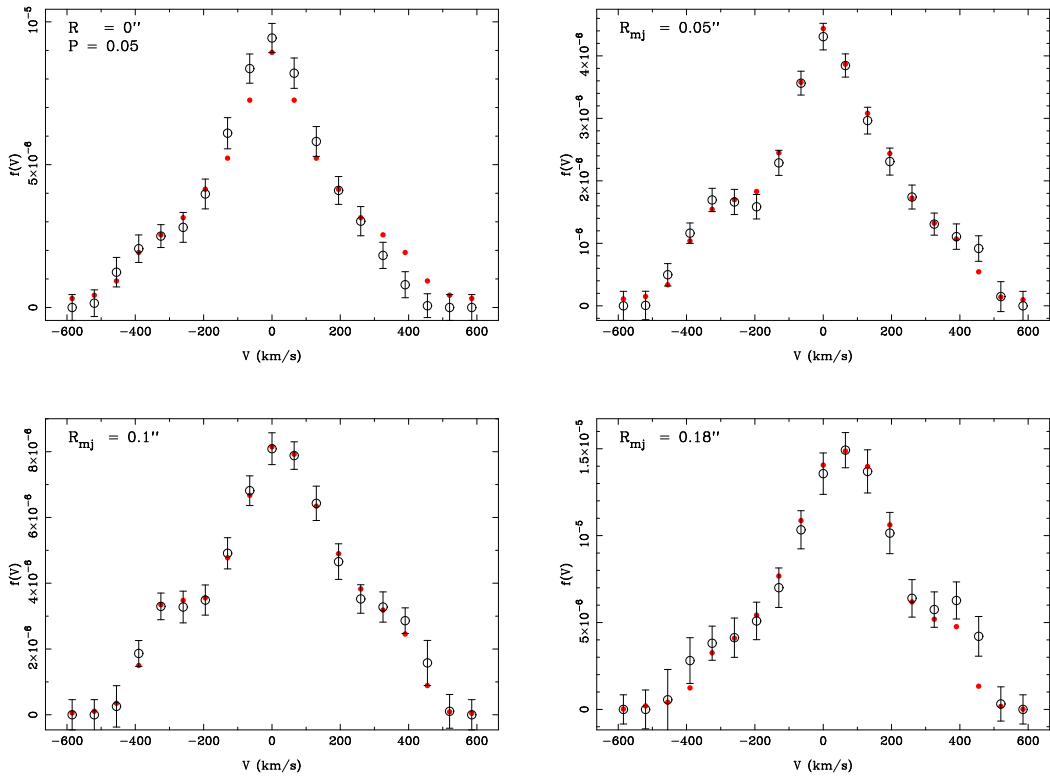


Figure 4.6: Match of data and no dark halo model LOSVDs for the central four stellar bins along the major axis. The open circles are the data values with error bars and the closed red circles are the model values. The area is normalized to the total light in that bin.

4.4.1 Stellar data with no dark halo

We first reproduced the results of Gebhardt et al. (2003) by running models with no dark halo using just the stellar data. The only difference between this analysis and those of Gebhardt et al. (2003) is the improved light profile and slight modifications to the modeling code, such as the improved orbit library sampling of Thomas et al. (2005). The resulting χ^2 grid is shown in Figure 4.7. Our best-fitted M/L of 5.1 is slightly higher than theirs, but overall our results are consistent with their values of M_{BH} from 1.6 to $1.9 \times 10^8 M_\odot$ and M/L_V from 4.7 to 4.9.

4.4.2 All data with no dark halo

Next we include the large-radii planetary nebula data but again do not include a dark halo in the models. The resulting χ^2 grid is shown in Figure 4.8. The addition of kinematic data at large radii increases the mass-to-light ratio significantly, up to 7.4. Since the mass-to-light ratio is constant over all parts of the galaxy, more of the central matter is now attributed to stars and the black hole mass decreases accordingly to $8.75 \times 10^7 M_\odot$. This clearly demonstrates the need to understand the large-radii properties of the galaxy while measuring the central black hole.

4.4.3 All data with logarithmic potential dark halo

Lastly, we model both the black hole and a logarithmic potential dark halo using both the central stellar data and the large radii planetary nebula

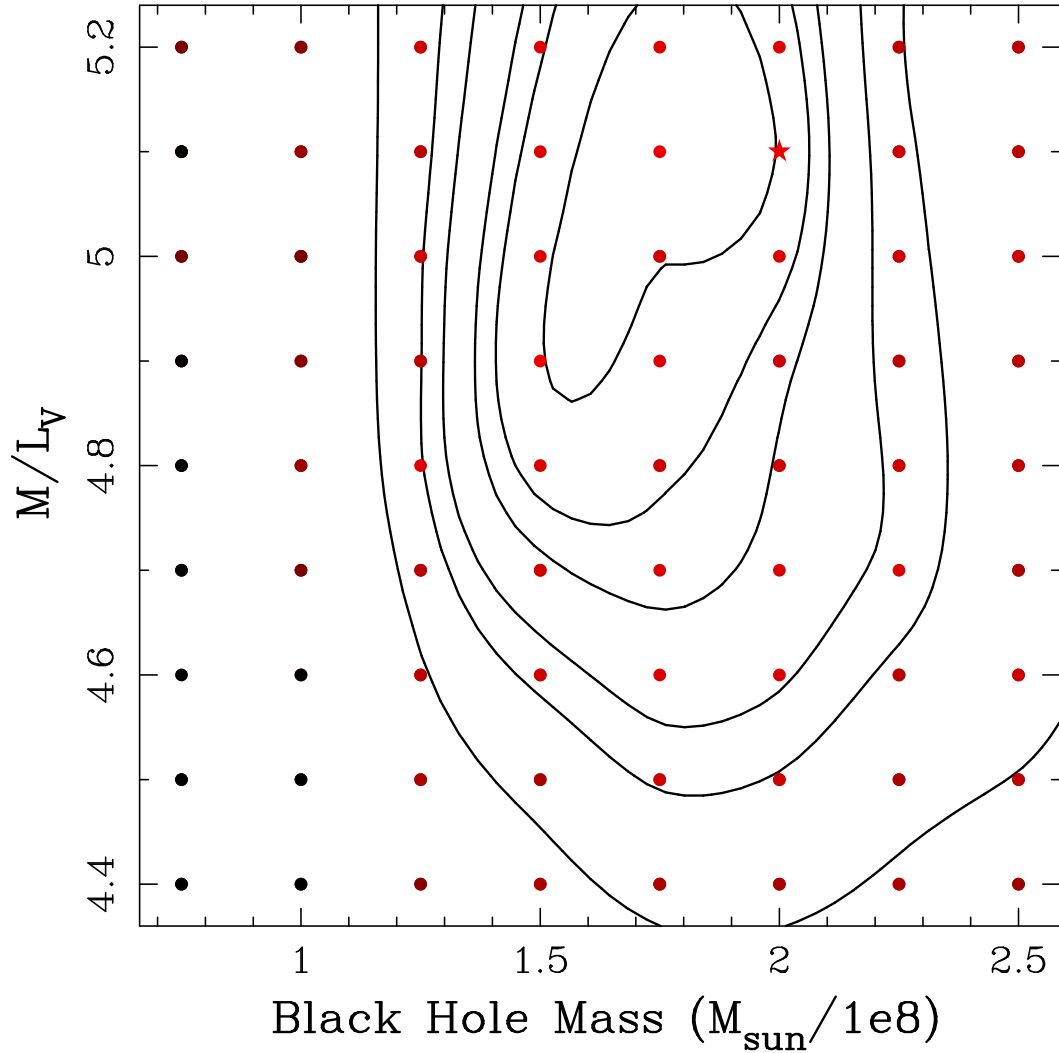


Figure 4.7: χ^2 grid in M/L_V and black hole mass for the models with no dark halo and stellar data only (no planetary nebulae data). Each point represents a model and the redder points have a lower χ^2 . Contours show 68.3%, 90%, 95.4%, 99%, 99.73%, and 99.99% confidence levels. The star is the model with the minimum χ^2 .

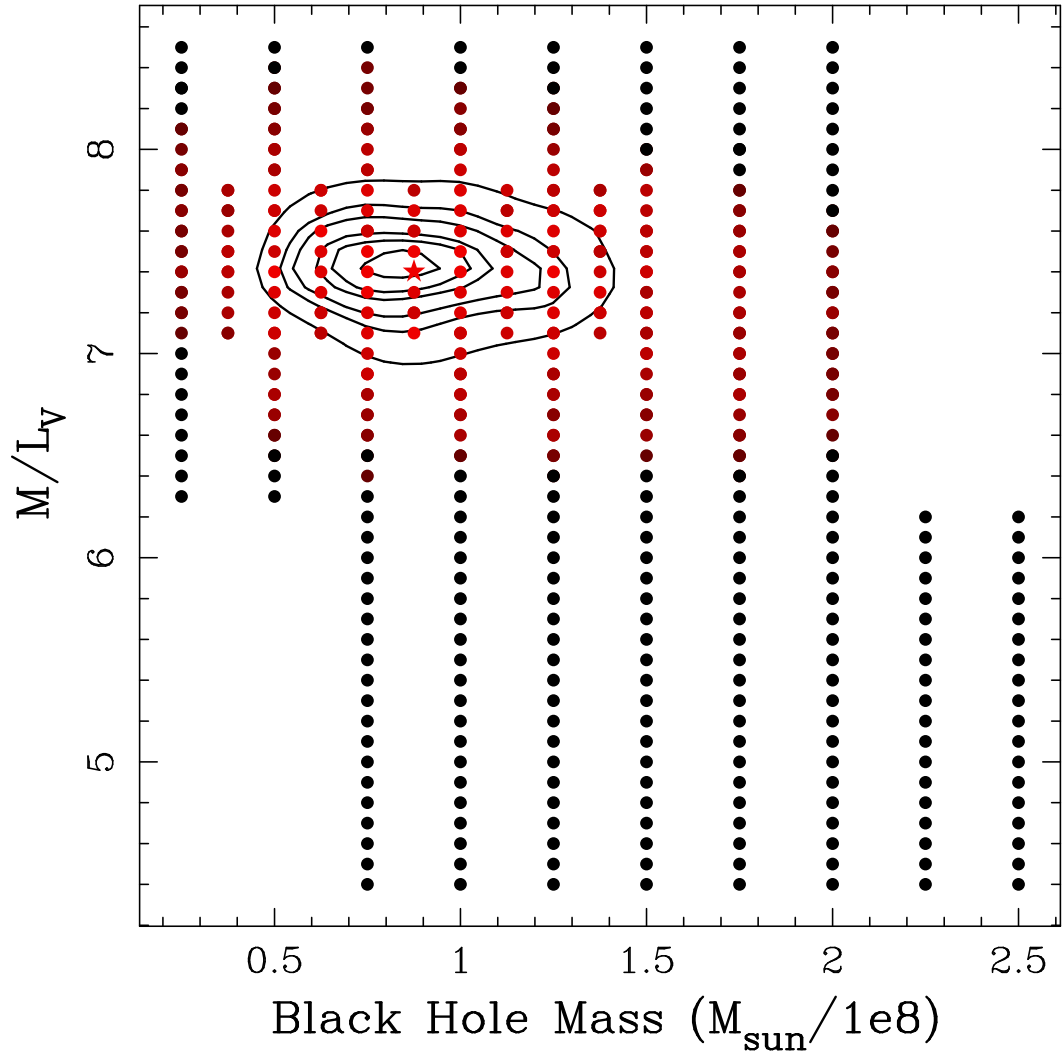


Figure 4.8: χ^2 grid in M/L_V and black hole mass for the models with no dark halo. Each point represents a halo modeled and the redder points have a lower χ^2 . Contours show 68.3%, 90%, 95.4%, 99%, 99.73%, and 99.99% confidence levels. The star is the model with the minimum χ^2 .

data. With four parameters we run over 25,000 models to fully explore the parameter space. The resulting χ^2 grids are shown in Figure 4.9. We have 51 LOSVDs (30 from stars and 21 from planetary nebulae) which given the smoothing bins of the LOSVDs provides about 340 degrees of freedom. Thus our best-fitted models have a reduced χ^2 of roughly 1.6.

The best-fitted model has an M/L of 4.35 (4.25, 4.55), M_{BH} of 2.1 (1.7, 2.4) $\times 10^8 M_\odot$, V_c of 387.5 (310, 395) km/s and R_c of 9.0 (7.0, 10.5) kpc . The (*low, high*) values are obtained from the $\Delta\chi^2 = 1$ envelopes of each parameter, as shown along the bottom of Figure 4.9. A summary of all of the best-fitted model parameters is given in Table 4.1. The best-fitted halo density profile and circular velocity curve are shown in Figure 4.10. The no halo model is ruled out with a change in χ^2 of 1050 from the best-fitted logarithmic potential halo. This preferred fit is not dominated by any one region of the galaxy; the halo model provides a better LOSVD fit in nearly all of the 51 data bins. This is illustrated in Figure 4.11.

Figures 4.12 and 4.13 show the internal moments σ_r , σ_θ , and σ_ϕ and ratio of radial to tangential dispersion along the major and minor axes for the model with no dark halo and the best-fitted halo model. The model without a dark halo shows slightly tangential anisotropy at intermediate to large radii. This could be an indication of the need for a dark halo, as discussed in §2.5.1. The best-fitted halo model shows isotropy at intermediate radii and extremely radial anisotropy at large radii. This is interesting given our previous results from NGC 821 which similarly show that planetary nebulae data would have

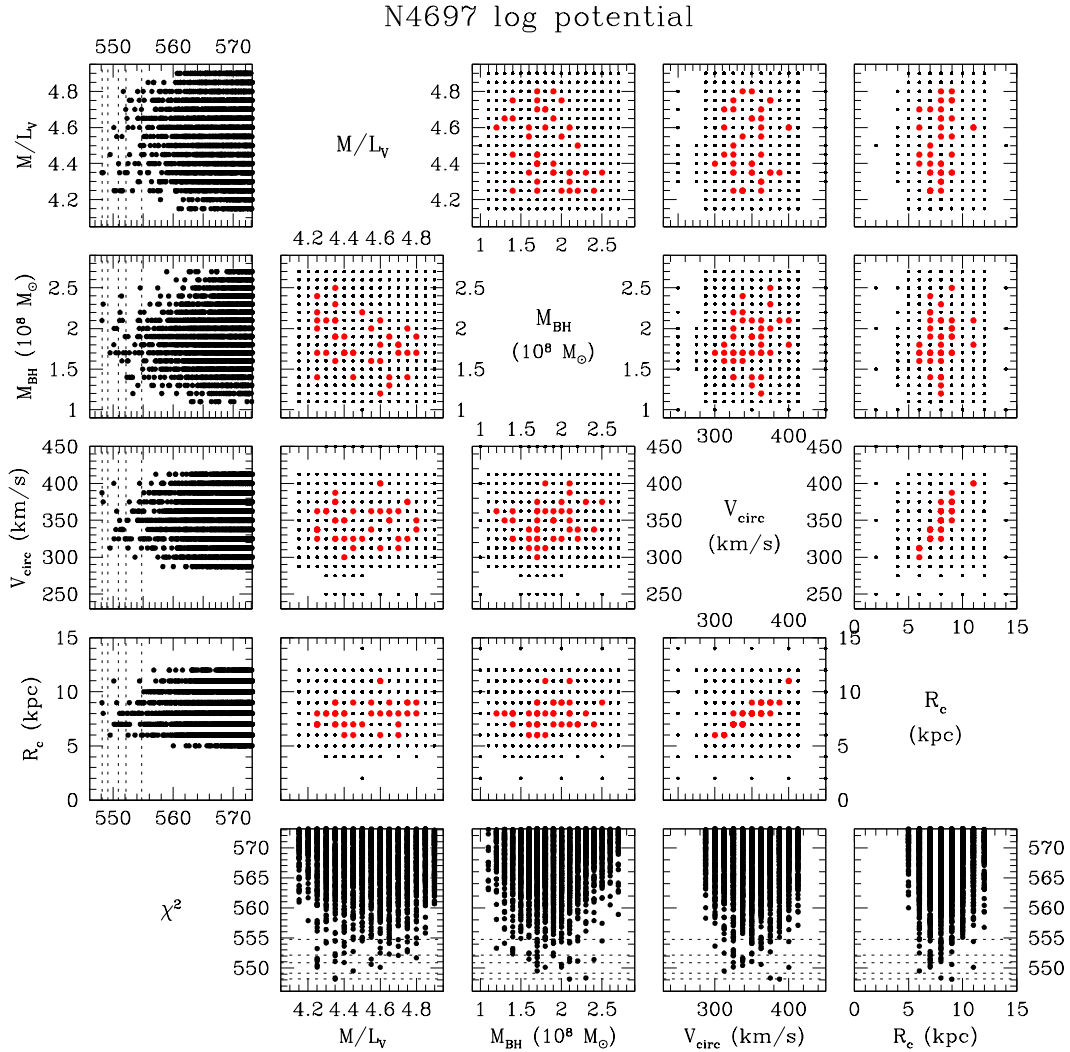


Figure 4.9: χ^2 grids in M/L_V , black hole mass, circular velocity, and characteristic radius for each of the logarithmic potential halo models. Black points show each halo modeled. Red points show models within 4σ of the minimum value. The plots along the left and bottom show each parameter as a function of χ^2 for all models. The plotting ranges are selected to highlight the best fit for each parameter; there are many models beyond the plotting range that have significantly worse fits.

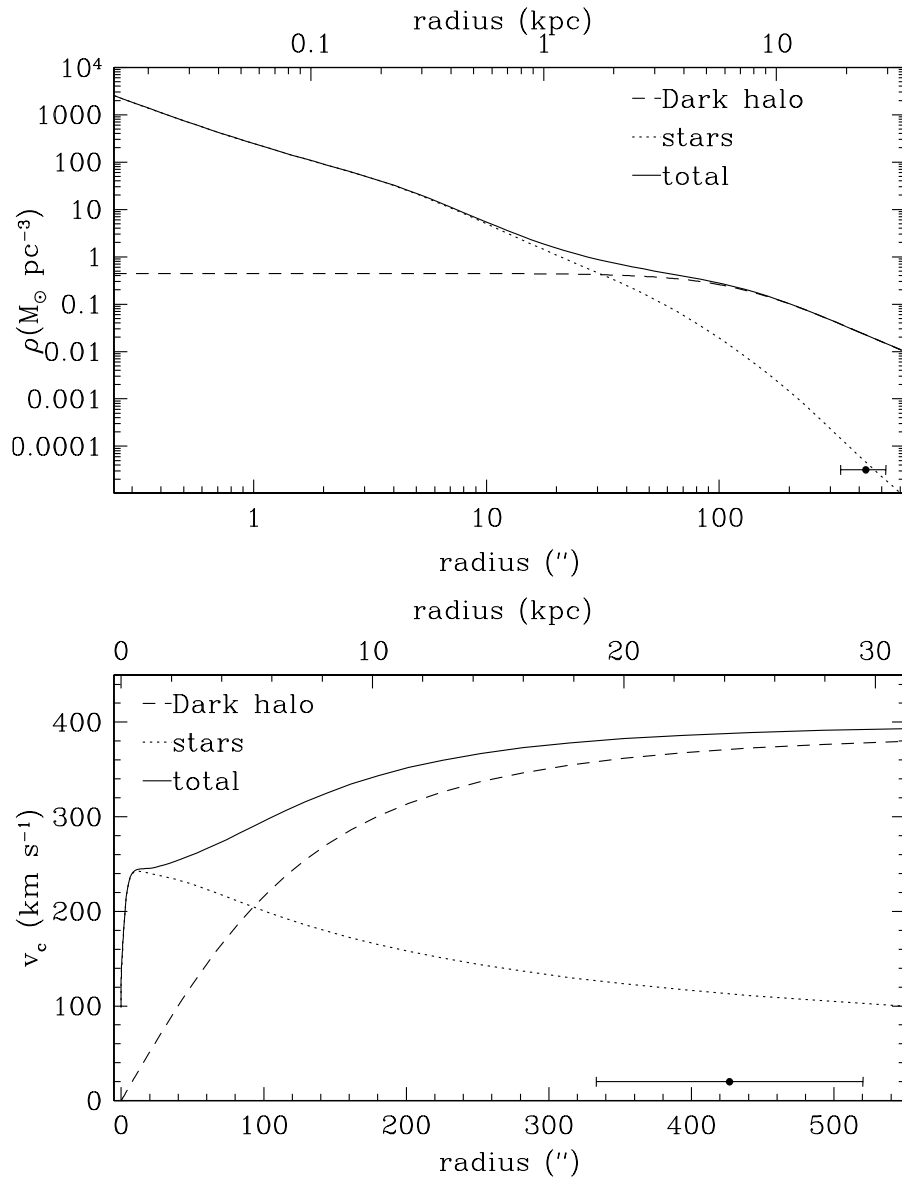


Figure 4.10: Density (top) and circular velocity (bottom) as a function of radius for the best-fitted dark halo profile. The dotted lines are stars only, dashed lines are halo only, and solid lines are halo plus stars. The data point shows the radial extent of our data.

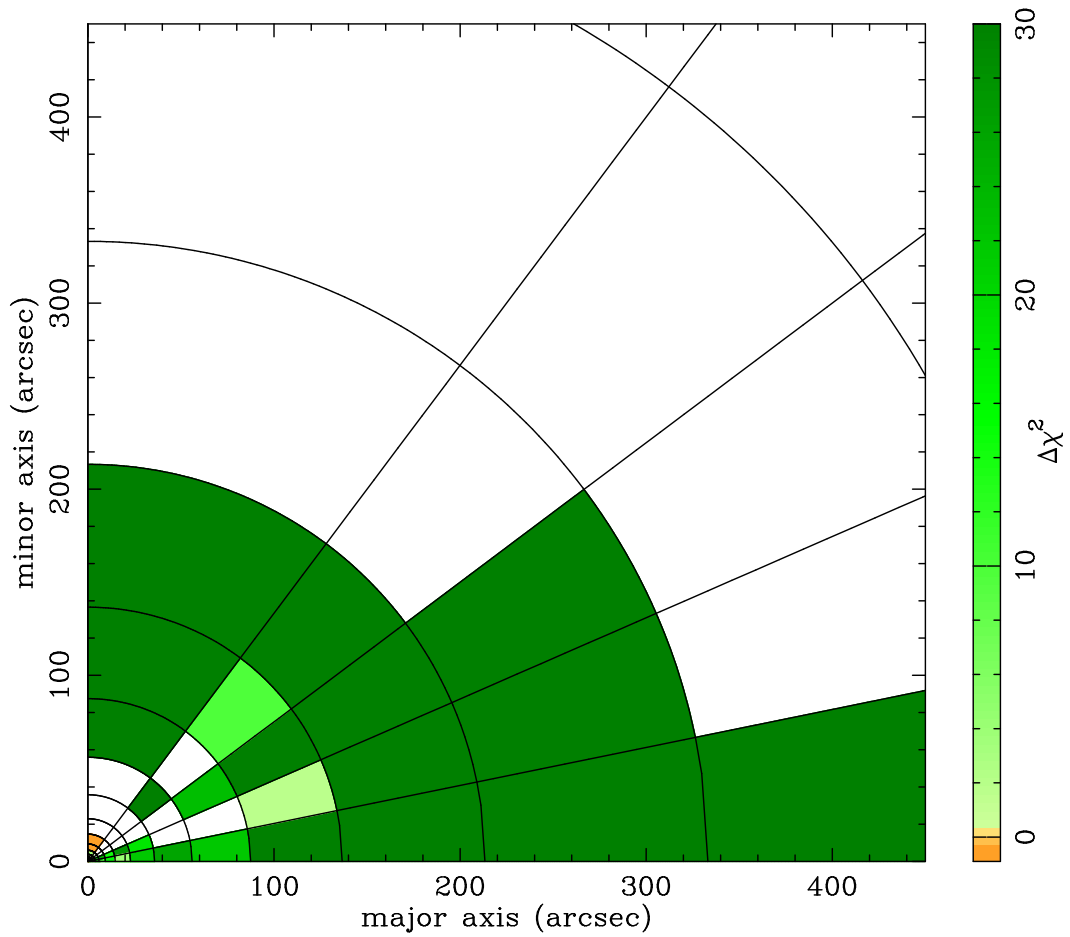


Figure 4.11: Difference in χ^2 between the LOSVDs of the model with no dark halo and the best-fitted logarithmic potential halo model averaged in each spatial bin. Green indicates that the no-halo model has a larger χ^2 than the halo model and therefore the halo is a better fit, while orange indicates that the halo model has a larger χ^2 than the no-halo model and therefore the no-halo model is a better fit.

very radial orbits in the assumed stellar potential (see §2.5.6).

4.4.4 NFW Halo

We also ran about 9800 models to test the NFW dark halo profile. The resulting χ^2 grids are shown in Figure 4.14. We find that the logarithmic potential halo is a better fit than the NFW halo with a $\Delta\chi^2$ of 27. Additionally, the NFW halo parameters (concentration and core radius) are not well constrained, indicating that the NFW shape does not provide an ideal fit. We do find that the mass-to-light ratio of 4.4 (4.0, 4.6) and black hole mass of 1.7 (1.4, 2.1) $\times 10^8 M_\odot$ are well constrained and agree with the logarithmic potential results. We continue our discussion using only the logarithmic potential halo models because of their better fit, well-determined halo parameters, and more thorough exploration of parameter space.

4.4.5 Mass-to-light ratio

One assumption of this analysis is that the mass-to-light ratio of the stellar component is constant over the entire galaxy. While our models are really measuring the total mass of the galaxy, it may be interesting to see how that total mass is separated into stars and halo given a varying M/L . We examine this by estimating the mass-to-light ratio using color measurements. A $B - R$ color profile was provided by D. Fisher based on Jacobus Kapteyn Telescope archival data. We then used Bell & de Jong (2001) to convert this color to M/L_V . This conversion is dependent on several assumptions

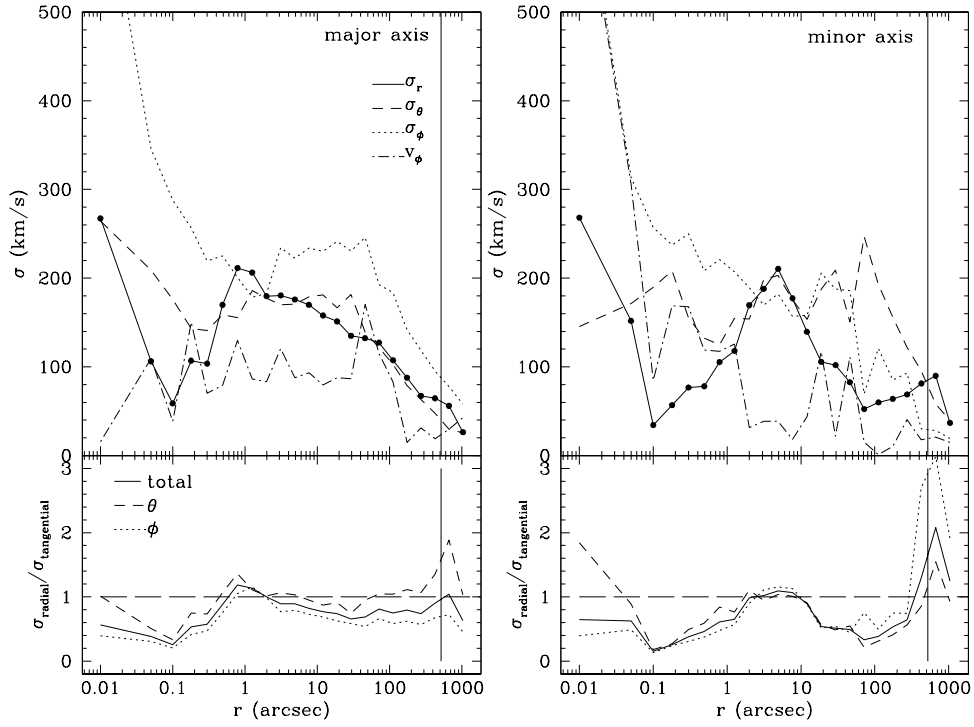


Figure 4.12: Internal moments σ_r , σ_θ , and σ_ϕ (top) and the ratio of radial to tangential dispersion (bottom) along the major axis (left) and minor axis (right) for the model with no dark halo. Note that our major and minor axes results are for the full angular bins around the axes. σ_ϕ includes both random and ordered motions, which are shown (dot-dashed line). The vertical line shows the limit of our kinematic data; results beyond this radius are not reliable.

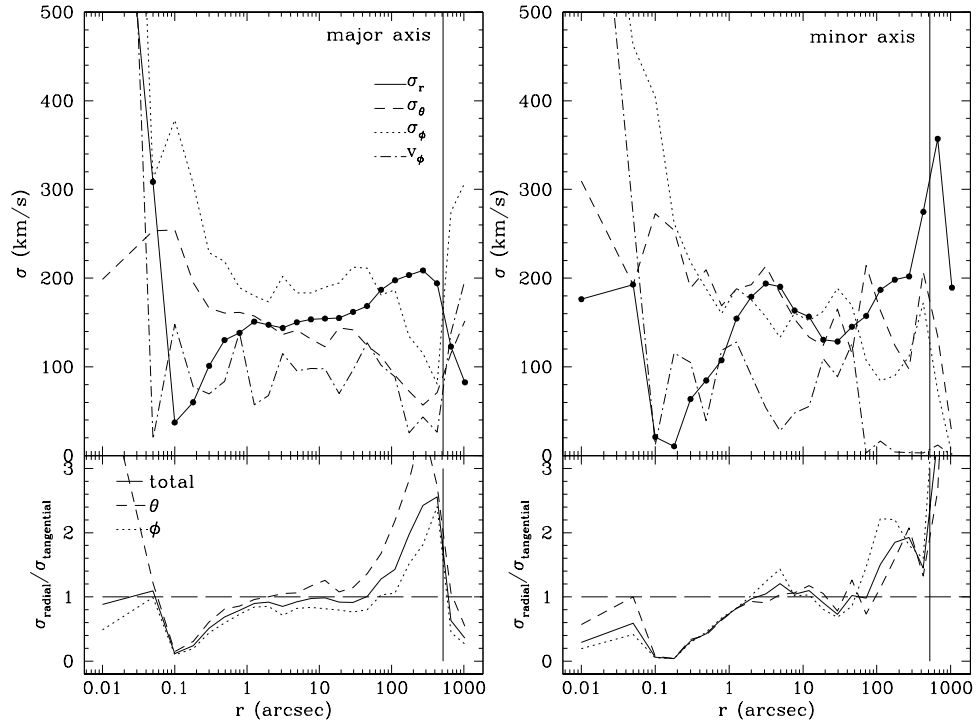


Figure 4.13: Internal moments σ_r , σ_θ , and σ_ϕ (top) and the ratio of radial to tangential dispersion (bottom) along the major axis (left) and minor axis (right) for the model with the best-fitted halo. Note that our major and minor axes results are for the full angular bins around the axes. σ_ϕ includes both random and ordered motions, which are shown (dot-dashed line). The vertical line shows the limit of our kinematic data; results beyond this radius are not reliable.

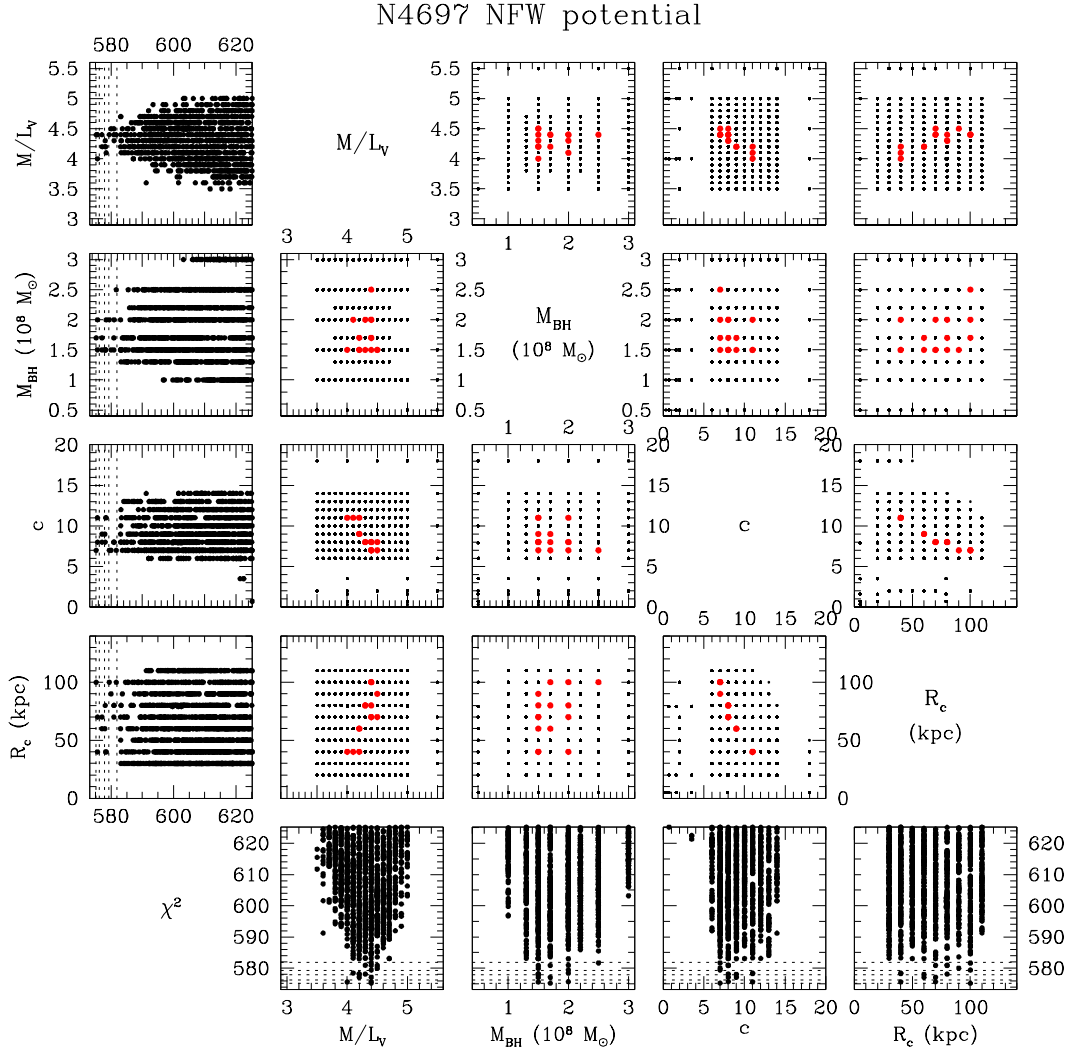


Figure 4.14: χ^2 grids in M/L_V , black hole mass, concentration, and core radius for each of the NFW halo models. Black points show each halo modeled. Red points show models within 4σ of the minimum value. The plots along the left and bottom show each parameter as a function of χ^2 for all models. The plotting ranges are selected to highlight the best fit for each parameter; there are many models beyond the plotting range that have significantly worse fits.

(IMF, lower-mass cut-off, AGB stars), but is nonetheless a useful exercise. The color and mass-to-light ratio profiles are shown in Figure 4.15. Correcting our dynamical M/L_V of 4.35 for galactic extinction using $A_V = 0.101\text{mag}$ (Schlegel et al., 1998, NED extragalactic database) we find an M/L_V of 3.97. This is in agreement with the M/L calculated above, which ranges from 2.7 to 4.9 over the galaxy.

We used the derived mass-to-light ratio to calculate a new stellar density profile. The radial range of our color data is smaller than our models so we assumed that the M/L remained constant beyond the last data point. While this is likely not correct, the sharp decline in color at about $80''$ makes it difficult to predict how the color will change at large radii. We then subtracted the new stellar density profile from our best-fitted total mass profile to get the implied dark halo profile. The derived stellar and halo density profiles are shown in Figure 4.16. It is clear that the need for a dark halo is a robust result regardless of mass-to-light ratio variations. The overall shape of a logarithmic potential halo seems to still be a good fit, although it is likely that a halo with a larger circular velocity and smaller core radius would be a better fit using the new stellar profile.

4.4.6 Mass results

Regardless of the exact halo shape, our models robustly measure the total mass of the galaxy. Figures 4.17 and 4.18 show the mass enclosed within $1 R_e$ and within the last bin of kinematic data as a function of χ^2 for the loga-

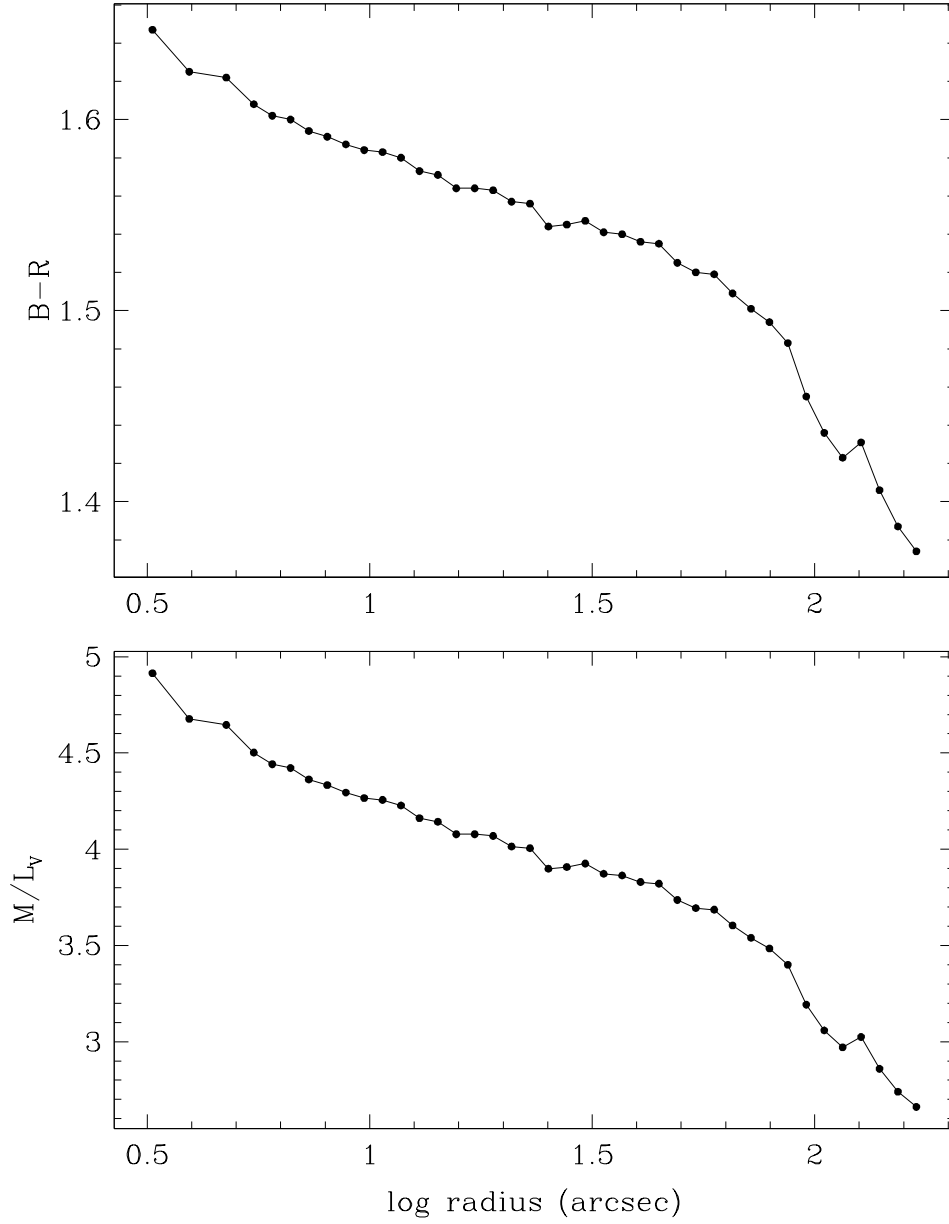


Figure 4.15: $B - R$ color and derived V band mass-to-light ratio as a function of radius.

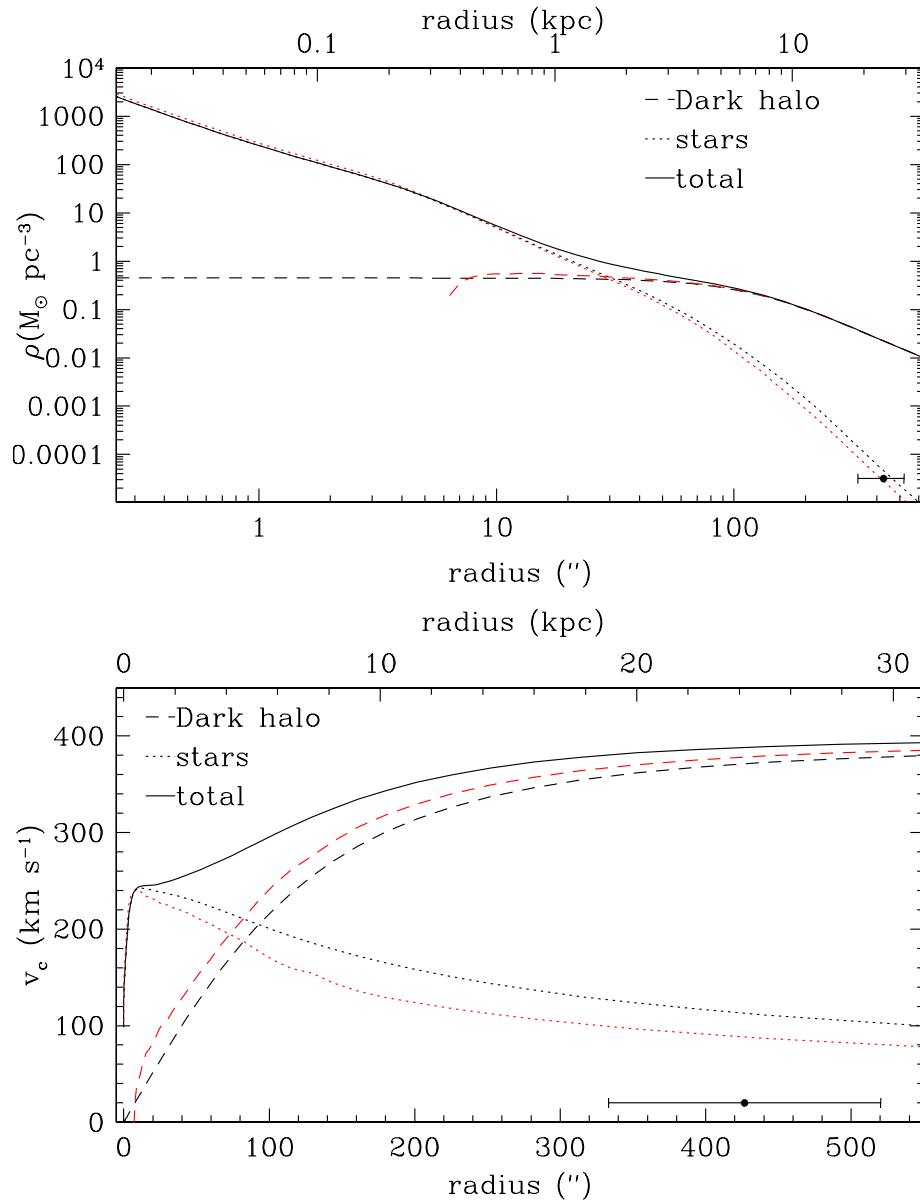


Figure 4.16: As in Figure 4.10. The red lines show the stellar contribution using the mass-to-light ratio derived from data (dotted) and the implied halo given the new stellar contribution (dashed).

rithmic potential halos within 4σ of the best-fitted model. The corresponding mass measurements are given in Tables 4.2 and 4.3. We use 4σ confidence levels because of the scarcity of models within 1σ of the best-fitted halo. Figures 4.18 and 4.17 show that the range of masses appears to be similar at 1σ and 4σ , so these errors are sensible. We find that the total mass of the galaxy at $1R_e$ is $5.63 \times 10^{10} M_\odot$ and at the last data bin (about $8R_e$) is $1.02 \times 10^{12} M_\odot$. Without including a halo we underestimate the total mass within our data range by nearly an order of magnitude.

Figure 4.19 shows the enclosed mass, total mass to light ratio, and halo mass fraction as a function of radius for all halo models within 4σ of the best-fitted model. At $1R_e$ the dark matter fraction is .30 and at our last data bin the galaxy is 93% dark matter. The ratio at $1R_e$ agrees with previous studies (e.g. Saglia et al., 2000; Gerhard et al., 2001; Mamon & Łokas, 2005) as well as our own previous results.

4.5 Conclusions

We perform axisymmetric orbit superposition dynamical models on NGC 4697 using both stellar and planetary nebula kinematic data. We fit the models for stellar mass-to-light ratio, central black hole mass, and dark halo parameters (circular velocity and characteristic radius).

We first reproduce the black hole mass and mass-to-light ratio results of Gebhardt et al. (2003) using only stellar data and no dark halo. We then include the planetary nebula data (but still no halo) and find that stellar

Table 4.1: NGC 4697 Best-Fitted Parameters

Halo	M_{bh} (low,high) $10^8 M_{\odot}$	M/L_V
Gebhardt et al. (2003)	1.7 (1.6, 1.9)	4.7
No halo, no PN data	2.0 (1.6, 2.1)	5.1 (4.9, 5.3)
No halo	.875 (.75, .95)	7.4 (7.35, 7.5)
Log halo	2.1 (1.7, 2.4)	4.35 (4.25, 4.55)
NFW halo	1.7 (1.4, 2.1)	4.4 (4.0,4.6)

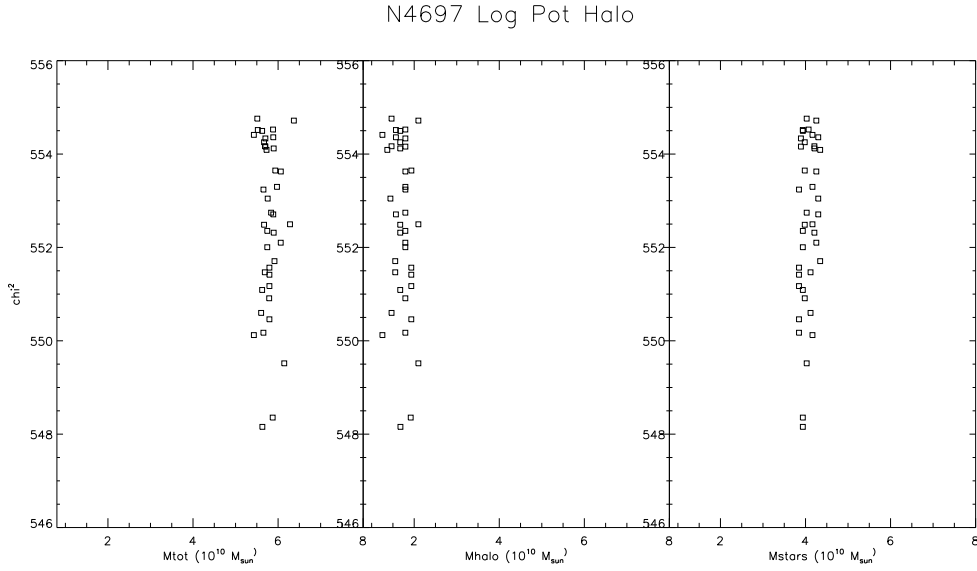


Figure 4.17: Total mass, mass in halo and mass in stars all within $1R_e$ ($60''$) for all of the models within 4σ of the minimum value.

N4697 Log Pot Halo

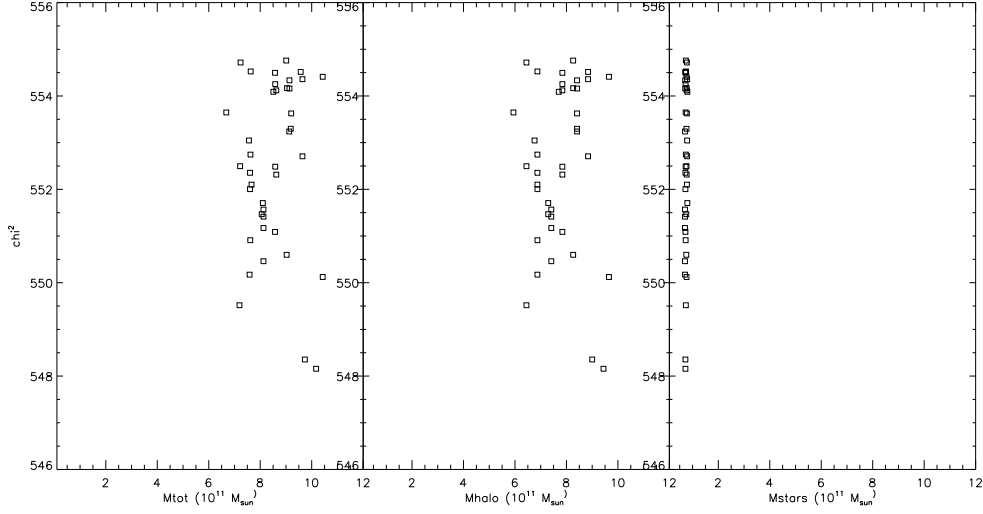


Figure 4.18: Total mass, mass in halo and mass in stars all within our kinematic data range for all of the models within 4σ of the minimum value.

Table 4.2: NGC 4697 Best-Fitted Halo Model Mass Results at $1R_e$ ($60''$)

Halo	M_{tot} (low,high) $10^{10}M_{\odot}$	M_{stars} (low,high) $10^{10}M_{\odot}$	M_{halo} (low,high) $10^{10}M_{\odot}$
No halo	6.65 (6.56,6.83)	6.65 (6.56,6.83)	0.00
Log halo	5.63 (5.43,6.37)	3.94 (3.85,4.34)	1.68 (1.25,2.10)

Note. — Low and high values are given for the 4 sigma confidence levels.

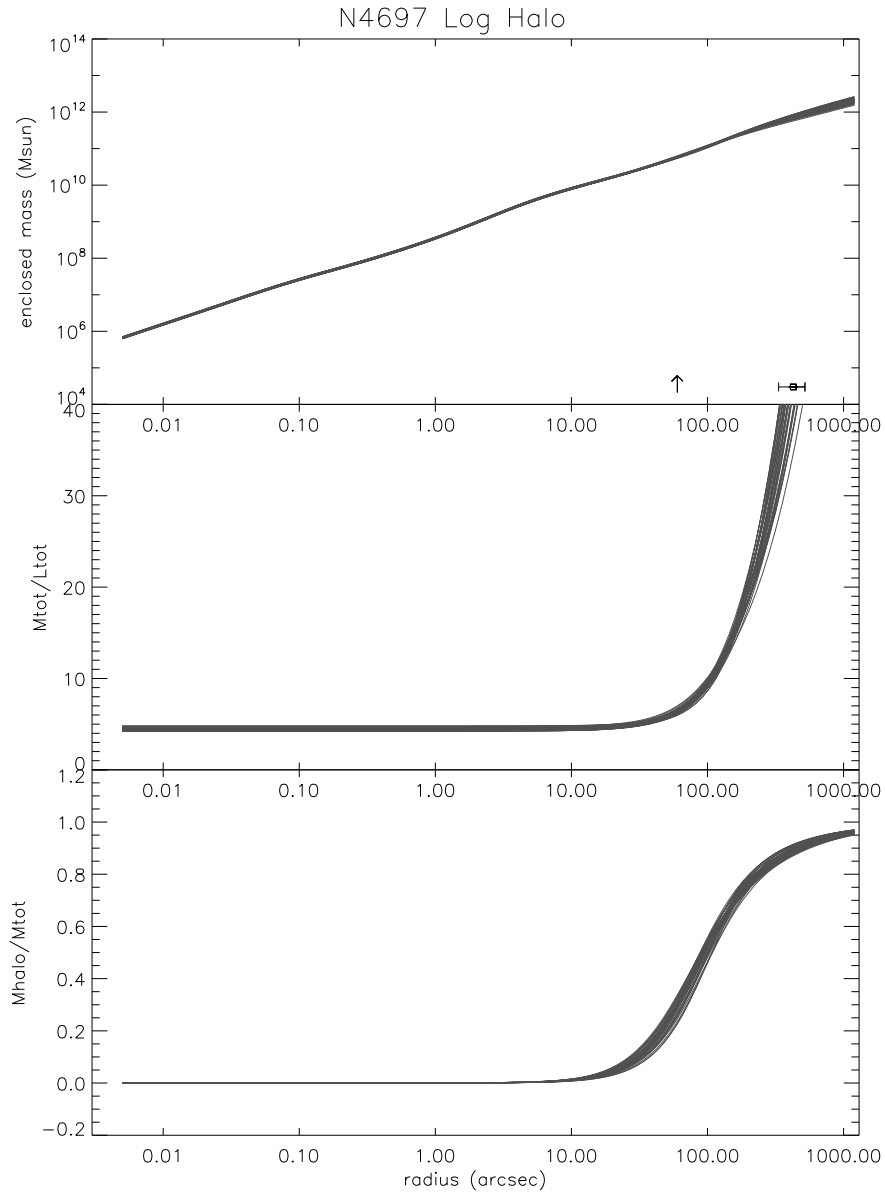


Figure 4.19: Enclosed mass, total mass to light ratio, and halo mass fraction as a function of radius for all halo models within 4σ of the best-fitted halo model. The data point shows the radial extent of our kinematic data and the arrow indicates $1R_e$

mass-to-light ratio significantly increases, from 5.1 to 7.4. The black hole mass decreases accordingly, from $2.0 \times 10^8 M_\odot$ to $.875 \times 10^8 M_\odot$. This result is to be expected with the inclusion of extended data because in order to explain the large velocities at large radii a bigger stellar mass-to-light ratio is needed to compensate for the lack of a dark halo in the models.

We include a logarithmic potential dark halo and find that the fit is significantly better than without a dark halo. The best-fitted model has an M/L of 4.35, M_{BH} of $2.1 \times 10^8 M_\odot$, V_c of $387.5 km/s$ and R_c of $9 kpc$. This halo is consistent with the results of de Lorenzi et al. (2008), who do not do a detailed analysis of the shape but find that the best fits to the data include a logarithmic potential halo with $V_c \geq 250 km/s$. This mass-to-light ratio and black hole mass are once again consistent with the results of Gebhardt et al. (2003). Gebhardt & Thomas (2009) recently showed that the black hole mass of M87 did change with the inclusion of globular cluster data at large radii. NGC 4697 is different because the previous analysis used data that did not extend to where dark matter is a significant fraction of the total mass. Also NGC 4697 had the most significant black hole detection of Gebhardt et al. (2003), with a very well-constrained mass.

The model without a dark halo shows slightly tangential anisotropy at intermediate to large radii, which is indicative of the need for a dark halo. The best-fitted halo model shows isotropy at intermediate radii and radial anisotropy at large radii. This is interesting given our previous results from NGC 821 which similarly show that planetary nebulae data would have radial

orbits in the assumed stellar potential. This could indicate that there is something something inherent to the PNe that put them on radial orbits, a bias of the PNe detections at large radii, or simply that the galaxy as a whole has radial motions at large radii.

We tested the NFW halo profile and found that the halo parameters were not well constrained and overall it was a worse fit than the logarithmic potential halo. The mass-to-light ratio and black hole mass found using the NFW halo agreed with the result using a logarithmic potential halo, as expected.

We use the stellar population method of Bell & de Jong (2001) to convert stellar color to mass-to-light ratio as a function of radius. The stellar population M/L_V ranges from 2.7 to 4.9 and is in agreement with our dynamical M/L_V corrected for extinction to 3.97. We compare the stellar mass and density using a constant M/L and the derived varying M/L and find that the need for a halo is still robust and the shape of the implied dark halo still resembles a logarithmic potential halo.

We find that the total mass of the galaxy at $1R_e$ is $5.63 \times 10^{10} M_\odot$ and at the last data bin (about $8R_e$) is $1.02 \times 10^{12} M_\odot$. At $1R_e$ the dark matter fraction is .30 and at our last data bin the galaxy is 93% dark matter.

Table 4.3: NGC 4697 Best-Fitted Halo Model Mass Results Within The Kinematic Data

Halo	M_{tot} (low,high) $10^{11}M_{\odot}$	M_{stars} (low,high) $10^{11}M_{\odot}$	M_{halo} (low,high) $10^{11}M_{\odot}$
No halo	1.23 (1.21,1.26)	1.23 (1.21,1.26)	0.00
Log halo	10.17 (6.68,10.42)	0.72 (0.71,0.80)	9.44 (5.94, 9.65)

Note. — Low and high values are given for the 4 sigma confidence levels.

Chapter 5

Galaxy Kinematic Data

This chapter presents the kinematic analysis of the remaining galaxies for which dynamical modeling has not yet been undertaken.

5.1 Observations

The observations were taken using the Hobby-Eberly Telescope's Low-Resolution Spectrograph (Hill et al., 1998). The CCD is a Ford Aerospace 3072x1024 and has a plate scale of 0.235 arcsec/pixel, which we bin 2x2. The gain is $1.832 e^- \text{ ADU}^{-1}$ and readout noise is $5.10 e^-$. The long slit extends across the $4'$ field of view. We use either the g2 or g3 grism, whose specifications are given in Table 5.1. Cadmium and Neon calibration lamp exposures and white light illumination flat fields were taken each night.

The galaxies were observed over several nights in 2002 and 2003 under queue scheduling. Table 5.2 gives information about the observations of each galaxy. Table 5.3 shows basic properties of each galaxy from the NED extragalactic database.

Figures 5.1 through 5.10 give the preparatory images showing the sky

Table 5.1: Grisms

Grism	g2	g3
Description	600 l/mm	holographic
Dispersion	2 Å/pix	1.88 Å/pix
Range	4280 - 7278 Å	6250 - 9100 Å
Filter [†]	GG385	OG515
Main feature	Mg b	Ca II triplet
Resolving Power (1" slit)	1300	1900
Resolving Power (2" slit)	650	950

[†]Schott Glass blocking filters. The number in the name is the approximate half-power point of the transmission cut-on in nm.

before the slit has been inserted for each galaxy set up. The slit runs from top center to bottom center.

Table 5.2. Galaxy Observations

Trimester	Name	Axis	Integration Time (sec)	Time (hr)	N_{exp}	Grism	Slit Size ($''$)
2003-1	NGC 2832	major	9600	2.7	8	g2	2.0
2003-1	NGC 2832	minor	7200	2.0	6	g3	2.0
2004-1	NGC 3379	major	4394	1.2	4	g2	1.0
2003-1	NGC 3842	major	6284	1.7	7	g3	2.0
2003-1	NGC 3842	minor	9600	2.7	8	g3	2.0
2003-1	NGC 4889	major	7200	2.0	8	g2	2.0
2003-1	NGC 4889	minor	7200	2.0	6	g2	2.0
2003-1	NGC 6086	major	9506	2.7	8	g3	2.0
2003-1	NGC 6086	minor	4800	1.3	4	g3	2.0
2002-3	NGC 661	major	25040	7.0	12	g2	1.0
2002-2	NGC 6702	major	24159	6.7	12	g2	1.0
2002-3	NGC 6702	minor	16520	4.6	8	g2	1.0
2003-3	NGC 821	major	19727	5.5	14	g2	1.0
2003-3	NGC 821	minor	8380	2.3	6	g2	1.0

Note. — NGC 6702 and NGC 821 are included here for completeness of the sample, but will not be discussed further in this chapter. See §2 and §3 for their analysis.

Table 5.3. Galaxy Properties

Name	Type	R_e (")	R_e (kpc)	Distance (Mpc)	Environment
NGC 2832	E2, cD	25.5	11.71	94.72	cluster
NGC 3379	E1	35.1	1.80	10.60	group
NGC 3842	E, BCG	37.8	16.05	87.56	cluster
NGC 4889	E4, cD	30	13.73	94.38	cluster
NGC 6086	E, cD	24.3	16.03	136.03	cluster
NGC 661	E	14.1	2.27	33.24	field
NGC 6702	E	24.3	6.10	51.79	field
NGC 821	E6?	48	5.75	24.72	field

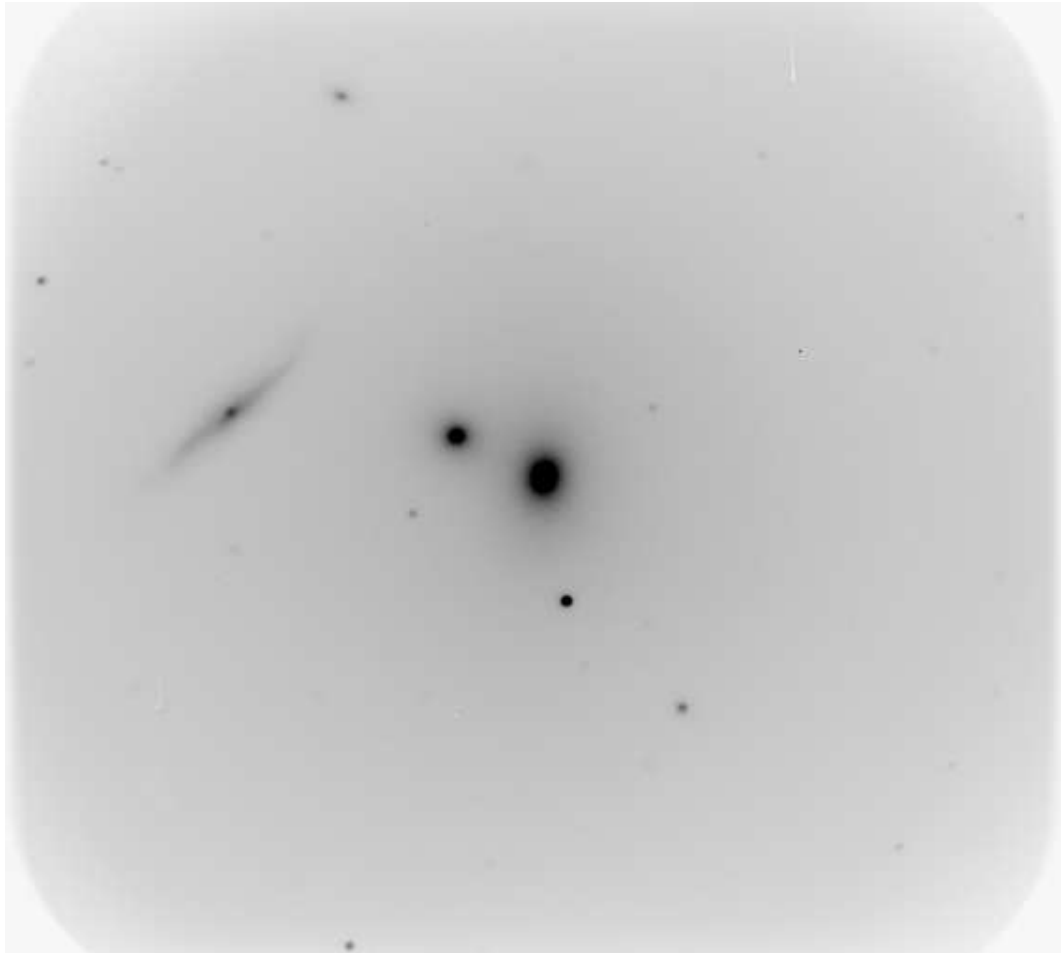


Figure 5.1: NGC 2832 major axis preparatory image.

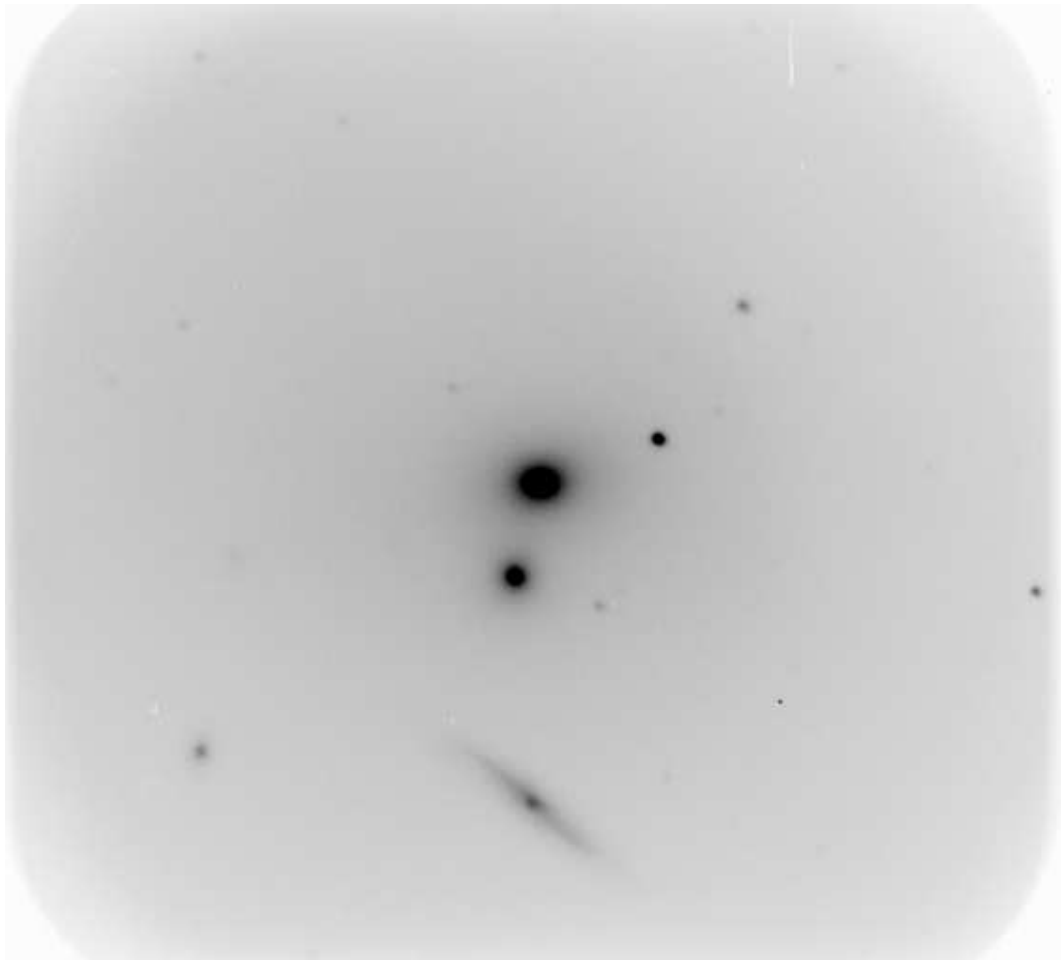


Figure 5.2: NGC 2832 minor axis preparatory image.

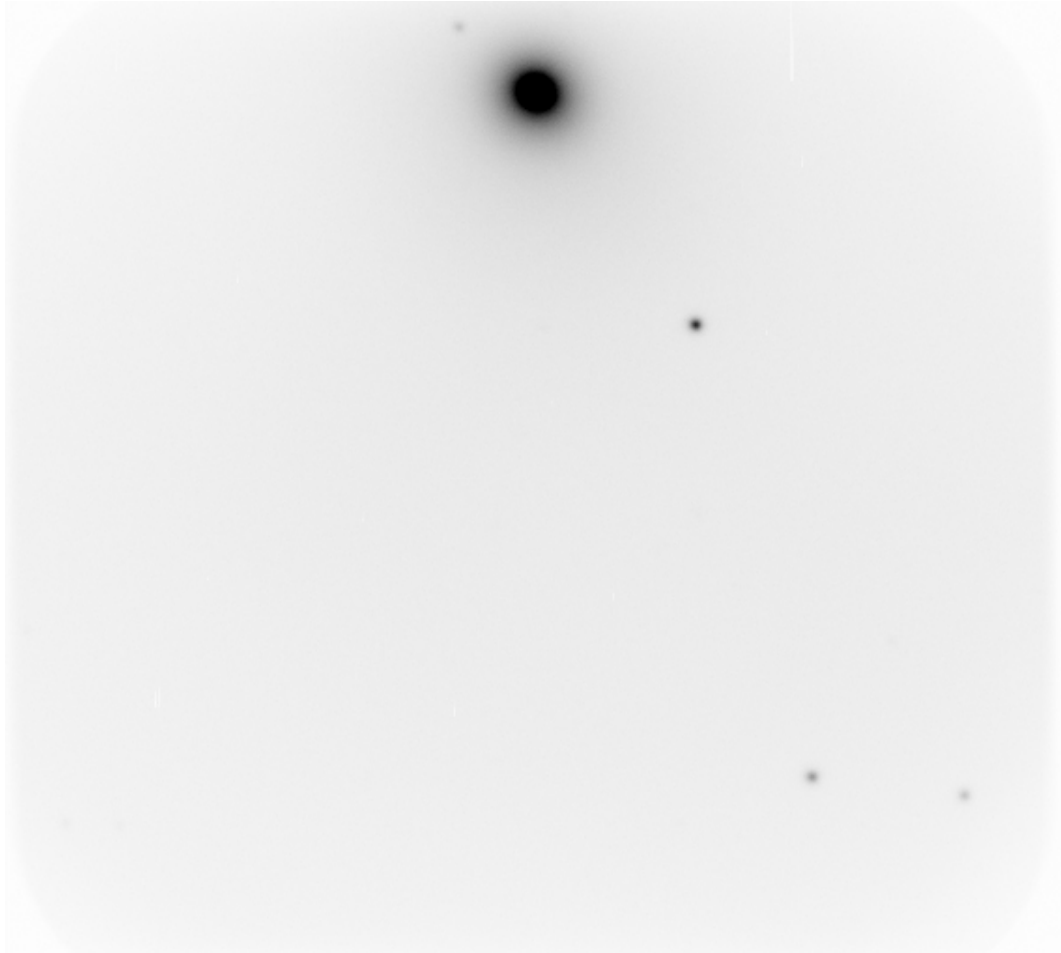


Figure 5.3: NGC 3379 major axis preparatory image.

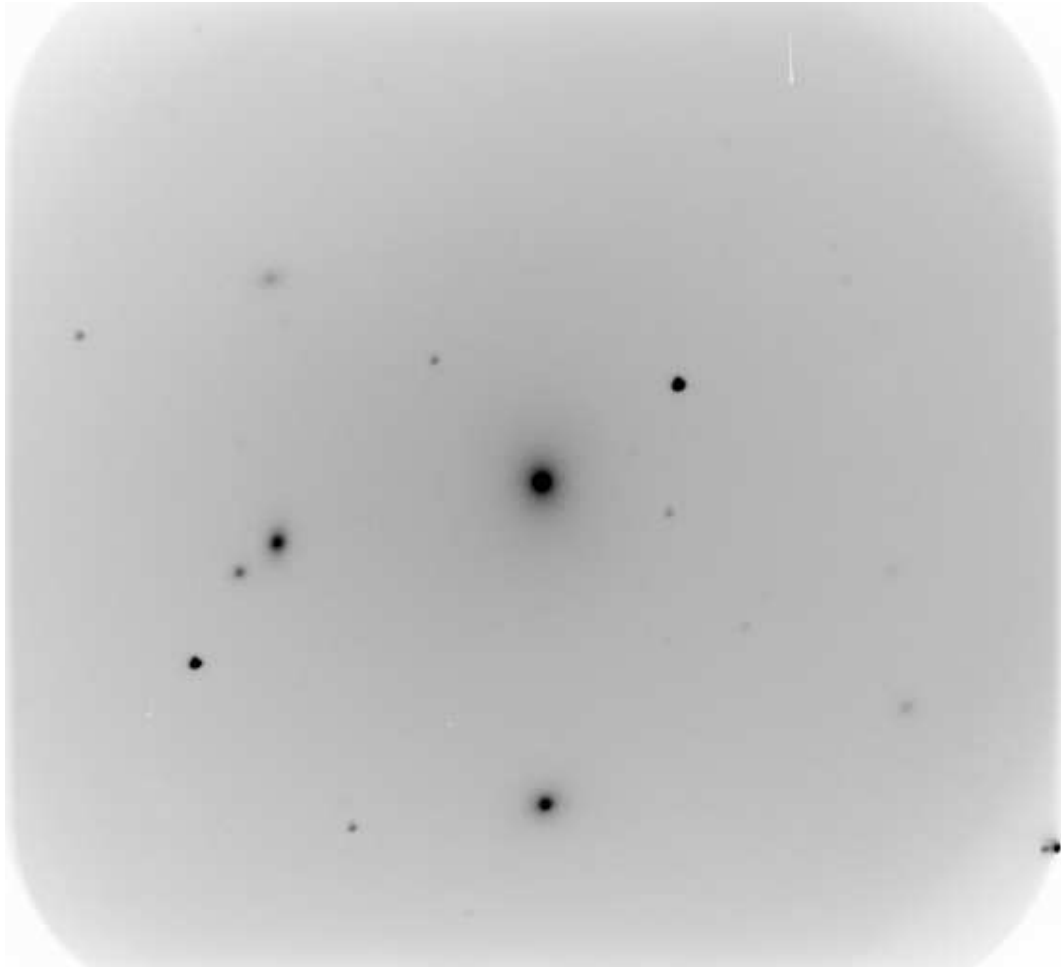


Figure 5.4: NGC 3842 major axis preparatory image.

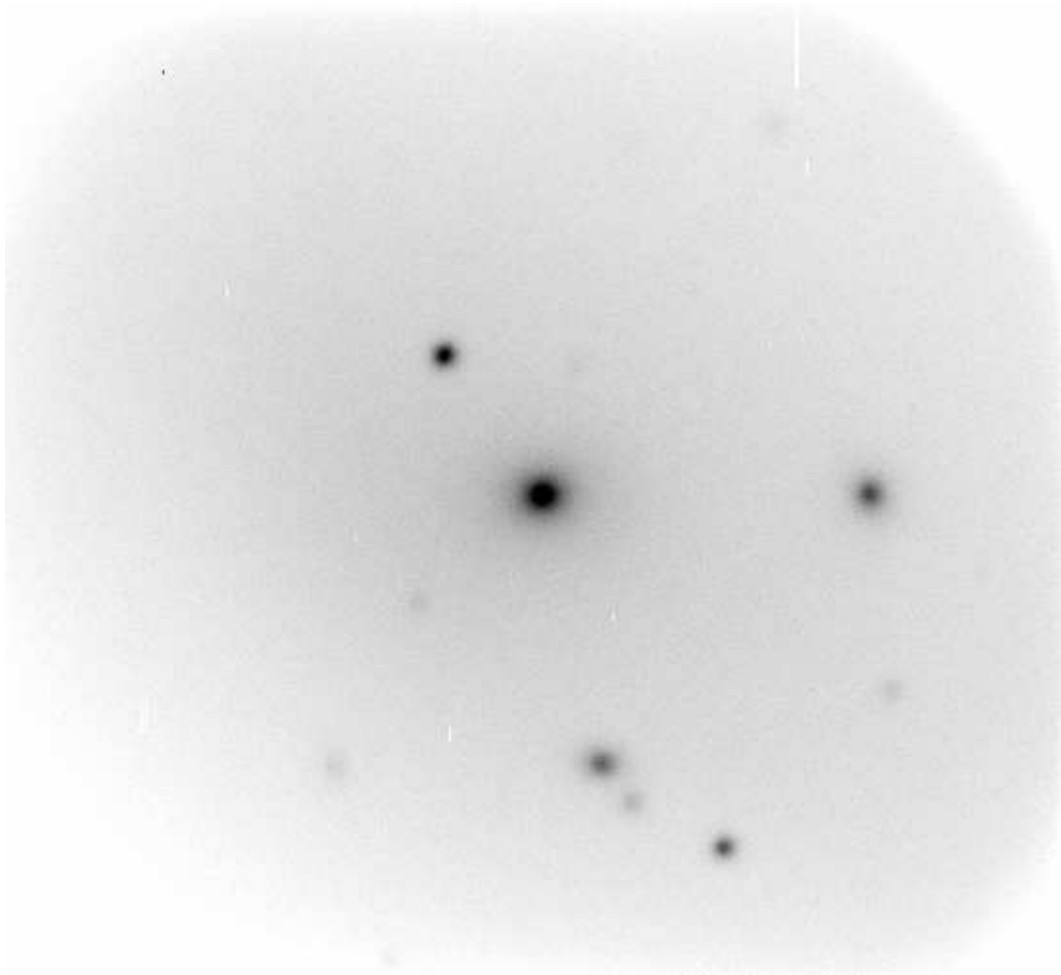


Figure 5.5: NGC 2832 minor axis preparatory image.

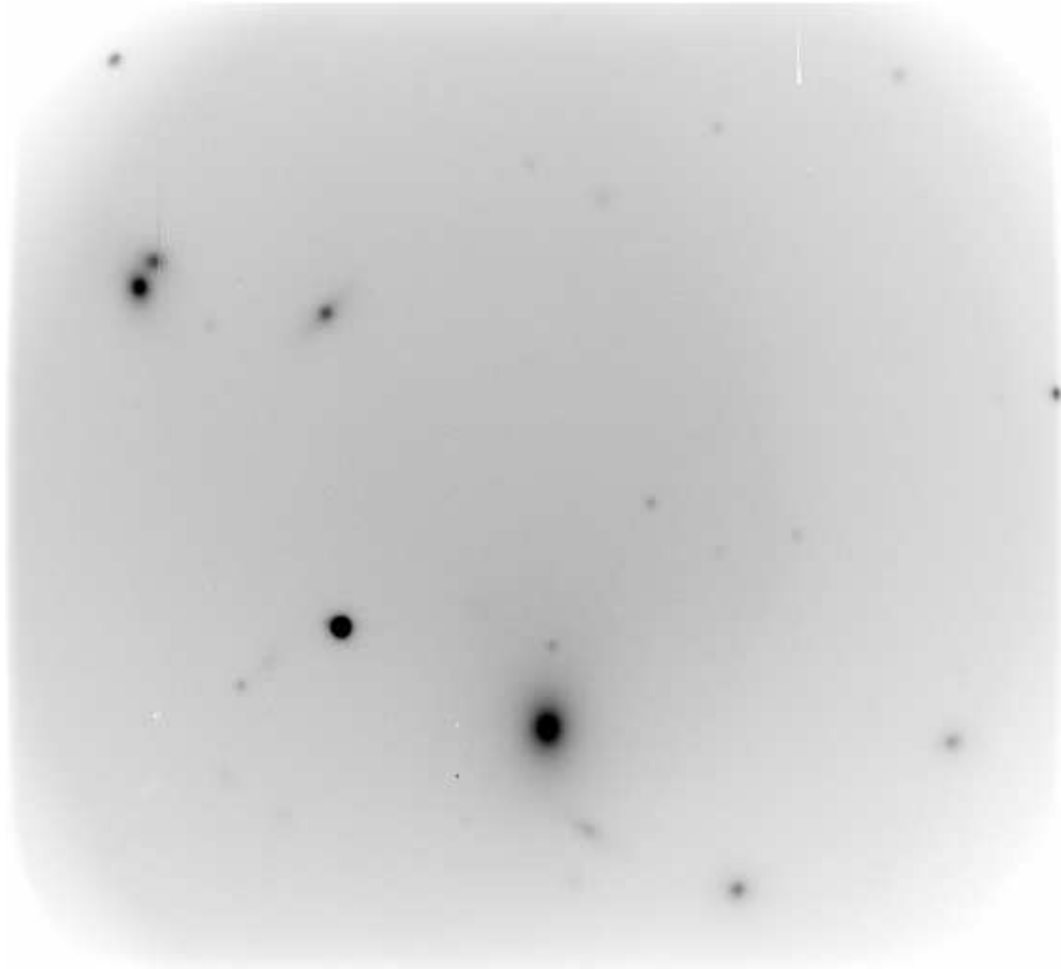


Figure 5.6: NGC 4889 major axis preparatory image.

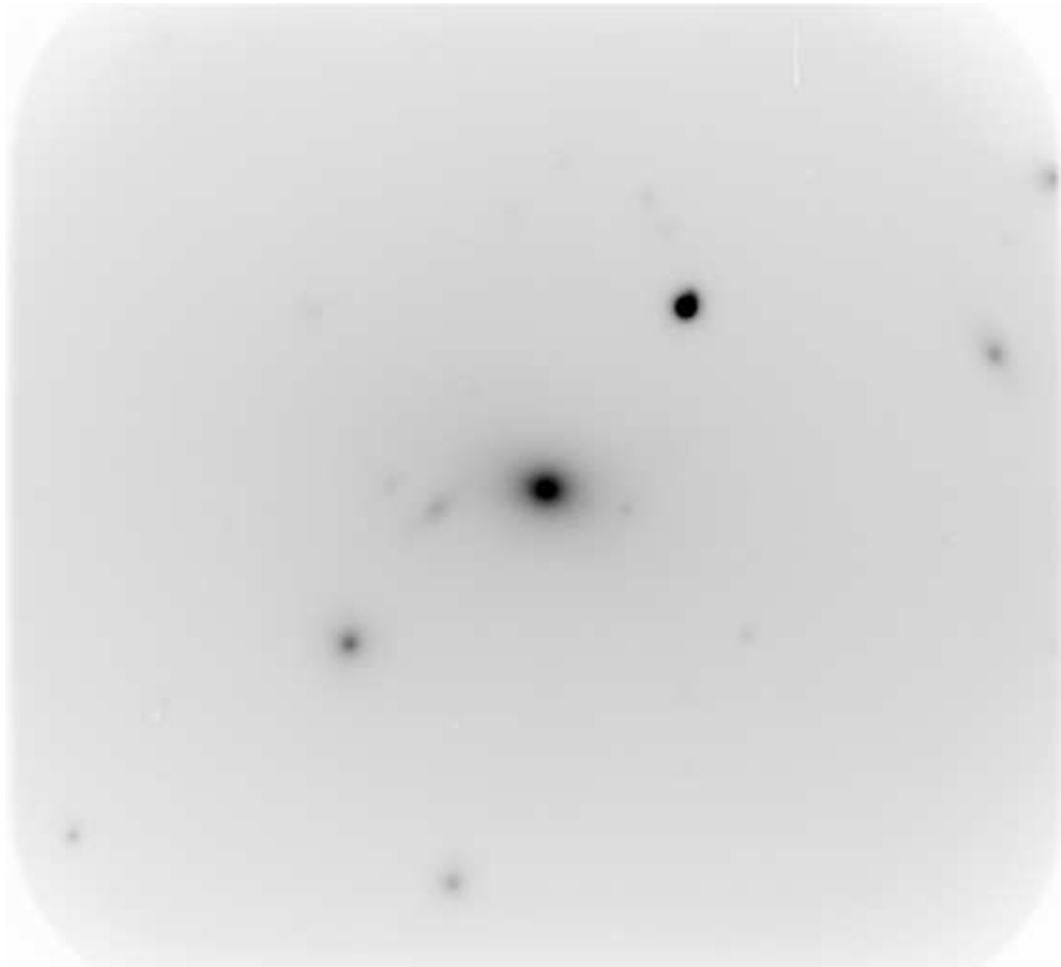


Figure 5.7: NGC 4889 minor axis preparatory image.

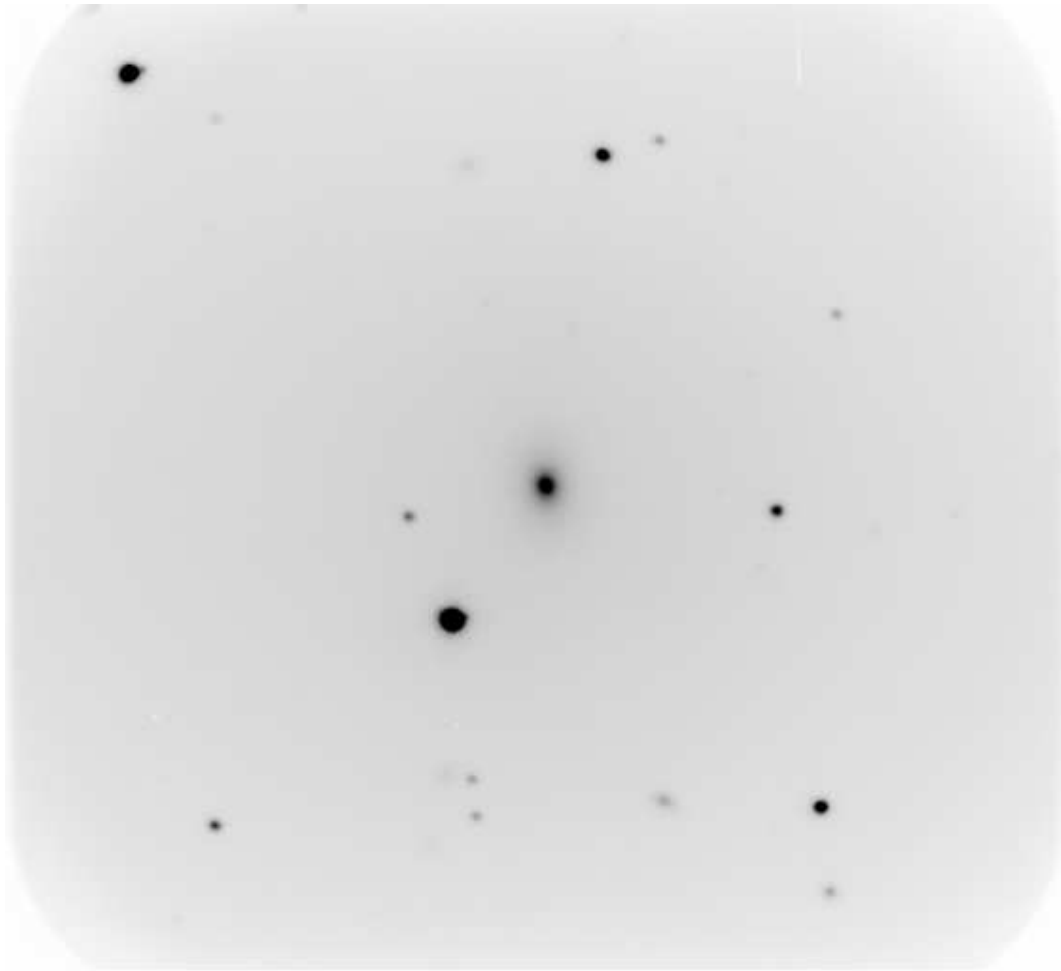


Figure 5.8: NGC 6086 major axis preparatory image.

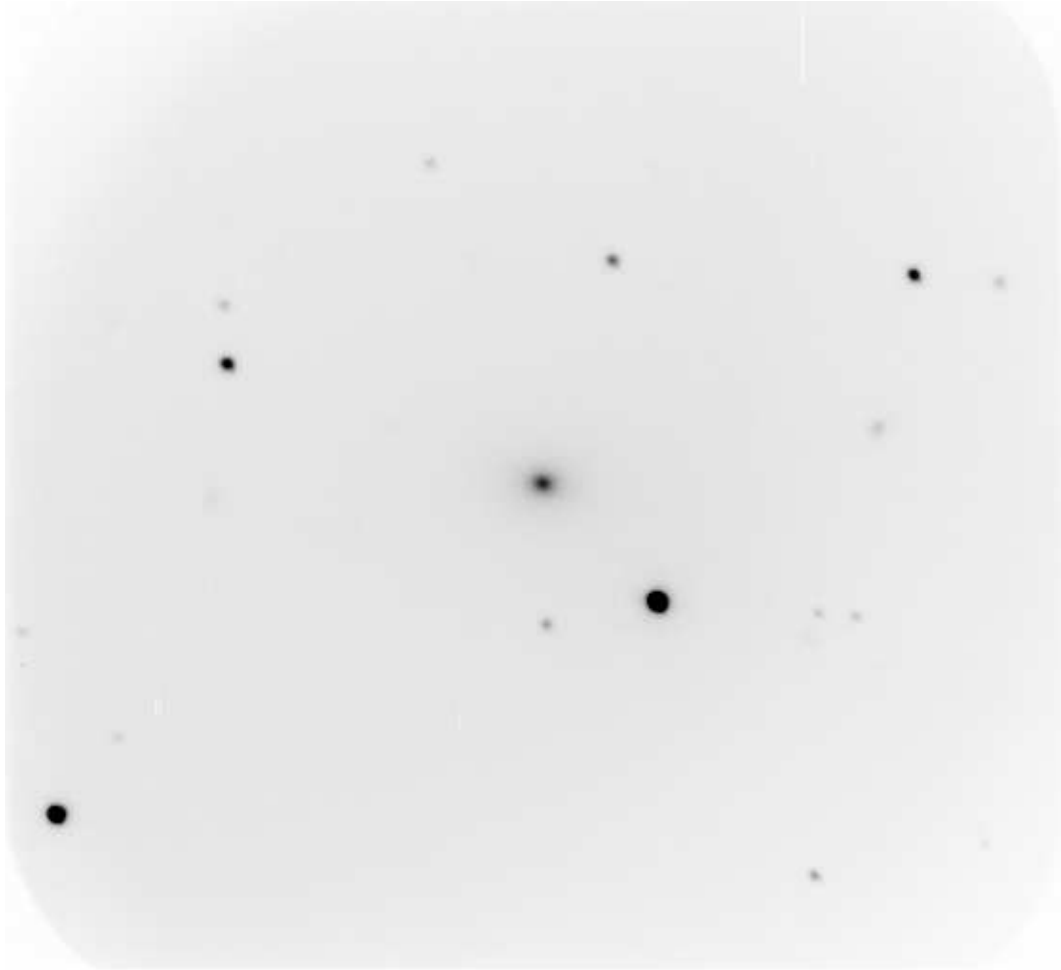


Figure 5.9: NGC 6086 minor axis preparatory image.

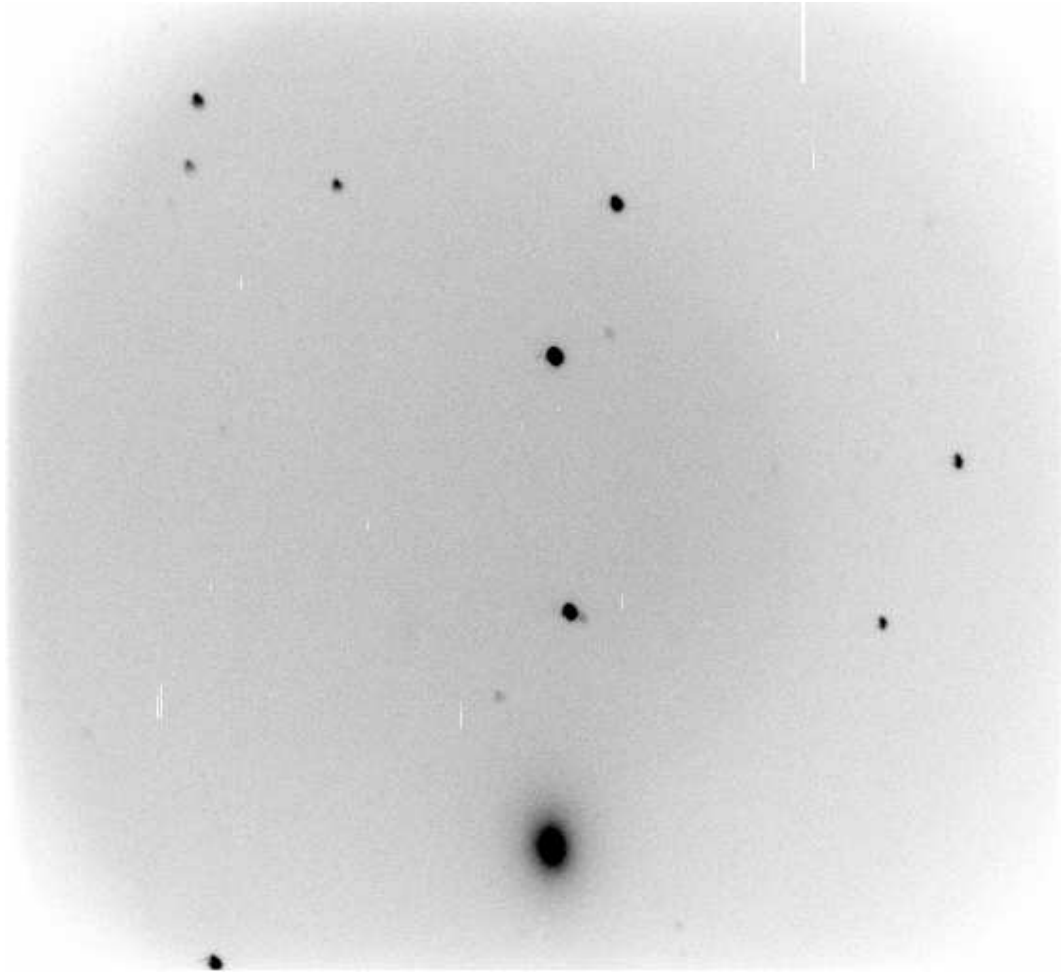


Figure 5.10: NGC 661 major axis preparatory image.

5.2 Data Reductions

The data reduction was performed using standard techniques with fortran code developed from FITSIO programs. First we overscan correct and trim the images. Then we apply a flat correction using a normalized flat frame, taken from averaged instrumental flats obtained each night of observations. Next we rectify the images along the spatial axis using the calibration lamp lines as a reference. We subtract sky using the region of the slit that is furthest from the galaxy center. Finally we align and combine the images using the night sky lines and the galaxy as references. Figures 5.11 and 5.12 show example data before and after these reduction steps for the g2 grism. Figures 5.13 and 5.14 show the same for the g3 grism. The g3 grism is dominated by sky lines in the region of the Ca II triplet (near the left of the chip, the bottom of Figure 5.13), which prove to be a problem for the kinematic extraction.

The wavelength solution was found using Cd and Ne calibration lamps. For the g2 grism a solution of $y(\text{\AA}) = 4274.93701 + 1.70254946x + 0.000402572157x^2 - 1.38921877 \times 10^7 x^3$ was used. For the g3 grism the solution $9142.03906 - 1.8808496x - 0.000150332693x^2 + 9.63607647 \times 10^8 x^3$ was found and flipped to $y(\text{\AA}) = 6247.57448 + 1.6606409x + 0.000293697721x^2 - 9.63607670 \times 10^8 x^3$ before kinematic analysis.

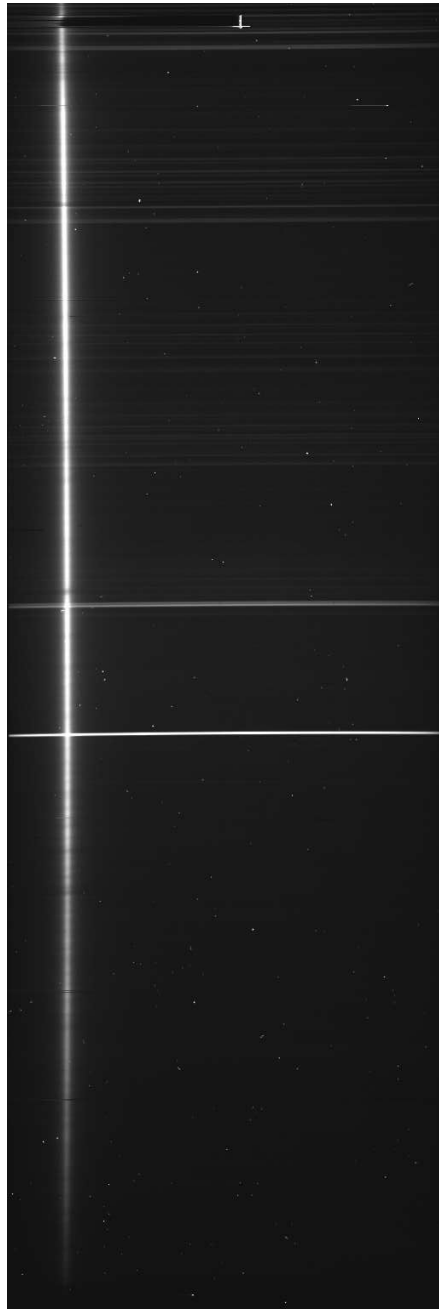


Figure 5.11: Single frame of NGC 821 major axis data (grism g2) before reductions.

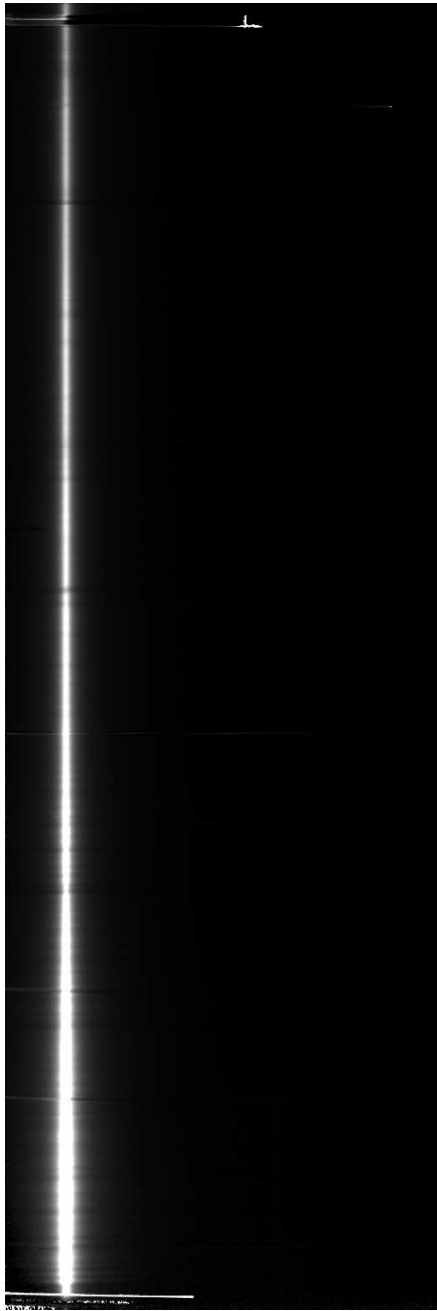


Figure 5.12: NGC 821 major axis reduced data (grism g2).

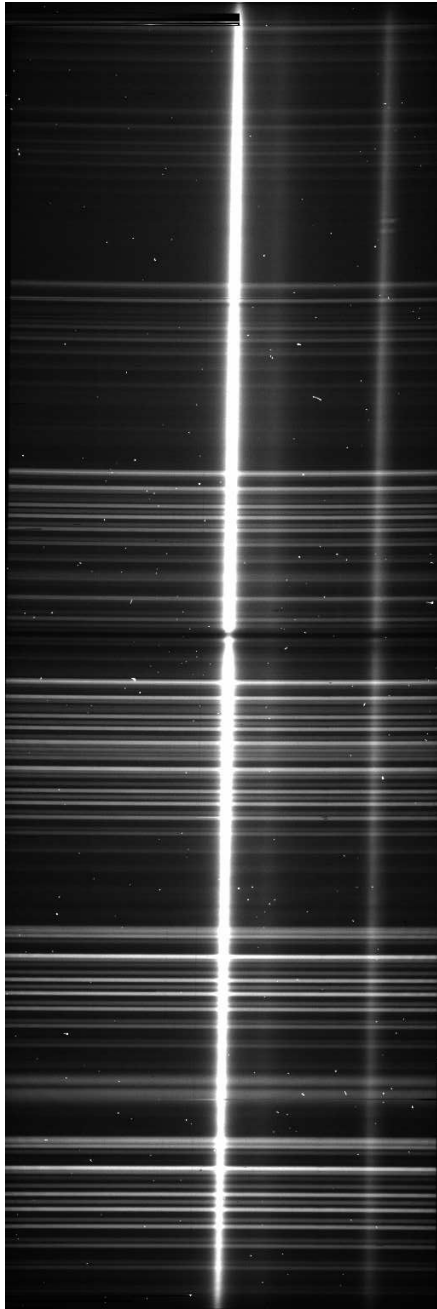


Figure 5.13: Single frame of NGC 2832 minor axis data (grism g3) before reductions.

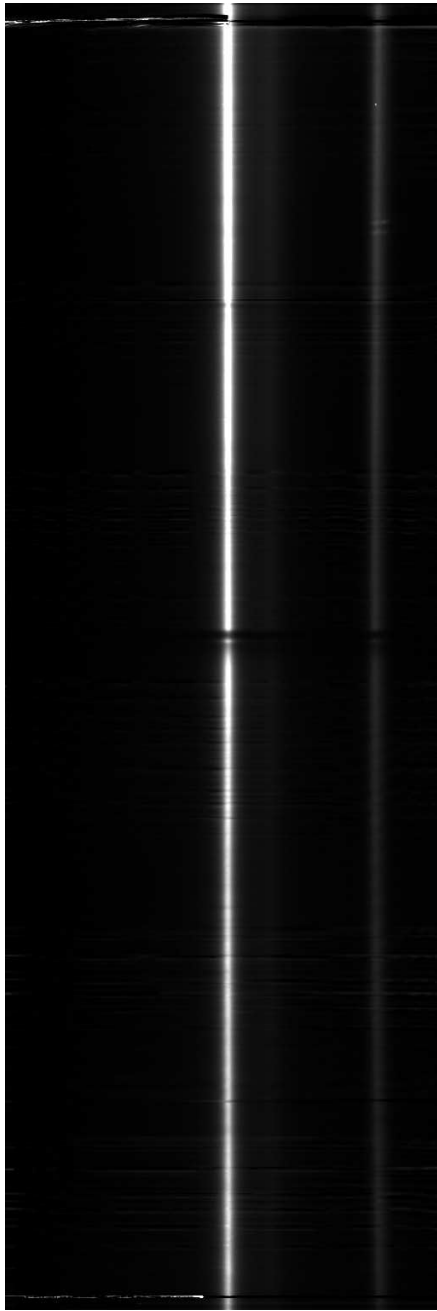


Figure 5.14: NGC 2832 minor axis reduced data (grism g3).

5.3 Kinematic Measurements

We extract the one-dimensional spectra in radial bins. Toward the center we set the bins to match the seeing, about $2''$ or 5 pixels. The outer bins are sized to contain sufficient signal for the line-of-sight velocity distribution (LOSVD) extraction. For minor axis data the spectra on either side of the galaxy are averaged at each radius. For the major axis some galaxies are placed at the edge of the chip (See Figures above) and only one side of the galaxy is used. For the galaxies placed in the center of the chip the extraction is done separately along each side of the galaxy. The g3 grism runs backward such that the low number pixels are at the highest wavelength. We flipped these spectra along the wavelength direction in order to standardize the data.

We do not flux calibrate the spectra, and thus we remove the continuum in each spectra. The first step is to fit a low order polynomial to the spectrum in two iterations. An example is shown in Figure 5.15. Next we fit the local continuum by finding the biweight (Beers et al., 1990) in wavelength windows as described in Pinkney et al. (2003). This is illustrated in Figure 5.16.

We use the LOSVD extraction technique of Gebhardt et al. (2000) and Pinkney et al. (2003). This is a non-parametric maximum penalized likelihood method similar to that of Saha & Williams (1994). First we choose an initial velocity and velocity dispersion to create an initial velocity profile. The profile is described in 29 equally spaced velocity bins. We convolve this profile with a weighted-average template (see below) and calculate the residuals to the observed galaxy spectrum. We vary the height in each bin and the weights

cenn2832mj.fits

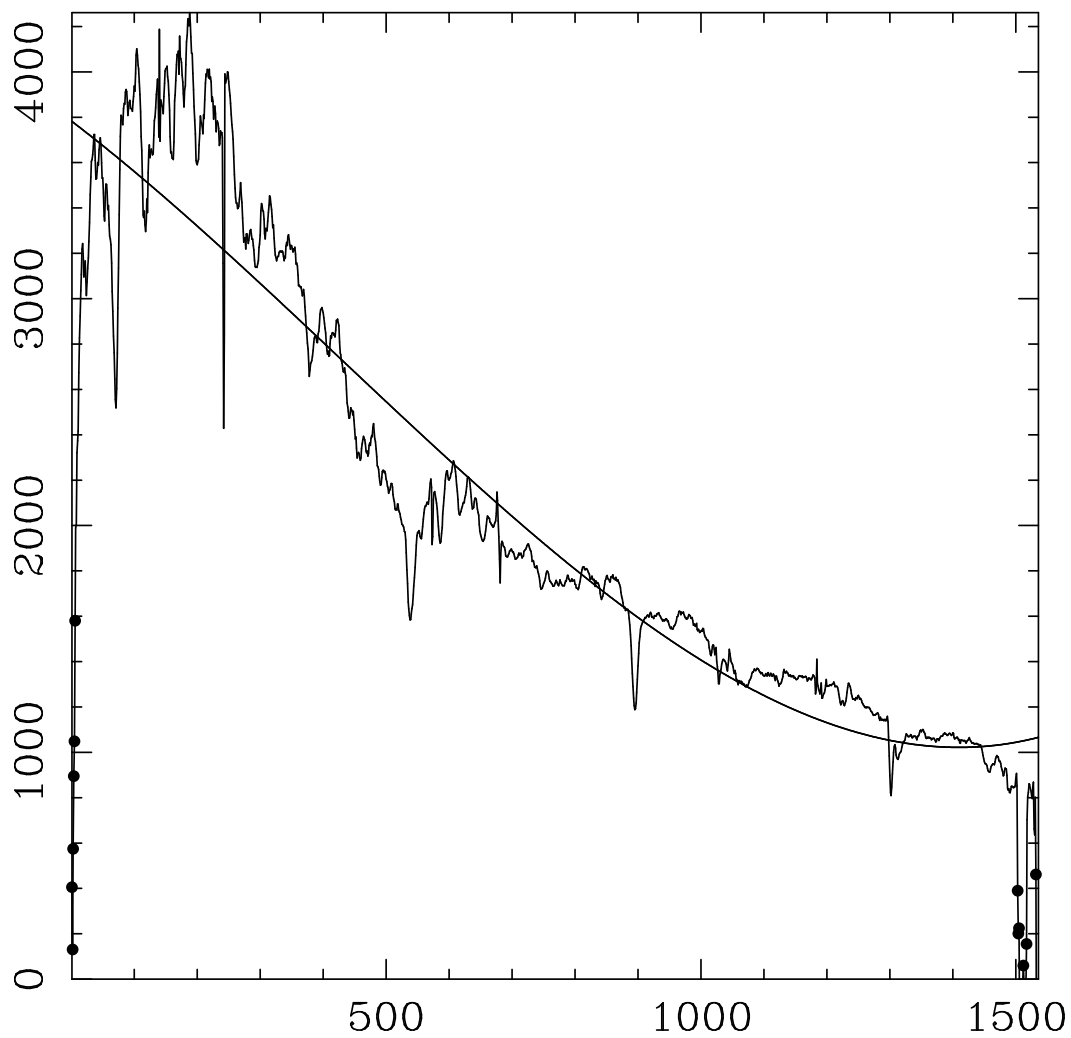


Figure 5.15: First step of the continuum fit for the central bin along the NGC 2832 major axis.

cenn2832mj.fits

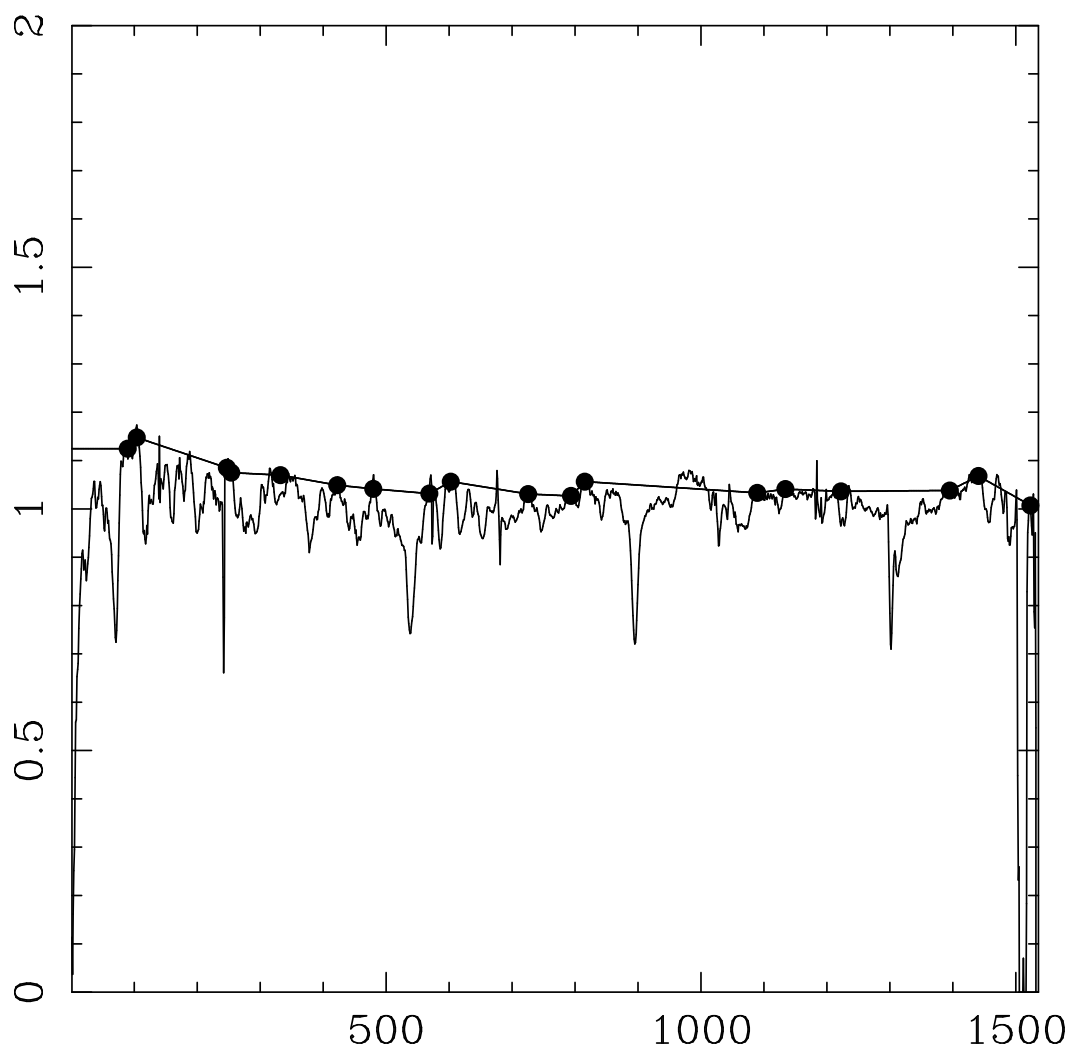


Figure 5.16: Second step of the continuum fit for the central bin along the NGC 2832 major axis.

of each template star to find the best match to the galaxy spectrum. In some cases small wavelength ranges are excluded from the fit due to bad sky subtraction residuals. Examples of these spectrum fits are shown in Figures 5.17 (g2 grism) and 5.18 (g3 grism).

The uncertainty of each velocity bin is obtained from Monte Carlo simulations. We convolve the best-fitted LOSVD and weighted stellar templates to obtain an initial galaxy spectrum. We then generate 100 realizations of the galaxy spectrum by adding Gaussian noise using an estimate of the initial rms. The LOSVD is determined for each realization as described above. The distribution of values in each velocity bin of the LOSVD provides an estimate of the 68% confidence bands.

Our initial analysis focused on the g2 grism and used the stellar templates from Leitherer et al. (1996), convolved to our spectral resolution. Table 5.4 shows the nine template stars available to the fit. Because of the wavelength limits of the templates we use the spectral range 4800-5450Å for the LOSVD extraction. This region includes the H β and Mgb lines, however we exclude the Mgb region because it is typically enhanced and the template stars do not provide a proper fit.

The g3 grism covers a different wavelength range that the above templates do not cover so we used template stars from the Indo-U.S. Library of Coud Feed Stellar Spectra (Valdes et al., 2004), again convolved to our spectral resolution. Table 5.5 shows the template stars available to the fit. We focus our kinematic extraction on the region around the Ca II triplet, from

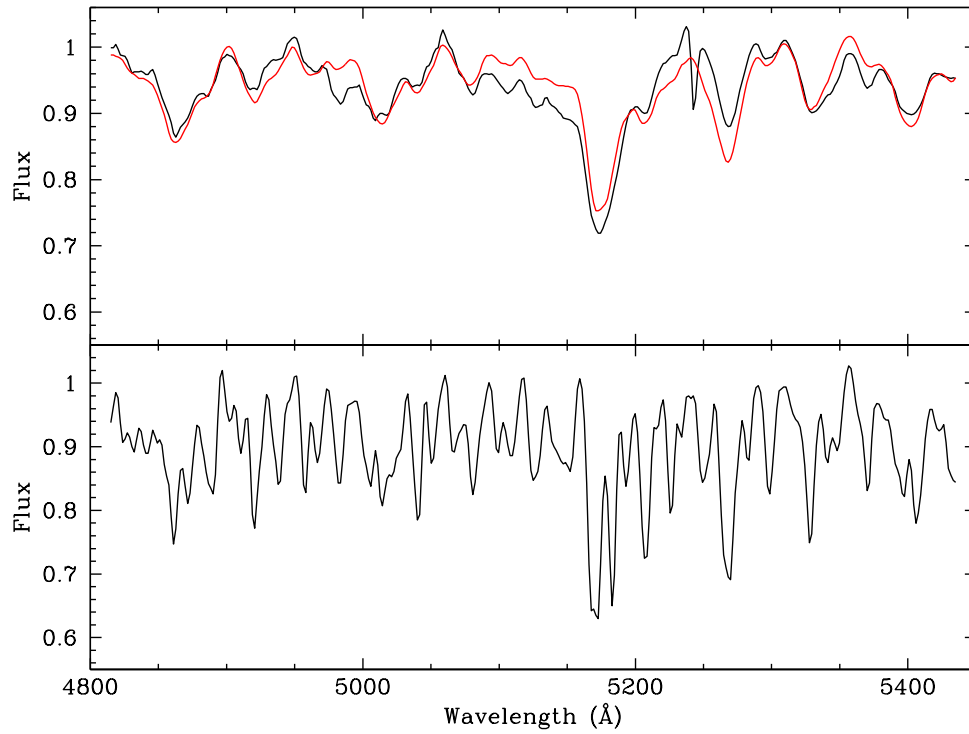


Figure 5.17: Spectrum of the combined, weighted template stars (lower panel), data from the central bin along the NGC 2832 major axis (dashed line, upper panel), and the template spectrum convolved with the best-fitted LOSVD (solid line, upper panel). The region from 5163 Å to 5228 Å is excluded from the fit.

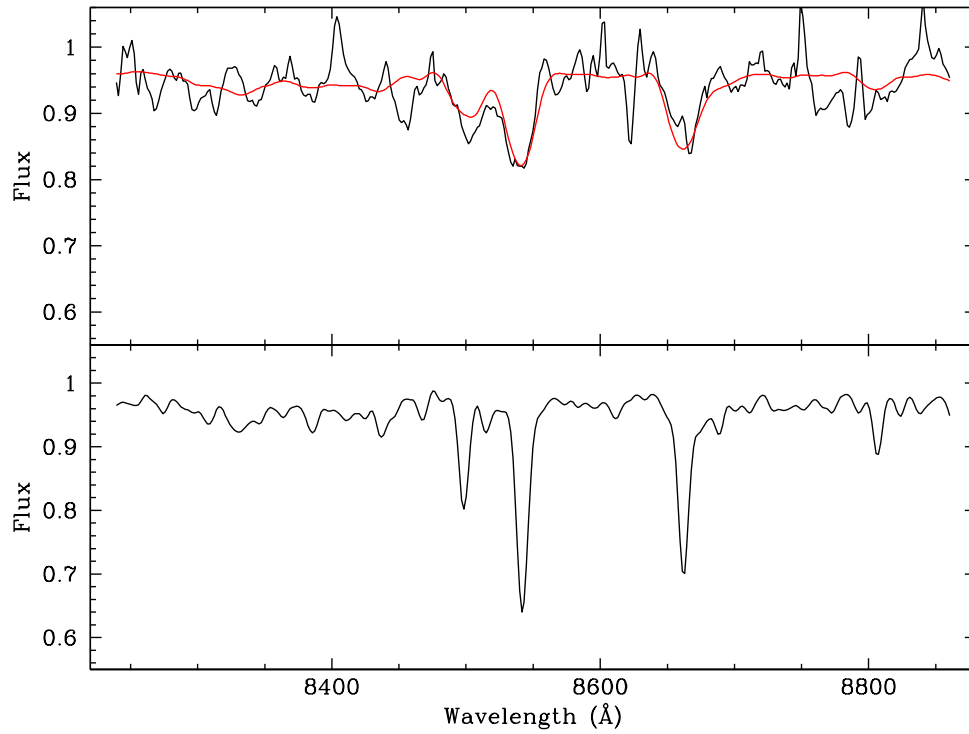


Figure 5.18: Spectrum of the combined, weighted template stars (lower panel), data from the central bin along the NGC 2832 minor axis (dashed line, upper panel), and the template spectrum convolved with the best-fitted LOSVD (solid line, upper panel). The obvious sky line residuals, such as from 8630 Å to 8650 Å are excluded from the fit.

Table 5.4: g2 Template Stars

Name	spectral type	[Fe/H]
HD10307	G1.5V	-0.02
HD52711	G4V	-0.15
HD111812	G0III	INDEF
HD107950	G7III	-0.22
HD81146	K2III	0.15
HD124547	K3III	0.17
HD136726	K4III	0.07
HD120933	K5III	0.50
HD112300	M3III	0.06

8300-8900Å.

Figure 5.19 through Figure 5.22 show the spectra from the LOSVD fits in the central regions of each galaxy. As mentioned above, the abundance of sky lines in the Ca II triplet region of the g3 grism is a problem. The NGC 3842 minor axis can only be well fit in the central two bins, and thus is not shown in the results below. Both the major and minor axis of NGC 6086 prove too difficult to fit at all. Some argue that the Ca II triplet region is better for kinematic study than the *Mgb* region due to template mismatch (Barth et al., 2002). However based on this data I would strongly recommend avoiding this region, particularly using the holographic g3 grism on HET's LRS.

Table 5.5: g3 Template Stars

Name	spectral type	[Fe/H]
HD 50420	A7 III	0.30
HD 72968	A0 V	1.60
HD 74721	A0 V	-1.48
HD 78362	F5 III	0.52
HD 82328	F5 IV	-0.20
HD 5015	F8 V	0.00
HD 693	F5 V	-0.38
HD 39833	G0 III	0.04
HD 10761	G8 III	-0.11
HD 161797	G5 IV	0.16
HD 199960	G1 V	0.11
HD 17820	G5 V	-0.69
HD 8207	K0 III	0.03
HD 135148	K0 III	-1.90
HD 20893	K3 III	-0.13
HD 6734	K0 IV	-0.25
HD 92588	KI IV	-0.10
HD 130025	K0 V	-0.19

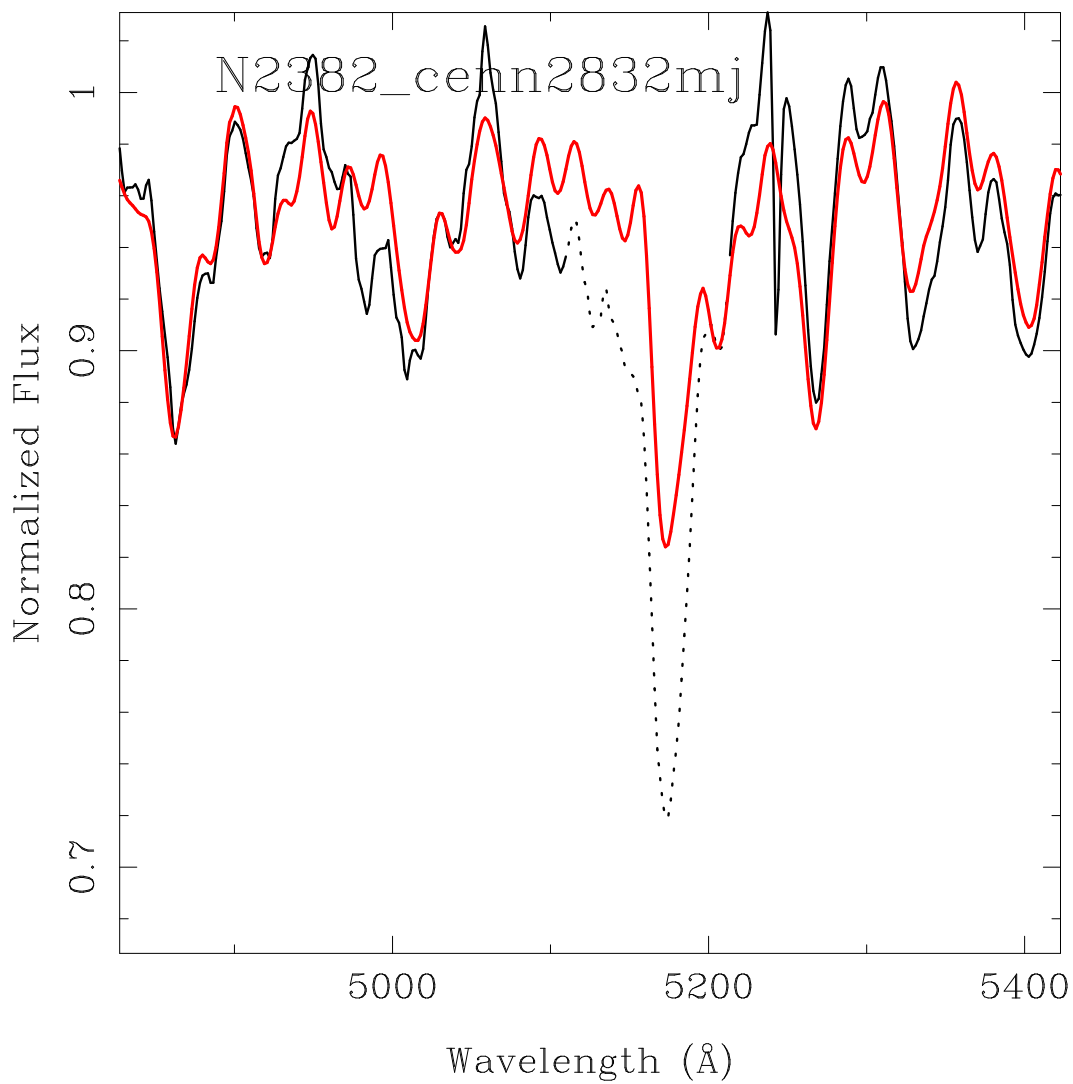


Figure 5.19: Spectrum from the central bin along the NGC 2832 major axis (black line) and spectrum of the combined, weighted template stars convolved with the best-fitted LOSVD (red line). The dashed line region is excluded from the fit.

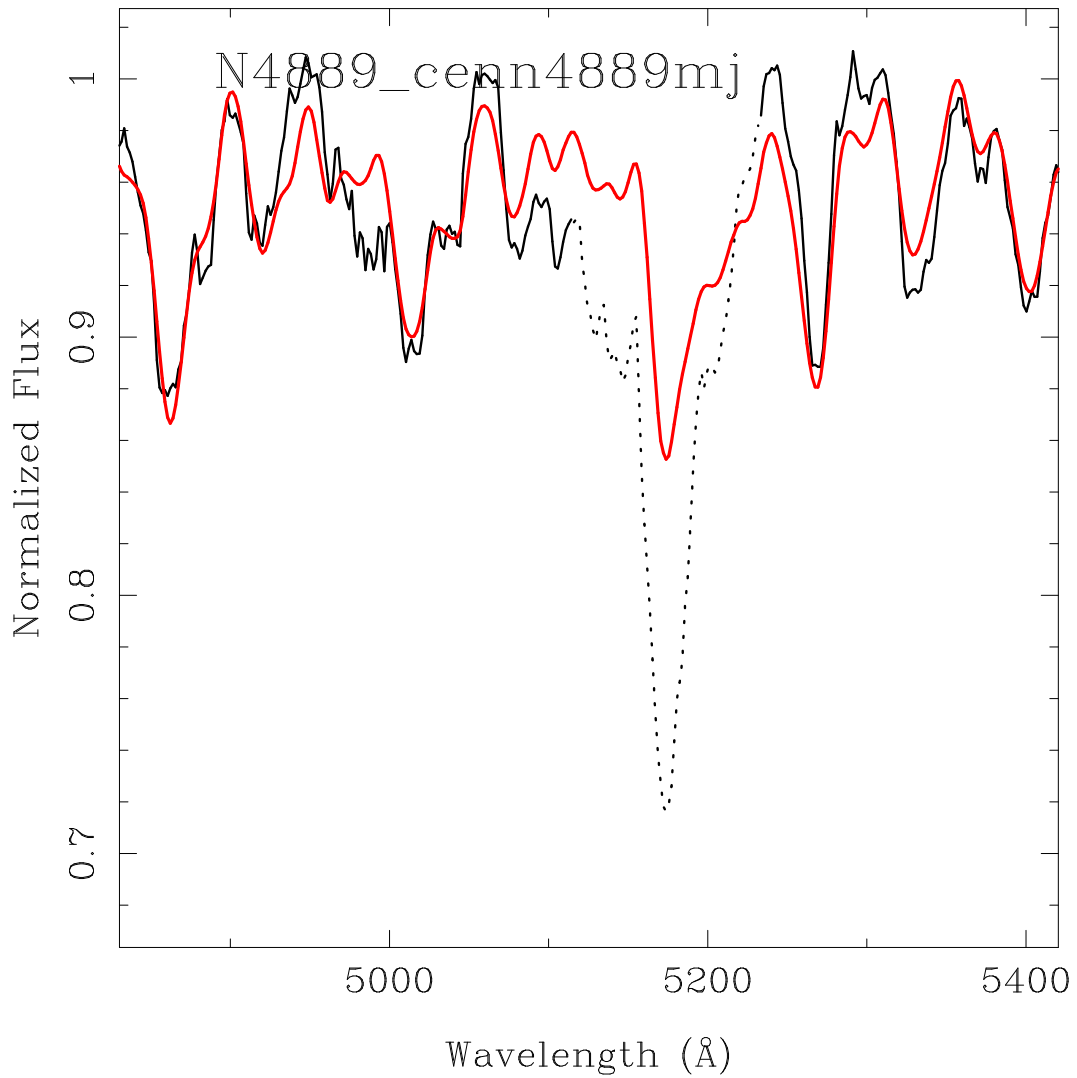


Figure 5.20: Spectrum from the central bin along the NGC 4889 major axis (black line) and spectrum of the combined, weighted template stars convolved with the best-fitted LOSVD (red line). The dashed line region is excluded from the fit.

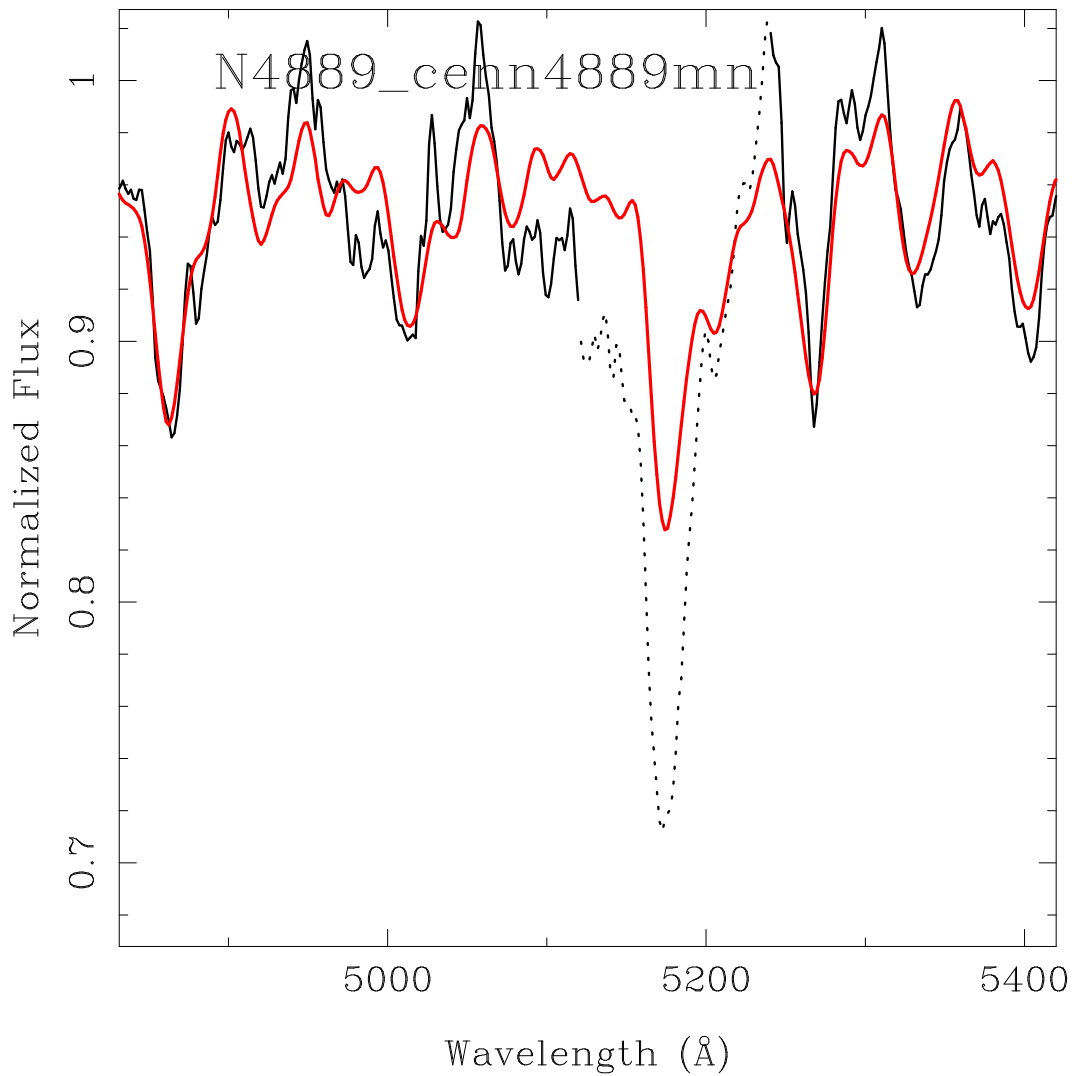


Figure 5.21: Spectrum from the central bin along the NGC 4889 minor axis (black line) and spectrum of the combined, weighted template stars convolved with the best-fitted LOSVD (red line). The dashed line region is excluded from the fit.

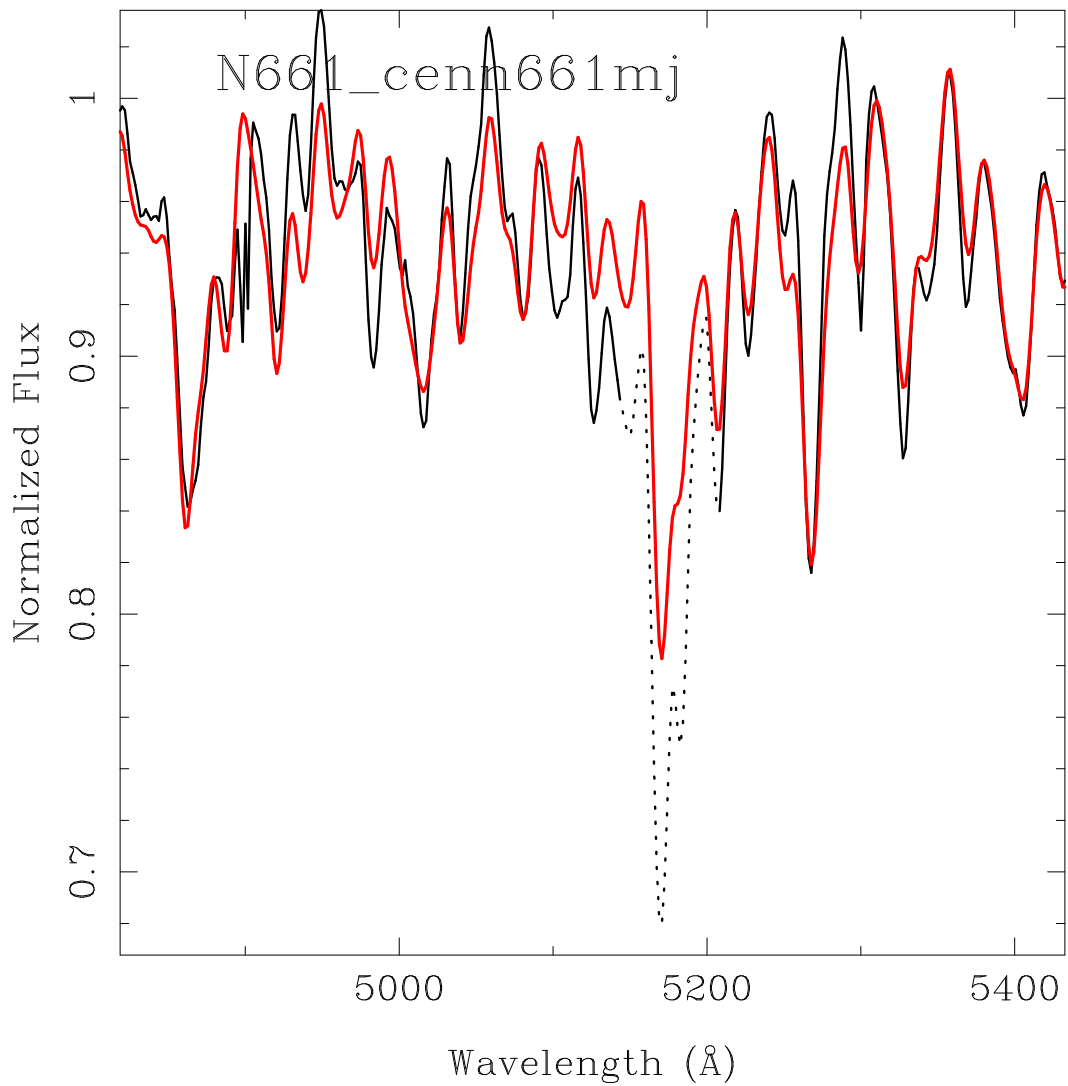


Figure 5.22: Spectrum from the central bin along the NGC 661 major axis (black line) and spectrum of the combined, weighted template stars convolved with the best-fitted LOSVD (red line). The dashed line region is excluded from the fit.

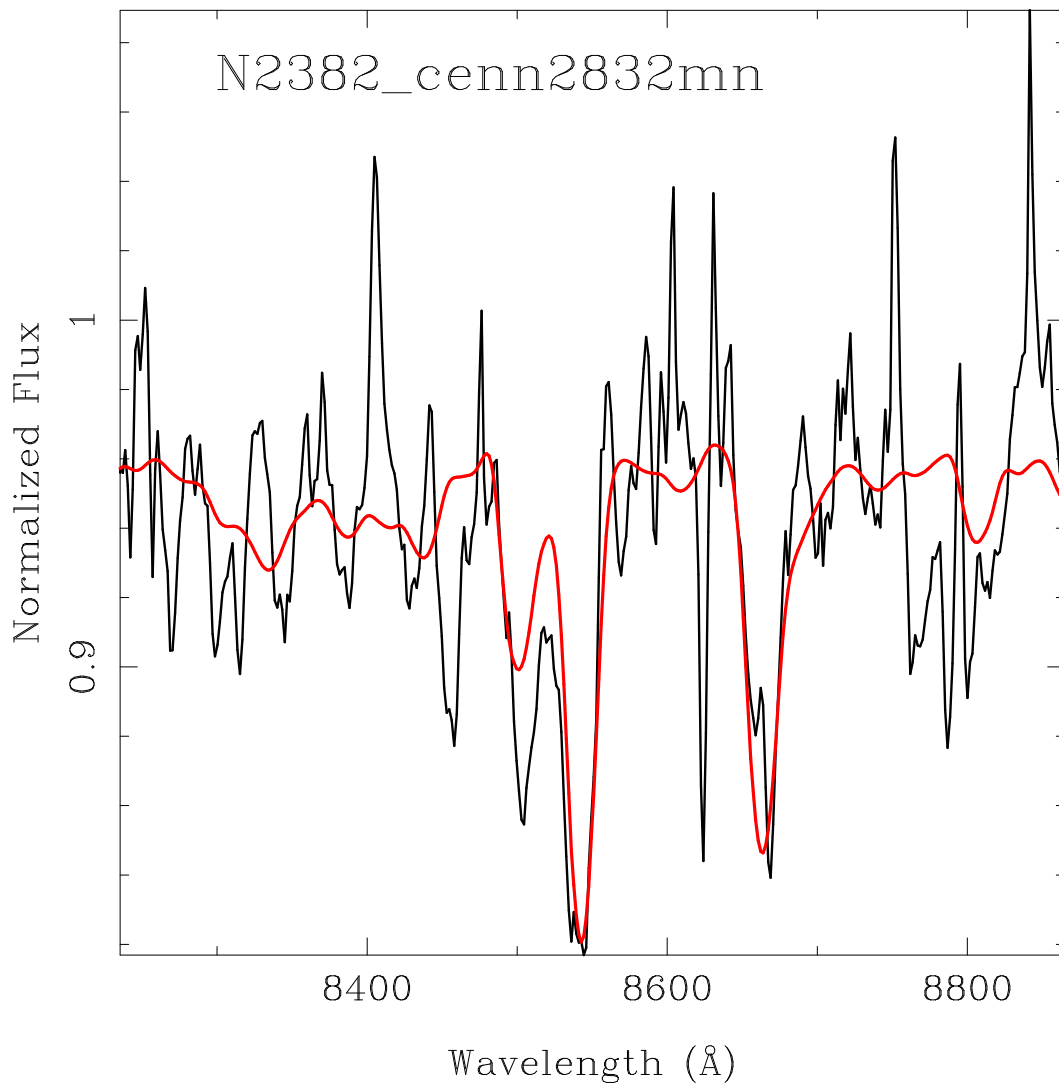


Figure 5.23: Spectrum from the central bin along the NGC 2832 minor axis (black line) and spectrum of the combined, weighted template stars convolved with the best-fitted LOSVD (red line). The dashed line region is excluded from the fit.

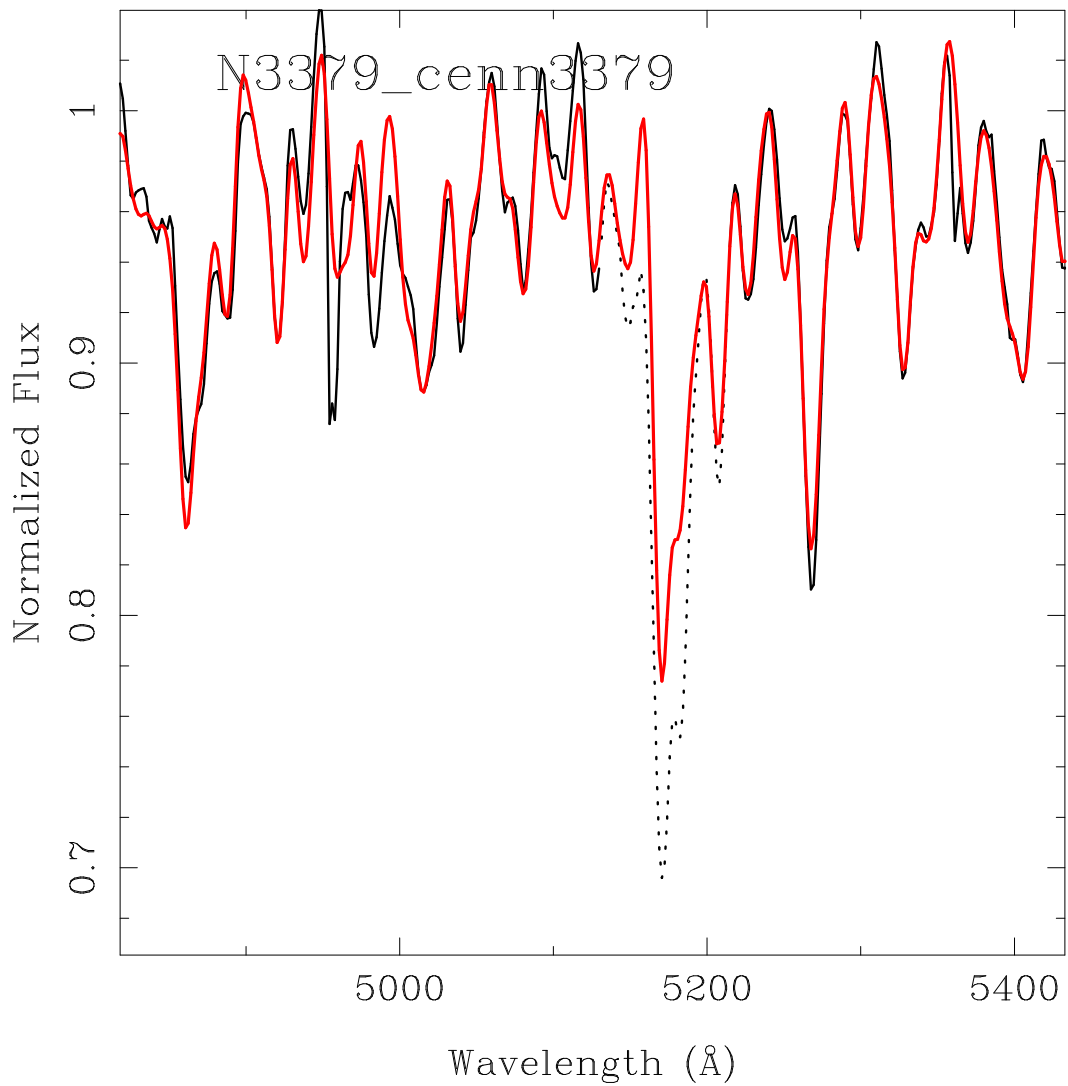


Figure 5.24: Spectrum from the central bin along the NGC 3379 major axis (black line) and spectrum of the combined, weighted template stars convolved with the best-fitted LOSVD (red line). The dashed line region is excluded from the fit.

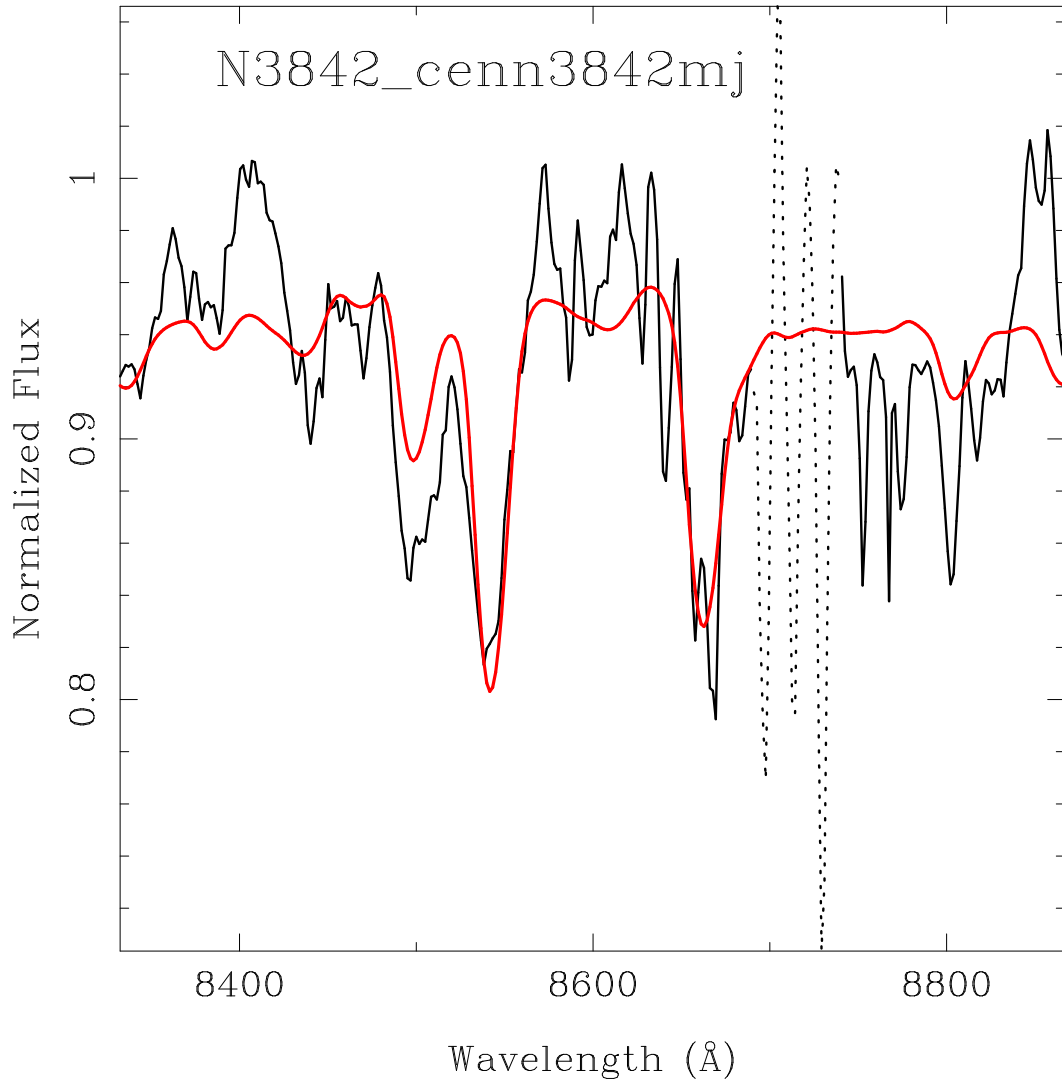


Figure 5.25: Spectrum from the central bin along the NGC 3842 major axis (black line) and spectrum of the combined, weighted template stars convolved with the best-fitted LOSVD (red line). The dashed line region is excluded from the fit.

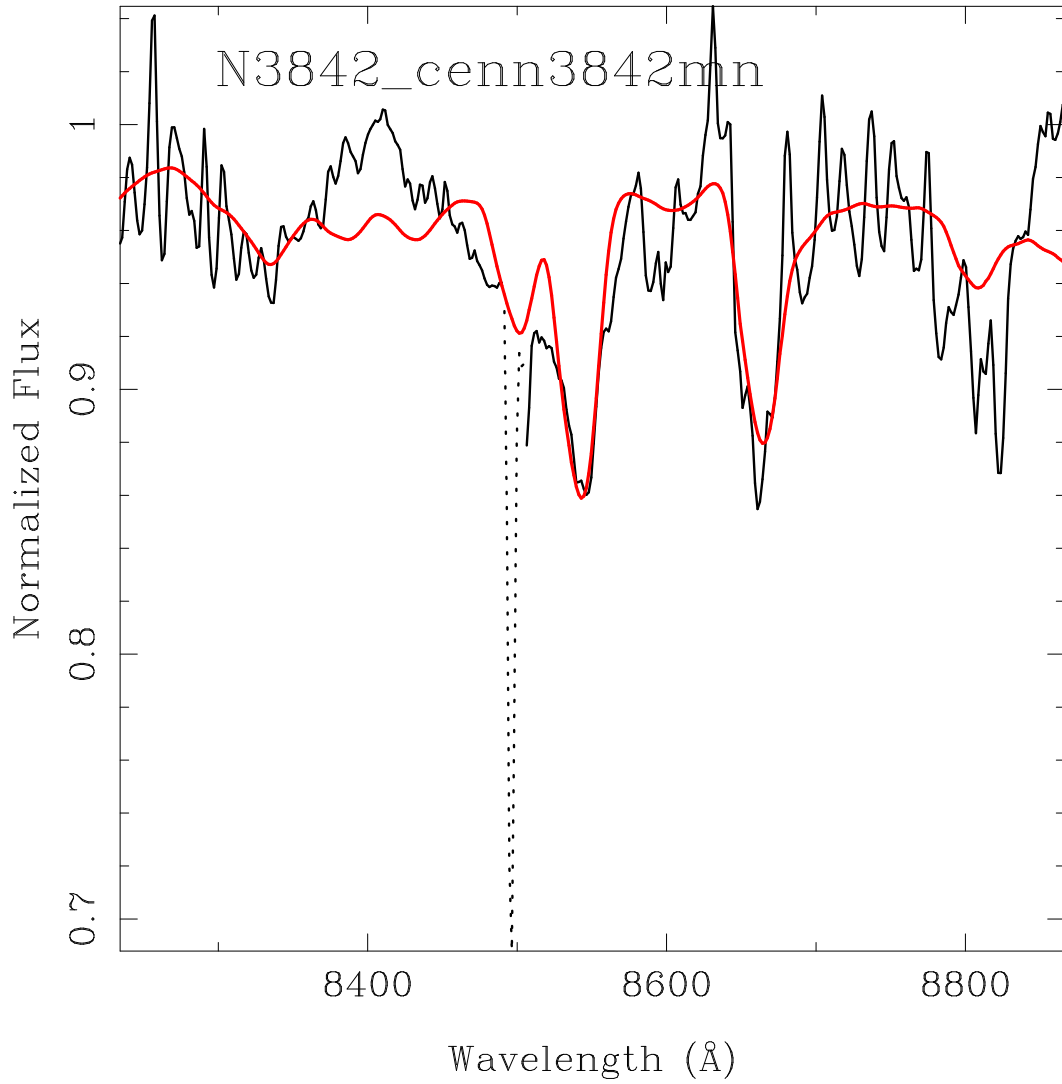


Figure 5.26: Spectrum from the central bin along the NGC 3842 minor axis (black line) and spectrum of the combined, weighted template stars convolved with the best-fitted LOSVD (red line). The dashed line region is excluded from the fit.

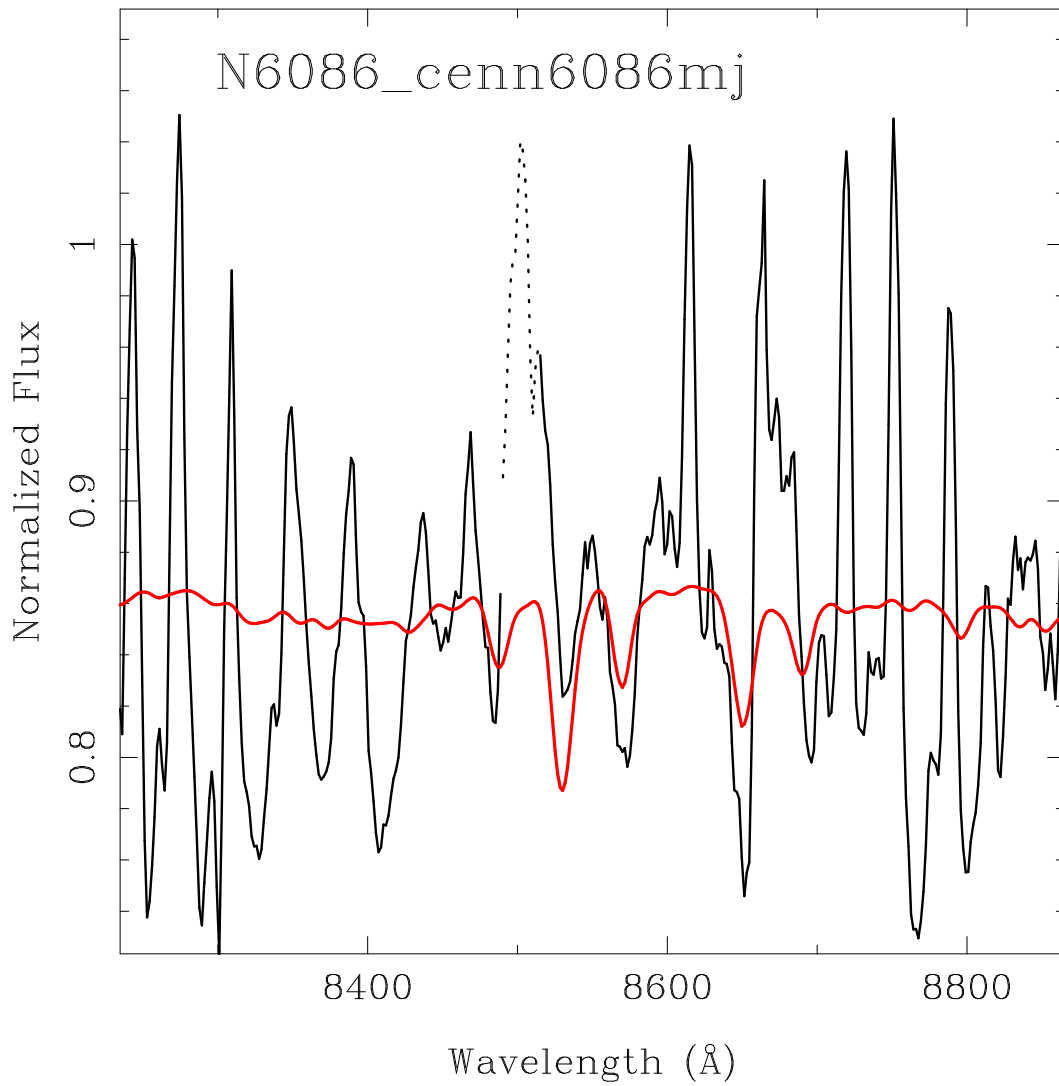


Figure 5.27: Spectrum from the central bin along the NGC 6086 major axis (black line) and spectrum of the combined, weighted template stars convolved with the best-fitted LOSVD (red line). The dashed line region is excluded from the fit.

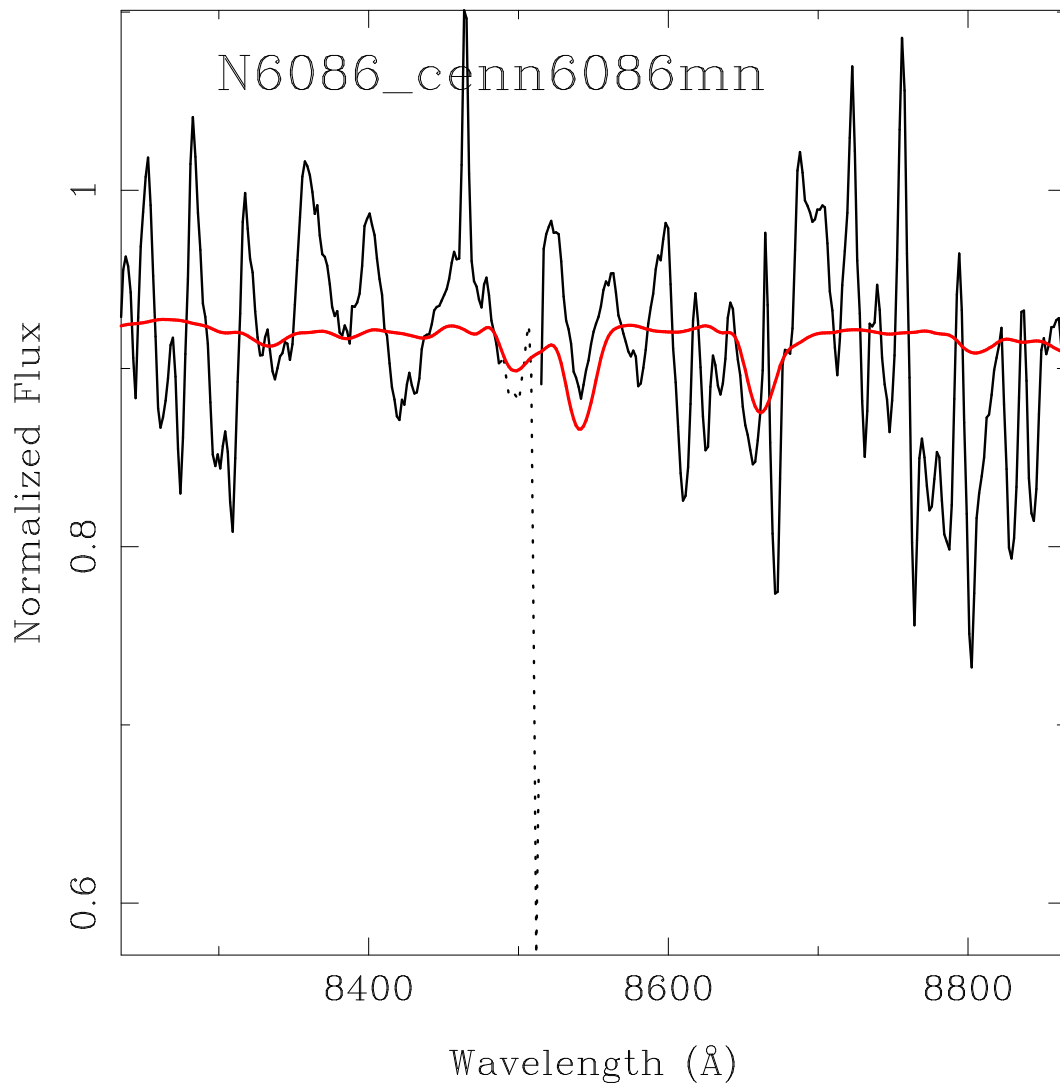


Figure 5.28: Spectrum from the central bin along the NGC 6086 minor axis (black line) and spectrum of the combined, weighted template stars convolved with the best-fitted LOSVD (red line). The dashed line region is excluded from the fit.

5.4 Results

Our final result is the full nonparametric velocity profile at each radius of the galaxy. Example LOSVDs are shown in Figure 5.29. It is also useful to look at the moments of the distribution. Figures 5.30 through 5.36 show the second moment as measured by $\sqrt{V^2 + \sigma^2}$, and the first four Gauss-Hermite moments (mean velocity V , velocity dispersion σ , asymmetric deviations from Gaussian (skewness) h_3 , and symmetric deviations from Gaussian (kurtosis) h_4) for each of our galaxies. These kinematic data are given in Tables 5.6 through 5.12.

These data will be of use in future kinematic studies of these galaxies.

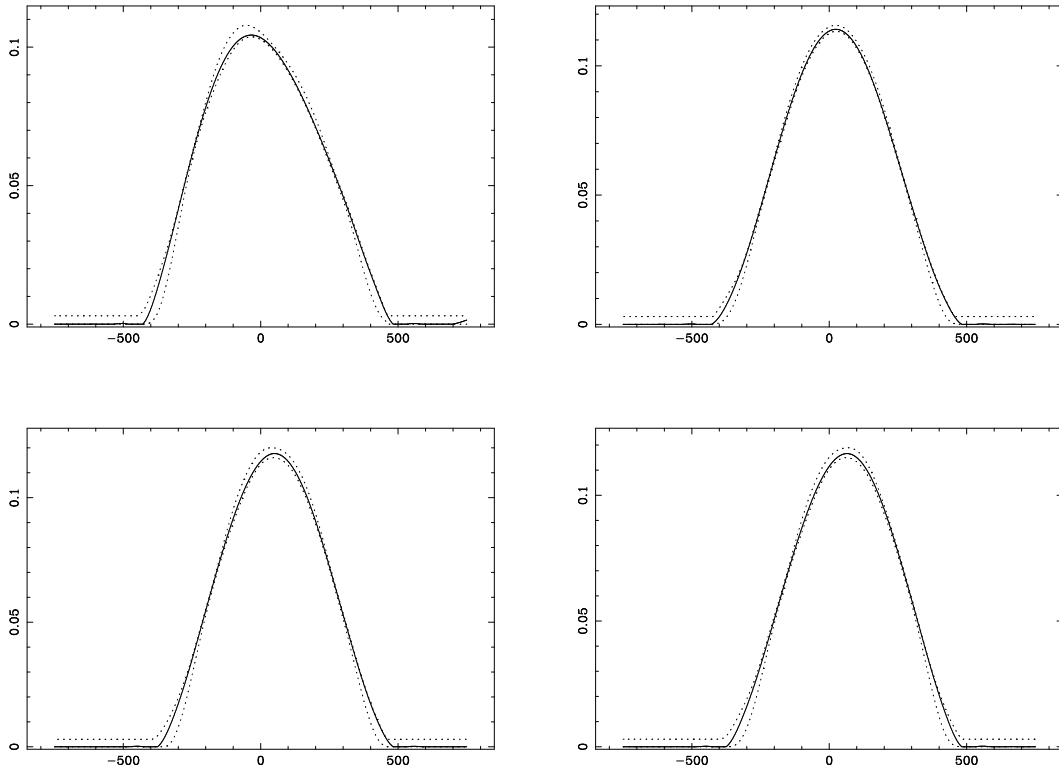


Figure 5.29: Example line-of-sight velocity distributions (solid lines) with errors (dashed lines).

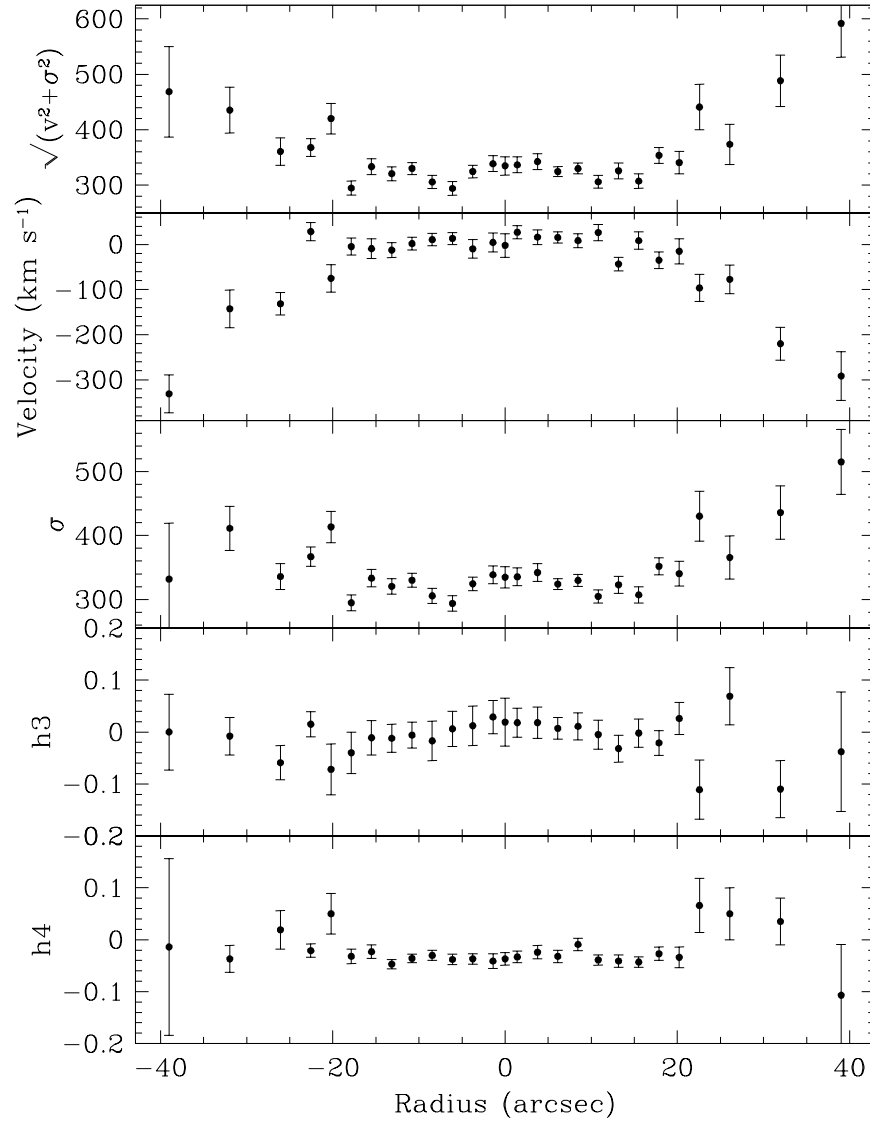


Figure 5.30: The second moment as measured by $\sqrt{V^2 + \sigma^2}$ and the first four Gauss-Hermite moments (mean velocity V , velocity dispersion σ , asymmetric deviations from Gaussian (skewness) h_3 , and symmetric deviations from Gaussian (kurtosis) h_4) for NGC 2832 along the major axis.

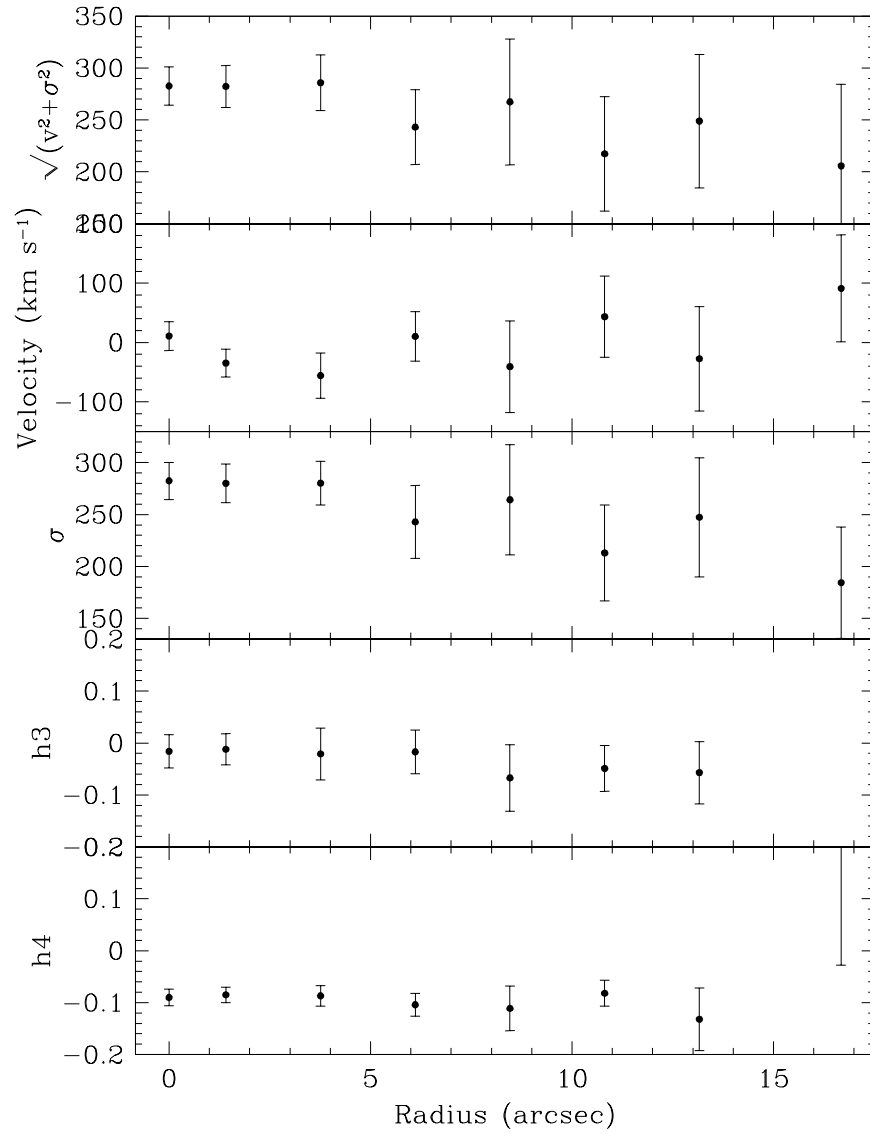


Figure 5.31: The second moment as measured by $\sqrt{V^2 + \sigma^2}$ and the first four Gauss-Hermite moments (mean velocity V , velocity dispersion σ , asymmetric deviations from Gaussian (skewness) h_3 , and symmetric deviations from Gaussian (kurtosis) h_4) for NGC 2832 along the minor axis.

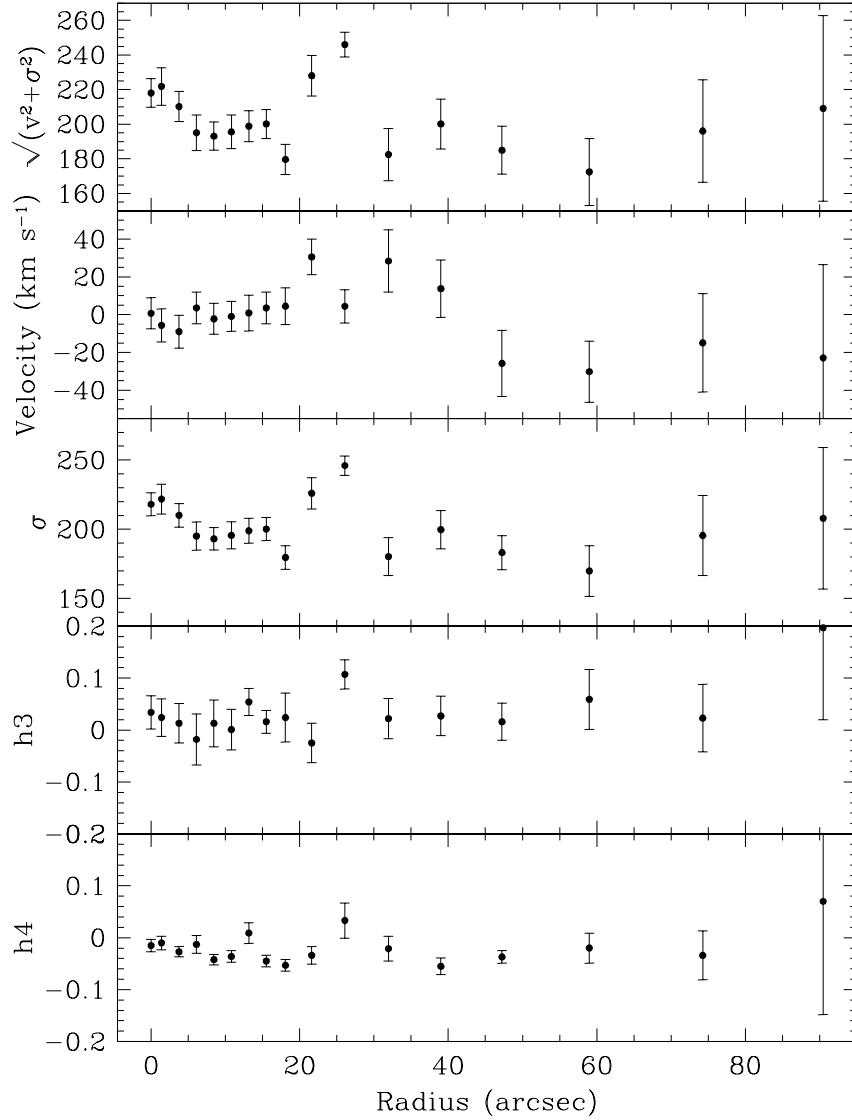


Figure 5.32: The second moment as measured by $\sqrt{V^2 + \sigma^2}$ and the first four Gauss-Hermite moments (mean velocity V , velocity dispersion σ , asymmetric deviations from Gaussian (skewness) h_3 , and symmetric deviations from Gaussian (kurtosis) h_4) for NGC 3379 along the major axis.

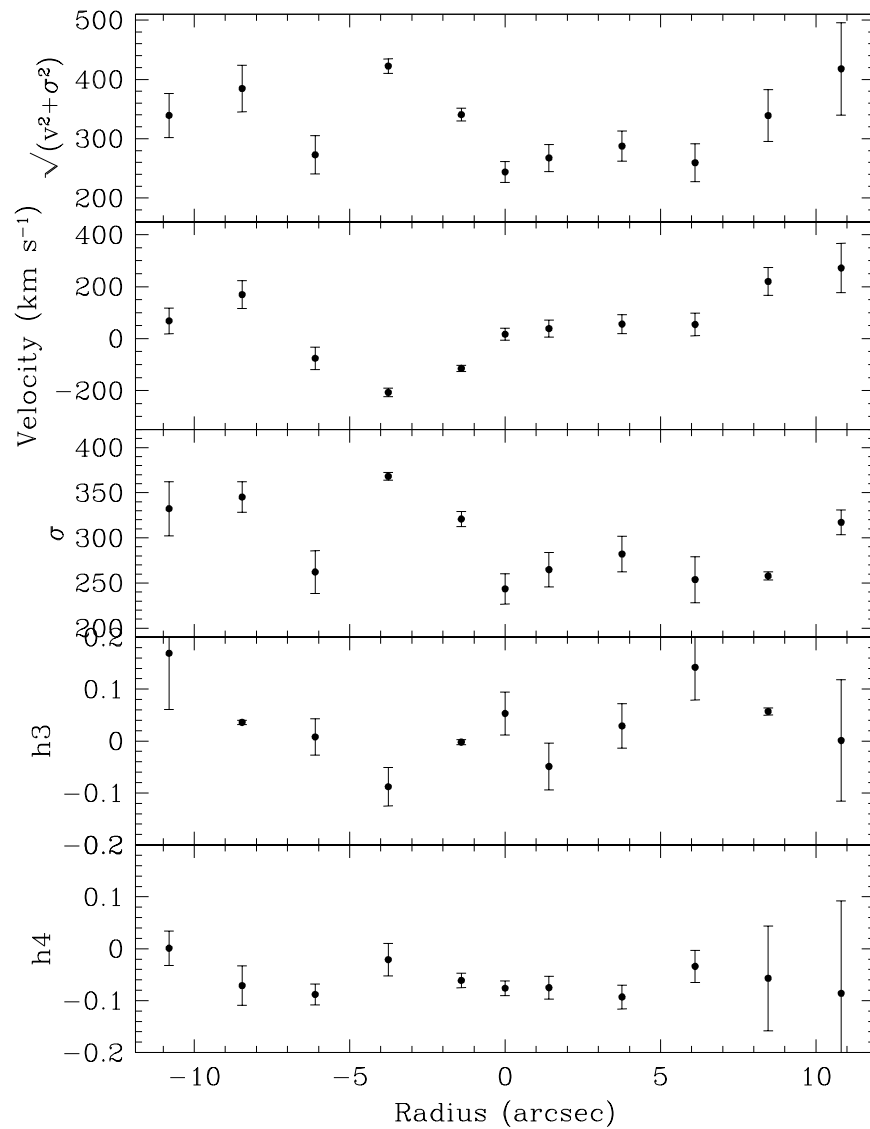


Figure 5.33: The second moment as measured by $\sqrt{V^2 + \sigma^2}$ and the first four Gauss-Hermite moments (mean velocity V , velocity dispersion σ , asymmetric deviations from Gaussian (skewness) h_3 , and symmetric deviations from Gaussian (kurtosis) h_4) for NGC 3842 along the major axis.

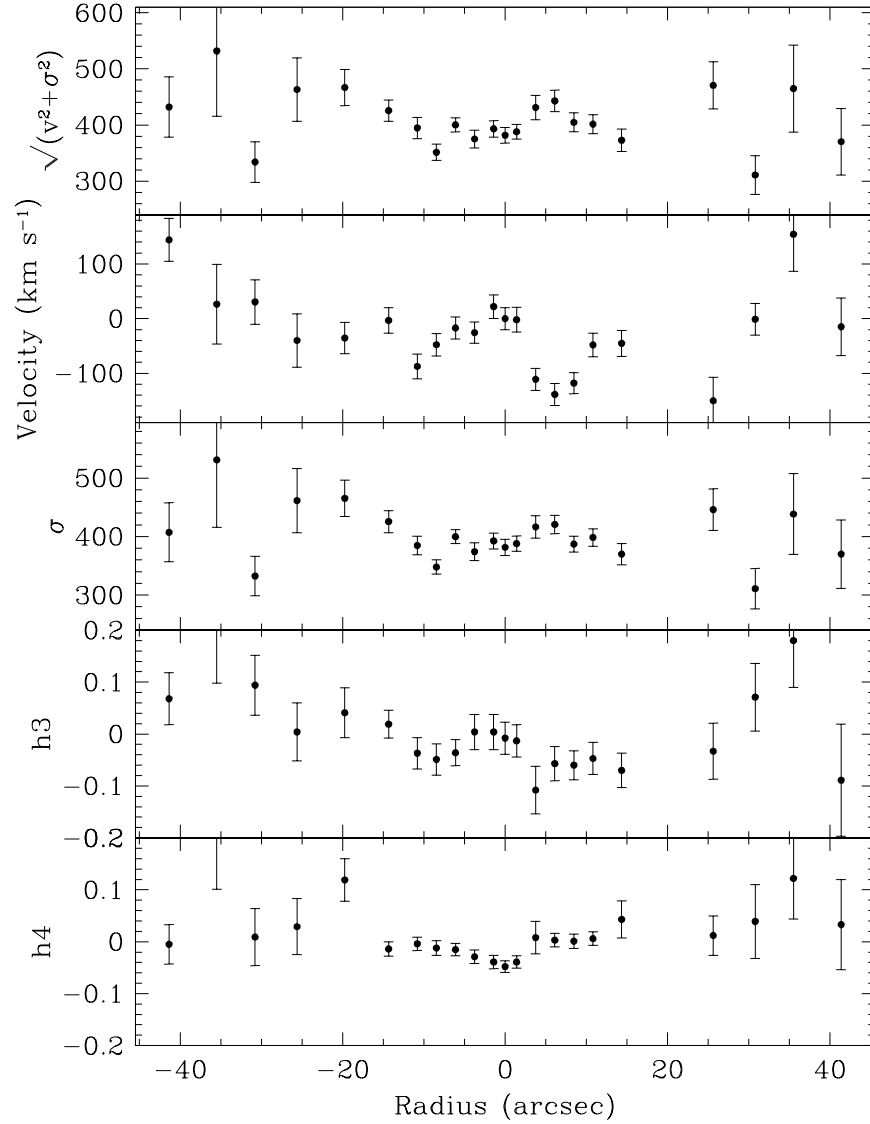


Figure 5.34: The second moment as measured by $\sqrt{V^2 + \sigma^2}$ and the first four Gauss-Hermite moments (mean velocity V , velocity dispersion σ , asymmetric deviations from Gaussian (skewness) h_3 , and symmetric deviations from Gaussian (kurtosis) h_4) for NGC 4889 along the major axis.

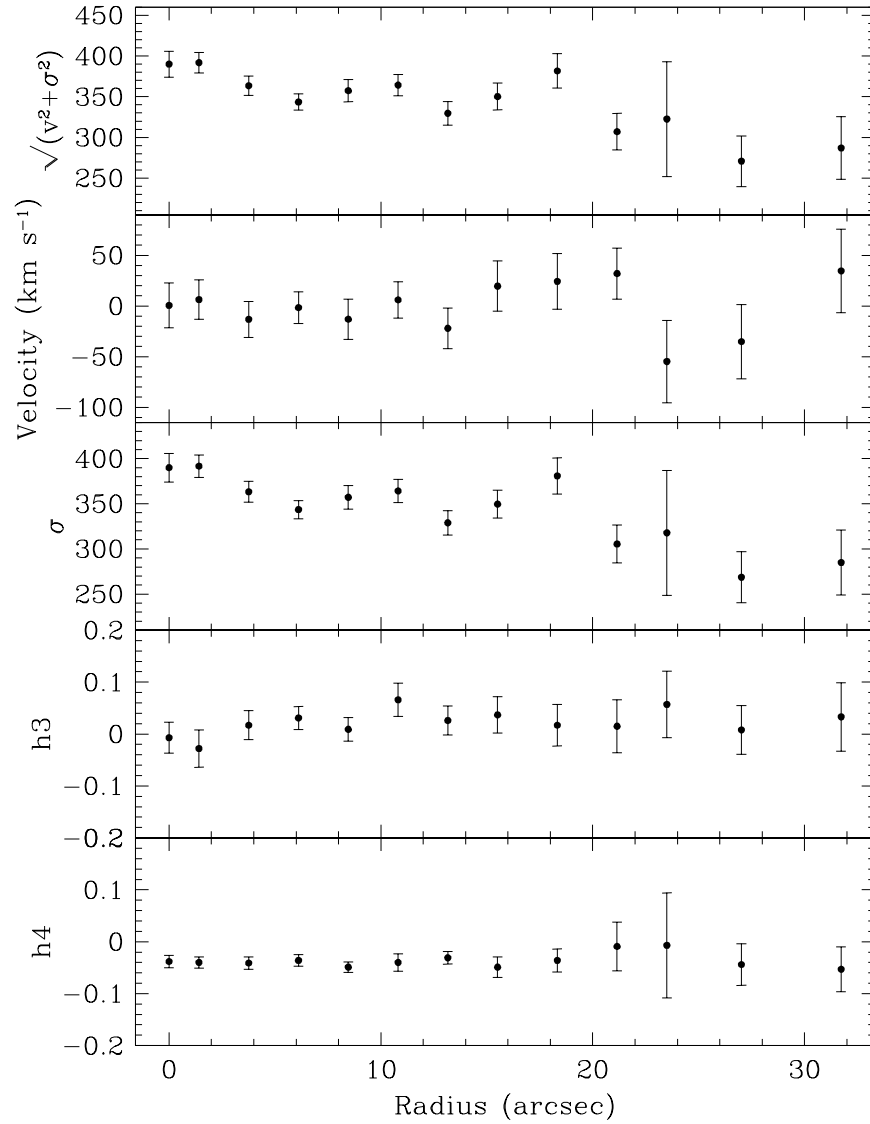


Figure 5.35: The second moment as measured by $\sqrt{V^2 + \sigma^2}$ and the first four Gauss-Hermite moments (mean velocity V , velocity dispersion σ , asymmetric deviations from Gaussian (skewness) h_3 , and symmetric deviations from Gaussian (kurtosis) h_4) for NGC 4889 along the minor axis.

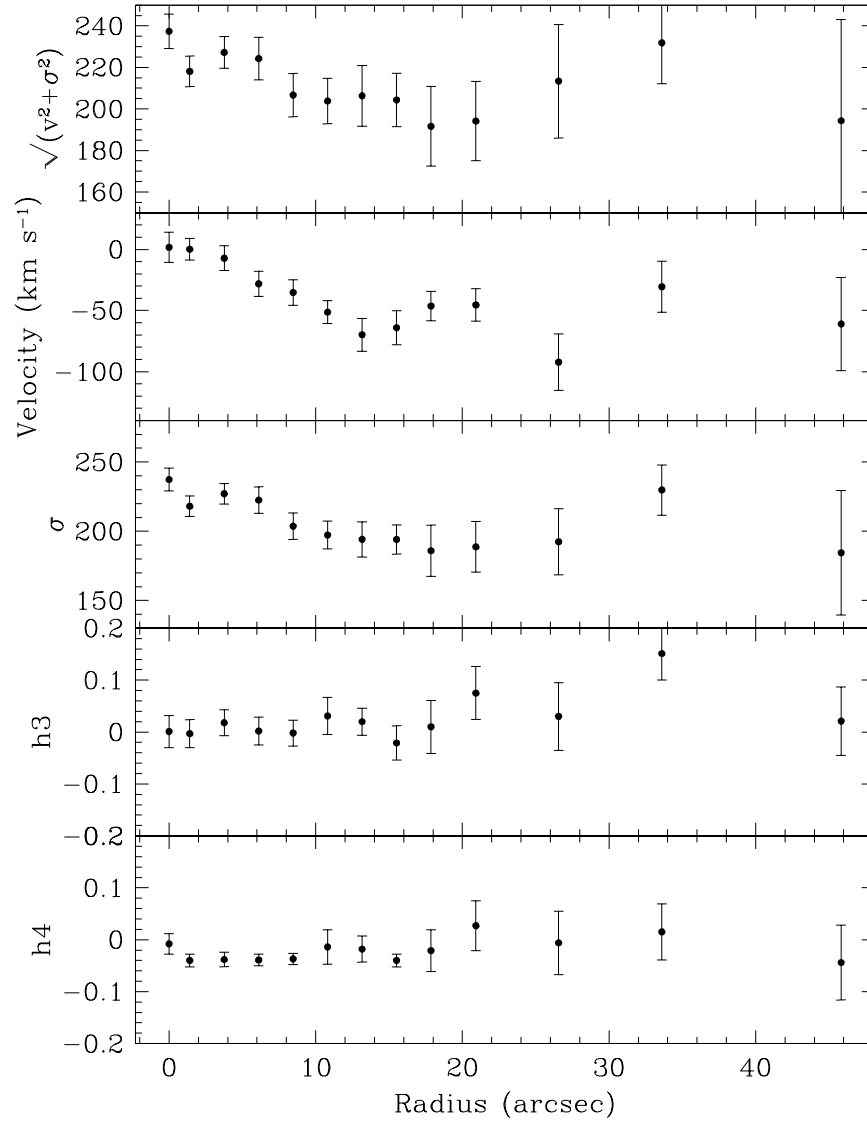


Figure 5.36: The second moment as measured by $\sqrt{V^2 + \sigma^2}$ and the first four Gauss-Hermite moments (mean velocity V , velocity dispersion σ , asymmetric deviations from Gaussian (skewness) h_3 , and symmetric deviations from Gaussian (kurtosis) h_4) for NGC 661 along the major axis.

Table 5.6: NGC 2832 Major Axis Kinematics

r <i>arcsec</i>	v $km\ s^{-1}$	ϵ_v	σ $km\ s^{-1}$	ϵ_σ	h_3	ϵ_{h_3}	h_4	ϵ_{h_4}
0.00	-2.219	26.093	334.679	16.620	0.019	0.046	-0.037	0.012
1.41	26.866	14.537	335.523	13.680	0.018	0.028	-0.033	0.011
3.76	16.058	16.282	341.991	13.924	0.018	0.030	-0.024	0.013
6.11	15.368	12.614	324.093	8.441	0.007	0.021	-0.032	0.012
8.46	8.482	15.303	329.776	9.466	0.011	0.026	-0.009	0.012
10.81	26.310	17.861	304.746	10.329	-0.005	0.028	-0.039	0.010
13.16	-43.542	14.731	322.868	13.284	-0.032	0.026	-0.041	0.012
15.51	8.361	19.267	307.217	12.693	-0.002	0.027	-0.043	0.010
17.86	-35.057	18.436	351.848	13.342	-0.021	0.024	-0.027	0.013
20.21	-15.370	28.180	340.215	19.479	0.026	0.031	-0.034	0.020
22.56	-96.316	30.022	430.283	39.126	-0.111	0.057	0.066	0.052
26.08	-77.428	31.370	365.539	33.868	0.069	0.055	0.050	0.050
31.96	-220.085	36.626	435.953	41.870	-0.110	0.055	0.035	0.045
39.01	-291.418	54.219	515.214	51.042	-0.038	0.115	-0.107	0.098
-1.41	4.346	21.049	338.635	14.086	0.029	0.032	-0.041	0.014
-3.76	-9.964	20.491	324.335	10.785	0.012	0.038	-0.037	0.010
-6.11	13.215	13.307	293.690	11.973	0.006	0.034	-0.038	0.010
-8.46	10.644	13.818	305.612	11.606	-0.017	0.038	-0.030	0.010
-10.81	1.679	14.354	330.043	10.715	-0.006	0.025	-0.036	0.008
-13.16	-12.786	16.316	320.426	12.110	-0.012	0.027	-0.047	0.009
-15.51	-9.448	21.602	333.270	13.628	-0.011	0.033	-0.023	0.013
-17.86	-4.875	18.807	294.652	12.591	-0.040	0.040	-0.032	0.014
-20.21	-75.252	30.243	413.399	24.628	-0.072	0.049	0.050	0.039
-22.56	28.398	20.264	366.902	15.116	0.015	0.024	-0.021	0.013
-26.08	-131.450	25.014	335.710	20.147	-0.059	0.033	0.019	0.037
-31.96	-142.669	41.685	411.268	34.597	-0.008	0.036	-0.037	0.026
-39.01	-330.911	41.967	331.853	87.455	0.000	0.073	-0.014	0.170

Table 5.7: NGC 2832 Minor Axis Kinematics

r <i>arcsec</i>	v $km\ s^{-1}$	ϵ_v	σ $km\ s^{-1}$	ϵ_σ	h_3	ϵ_{h_3}	h_4	ϵ_{h_4}
0.00	10.788	24.308	282.479	17.863	-0.016	0.032	-0.090	0.016
1.41	-34.734	23.212	280.097	18.550	-0.012	0.030	-0.085	0.015
3.76	-55.896	38.060	280.236	21.004	-0.021	0.050	-0.087	0.020
6.11	10.351	41.525	242.969	35.069	-0.017	0.042	-0.104	0.022
8.46	-40.609	77.212	264.290	52.971	-0.067	0.064	-0.111	0.043
10.81	43.349	68.461	213.046	46.230	-0.049	0.044	-0.082	0.025
13.16	-27.346	87.889	247.382	57.331	-0.057	0.060	-0.132	0.060
16.68	91.124	90.188	184.423	53.746	-0.471	0.157	0.352	0.380

Table 5.8: NGC 3379 Major Axis Kinematics

r <i>arcsec</i>	v $km\ s^{-1}$	ϵ_v	σ $km\ s^{-1}$	ϵ_σ	h_3	ϵ_{h_3}	h_4	ϵ_{h_4}
0.00	0.719	8.279	218.037	8.265	0.034	0.032	-0.015	0.012
1.41	-5.711	8.763	221.775	10.794	0.024	0.036	-0.010	0.013
3.76	-9.015	8.625	210.024	8.514	0.013	0.038	-0.027	0.010
6.11	3.577	8.369	195.092	10.199	-0.018	0.049	-0.013	0.017
8.46	-2.228	8.202	193.114	8.084	0.013	0.045	-0.042	0.010
10.81	-0.934	7.905	195.622	9.693	0.001	0.039	-0.036	0.011
13.16	0.853	9.455	198.889	8.970	0.054	0.026	0.009	0.020
15.51	3.584	8.365	200.156	8.286	0.016	0.022	-0.045	0.011
18.09	4.476	9.750	179.640	8.536	0.024	0.047	-0.053	0.011
21.62	30.571	9.479	225.975	11.262	-0.025	0.038	-0.034	0.017
26.08	4.400	8.803	245.986	7.041	0.107	0.028	0.033	0.034
31.96	28.386	16.492	180.275	13.618	0.022	0.039	-0.021	0.024
39.01	13.772	15.230	199.721	13.838	0.027	0.038	-0.055	0.016
47.24	-25.803	17.497	183.167	12.297	0.016	0.036	-0.037	0.012
58.99	-30.184	16.219	169.792	18.195	0.059	0.058	-0.020	0.029
74.26	-14.921	26.042	195.524	28.815	0.023	0.065	-0.034	0.047
90.47	-22.929	49.363	207.904	51.169	0.197	0.177	0.070	0.218

Table 5.9: NGC 3842 Major Axis Kinematics

r <i>arcsec</i>	v $km\ s^{-1}$	ϵ_v	σ $km\ s^{-1}$	ϵ_σ	h_3	ϵ_{h_3}	h_4	ϵ_{h_4}
0.00	16.947	22.938	243.448	16.809	0.053	0.041	-0.076	0.014
1.41	38.872	32.437	264.779	19.192	-0.049	0.045	-0.075	0.022
3.76	55.912	36.851	282.091	19.870	0.029	0.043	-0.093	0.023
6.11	54.423	43.315	253.792	25.450	0.142	0.063	-0.034	0.031
8.46	220.209	53.939	257.823	4.457	0.057	0.007	-0.057	0.101
10.81	271.916	95.315	317.188	13.802	0.001	0.117	-0.086	0.178
-1.41	-114.409	12.153	320.849	8.382	-0.002	0.005	-0.061	0.014
-3.76	-207.258	16.267	368.132	4.377	-0.088	0.037	-0.021	0.031
-6.11	-75.654	43.030	262.163	23.564	0.008	0.035	-0.088	0.020
-8.46	169.587	54.087	345.202	16.901	0.036	0.004	-0.071	0.038
-10.81	68.489	49.863	332.313	29.959	0.169	0.108	0.001	0.033

Table 5.10: NGC 4889 Major Axis Kinematics

r <i>arcsec</i>	v <i>km s⁻¹</i>	ϵ_v	σ <i>km s⁻¹</i>	ϵ_σ	h_3	ϵ_{h_3}	h_4	ϵ_{h_4}
0.00	-0.118	20.369	381.677	13.960	-0.008	0.031	-0.048	0.011
1.41	-1.899	22.811	388.038	12.957	-0.013	0.031	-0.039	0.012
3.76	-111.080	20.219	416.578	19.354	-0.108	0.046	0.008	0.031
6.11	-138.655	20.249	420.693	15.757	-0.057	0.033	0.003	0.013
8.46	-118.049	19.299	387.090	13.635	-0.060	0.028	0.001	0.014
10.81	-48.188	21.352	398.535	14.899	-0.047	0.031	0.006	0.013
14.34	-45.303	23.640	369.980	18.251	-0.070	0.033	0.043	0.036
25.61	-150.145	42.915	446.074	35.546	-0.033	0.054	0.012	0.038
30.78	-1.068	28.719	311.031	34.439	0.071	0.065	0.039	0.071
35.49	154.406	67.530	438.499	69.064	0.180	0.090	0.122	0.078
41.36	-14.892	52.789	369.877	58.358	-0.089	0.108	0.033	0.087
-1.41	21.984	21.372	392.540	13.644	0.004	0.034	-0.039	0.013
-3.76	-25.665	19.613	374.186	15.016	0.004	0.034	-0.029	0.013
-6.11	-17.057	19.940	399.994	11.951	-0.036	0.025	-0.015	0.012
-8.46	-47.659	20.546	347.997	12.367	-0.049	0.030	-0.012	0.014
-10.81	-87.315	22.711	384.881	15.825	-0.037	0.030	-0.004	0.013
-14.34	-3.114	23.388	425.573	18.877	0.019	0.027	-0.014	0.014
-19.74	-35.532	28.827	465.412	31.294	0.041	0.048	0.119	0.041
-25.61	-39.918	48.822	461.539	54.633	0.004	0.056	0.029	0.054
-30.78	30.488	40.638	332.522	33.861	0.094	0.058	0.009	0.055
-35.49	26.476	72.742	531.145	115.399	0.201	0.103	0.207	0.106
-41.36	144.141	39.308	407.335	50.449	0.068	0.050	-0.005	0.038

Table 5.11: NGC 4889 Minor Axis Kinematics

r <i>arcsec</i>	v <i>km s⁻¹</i>	ϵ_v	σ <i>km s⁻¹</i>	ϵ_σ	h_3	ϵ_{h_3}	h_4	ϵ_{h_4}
0.00	0.615	22.206	390.007	15.883	-0.007	0.030	-0.038	0.012
1.41	6.258	19.500	391.685	12.417	-0.028	0.036	-0.040	0.011
3.76	-13.206	17.699	363.303	11.423	0.017	0.028	-0.041	0.012
6.11	-1.562	15.690	343.530	10.080	0.031	0.022	-0.036	0.011
8.46	-13.055	19.808	357.180	13.102	0.009	0.023	-0.049	0.010
10.81	6.053	17.924	364.251	12.824	0.066	0.032	-0.040	0.017
13.16	-22.104	19.987	328.823	13.325	0.026	0.028	-0.031	0.012
15.51	19.628	24.782	349.704	15.374	0.037	0.035	-0.049	0.020
18.33	24.228	27.436	380.830	19.982	0.017	0.040	-0.036	0.022
21.15	32.063	25.146	305.441	20.957	0.015	0.051	-0.009	0.047
23.50	-54.827	40.532	317.795	69.078	0.057	0.064	-0.007	0.101
27.02	-35.179	36.698	268.569	28.260	0.008	0.047	-0.044	0.040
31.73	34.639	41.222	284.902	35.852	0.033	0.066	-0.053	0.043

Table 5.12: NGC 661 Major Axis Kinematics

r	v	ϵ_v	σ	ϵ_σ	h_3	ϵ_{h_3}	h_4	ϵ_{h_4}
<i>arcsec</i>	<i>km s⁻¹</i>		<i>km s⁻¹</i>					
0.00	1.759	12.305	237.366	8.258	0.001	0.031	-0.008	0.020
1.41	0.215	8.863	218.107	7.349	-0.003	0.027	-0.040	0.012
3.76	-7.165	10.100	227.127	7.455	0.018	0.025	-0.038	0.014
6.11	-28.090	10.273	222.522	9.573	0.002	0.027	-0.039	0.011
8.46	-35.190	10.502	203.661	9.554	-0.002	0.025	-0.037	0.011
10.81	-51.267	9.437	197.285	10.049	0.031	0.036	-0.014	0.033
13.16	-69.811	13.453	194.110	12.802	0.020	0.026	-0.018	0.025
15.51	-64.045	13.892	194.063	10.576	-0.021	0.033	-0.040	0.012
17.86	-46.288	12.056	185.937	18.502	0.010	0.051	-0.021	0.040
20.92	-45.405	13.278	188.769	18.247	0.075	0.051	0.027	0.048
26.56	-92.257	23.186	192.392	23.915	0.030	0.065	-0.006	0.061
33.60	-30.492	20.848	229.798	18.168	0.151	0.051	0.015	0.054
45.83	-61.049	38.215	184.484	44.844	0.021	0.066	-0.044	0.072

Chapter 6

Summary and Conclusions

In this dissertation I have studied a sample of elliptical galaxies in order to learn about their dark matter content. This analysis uses some of the best data and dynamical models available to provide a result at the forefront of the field.

We present deep long-slit spectroscopy from the Hobby-Eberly Telescope, providing kinematics out to approximately 1-2 R_e for our sample. For a subsample of these galaxies we perform axisymmetric orbit superposition dynamical models of their dark halos.

In all three galaxies modeled we found that dark matter is necessary to explain the motions at large radii. NGC 821 has the smallest dark matter content with about 15-20% dark matter at $1R_e$ and 45-50% dark matter at $2R_e$. NGC 6702 and NGC 4697 have comparable dark matter fractions; NGC 6702 is 20-35% dark matter at $1R_e$ and 50-60% dark matter at $2R_e$ while NGC 4697 is 30% dark matter at $1R_e$ and about 65% dark matter at $2R_e$. The analysis of NGC 4697 extends even farther to show 93% dark matter at roughly $8R_e$. Given the variations in effective radius measurements, the above numbers carry considerable uncertainty and are given only for comparison with other work.

For two of the three galaxies we find that a halo with a flat central slope (i.e. a flat power law or logarithmic potential halo) is a better fit to the data than the canonical NFW halo. For the third galaxy, NGC 6702, we do not find a difference in the fits of the two halos.

In chapter 4 we show that our assumption of constant stellar mass-to-light ratio over the whole galaxy, while not correct, does not affect the conclusion that dark matter is needed or the general shape of the halo. In chapter 2 we show that employing smoothing in the distribution function similar to other groups' methods does not change the halo results.

All of our galaxies show tangential anisotropy at large radii when a dark halo is not included. This is indicative of the need for a dark halo because the observations at large radii mainly constrain only σ_ϕ , so both σ_r and σ_θ may be artificially decreased to create a smaller total sigma that can be fit without a dark halo. In all cases the motions become isotropic to radial at large radii with the inclusion of a dark halo.

For NGC 821 we model the planetary nebula kinematics of Romanowsky et al. (2003) while assuming the best-fitted halo derived from stellar kinematics. The planetary nebulae need to be on extremely radial orbits in order to be in this potential and have their motions. We find a similar result with NGC 4697. At the center our kinematic data is from stars and at large radii our data are from planetary nebulae. When our best-fitted dark halo is included we again find very large radial anisotropy at large radii. This could indicate that there is something something inherent to the PNe that put them

on radial orbits, a bias of the PNe detections at large radii, or simply that the galaxy as a whole has radial motions at large radii. Regardless, these results demonstrate the degeneracy between mass and anisotropy and reiterates that anisotropy needs to be considered in dynamical studies of galaxies.

Our derived stellar mass-to-light ratios agree with those in the literature when available. Including a correction for galactic extinction the M/L_V are 4.47 for NGC 821, 1.72 for NGC 6702, and 3.97 for NGC 4697.

For NGC-4697 we re-measure the central black hole mass and find that it does not change significantly from the previous measurement of Gebhardt et al. (2003). We may have expected the inclusion of a dark halo to change the stellar mass-to-light ratio and therefore the black hole mass. However, the previous analysis used data that did not extend to where dark matter is a significant fraction of the total mass. Also NGC 4697 had the most significant black hole detection of Gebhardt et al. (2003), with a very well-constrained mass.

In the future I will continue to model galaxy dark halos with several goals. With a large enough sample we can begin to find correlations between halo properties and galaxy characteristics such as environment, age, and structure. We can also provide more constraints on dark matter masses and halo shapes for cosmological simulations of the universe and galaxy formation. In some cases we can modify or corroborate the black hole mass measurements. And lastly, I think perhaps the most interesting future question is why dark halos appear to be flat in the center. In dwarf galaxies supernova-driven winds

can blow out gas, causing a rebound in the dark matter that results in a core (Navarro et al., 1996a). However, in large elliptical galaxies this would not occur and adiabatic contraction would actually cause the dark matter to build up at the center, the opposite of what we are now finding.

Bibliography

- Barth, A. J., Ho, L. C., & Sargent, W. L. W. 2002, *AJ*, 124, 2607
- Beers, T. C., Flynn, K., & Gebhardt, K. 1990, *AJ*, 100, 32
- Bell, E. F. & de Jong, R. S. 2001, *ApJ*, 550, 212
- Bender, R., Doebereiner, S., & Moellenhoff, C. 1988, *A&AS*, 74, 385
- Bertin, G., Bertola, F., Buson, L. M., Danzinger, I. J., Dejonghe, H., Sadler, E. M., Saglia, R. P., de Zeeuw, P. T., & Zeilinger, W. W. 1994, *A&A*, 292, 381
- Binney, J. 1978, *MNRAS*, 183, 501
- Binney, J. & Tremaine, S. 1987, *Galactic dynamics* (Princeton, NJ, Princeton University Press, 1987, 747 p.)
- Binney, J. J., Davies, R. L., & Illingworth, G. D. 1990, *ApJ*, 361, 78
- Blumenthal, G. R., Faber, S. M., Flores, R., & Primack, J. R. 1986, *ApJ*, 301, 27
- Blumenthal, G. R., Faber, S. M., Primack, J. R., & Rees, M. J. 1984, *Nature*, 311, 517

- Bullock, J. S., Kolatt, T. S., Sigad, Y., Somerville, R. S., Kravtsov, A. V., Klypin, A. A., Primack, J. R., & Dekel, A. 2001, *MNRAS*, 321, 559
- Burkert, A. 1995, *ApJ*, 447, L25+
- Cappellari, M., Bacon, R., Bureau, M., Damen, M. C., Davies, R. L., de Zeeuw, P. T., Emsellem, E., Falcón-Barroso, J., Krajnović, D., Kuntschner, H., McDermid, R. M., Peletier, R. F., Sarzi, M., van den Bosch, R. C. E., & van de Ven, G. 2006, *MNRAS*, 366, 1126
- Cappellari, M., Emsellem, E., Bacon, R., Bureau, M., Davies, R. L., de Zeeuw, P. T., Falcón-Barroso, J., Krajnović, D., Kuntschner, H., McDermid, R. M., Peletier, R. F., Sarzi, M., van den Bosch, R. C. E., & van de Ven, G. 2007, *MNRAS*, 379, 418
- Cappellari, M., Verolme, E. K., van der Marel, R. P., Kleijn, G. A. V., Illingworth, G. D., Franx, M., Carollo, C. M., & de Zeeuw, P. T. 2002, *ApJ*, 578, 787
- Carter, D. 1987, *ApJ*, 312, 514
- Cocato, L., Gerhard, O., Arnaboldi, M., Das, P., Douglas, N. G., Kuijken, K., Merrifield, M. R., Napolitano, N. R., Noordermeer, E., Romanowsky, A. J., Capaccioli, M., Cortesi, A., de Lorenzi, F., & Freeman, K. C. 2009, *MNRAS*, 394, 1249
- Cretton, N., de Zeeuw, P. T., van der Marel, R. P., & Rix, H.-W. 1999, *ApJS*, 124, 383

- CWP. 2001, "Rubin, Vera Cooper" Contributions of 20th Century Women to Physics (CWP), <http://cwp.library.ucla.edu/>
- Davies, R. L., Efstathiou, G., Fall, S. M., Illingworth, G., & Schechter, P. L. 1983, *ApJ*, 266, 41
- de Lorenzi, F., Gerhard, O., Saglia, R. P., Sambhus, N., Debattista, V. P., Pannella, M., & Méndez, R. H. 2008, *MNRAS*, 385, 1729
- de Vaucouleurs, G., de Vaucouleurs, A., Corwin, Jr., H. G., Buta, R. J., Paturel, G., & Fouque, P. 1991, *Third Reference Catalogue of Bright Galaxies (Volume 1-3, XII, 2069 pp. 7 figs.. Springer-Verlag Berlin Heidelberg New York)*
- de Vaucouleurs, G., de Vaucouleurs, A., & Corwin, J. R. 1976, in *Second reference catalogue of bright galaxies, 1976, Austin: University of Texas Press., 0-+*
- Dejonghe, H., de Bruyne, V., Vauterin, P., & Zeilinger, W. W. 1996, *A&A*, 306, 363
- Dekel, A., Stoehr, F., Mamon, G. A., Cox, T. J., Novak, G. S., & Primack, J. R. 2005, *Nature*, 437, 707
- Douglas, N. G., Napolitano, N. R., Romanowsky, A. J., Coccato, L., Kuijken, K., Merrifield, M. R., Arnaboldi, M., Gerhard, O., Freeman, K. C., Merrett, H. R., Noordermeer, E., & Capaccioli, M. 2007, *ApJ*, 664, 257

- Einasto, J., Kaasik, A., & Saar, E. 1974, *Nature*, 250, 309
- Emsellem, E., Cappellari, M., Krajnović, D., van de Ven, G., Bacon, R., Bureau, M., Davies, R. L., de Zeeuw, P. T., Falcón-Barroso, J., Kuntschner, H., McDermid, R., Peletier, R. F., & Sarzi, M. 2007, *MNRAS*, 379, 401
- Emsellem, E., Cappellari, M., Peletier, R. F., McDermid, R. M., Bacon, R., Bureau, M., Copin, Y., Davies, R. L., Krajnović, D., Kuntschner, H., Miller, B. W., & de Zeeuw, P. T. 2004, *MNRAS*, 352, 721
- Faber, S. M. & Gallagher, J. S. 1979, *ARA&A*, 17, 135
- Faber, S. M., Tremaine, S., Ajhar, E. A., Byun, Y.-I., Dressler, A., Gebhardt, K., Grillmair, C., Kormendy, J., Lauer, T. R., & Richstone, D. 1997, *AJ*, 114, 1771
- Faber, S. M., Wegner, G., Burstein, D., Davies, R. L., Dressler, A., Lynden-Bell, D., & Terlevich, R. J. 1989, *ApJS*, 69, 763
- Fabricant, D. & Gorenstein, P. 1983, *ApJ*, 267, 535
- Freedman, W. L., Madore, B. F., Gibson, B. K., Ferrarese, L., Kelson, D. D., Sakai, S., Mould, J. R., Kennicutt, Jr., R. C., Ford, H. C., Graham, J. A., Huchra, J. P., Hughes, S. M. G., Illingworth, G. D., Macri, L. M., & Stetson, P. B. 2001, *ApJ*, 553, 47
- Gebhardt, K., Richstone, D., Ajhar, E. A., Lauer, T. R., Byun, Y.-I., Kormendy, J., Dressler, A., Faber, S. M., Grillmair, C., & Tremaine, S. 1996, *AJ*, 112, 105

- Gebhardt, K., Richstone, D., Kormendy, J., Lauer, T. R., Ajhar, E. A., Bender, R., Dressler, A., Faber, S. M., Grillmair, C., Magorrian, J., & Tremaine, S. 2000, *AJ*, 119, 1157
- Gebhardt, K., Richstone, D., Tremaine, S., Lauer, T. R., Bender, R., Bower, G., Dressler, A., Faber, S. M., Filippenko, A. V., Green, R., Grillmair, C., Ho, L. C., Kormendy, J., Magorrian, J., & Pinkney, J. 2003, *ApJ*, 583, 92
- Gebhardt, K. & Thomas, J. 2009, ArXiv e-prints
- Gerhard, O., Kronawitter, A., Saglia, R. P., & Bender, R. 2001, *AJ*, 121, 1936
- Gnedin, O. Y., Kravtsov, A. V., Klypin, A. A., & Nagai, D. 2004, *ApJ*, 616, 16
- Governato, F., Willman, B., Mayer, L., Brooks, A., Stinson, G., Valenzuela, O., Wadsley, J., & Quinn, T. 2007, *MNRAS*, 374, 1479
- Hernquist, L. 1990, *ApJ*, 356, 359
- Hill, G. J., Nicklas, H. E., MacQueen, P. J., Tejada, C., Cobos Duenas, F. J., & Mitsch, W. 1998, in Presented at the Society of Photo-Optical Instrumentation Engineers (SPIE) Conference, Vol. 3355, Proc. SPIE Vol. 3355, p. 375-386, Optical Astronomical Instrumentation, Sandro D'Odorico; Ed., ed. S. D'Odorico, 375–386
- Hinshaw, G., Weiland, J. L., Hill, R. S., Odegard, N., Larson, D., Bennett, C. L., Dunkley, J., Gold, B., Greason, M. R., Jarosik, N., Komatsu, E.,

- Nolta, M. R., Page, L., Spergel, D. N., Wollack, E., Halpern, M., Kogut, A., Limon, M., Meyer, S. S., Tucker, G. S., & Wright, E. L. 2009, *ApJS*, 180, 225
- Ho, L. C., Filippenko, A. V., & Sargent, W. L. W. 1997, *ApJS*, 112, 315
- Houghton, R. C. W., Magorrian, J., Sarzi, M., Thatte, N., Davies, R. L., & Krajnović, D. 2006, *MNRAS*, 367, 2
- Jarrett, T. H., Chester, T., Cutri, R., Schneider, S. E., & Huchra, J. P. 2003, *AJ*, 125, 525
- Kahn, F. D. & Woltjer, L. 1959, *ApJ*, 130, 705
- Katz, N. & Richstone, D. O. 1985, *ApJ*, 296, 331
- Keeton, C. R. 2001, *ApJ*, 561, 46
- Kleyna, J., Wilkinson, M. I., Evans, N. W., Gilmore, G., & Frayn, C. 2002, *MNRAS*, 330, 792
- Komatsu, E., Dunkley, J., Nolta, M. R., Bennett, C. L., Gold, B., Hinshaw, G., Jarosik, N., Larson, D., Limon, M., Page, L., Spergel, D. N., Halpern, M., Hill, R. S., Kogut, A., Meyer, S. S., Tucker, G. S., Weiland, J. L., Wollack, E., & Wright, E. L. 2008, *ArXiv e-prints*, 803
- Kronawitter, A., Saglia, R. P., Gerhard, O., & Bender, R. 2000, *A&AS*, 144, 53

- Lauer, T. R. 1985, MNRAS, 216, 429
- Lauer, T. R., Ajhar, E. A., Byun, Y.-I., Dressler, A., Faber, S. M., Grillmair, C., Kormendy, J., Richstone, D., & Tremaine, S. 1995, AJ, 110, 2622
- Lauer, T. R., Faber, S. M., Gebhardt, K., Richstone, D., Tremaine, S., Ajhar, E. A., Aller, M. C., Bender, R., Dressler, A., Filippenko, A. V., Green, R., Grillmair, C. J., Ho, L. C., Kormendy, J., Magorrian, J., Pinkney, J., & Siopis, C. 2005, AJ, 129, 2138
- Leitherer, C., Alloin, D., Fritze-v. Alvensleben, U., Gallagher, J. S., Huchra, J. P., Matteucci, F., O'Connell, R. W., Beckman, J. E., Bertelli, G., Bica, E., Boisson, C., Bonatto, C., Bothun, G. D., Bressan, A., Brodie, J. P., Bruzual, G., Burstein, D., Buser, R., Caldwell, N., Casuso, E., Cerviño, M., Charlot, S., Chavez, M., Chiosi, C., Christian, C. A., Cuisinier, F., Dallier, R., de Koter, A., Delisle, S., Diaz, A. I., Dopita, M. A., Dorman, B., Fagotto, F., Fanelli, M. N., Fioc, M., Garcia-Vargas, M. L., Girardi, L., Goldader, J. D., Hardy, E., Heckman, T. M., Iglesias, J., Jablonka, P., Joly, M., Jones, L., Kurth, O., Lancon, A., Lejeune, T., Loxen, J., Maeder, A., Malagnini, M. L., Marigo, P., Mas-Hesse, J. M., Meynet, G., Moller, C. S., Molla, M. L., Morossi, C., Nasi, E., Nichols, J. S., Odegaard, K. J. R., Parker, J. W., Pastoriza, M. G., Peletier, R., Robert, C., Rocca-Volmerange, B., Schaerer, D., Schmidt, A., Schmitt, H. R., Schommer, R. A., Schmutz, W., Roos, M. S., Silva, L., Stasinska, G., Sutherland, R. S., Tantaló, R., Traat,

- P., Vallenari, A., Vazdekis, A., Walborn, N. R., Worthey, G., & Wu, C.-C. 1996, *PASP*, 108, 996
- Loewenstein, M. & White, III, R. E. 1999, *ApJ*, 518, 50
- Macchetto, F., Pastoriza, M., Caon, N., Sparks, W. B., Giavalisco, M., Bender, R., & Capaccioli, M. 1996, *A&AS*, 120, 463
- Magorrian, J. 2006, *MNRAS*, 373, 425
- Mamon, G. A. & Lokas, E. L. 2005, *MNRAS*, 363, 705
- Mandelbaum, R., van de Ven, G., & Keeton, C. R. 2008, *ArXiv e-prints*
- Mateo, M. L. 1998, *ARA&A*, 36, 435
- Mathews, W. G. & Brighenti, F. 2003, *ARA&A*, 41, 191
- Méndez, R. H., Riffeser, A., Kudritzki, R.-P., Matthias, M., Freeman, K. C., Arnaboldi, M., Capaccioli, M., & Gerhard, O. E. 2001, *ApJ*, 563, 135
- Méndez, R. H., Teodorescu, A. M., & Kudritzki, R.-P. 2008, *ApJS*, 175, 522
- Méndez, R. H., Teodorescu, A. M., Kudritzki, R.-P., & Burkert, A. 2009, *ApJ*, 691, 228
- Moore, B., Quinn, T., Governato, F., Stadel, J., & Lake, G. 1999, *MNRAS*, 310, 1147
- Naab, T., Johansson, P. H., Ostriker, J. P., & Efstathiou, G. 2007, *ApJ*, 658, 710

- Navarro, J. F., Eke, V. R., & Frenk, C. S. 1996a, MNRAS, 283, L72
- Navarro, J. F., Frenk, C. S., & White, S. D. M. 1996b, ApJ, 462, 563
- Neyman, J., Page, T., & Scott, E. 1961, AJ, 66, 633
- Ostriker, J. P. & Peebles, P. J. E. 1973, ApJ, 186, 467
- Ostriker, J. P., Peebles, P. J. E., & Yahil, A. 1974, ApJ, 193, L1
- Ostriker, J. P. & Steinhardt, P. 2003, Science, 300, 1909
- Peletier, R. F., Davies, R. L., Illingworth, G. D., Davis, L. E., & Cawson, M. 1990, AJ, 100, 1091
- Pellegrini, S., Baldi, A., Kim, D. W., Fabbiano, G., Soria, R., Siemiginowska, A., & Elvis, M. 2007a, ApJ, 667, 731
- Pellegrini, S., Siemiginowska, A., Fabbiano, G., Elvis, M., Greenhill, L., Soria, R., Baldi, A., & Kim, D. W. 2007b, ApJ, 667, 749
- Persic, M., Salucci, P., & Stel, F. 1996, MNRAS, 281, 27
- Pierce, M., Beasley, M. A., Forbes, D. A., Bridges, T., Gebhardt, K., Faifer, F. R., Forte, J. C., Zepf, S. E., Sharples, R., Hanes, D. A., & Proctor, R. 2006, MNRAS, 366, 1253
- Pinkney, J., Gebhardt, K., Bender, R., Bower, G., Dressler, A., Faber, S. M., Filippenko, A. V., Green, R., Ho, L. C., Kormendy, J., Lauer, T. R., Magorrian, J., Richstone, D., & Tremaine, S. 2003, ApJ, 596, 903

- Proctor, R. N., Forbes, D. A., Forestell, A., & Gebhardt, K. 2005, MNRAS, 362, 857
- Ramírez, I. & Meléndez, J. 2005, ApJ, 626, 465
- Ravindranath, S., Ho, L. C., Peng, C. Y., Filippenko, A. V., & Sargent, W. L. W. 2001, AJ, 122, 653
- Richstone, D. O. & Tremaine, S. 1984, ApJ, 286, 27
- . 1988, ApJ, 327, 82
- Rix, H.-W., de Zeeuw, P. T., Cretton, N., van der Marel, R. P., & Carollo, C. M. 1997, ApJ, 488, 702
- Romanowsky, A. J., Douglas, N. G., Arnaboldi, M., Kuijken, K., Merrifield, M. R., Napolitano, N. R., Capaccioli, M., & Freeman, K. C. 2003, Science, 301, 1696
- Rubin, V. C. & Ford, W. K. J. 1970, ApJ, 159, 379
- Rubin, V. C., Ford, W. K. J., & Thonnard, N. 1980, ApJ, 238, 471
- Saglia, R. P., Bertin, G., & Stiavelli, M. 1992, ApJ, 384, 433
- Saglia, R. P., Kronawitter, A., Gerhard, O., & Bender, R. 2000, AJ, 119, 153
- Saha, P. & Williams, T. B. 1994, AJ, 107, 1295
- Sandage, A. & Visvanathan, N. 1978, ApJ, 223, 707

- Sarzi, M., Falcón-Barroso, J., Davies, R. L., Bacon, R., Bureau, M., Cappellari, M., de Zeeuw, P. T., Emsellem, E., Fathi, K., Krajnović, D., Kuntschner, H., McDermid, R. M., & Peletier, R. F. 2006, *MNRAS*, 366, 1151
- Schlegel, D. J., Finkbeiner, D. P., & Davis, M. 1998, *ApJ*, 500, 525
- Schwarzschild, M. 1979, *ApJ*, 232, 236
- Siopis, C., Gebhardt, K., Lauer, T. R., Kormendy, J., Pinkney, J., Richstone, D., Faber, S. M., Tremaine, S., Aller, M. C., Bender, R., Bower, G., Dressler, A., Filippenko, A. V., Green, R., Ho, L. C., & Magorrian, J. 2009, *ApJ*, 693, 946
- Skrutskie, M. F., Cutri, R. M., Stiening, R., Weinberg, M. D., Schneider, S., Carpenter, J. M., Beichman, C., Capps, R., Chester, T., Elias, J., Huchra, J., Liebert, J., Lonsdale, C., Monet, D. G., Price, S., Seitzer, P., Jarrett, T., Kirkpatrick, J. D., Gizis, J. E., Howard, E., Evans, T., Fowler, J., Fullmer, L., Hurt, R., Light, R., Kopan, E. L., Marsh, K. A., McCallon, H. L., Tam, R., Van Dyk, S., & Wheelock, S. 2006, *AJ*, 131, 1163
- Sofue, Y. & Rubin, V. 2001, *ARA&A*, 39, 137
- Sofue, Y. & Wakamatsu, K.-I. 1993, *PASJ*, 45, 529
- Thomas, J., Saglia, R. P., Bender, R., Thomas, D., Gebhardt, K., Magorrian, J., Corsini, E. M., & Wegner, G. 2005, *MNRAS*, 360, 1355
- . 2007, *MNRAS*, 382, 657

- Thomas, J., Saglia, R. P., Bender, R., Thomas, D., Gebhardt, K., Magorrian, J., & Richstone, D. 2004, MNRAS, 353, 391
- Tonry, J. L., Dressler, A., Blakeslee, J. P., Ajhar, E. A., Fletcher, A. B., Luppino, G. A., Metzger, M. R., & Moore, C. B. 2001, ApJ, 546, 681
- Trager, S. C., Faber, S. M., Worthey, G., & González, J. J. 2000, AJ, 120, 165
- Trimble, V. 1987, ARA&A, 25, 425
- Valdes, F., Gupta, R., Rose, J. A., Singh, H. P., & Bell, D. J. 2004, ApJS, 152, 251
- van Albada, T. S., Bahcall, J. N., Begeman, K., & Sancisi, R. 1985, ApJ, 295, 305
- van der Marel, R. P. 1991, MNRAS, 253, 710
- van der Marel, R. P., Cretton, N., de Zeeuw, P. T., & Rix, H.-W. 1998, ApJ, 493, 613
- Verolme, E. K., Cappellari, M., Copin, Y., van der Marel, R. P., Bacon, R., Bureau, M., Davies, R. L., Miller, B. M., & de Zeeuw, P. T. 2002, MNRAS, 335, 517
- Weijmans, A., Cappellari, M., Bacon, R., de Zeeuw, P. T., Emsellem, E., Falcon-Barroso, J., Kuntschner, H., McDermid, R. M., van den Bosch, R. C. E., & van de Ven, G. 2009, ArXiv e-prints

White, S. D. M. & Rees, M. J. 1978, MNRAS, 183, 341

Zepf, S. E., Beasley, M. A., Bridges, T. J., Hanes, D. A., Sharples, R. M.,
Ashman, K. M., & Geisler, D. 2000, AJ, 120, 2928

Vita

Amy Dove Forestell was born in Fairfax, Virginia on November 30, 1979 and was raised in Reston, Virginia. In 2001 she received a Bachelor of Arts in Astronomy-Physics with High Distinction from the University of Virginia. She came to The University of Texas in 2001 to pursue her graduate studies in Astronomy and earned a Master of Arts in 2003 under the guidance of Dr. Thomas Barnes. During her time at the university she has been very involved in the campus community, eventually serving in 2006-2007 as President of the Graduate Student Assembly, the official governing body of graduate students at UT. She also was selected as a member and later as Abbot (President) of the Friar Society, the university's oldest and most prestigious honor society, for which members are selected based on significant contribution to the university and character. In addition to research she has been committed to teaching, and is the only graduate student to have won the Astronomy Department's Board of Visitors Teaching Excellence Award. She is excited to continue teaching as an Assistant Professor at the State University of New York at New Paltz in the fall. At New Paltz she will lead a new astronomy program, including creating a Bachelor of Arts in astronomy and building an on-campus observatory.

Permanent address: 8541 N Capital of Texas Hwy Apt 3082
Austin, Texas 78759

This dissertation was typeset with L^AT_EX by the author.